University of Oxford

Department of Engineering Science

Metal-Organic Framework Materials for Low-κ Dielectrics and Selective Sensing Applications

Arun Singh Babal
St. Cross College

Michaelmas 2021

A dissertation submitted for the degree of Doctor of Philosophy

This thesis is dedicated to my parents and sister,

Surendra Singh Babal and Subhita Babal, Anamika Sohu,

and to my family in India.

. . .

Their endless love and support are what made me the person that I am today.

I would not be standing at the end of this long journey if it were not for them

Preface

This thesis is submitted for the degree of Doctor of Philosophy in the University of Oxford, United Kingdom. The research presented in this work was carried out by the author between October 2017 and December 2021 in the Department of Engineering Science, under the supervision of Professor Jin-Chong Tan.

To the best of my knowledge, the work described in this dissertation is original, except where due reference has been made, acknowledging the work of others. Nothing has been included that is the outcome of work done in collaboration with others, except where explicitly noted. No part of this dissertation, or any similar to it, has been, or is currently being submitted for any degree at this, or any other university. This thesis is less than 250 pages in length.

The work presented herein has been partially published in the following journal papers:

1. **A. S. Babal**; L. Dona; M. R. Ryder; K. Titov; A. K. Chaudhari; Z. Zeng; C. S. Kelley; M. D. Frogley; G. Cinque; B. Civalleri, Impact of pressure and temperature on the broadband dielectric response of the HKUST-1 metal-organic framework. *J. Phys. Chem. C* **2019**, 123, 29427-29435.

2. **A. S. Babal**; B. E. Souza; A. F. Möslein; M. Gutiérrez; M. D. Frogley; J. C. Tan, Broadband dielectric behavior of an MIL-100 metal-organic framework as a function of structural amorphization. *ACS Appl. Electron. Mater.* **2021**, 3, 1191-1198.

3. **A. S. Babal**; J. C. Tan, Influence of mechanical, thermal, and electrical perturbations on the dielectric behaviour of guest-encapsulated HKUST-1 crystals. *J. Mater. Chem. C* **2020**, 8, 12886-12892.

4. **A. S. Babal**; A. K. Chaudhari; H. M. Yeung; J. C. Tan, Guest-tunable dielectric sensing using a single crystal of HKUST-1. *Adv. Mater. Interfaces* **2020**, 7, 2000408.

Arun Singh Babal

Oxford, U.K.

December 2021

Abstract

Metal-organic frameworks (MOF) are fascinating hybrid materials, gained widespread attention from the scientific community since their emergence about three decades ago. The high porosity and tailorability of MOF structures make them an ideal candidate material for both low-κ dielectrics and electrical sensing applications. In this work, an in-depth study on different MOFs was carried out to explore the influence of host-guest interaction and external stimuli including pelleting stress, operating temperature, and frequency, on MOF dielectrics. Additionally, a mechanism was proposed to identify the exceptional MOF materials for target guided electrical sensing and optimise the sensor preparation parameters to enhance its selectivity and sensitivity to revolutionise the conventional electrical sensors. Both polycrystalline (in the form of pellets) and single-crystal MOF samples were studied to gain a deeper insight into both areas.

First, the influence of different external stimuli (temperature, pressure and amorphization) on broadband dielectrics (Hz-MHz and THz) was investigated for both HKUST-1 and MIL-100 MOF systems, to gain a greater understanding of structure-property relation. Secondly, by leveraging the different synthesis approaches, the role of guest molecules was also analyzed for both the polycrystalline powder pellets and single-crystal HKUST-1 MOF systems in the Hz-MHz frequency range. The single-crystal study, which is independent of pelleting pressure and free of grain boundary influence, provided a greater insight into the MOFs intrinsic properties. Thirdly, the impact of host-guest interaction

dependent electrical response was materialised in the form of proof-of-concept electrical sensor applications.

Overall, this work consolidates the candidacy of MOFs as an efficient low-κ material and also expands its future portfolio to the realm of ultra-trace highly sensitive electrical sensing.

Acknowledgements

Firstly, I would like to thank my DPhil supervisor, Prof. Jin-Chong Tan, for helping me at every stage, right from joining DPhil at Oxford till the end of the course. During my doctoral study, his continuous guidance, encouragement, and advice about my work kept me optimistic, energetic and enthusiastic all the time. His endless efforts in making my research presentable in the high impact factor journals are unquestionably admirable. I am especially grateful to Professor Tan for giving me the chance to study at the University of Oxford, for encouraging me to be the best that I can be, and for his constant motivation with my research. Thank you, Professor Tan, for introducing me to the world of the amazing nano-sized MOFs and helping me to bring about an impact in the fields of low-κ dielectric and electrical sensors.

I would like to thank the Engineering and Physical Sciences Research Council (EPSRC) and Samsung for the doctorate scholarship that allowed me to pursue my studies at the University of Oxford. I would also be grateful to the Diamond Light Source for providing excellent facilities and much-needed support during the beamtime experiments, which were conducted to the completion of this thesis. I also have enormous gratitude for all the scientists in ISIS Neutron and Muon Source and Diamond Light Source, with whom I have learned so much about the dedication needed to achieve great science, namely: Dr Svemir Rudic, Dr Gianfelice Cinque, Dr James Taylor, Dr Gavin Stenning and Dr Mark Frogley, whose hard work and motivation continue to inspire me. I would also like to thank my collaborators: Lorenzo Donà and Bartolomeo Civalleri.

I am also grateful to all my colleagues in the Multifunctional Materials and Composites Laboratory lab not only for instigating scientific conversations but also for the numerous happy moments we have shared in the lab. Special thanks go to Dr Abhijeet Chaudhari, Annika F. Möslein, Dr Bárbara Emanuella Souza, Dylan Sherman, Jiahao Ye, Dr Kirill Titov, Dr Mario Gutierrez, Michele Tricarico, Dr Samraj Mollick, Dr Sujeet Rai, Dr Vishal Kachwal, Dr Zhixin Zeng, Dr Yueting Sun and Yang Zhang for their companionship and being part of my everyday life. To all of you, thank you for the laughs, advice, and friendship.

Last but certainly not least, I want to acknowledge both Dr Bhanu Pratap and Dr Sanjay Dhakate, who made me fall in love with scientific research. Finally, I want to sincerely thank my incredible family. I am eternally grateful to my parents for continuously supporting me in every way possible, my sister Anamika for always being there for me and my brother-in-law Naveen Sohu for giving me the best advice along with Sohan Choudhary and Pushpa Sihag for making my life an adventure. They make me feel like I can do anything.

I also want to thank anyone who reads this thesis; I sincerely hope you enjoy it!

Contents

List of Figures

List of Abbreviations

3D	Three-dimensional
AC	Alternating current
AFM	Atomic force microscope
Ag	Silver
Al	Aluminium
ATR-FTIR	Attenuated total reflectance Fourier transform infrared spectroscopy
BDC	Benzene-1,4-dicarboxylate
BET	Brunauer–Emmett–Teller
bIm	Benzimidazole
BM	Birch-Murnagham
BPDC	4,4′-biphenyl-dicarboxylate
BTC	Benzene-1,3,5-tricarboxylate
BTT	1,3,5-benzenetristetrazolate
Cd	Cadmium
Cl	Chlorine
$CuNO_3$	Copper (II) nitrate
Cu	Copper
DC	Direct current
DFT	Density functional theory
DMF	Dimethylformamide

DP	Drop-casting
EtOH	Ethanol
Fe	Iron
$FeNO_3$	Iron (III) nitrate
FMA	Fumarate
FWHM	Full width at half maximum
H	Hydrogen
Hz	Hertz
H_2O	Water
H_3BTC	Benzene-1,3,5-tricarboxylic acid
HFDPA	4,4′-(hexafluoroisopropylidene) diphthalic anhydride
HKUST	Hong Kong University of Science and Technology
HNO_3	Nitric acid
I	Iodine
IC	Integrated circuit
IDE	Interdigitated electrodes
ILD	Interlayer dielectric
Im	Imidazole
IP	Inkjet printing
IPA	Isopropanol
IR	Infrared
IRMOF	Isorecticular metal-organic framework
ITRS	International Technology Roadmap for Semiconductors

kHz	Kilohertz
KKT	Kramer−Kronig transformation
KM	Kubelka−Munk
LP	Large pore
LCR	Inductance (l), Capacitance (C), and Resistance (R)
MHz	Megahertz
Mg	Magnesium
MeOH	Methanol
MIL	Materials of Institute Lavoisier
MG	Manual grinding
MOF	Metal-organic framework
N	Nitrogen
NP	Narrow pore
O	Oxygen
phen	1,10-phenanthroline
ppb	Parts per million
ppm	Parts per billion
PXRD	Powder X-ray diffraction
S	Sulphur
SC	Single-crystal
SEM	Scanning electron microscope
Si	Silicon
Sr	Strontium

TEA, NEt_3	Triethylamine
THz	Terahertz
TPDC	Terphenyl dicarboxylate
TGA	Themo-gravimetric analysis
UiO	University of Oslo
UV-Vis	Ultraviolet-visible
VOC	Volatile organic compound
Zn	Zinc
ZIF	Zeolite imidazolate framework

List of Symbols

A	Absorbance
$\mathring{A}$	Angstroms
θ	Bragg angle
C	Capacitance
cm	Centimetres
ε^*	Complex dielectric constant
n^*	Complex refractive index
σ	Conductivity
ε_∞	Dielectric constant at infinite frequency
^oC	Degrees Celsius
μ	Dipole moment
ω	Frequency
g	Grams
h	Hour
k	Imaginary part of the complex refractive index
ε''	Imaginary part of the dielectric constant
Z	Impedance
K	Kelvin
tan δ	Loss tangent
m	Mass
mm	Micrometres

mg	Milligrams
mm	Millimetres
mmol	Millimole
min	Minutes
nm	Nanometres
n	Real part of the complex refractive index
ε'	Real part of dielectric constant
κ, ε_r	Relative permittivity
T	Relaxation time
ε_s	Static dielectric constant
v	Symmetric stretching mode
ε_0	Vacuum permittivity
λ	Wavelength

Derivation and Application of Metal-Organic Frameworks as a Low-κ Dielectric and Sensing Material

"The good thing about science is that it's true whether or not you believe in it."

– Neil deGrasse Tyson

1

Introduction

With the modern technological advancement in ultra-large-scale integrated circuits (ULSIC), the size of the silicon chips has been constantly shrinking and declined to 5 nm.[1] Thus, it requires the development of interconnection and packaging techniques, which can maintain a high level of the electrical resistance between the interconnects and reduce the capacitance responsible for the cross-talk between wires, while accommodating faster signal propagation with lesser power dissipation.[2, 3] To meet these challenges a few advancements have been made by the scientific community in recent years. First, the conventionally used aluminium is replaced with the highly conductive copper (low bulk resistivity, superior resistance toward the electromigration) as an interconnect and deposited into the already patterned channels in the interlayer dielectric (ILD) materials followed by chemical-mechanical polishing to planarize the surface. Secondly, the physical and interconnection density requirements for the interconnection have been addressed by optimizing the material, which can sustain high mechanical and thermal stress during packaging and its operational environment. Finally, many alternatives for

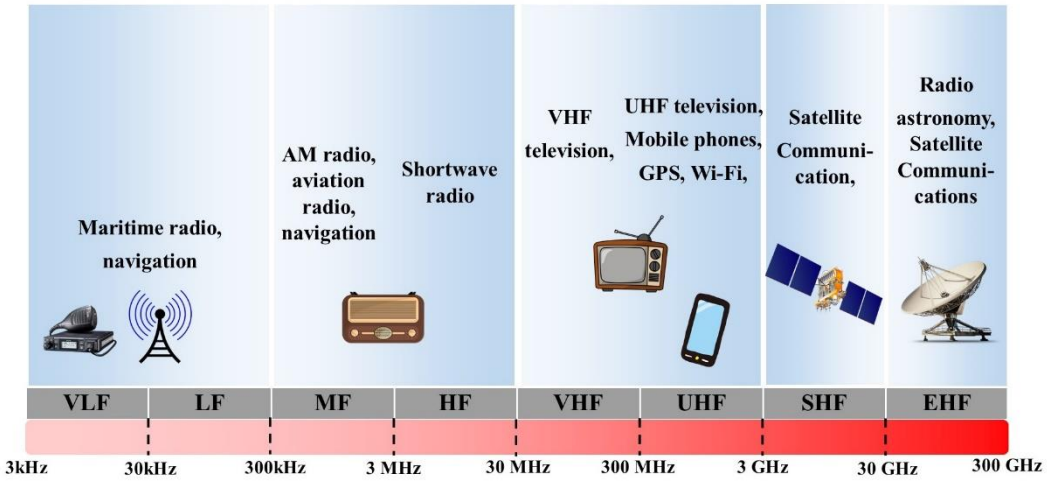

Figure 1.1: The radio-frequency spectrum and corresponding applications. VLF = Very low frequency, LF = Low frequency, MF = Medium frequency, HF = High frequency, VHF = Very high frequency, UHF = Ultra-high frequency, SHF = Super high frequency, EHF = Extremely high frequency.

conventionally used SiO_2 have been proposed. Dielectric materials have several applications in the radio-frequency spectrum as shown in Figure 1.1. For a material to be considered as an interlayer dielectric, it must possess high thermal stability, mechanical robustness, and excellent adhesion to the substrate, while preserving its lower dielectric constant, dielectric loss, a high breakdown field and insulating properties during these circumstances. A low dielectric constant in a material can be obtained *via* tailor-made material by choosing the individual precursor components in a way that allows them to bind in an appropriate configuration causing an overall reduction in molecular polarisation or lowering the material density by introducing porosity. Since air has the lowest dielectric constant of 1, it reduces the material permittivity as well as its density for a composite system

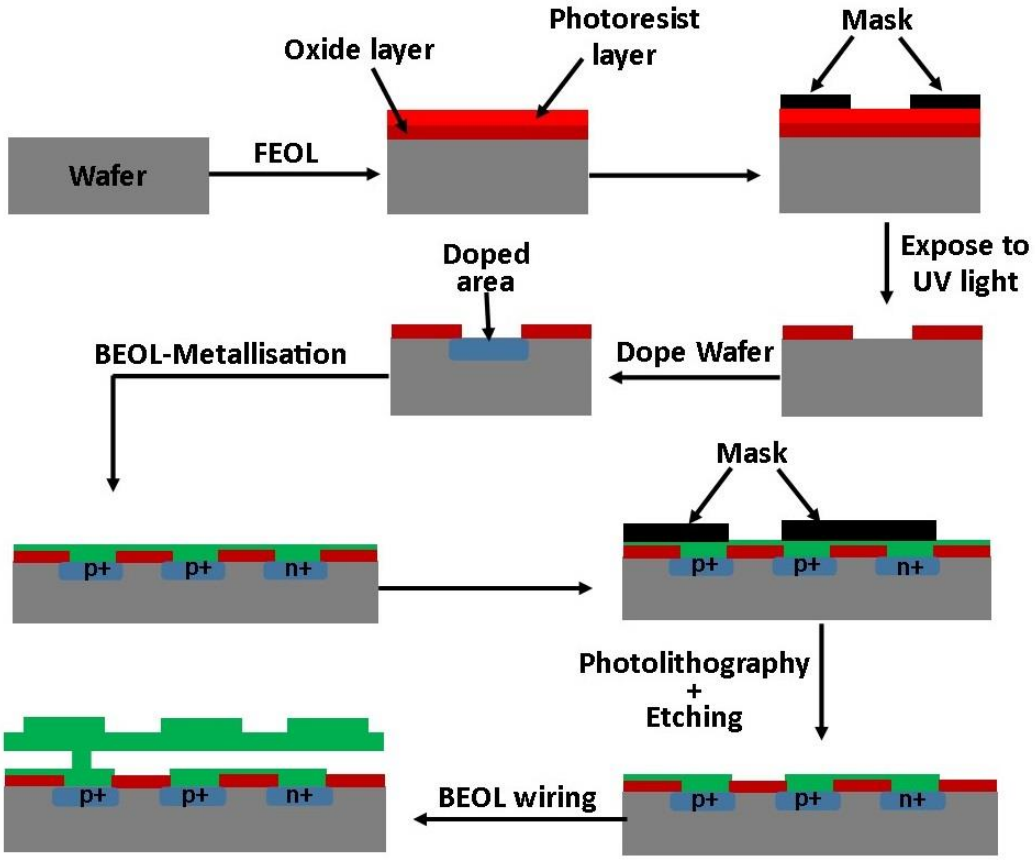

Figure 1.2: Steps of FEOL and BEOL fabrication processes.

incorporating air pockets. According to the International Technology Roadmap for Semiconductors (ITRS), the porous materials will replace the existing interlayer dielectric materials and play a key role by ensuring the charge insulation in integrated circuits (IC).

Integrated circuits are extremely small, and their fabrication is a complex process requiring atomic-level precision. The IC manufacturing comprises 2 stages, namely front-end-of-line (FEOL) processing and back-end-of-line (BEOL) processing. The basic manufacturing steps for both FEOL and BEOL are shown in Figure 1.2. In the FEOL stage, the individual IC components (transistors,

capacitors, and resistors) are constructed inside the wafer by first preparing the silicon wafer and then growing an oxide layer, which is protected by a photoresist material. Exposing the intense UV light through the photomask results in the removal of the photoresist area. The chemical etching process is used to remove the unprotected insulating material and the remaining photoresist material is removed using the developer solution. The electrical properties of the exposed areas are modified by doping processes to create the source and drain of the transistors. After the construction of the individual IC components, the BEOL processing step is performed by depositing the conducting material between the devices in order to connect them (metallization). A layer of UV-sensitive photoresist is added on the top of the metal and UV light is exposed through the mask for the desired layout of the metal wires followed by a chemical etching step removing the unprotected metal. The metal interconnecting wires are isolated by a dielectric layer to prevent short circuits with other layers. The layers in the IC are interconnected by the etching holes known as vias. Finally, the post-fab step is performed including wafer testing, die separation and testing, IC packaging and device testing.

Two different types of dielectrics are used in the VLSI: gate dielectric and interlayer dielectrics. Conventionally, Silicon oxide (SiO_2) has been used as a dielectric. Scaling of transistors caused a decrease in the thickness of the SiO_2 gate dielectrics raising the device performance issues. As the thickness of SiO_2 approaches 1.5 nm, the leakage current becomes greater than 1 A/cm^2, leading to higher power consumption and reduced device reliability. To overcome the issue,

SiO_2 gate dielectrics must be replaced with a high-k dielectric material (κ>30) that possesses an interface density of less than 1011/cm^2-eV, tunnelling current less than 10 mA/cm^2, and negligible hysteresis, to increase the gate capacitance without the associated leakage. As the transistors count increases in the higher technology nodes the interconnect length also increases. The interconnect capacitance dominates the gate capacitance and is the source of the dynamic power dissipation causing a delay in the interconnects. Power dissipation is most significant due to the per performance area requirement. To address the issues, scientists have proposed to reduce the interlayer dielectric to decrease the parasitic capacitance by enabling faster switching speeds and lower heat dissipation. A low-k dielectric material must possess properties such as hydrophobicity, thermally stable (400-450 ^oC) during interconnect manufacturing, chemically stable to withstand the etching and cleaning process, good mechanical properties, i.e., the film should have enough mechanical strength to prevent cohesive failure, and interfaces delamination, compatible with other materials for better adhesion and possess long life for better reliability.

Metal-organic frameworks (MOFs) are the most promising class of porous material in this regard and gained significant attention from the scientific community in recent years due to their immense chemical and structural diversity, high surface area, huge porosity, fine tunability and crystallinity (long-range periodicity). MOFs are hybrid three-dimensional (3D) crystalline porous materials consisting of repeating symmetric units (metal ions or clusters coordinated to the

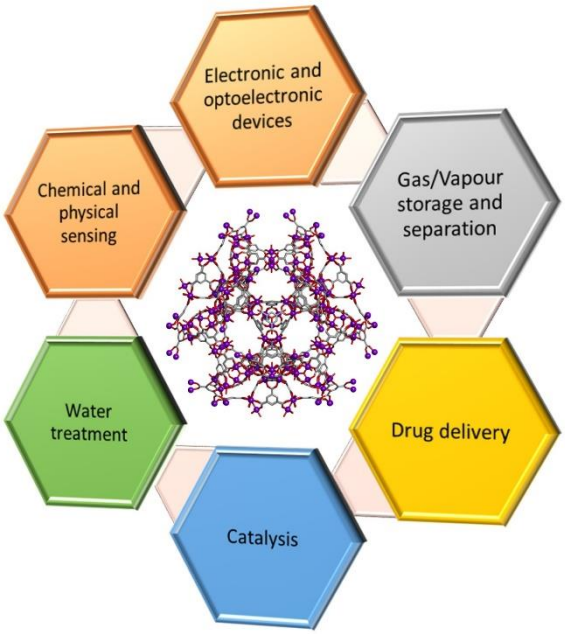

Figure 1.3: Potential application of MOFs in different fields.

organic ligands) through the self-assembly of molecular building blocks allowing many new avenues of research by designing and customising them to meet the specific applications. Theoretical calculations on MOF-based dielectrics have predicted hypothetical static dielectric constant values, κ, of less than 2.0, which is well below the conventionally used SiO_2, whose static dielectric constant is $\kappa \sim 4$, showing their future potential as an interlayer dielectric. While the pioneering studies concerned with MOFs were largely confined to the discipline such as gas storage, chemical separation, catalysis, sensing and drug delivery; nowadays, research activities on MOF-type materials are extraordinarily vibrant and highly cross-disciplinary leading to realising their potential in the field of microelectronics (see Figure 1.3), which is also evident from the exponential growth in the number

of scientific publications reported in recent years. Unlike the dielectric field, the potential of MOFs for gas sensing is well documented using the optical techniques but a handful of studies are available on their direct electrical response, which far outweighs the optical techniques in terms of setup compactness, cost, readability, and sensitivity.[4-7] The high surface area and a very large porosity of the MOF frameworks allows them to intimately enclose the guest species of a size similar to framework pore size. Furthermore, the capacity to precisely control and functionalise the nano-sized pore volume enhances the host-guest interaction resulting in structural, thermal, mechanical, and electrical behaviour changes, which was seldomly encountered in the conventional materials. These unique characteristics of MOFs have opened up new opportunities for exploitation in the fields of tuneable dielectrics and for targeting dielectric sensing applications. As MOFs show such promise in a wide range of applications, it is crucial to understand the underlying fundamental mechanisms and properties that allow such desirable features and to better comprehend the structural stability of the materials, which are yet to be achieved.

Currently, over 90,000 different MOFs have been synthesized and over 500,000 are predicted by a distinct combination of metal nodes and organic linkers. Based on MOFs properties and structure, a general name of the compound can be assigned followed by an ordinal number associated with individual MOF, i.e., MOFs with isorecticular topology IRMOF-1 to IRMOF-16. Russian and Chinese researchers use a specific term metal-organic coordination polymer for MOFs with

a specific composition. MOFs are also termed based on the place of discovery i.e., HKUST-1, UiO, MIL etc. MOFs with zeolite topology have metal ions surrounded by the tetrahedra of nitrogen atoms that are connected through the imidazole linker and abbreviated as ZIF (zeolite imidazole framework). MOFs can be categorized based on their inherent porosity and can be subdivided into 4 categories: a) Dot structure with the zero-dimension cavity, (b) Channel structure with 1D space, (c) Layered structure with 2D space and (d) intersecting channel material with 3D space. Based on guest inclusion and expulsion, MOFs can be categorized into 1st, 2nd and 3rd generation materials (see Figure 1.4). Unlike the 1st generation MOFs, 2nd generation MOFs possess stable porosity and remain intact without change in dimension against the guest removal, i.e., zeolite-like MOFs. In the 1st generation MOFs, the pores of the charged framework are filled with the counter anions. The 3rd generation MOFs also remain stable and show framework flexibility by changing the structural features upon inclusion of foreign guest molecules. Due to this reason, 3rd generation MOFs are also called dynamic and flexible frameworks. These MOFs have several applications such as molecular storage, solid-state sensors etc. The weak interaction between the framework and the guest molecule is the main reason behind the framework's stability. For example, in the compound Cu(ca)$(ROH)_2$, different layers are separated by the hydrogen-bonded guest species and held together by the ca and ROH linker.[8] The removal of the guest molecule leads to a collapse of the framework structure. However, some stacked structures show dynamic response without structural collapse i.e., Cu(ca)$(H_2O)_2$.phz. The 4th

generation MOFs are associated with post-synthetic modification and can retain their topology and structural integrity.

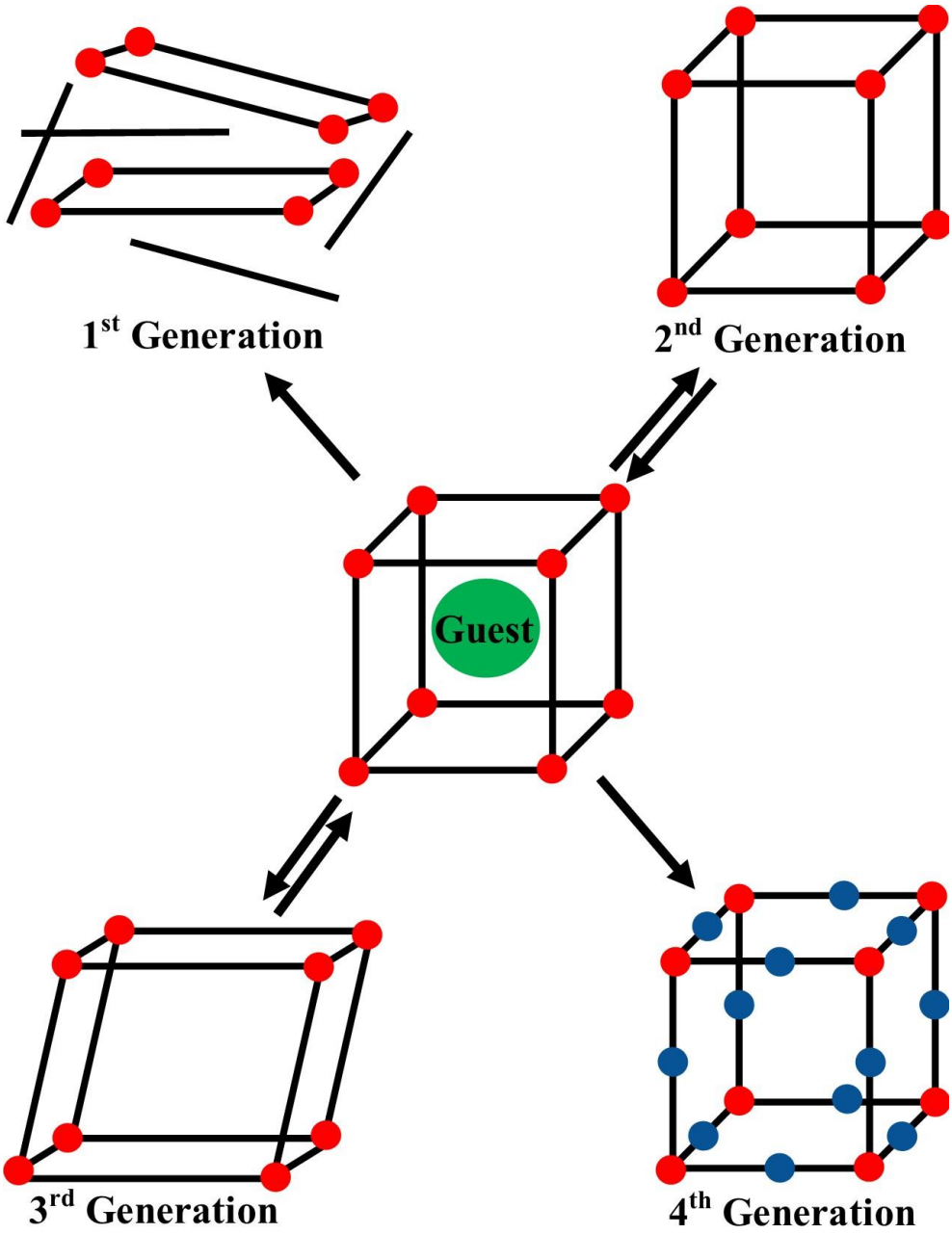

Figure 1.4: Different generations of porous materials based on guest inclusion and expulsion.

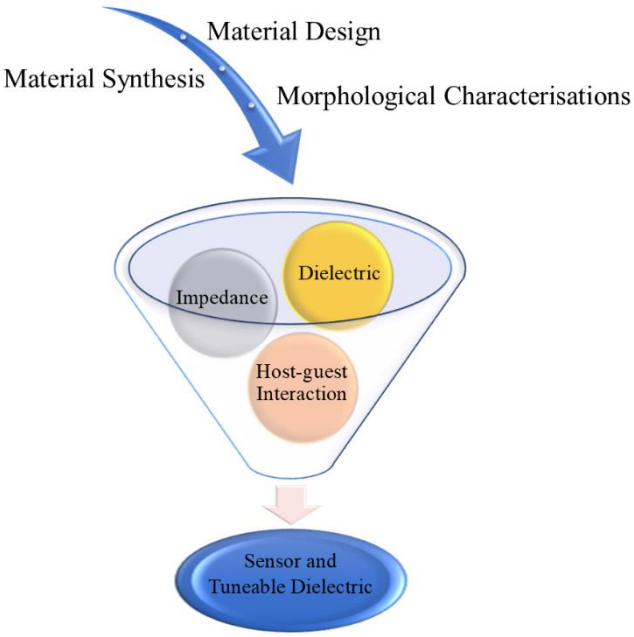

Figure 1.5: Schematic summarising the progression of this thesis.

This DPhil dissertation addresses these challenges by extensively studying the dielectric and electrical properties of different MOF systems and the impact of host-guest interaction on its properties for both interlayer dielectric and sensing purposes, as shown in Figure 1.5. To accomplish these goals using several intermediate milestones, this journal paper-based integrated thesis is divided into 2 parts:

- Part 1: Tuneable MOF dielectric properties and exploration of dielectric-based gas sensing applications,
- Part 2: Published papers (at the end of the chapter)

Part 1 of the thesis is composed of 5 chapters, as summarised in Figure 1.6. Each chapter sets out with a brief introduction and a goal followed by a review of literature, showing the past advancement in that corresponding field. After identifying and reporting the current limitations and challenges, a case study was presented that addressed these shortcomings, which is a summary of the published work. Part 1 can be perceived as a combination of three different tiers. The first tier is concerned with the study of pristine MOF systems for their role as an interlayer dielectric. Chapter 2 demonstrates the impact of different external stimuli (temperature, pressure and amorphization) on dielectric properties of MOF systems in the broadband frequency range (Hz-MHz using LCR meter and THz using synchrotron infrared specular reflectance spectroscopy) in a consolidated manner for an improved understanding of the structure-property relationships, which was lacking in the previous studies. The following was achieved through this approach:

I. Both commercially available Basolite C300 or HKUST-1 (pore diameter ~ 1.1 and 1.4 nm) and Basolite F300 (pore diameter ~ 3 nm) framework systems were employed to study the role of total pore volume on broadband dielectrics.

II. The dielectric measurements were carried out on pelletised polycrystalline pellets (0.5 ton to 10 ton) to understand the impact of the stress-induced crystalline to amorphous phase transition of different MOF systems on the dielectric constants in the broadband frequency range. The stress-dependent

density functional theory (DFT) calculation was also carried out for the HKUST-1 to simulate the experiments.

III. The temperature-dependent dielectric measurements to characterise the stability of the frameworks in the operational range of 20-100 °C.

The second tier of the thesis focuses on the impact of host-guest interactions on the electrical and dielectric properties of MOF systems in the Hz-MHz frequency range. Both pristine and guest-encapsulated frameworks were studied in their polycrystalline powder pellet and single-crystal forms to develop the understanding of the impact of synthesis techniques on materials morphology, its guest-dependent tuneable electrical and dielectric behaviour. The single-crystal study was carried out to gain an insight into the intrinsic value, which is independent of pelleting

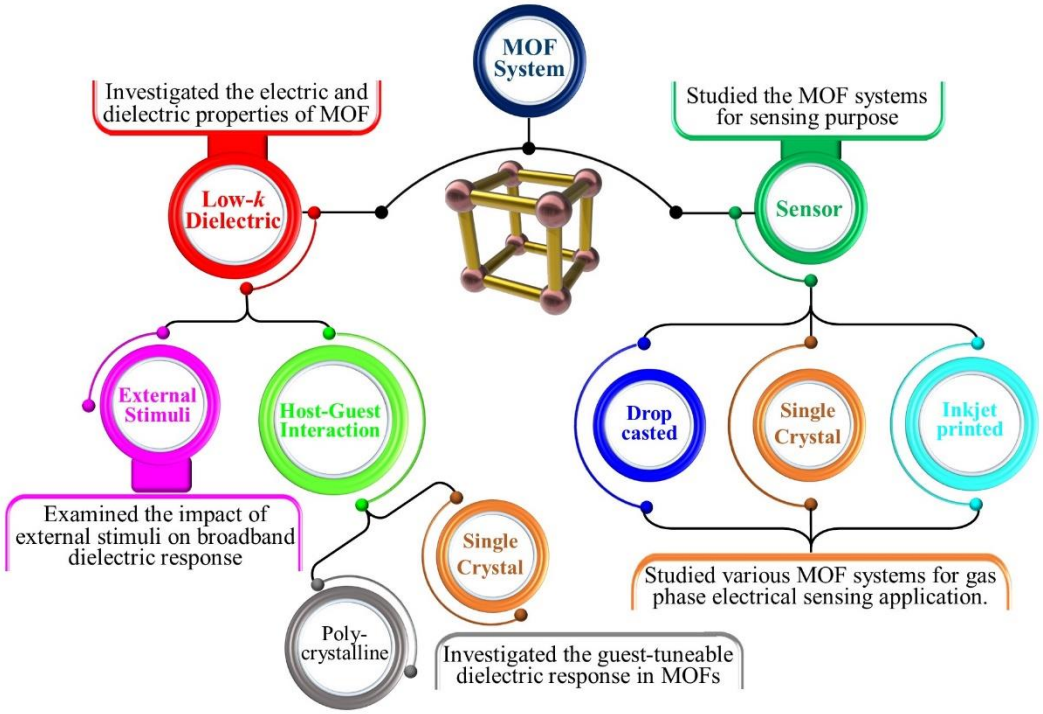

Figure 1.6: A summary of the interconnection of chapters presented in the thesis.

pressure and free of grain boundary influence. Moreover, the impact of mechanical and thermal stimuli, which can result in MOFs structural collapse or framework amorphisation, on the electrical and dielectric response of MOFs was also investigated in addition to the host-guest interaction. The ultimate goal was to utilise the high surface area, porosity and customisability of MOFs to make them a key candidate for the tuneable low-κ material to cater to the need of modern high-speed electronics. Chapter 3 tackles these challenges by discussing the role of guests on tuneable MOF properties using the HKUST-1 framework, due to its low cost, high yield, ease of synthesis and commercial availability.

Finally, in tier 3, the impact of host-guest interaction dependent electrical response was materialised in the form of proof-of-concept electrical sensor applications. The optical techniques are widespread for the gas phase sensing whereas the electric-based sensing of MOF is almost non-existent due to the lack of proper design strategies. In Chapter 4, we addressed these limitations by providing an in-depth framework for iodine gas phase sensing by discussing the role of hydrophilicity, hydrophobicity and interaction sites of MOF structure on the host-guest interaction. This interaction derived alterations in the electrical response was realized in terms of phase angle, impedance and capacitance using the interdigitated electrodes. The experiments were carried out in a way to demonstrate the potential for real-world applications.

In the last Chapter 5, the concluding remarks are formulated and a personal perspective on the further development of MOFs as a key component material for

both the low-κ dielectrics and as a dielectric gas sensor, in order to aid in high-speed communication devices and chemical and physical sensing fields, respectively, are provided.

“I am among those who think that science has great beauty.”

– Marie Curie

2

Impact of External Stimuli on the Broadband Dielectric Response of the Metal–Organic Frameworks

As discussed in the introduction of Chapter 1, a low-κ interlayer dielectric material determines the overall performance and reliability of modern electronics. A better understanding of how the external stimuli (temperature, pressure, and structural amorphisation) could affect the material's dielectric properties at broadband frequency range will further minimise the potential risks associated with the material in harsh conditions and allow us to fine-tune these properties for practical applications. In section 2.1, a brief introduction about dielectric properties is provided along with the current limitations faced by the electronics industry in this area. Moreover, in Section 2.2, the advantages of MOFs as a dielectric material are discussed in detail with their past accomplishments in the field of interlayer dielectrics followed by the remaining challenges, which are yet to be resolved. It motivated the work presented in this D.Phil. dissertation, resolving these challenges

by summarising the two different MOF case studies: HKUST-1 and MIL-100 (encompassing experimental studies and theoretical calculations), which are discussed in Section 2.3.

2.1 A brief overview of dielectric properties of materials

Materials can be classified into one of the following categories: conductor, semiconductor, insulator or dielectric. A dielectric material is an insulating material that can be polarised if an electric field is applied to it, this phenomenon is called dielectric polarisation. Under the electric field, unlike conductors, the charge does not flow but slightly shifts from its equilibrium position. The positive charges shift toward the electric field direction and the negative charges shift in the opposite direction of the electric field resulting in the formation of the electric moment.

In a parallel-plate capacitor (Figure 2.1), when it is connected to the V_0 voltage source, this will result in the building-up of Q_0 free charge on both the plates establishing an E_0 electric field in the gap, which counteracts the source causing a stop in the current flow. Upon the source removal, a V_0 voltage will still be registered in the voltmeter. After the insertion of dielectric material in the gap, dipoles will be created in the material due to the existing electric field E_0, resulting in deposition of net additional counter charges on the plates, whose electric field E_d will be in the opposite direction to the E_0 causing a decrease in the overall voltage ($V_0 \rightarrow V$) and electric field ($E = E_0 - E_d$), as shown in Figure 2.1. When fully charged, the energy stored between the plates can be expressed in the terms of

capacitance *C* and difference in the potential ($\frac{CV^2}{2}$). A capacitor is constructed of two parallel plates with an area of *A* separated by a distance of *d*. It can be further represented in terms of permittivity as follows:[9]

$$\text{Charge } Q = A\sigma \tag{1}$$

$$\text{Electric field } E = \frac{\sigma}{\varepsilon_0} = \frac{Q}{\varepsilon_0 A} \tag{2}$$

$$\text{Voltage } V = \frac{Work\ done}{Charge} = \frac{Fd}{Q} = Ed \tag{3}$$

Where σ is the surface charge density, ε_0 is the vacuum permittivity and *F* is the force experienced by the test charge placed in the field *E*.

From equations (2) and (3), the obtained capacitance:

$$\text{Capacitance } C = \frac{Q}{V} = \frac{\varepsilon_0 AE}{Ed} = \frac{\varepsilon_0 A}{d} \tag{4}$$

The resultant change in the electric field, before and after the insertion of dielectric material between the plate gap is:

$$E_\mathrm{d} = E_0 - E \tag{5}$$

In this dissertation, we adopted κ as relative permittivity (ε_r) or dielectric constant, it can be described as the ratio of the capacitances of a capacitor with and without the dielectric material in place and expressed as:

$$\kappa = \varepsilon_r = \frac{\varepsilon}{\varepsilon_0} = \frac{C}{C_0} \tag{6}$$

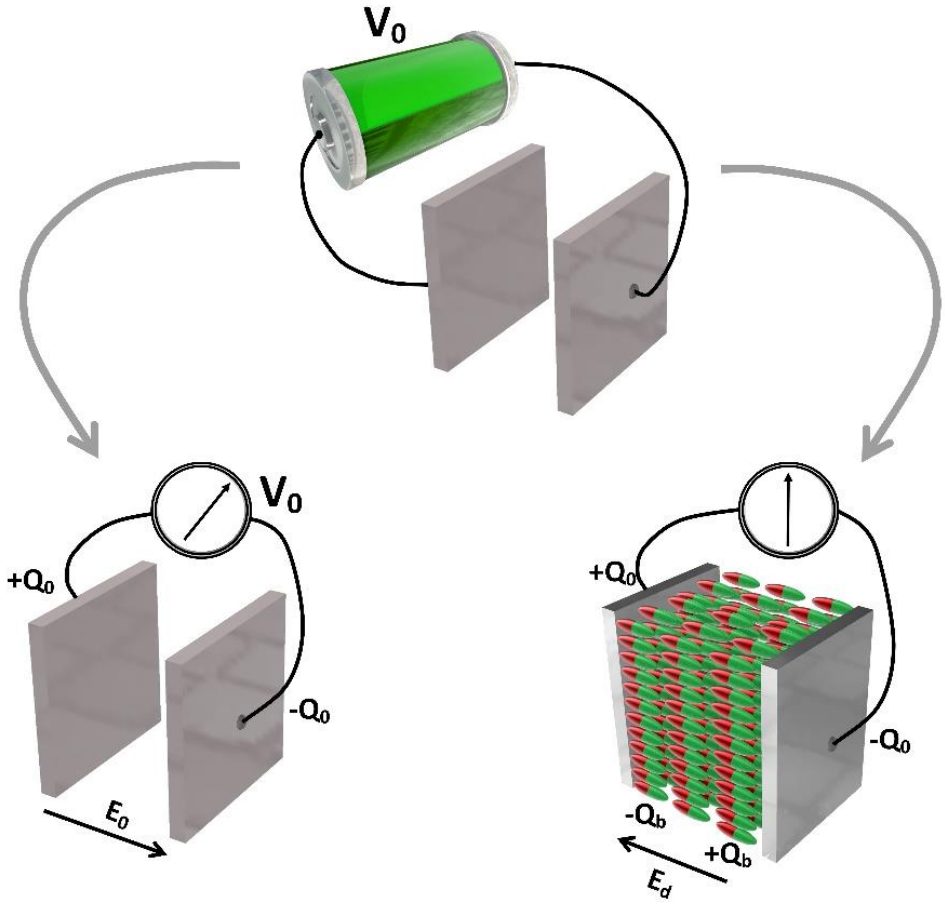

Figure 2.1: A representation of internal mechanisms in the parallel-plate capacitor with and without a dielectric material.

Where ε is the sample permittivity and C_o is the capacitance of a capacitor without the dielectric material.

The flux density D (electric displacement) can be expressed in terms of the produced electric field and permittivity, before and after the dielectric insertion as:

$$D = \varepsilon_0 E_0 \text{ (before)} = \varepsilon E \text{ (after)} \quad (7)$$

From equations (5) and (7), the flux density can also be expressed as follows:[9]

$$D = \varepsilon_0 E + \varepsilon_0 E_{\mathrm{d}}$$

$$= \varepsilon_0 E + P \tag{8}$$

$$= \varepsilon_0 E + N\mu_{\mathrm{E}}$$

$$= \varepsilon_0 E + N\alpha E \tag{9}$$

Where flux density is expressed in terms of material polarisability (α), dipole moment (μ_E), and the number of dipoles per unit volume (N).

The dielectric susceptibility (χ), which is a measure of degree of polarization in a dielectric material under the electric field E in vacuum ε_0, can be expressed using equations (6), (7), and (9) as:[10]

$$\varepsilon E = \varepsilon_0 E + P$$

$$\text{Dielectric constant } \varepsilon_r = 1 + \frac{P}{\varepsilon_0 E} \tag{10}$$

$$= 1 + \frac{N\mu_E}{\varepsilon_0 E} \tag{11}$$

$$= 1 + \chi \tag{12}$$

$$\chi = \varepsilon_r - 1 \tag{13}$$

In solid materials, the electric field experienced by the single dipole is not equal to the applied electric field, but slightly higher due to its proximity to the other dipoles leads to an "effective" electric field E_{eff} of:

$$E_{\text{eff}} = E + \frac{P}{3\varepsilon_0}$$

$$\text{since } P = N\alpha E_{\text{eff}}, \text{ therefore } P = \frac{N\alpha E}{1-\frac{N\alpha}{3\varepsilon_0}} \quad (14)$$

From equations (10) and (14), the relationship between the relative permittivity ε_0 and polarizability can be expressed *via* the Clausius–Mossotti equation as:[10]

$$\frac{(\varepsilon_r - 1)}{(\varepsilon_r + 2)} = \frac{N\alpha}{3\varepsilon_0} \quad (15)$$

The dielectric behaviour of a material is a combination of different polarisation mechanisms (see Figure 2.2), which can encompass the following:[9]

- **Space charge polarisation,** at a very low-frequency electric field (below ~100 Hz), the charges can migrate and can accumulate on the physical barriers such as grain boundaries resulting in the space charge or interfacial polarisation.

- **Dipole polarisation,** occurs due to the electric field (*E*) induced an applied torque on the dipole moment (μ, randomly oriented) of the molecules, causing them to align in the direction of *E*. The dipole polarisability dominates up to the GHz frequency and can be expressed as:

$$\alpha_d = \frac{\mu^2}{3kT} \quad (16)$$

Where *k* is the Boltzmann constant and T is the temperature.

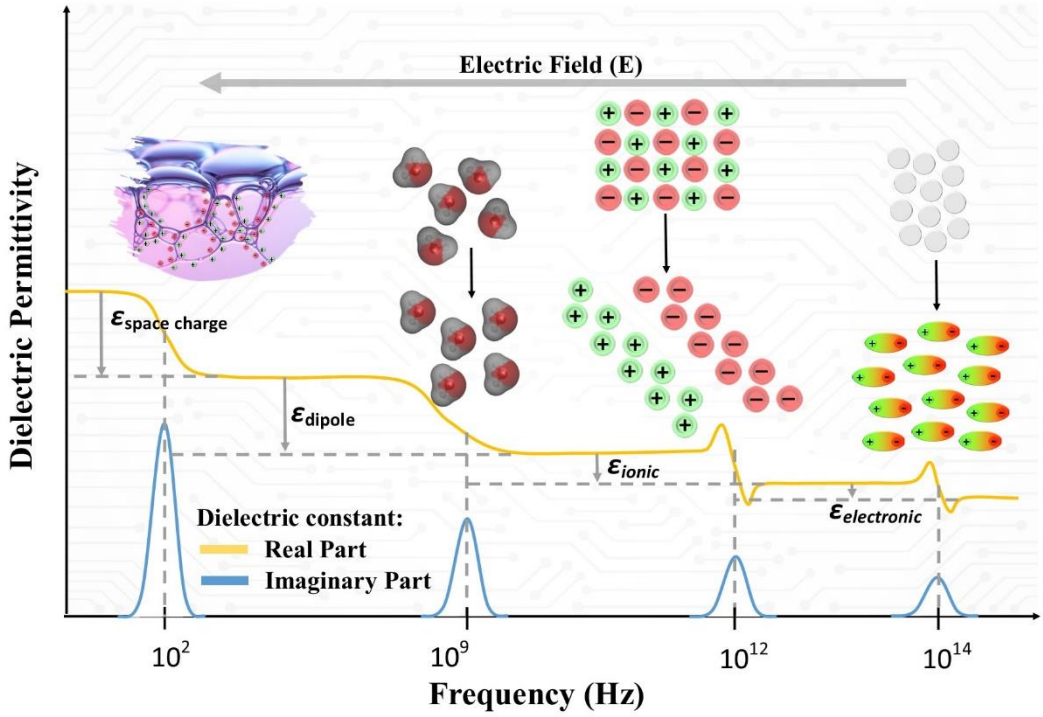

Figure 2.2: Illustration of the frequency-dependent dielectric spectrum, illustrating the various polarisation mechanisms.

- **Ionic polarisation,** occurs by shifting the positive and negative ions with respect to each other in a unit cell at the far-infrared frequency region (THz). The ionic polarisability can be represented in terms of effective charge (Q_{eff}), mass, and resonant frequency as:

$$\alpha_{\text{i}} = \frac{Q_{\text{eff}}^2}{m\omega_0^2} \tag{17}$$

  Where m is the effective mass and ω is the resonant frequency.

- **Electronic polarisation,** at very high frequencies of ~10^{14} Hz (ultraviolet frequency region), the polarisation is mainly contributed by the

displacement of the electrons to its nucleus in an atom under the influence of electric field *E*. Using the Gauss law, the electronic polarizability can be shown as:

$$\alpha_{\mathrm{e}} = 4\pi\varepsilon_0 R^3 \tag{18}$$

Where *R* is the radius of the negatively charged sphere surrounding the positively charged nucleus.

The contribution from all these mechanisms is additive, such that the dielectric constant can be written as:

$$\varepsilon_r = \varepsilon_{\text{space charge}} + \varepsilon_{\text{dipole}} + \varepsilon_{\text{ionic}} + \varepsilon_{\text{electronic/optical}} \tag{19}$$

In the response of the applied electric field, it takes a certain amount of time for the dipoles to rotate in the preferred direction due to friction by collision with the other molecules, resulting in energy dissipation known as dielectric loss (see Figure 2.3). Each polarisation mechanism has a characteristic cut-off frequency at which the contribution of the slower mechanism diminishes. As shown in Figure 2.2, this loss is represented as a peak in the frequency spectrum and is material dependent. Dielectric properties are measured in terms of complex relative permittivity, which consists of the real ε' and imaginary (ε'') parts and can be defined as:

$$\varepsilon^*(\omega) = \varepsilon'(\omega) - j\varepsilon''(\omega) \tag{20}$$

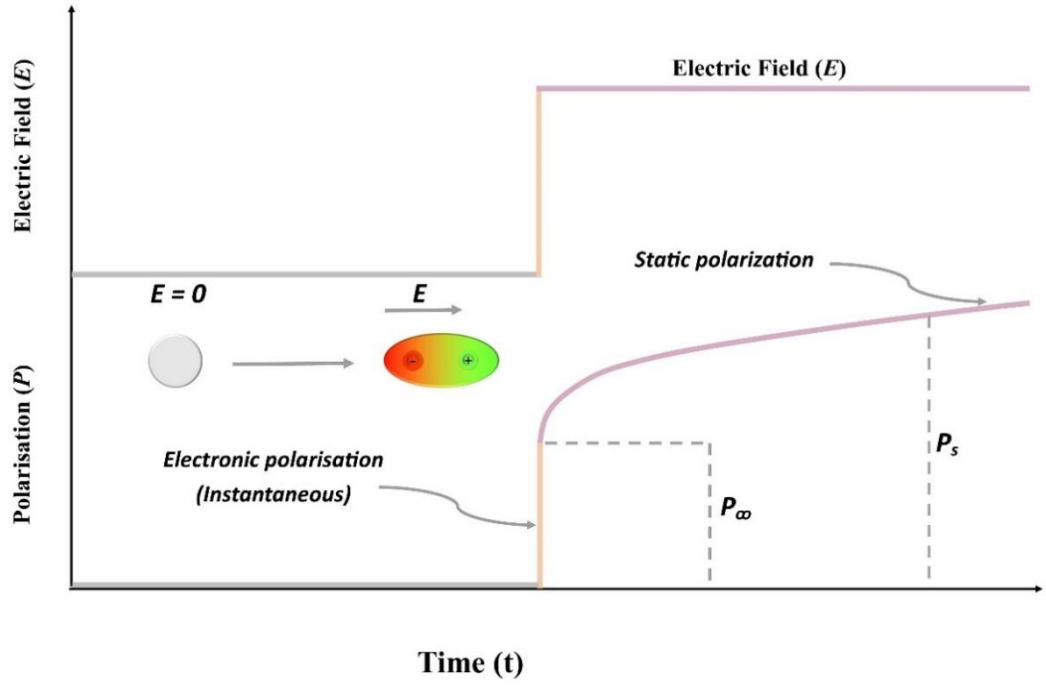

Figure 2.3: A depiction of electric field dependent polarisation in a material.[9] The static polarisation curve shows that the alignment of the dipoles leads to higher polarisation, which will flatten after their complete alignment to the electric field direction.

The real part (ε') represents the amount of energy stored in the dielectric material during the applied external electric field, whereas the imaginary part (ε'') represents the energy loss. The dissipation factor or loss tangent (tan δ) is the ratio of the imaginary part to the real part of the complex permittivity. During the design of high-frequency circuits, it is essential to have a knowledge of the dielectric constant and loss tangent of the material in the operating environment of the device.

Due to the non-instantaneous response of dipole, in complex permittivity (ε^*) the instantaneous contribution (ε_∞) is expected to be within the real part because it is in phase with the electric field, whereas the static contribution is out-of-phase

making it a complex quantity. The difference between the instantaneous and static contribution is dependent upon the relaxation time (τ). At $\tau = 0$, the imaginary part becomes zero and the complex permittivity becomes $\varepsilon^* = \varepsilon_s$ (static dielectric constant). The Debye′s equation was obtained as:[9, 10]

$$\text{Polarisation as a function of time } t,\ P(t) = (\varepsilon^* - 1)\varepsilon_0 E(t) \tag{21}$$

$$\text{In an alternating field, } E(t) = E_0 e^{j\omega t},\ \varepsilon^* = \varepsilon' - j\varepsilon'' = \varepsilon_\infty + \frac{\varepsilon_s - \varepsilon_\infty}{1 + j\omega\tau} \tag{22}$$

where $\varepsilon' = \varepsilon_\infty + \frac{\varepsilon_s - \varepsilon_\infty}{1+\omega^2\tau^2}$ and $\varepsilon'' = \frac{(\varepsilon_s - \varepsilon_\infty)\omega\tau}{1+\omega^2\tau^2}$

According to Maxwell's theory, the square of the refractive index (n) is equal to the relative permittivity ($n^2 = \varepsilon_r$). Due to the relation between the permittivity and polarisation, we can relate the refractive index to the molecular properties, leading to the Lorenz–Lorentz formula:

$$\frac{n_r^2 - 1}{n_r^2 + 2} = \frac{N\alpha(\omega)}{3\varepsilon_0} \tag{23}$$

2.2 Metal-organic frameworks (MOFs)

2.2.1 Implementation of MOFs as dielectric materials

Metal-organic frameworks (MOFs) are highly porous organic-inorganic (hybrid) crystalline materials that consist of a regular array of positively charged metal ions coordinated to organic ligands to form one-, two-, or three-dimensional structures. MOFs have been intensively studied for the past 25 years[11] due to their

high porosity and tuneable surface and structural properties for sensing, gas storage, chemical separation, optoelectronics, and biomedical applications. Except for a few conducting compounds, most MOFs are insulators in nature. This insulating behaviour arises from its ordered porous structure and the presence of covalent and coordination bonds that prevent charge delocalisation and hinder charge transport. Because air has the lowest dielectric constant ($\kappa = 1$) and MOFs are known for their high porosity and insulating nature, thereby making them an ideal candidate to be used as a next-generation interlayer dielectric (ILD) material.

MOFs can be designed based on the metal and linker molecules in a known geometry thus allowing the researchers to tune the structural properties as per the application requirement *via* short and long-range periodicity, tuneable pore size, host-guest interaction, and specific response to chemical and physical stimuli. With their high porosity, MOFs have the potential to offer a tuneable structure-property relation that can be used to meet industrial demands. In the next section, we will focus on the theoretical and experimental advancements of MOFs as a dielectric material followed by the unresolved challenges in the field of MOF dielectrics.

2.2.2 Theoretical studies on MOF dielectrics

A strong theoretical framework allows the researcher to reveal the possible vulnerabilities of material and allows to filter out the weak candidates among the strong ones. In the last decade, a handful of theoretical studies on MOF dielectrics provided much-needed attention to the scientific community toward the potential of MOFs as an emerging interlayer dielectric material. Hermann and co-workers

showed the scientific community the potential of MOF-based structures, for that they theoretically calculated the static dielectric constants for $Zn_4O(CO_2)_6$-based MOF series using the Clausius–Mossotti approach and considered dielectric constant to be a good approximation for alternating fields of frequencies in a microprocessor.[12] In this estimation, it was believed that each atom provides some specific value to the overall molecular polarisability while neglecting both orientational and ionic contributions to the dielectric constant value. They reported that IRMOF-M11 and IRMOF-M13 MOFs ($\kappa \approx 1.5$) are the best candidates for the low-κ dielectrics due to their high bandgap and bulk modulus suitable to the industrial standards. In addition to the Zn_4O-based systems, they also estimated the low dielectric constants for HKUST-1, ZIF-8, and 1,3,5-benzenetristetrazolate (BTT) MOFs indicating that the whole family of MOF-based structures are promising low-κ dielectric materials. The MOF-5 or IRMOF-1 system was further investigated using *ab initio* density functional theory (DFT) calculations, which undertook both electronic and ionic polarisation into consideration.[13] From the dielectric function of optical properties, the imaginary part of the dielectric constant was derived, which was later used to estimate the real part of the dielectric constant using the Kramer−Kronig relationship. A small bulk modulus and a low dielectric constant value of 1.56 at the infinite wavelength of MOF-5 framework showed a similar pattern as other soft materials $M_4O(FMA)_3$ (M = Zn, Cd, FMA = fumarate) systems, which were also studied for their low-κ behaviour (κ = 1.56 (Zn) and κ = 1.51 (Cd)).[14]

The dielectric property of a material can be tailored by either replacing the linker, which completely alters the framework structure or by functionalising the linker to give it additional functionalities. By taking the linker replacement approach, Dinca and co-workers studied the transformation in the electronic band structure of Ba- and Sr-based MOFs by alteration in linker molecules between acetate and trifluoroacetate using the Kohn−Sham DFT calculations in VASP.[15] They suggested that the linker plays a vital role in the electronic band position, band dispersion, and dielectric constants. The replacement of acetate with trifluoroacetate resulted in a slightly higher bandgap and dielectric constant, κ = 1.51 to 1.72 at the infinite frequency for Sr-based MOF. Linker modification approach was taken by Zhang and co-workers, they studied the titanium-based MIL-125 MOF and its derivatives, built by functionalising the benzene-1,4-dicarboxylate (BDC) linker with -OH, -NH_2, -$(NH_2)_2$ and -NO_2 groups and replaced it with linker 4,4′-biphenyl-dicarboxylate (BPDC, MIL-126 MOF) and terphenyl dicarboxylate (TPDC, MIL-127 MOF), using the periodic DFT calculations.[16] The static dielectric constant, obtained along with the directions of principal optical axes, showed an increase in κ with the linker functionalisation. On the other hand, the addition of benzene rings into the BDC linker molecule resulted in a drastic decrease in the dielectric constant from 1.9 (pristine MIL-125) to 1.74 and 1.59 for MIL-126 and MIL-127, respectively. This decrease was associated with the increased pore size resulting from the linker extension. Similarly in another study, they investigated the Zr-based UiO-66 MOF by functionalising its BDC linker with a series of isovalent substituents, including -NH_2, -OH, -$(OH)_2$, -SH,

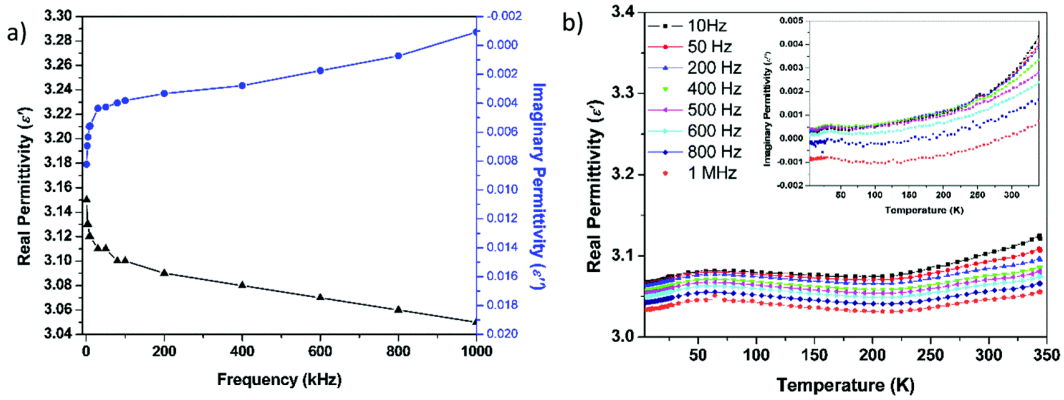

Figure 2.4: (a) Plot of the variation in the permittivity of MOF with frequency, obtained at room temperature; and (b) the corresponding variation in the real permittivity and imaginary permittivity (inset) of MOF with temperature.[18] Reprinted (adapted) with permission from Understanding the linear and second-order nonlinear optical properties of UiO-66-derived metal–organic frameworks: A comprehensive DFT study. The Journal of Physical Chemistry C 2020, 124 (21), 11595-11608. Copyright 2020 American Chemical Society.

-$(SH)_2$, and halogen atoms.[17] Their results indicated the formation of mixed-phase containing several structures because of the some monofunctionalized derivatives of BDC linker. As compared to the pristine MOF, the bandgap decreases with the degree of linker functionalisation, which in turn affects the optical properties leading to a higher dielectric constant. The DFT-calculated dielectric constant for pristine UiO-66 is 2.2, which increased up to 3.0 for UiO-66-$(SH)_2$.

A few theoretical studies were carried out in conjugation with the experiments to validate the claims and identify the reasoning behind the low dielectric behaviour of the MOF materials. Highly thermally stable (up to 450 ^{o}C)

and solvent robust $Zn_2(Hbbim)_2(bbim)]_n$ (H_2bbim = bisbenzimidazole) framework system was investigated for its stable low dielectric constant (κ = 3.05 at 1 MHz) in the Hz-MHz frequency and 3.5 K to 350 K temperature range (see Figure 2.4).[18] The physical origin of this theoretically obtained static dielectric constant of κ = 2, which is in good agreement with the experimentally obtained κ = 3.05 value, is mainly associated with the electronic polarisation with a minimal nuclei movement contribution and vibrational (rigid bbim linker) contribution.

In another study, different MOF systems (IRMOFs, UiO, MIL-140, and MOF-74 family) were studied to identify the role of linker, metal, and framework on dielectric properties by coupling the theoretically calculated values with the experimental values[19] obtained from the literature.[20] They proposed that functionalisation of the linker with fluorine or linker extension results in the higher polarisation of the MOF but its contribution in dielectric constant was negated by the increased porosity content, whereas metal substitution does not alter the dielectric response. Similarly, interpenetrated MOF structure has higher density over its non-interpenetrated counterpart resulting in an increased dielectric response. According to their investigation, they suggested that porosity plays a major role owing to the low dielectric constant of air ($\kappa \sim 1$) trapped in the MOF pores. From these studies, it was established that the introduction of polar functional groups causes an increase in overall polarisation, whereas interpenetrated MOF structure and small linkers lead to higher framework density, causing an enhanced dielectric response in both cases.

Additionally, it was seen that obtained dielectric constant values for materials from the theoretical calculations are quantitative and always lower compared to the experimentally obtained value because it did not take space charge and dipole polarization into consideration. So, a well-defined study that includes both experimental and theoretical calculations in a broadband frequency region rather than just the static value is very much needed to establish a meaningful understanding regarding the dielectric properties of MOFs.

2.2.3 Experimental studies on MOF dielectrics

In this section, we will discuss the advancements that have been carried out by the scientific community to understand the impact of solvent-dependent synthesis and material structure on MOFs dielectrics. The use of polar and non-polar solvents greatly impacts the grain growth of the MOF materials and can also lead to a slight change in the phase of the crystal structure causing a structure-property relation of dielectric response. For example, the ZIF-8 MOF was synthesised in 3 different solvents (methanol, ammonium hydroxide, and water).[21] The ZIF-8 system synthesised in water and ammonium hydroxide showed a phase coexistence between cubic and monoclinic, whereas the methanol synthesised showed a cubic single crystal with a dodecahedron morphology. Both water and ammonium hydroxide solvent synthesised ZIF-8 showed a higher dielectric constant ($\varepsilon'_{\text{Water}}$ = 2.98 and $\varepsilon'_{\text{Ammonium}}$ = 2.81) over methanol ($\varepsilon'_{\text{Methanol}}$ = 2.25), due to their low-symmetric structure and presence of water content in the pores. It includes higher framework polarisation, which is associated with the changes of

bond angles and preferred orientation. Additionally, the influence of structural interpenetration of the MOF framework on its dielectric properties cannot be neglected. Luo and co-workers studied a pair of interpenetrated and non-interpenetrated MOF structures (i.e., MOF-123 (non-interpenetrated) and MOF-246 (interpenetrated)) and showed that the framework interpenetration causes an increase in dielectric constant from 6.3 (MOF-123) to 14.7 (MOF-246) at 323.15 K.[22] They also suggested that the fabrication of interpenetrated MOFs on conductive substrates as thin films can enhance the dielectric constant of the MOFs. These detailed studies on the influence of both solvents and crystal structure on electrical properties pave the way to tune the dielectric properties of MOFs in the radio frequency region.

Both inter-and intraparticle porosity also play an important role in identifying the dielectric constant of a material.[23] To be a low-κ dielectric material, pores should be a few tens of nanometres wide and widths smaller than 5 nm are mandatory. The presence of intraparticle porosity is the material's inherent property and it is desired to achieve a low dielectric constant. However, the interparticle porosity must be reduced to realise a uniform thin film. The difficulty in sealing these voids is a considerable challenge in implementing the films as the low-κ dielectric. Eslava and co-workers studied the ZIF-8 films to assess their potential as future insulators in microelectronics.[24] They showed that the ZIF-8 hydrophobic film is stable at higher temperatures (350 ^{o}C) and effective seals the material with a barrier layer that avoids diffusion of copper atoms from the interconnects due to

the absence of intergranular voids in the synthesised film. They also reported a low dielectric constant (2.33 at 100 kHz), which resulted from the low polarizability and film density, which remained stable during the heating and cooling cycle. These properties were further complemented with sufficient rigidity for chip manufacturing processes (elastic modulus >3 GPa) and the good adhesion to the support showing that MOFs are promising candidates as low-κ dielectrics in microelectronic chip devices. Similarly, Ameloot and co-workers also studied the ZIF-8 and ZIF-67 MOFs for the application as gap-filling low-κ dielectrics in advanced on-chip interconnects.[25] They relied on the selective conversion of native metal-oxide films on the metal interconnect lines into MOFs by exposure to organic linker vapour. Further advances are required to fully grasp the importance of inter and intraparticle porosity in the dielectric candidate materials.

Despite these several advances at the radio frequency region, a firm understanding of the frequency-dependent dielectric constant of material at higher frequencies (<THz) is still lacking, which is essential for the future development of high-speed telecommunication devices. To bridge the gap, Tan and co-workers combined both theoretical and experimental approaches to investigate the flexible bistable MIL-53(Al) MOF that exists in a switchable large pore (LP) and narrow pore (NP) configurations, whose ratio of LP:NP can be tailored by controlling the externally applied stress (pelleting pressure of 7.39 to 739 MPa).[26] The DFT calculations were performed using the CRYSTAL-14 code with B3LYP-D3 functional that optimised the geometry of LP and NP in MIL-100 and calculated

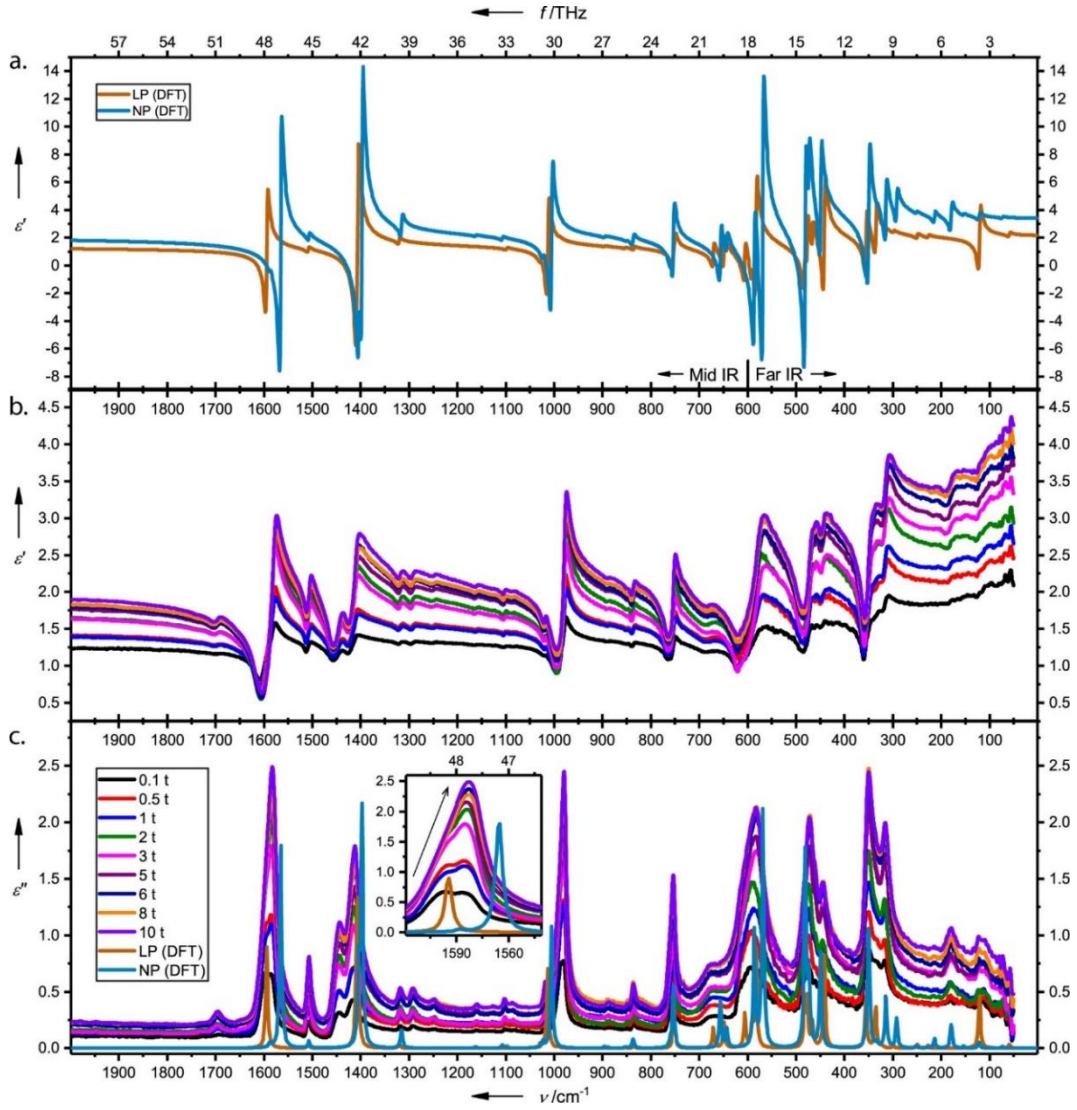

Figure 2.5: Complex dielectric functions of the MIL-53(Al) pellets: (a) real (*ε′*) and (c) imaginary (*ε″*) parts of the DFT-calculated complex dielectric functions showing the relation with experimentally obtained (b) real part (*ε′*) and the (c) imaginary part (*ε″*) as a function of frequency.[26] Reprinted (adapted) with permission from Probing dielectric properties of metal-organic frameworks: MIL-53(Al) as a model system for theoretical predictions and experimental measurements via synchrotron far- and mid-infrared spectroscopy. The Journal of Physical Chemistry Letters 2017, 8 (20), 5035-5040. Copyright 2017 American Chemical Society.

the vibrational frequency for the contribution of nuclear motions underpinning the value of static dielectric constant. The frequency-dependent complex dielectric and refractive index spectra in the IR region (1-120 THz) are obtained by applying the Kramers-Kronig Transformations (KKT) on reflectivity spectra measured using the high-resolution synchrotron infrared (IR) specular reflectance spectroscopy. Both the DFT predicted and experimentally obtained frequency-dependent dielectric spectra are in good agreement with each other and showed that pelleting pressure-dependent increase in dielectric constant is due to the loss of porosity from an initially LP + NP to an (amorphized LP) NP structure. The lowest obtained dielectric constant value for MIL-100 MOF (0.5-ton pellet) was 1.25 at 120 THz frequency (see Figure 2.5). In a similar approach, they also studied the ZIF MOF series and established structural dependency of dielectric constant by showing a strong correlation between the porosity and the framework density assuming that the role of the metal nodes is insignificant.[27] The theoretical studies are a good way to estimate the dielectric properties over a broadband frequency range and to correlate the structure-property relation in MOF frameworks but are currently limited by the type of polarisation and external stimuli that can be taken into consideration. To overcome this limitation, and to fully grasp the mechanisms of MOFs dielectric, theoretical studies must be coupled with the experimental data.

2.2.4 The limitations of existing dielectric materials

Over the past decade, the efficiency of the micro-electronic integrated circuits (ICs) was achieved through increasing the transistor density, circuit

complexity, operating speed, and frequency. So the main focus is on the scale down of the size of transistors and increasing their density on a single chip to improve the electrical and functional performance of ICs. The challenge is to overcome the signal delay caused by the interconnecting wirings, which is inversely proportional to the scaling, and it extends beyond the material properties limiting the overall performance of the ICs.

The interconnects can be explained as a series of resistors and capacitors. There are two major challenges for interconnects: signal delay and power consumption. By replacing the conventional Al/SiO_2 technology with Cu (with lower resistivity metal) and low-κ dielectric material (with a lower dielectric constant) the performance of the current electronics was improved but as with continuous downscaling of ICs, an ultra-low-κ material will be required to overcome the signal delay as we venture into the nanoscale regime.[28] For modern high-speed communication at higher operating frequencies, the power consumption increases drastically in the densely packed ICs, which is proportional to the transistor and wire capacitance, contributed by the power dissipation during signal propagation and leakage between the circuits. Both signal delay and power consumption issues are influenced by the dielectric property of the material, which ultimately affects the electrical system performance.

The research in the low-κ dielectric material is mainly motivated by industrial needs and has been coordinated by the International Technology Roadmap for Semiconductors (ITRS), which layout a roadmap by specifying the

direction and targets to meet the projected overall technological requirements. After the adoption of Cu as a conductor in ICs, the main focus was shifted towards the low-κ dielectric materials, but the advances in this field are slowing down due to the manufacturing complexities, high cost, and reliability issues. In 2015, The ITRS report suggested that further improvements can only be made possible by utilizing the air gap structures to achieve an ultra-low-κ dielectric.[29] Porous materials such as MOFs offer many advantages over their predecessors, including a very high tuneable porosity, which helps in realizing the ultra-low dielectric permittivity, but it is only one of the factors among many to satisfy the ILD specific requirements. To achieve a truly next-generation dielectric material, it must possess a combination of properties such as a huge porosity (up to 90% of its structure), high mechanical, chemical, and thermal stability, low leakage current, permittivity, and dielectric loss in addition to the high breakdown voltage under harsh conditions. A fundamental understanding of all these properties for the material along with the external factors that may impact their real-world performance is necessary to filter out the vulnerabilities of the proposed candidates. Only a handful of studies on MOF dielectrics are available, so an in-depth study on alteration in permittivity resulting from the material synthesis technique, its structure, phase transition, operating temperature, and stress conditions over a broadband frequency range (Hz-THz) is required, which is essential for MOFs reliability and performance for allowing it to be adopted by the industry.

2.3 Case studies (Papers I & II)

In this section, we addressed the lack of understanding on the impact of different external stimuli (temperature, pressure, and structural amorphisation) on MOF dielectrics by carrying out in-depth experimental studies on two different MOF systems- HKUST-1 and MIL-100 in the broadband frequency range (Hz-MHz using LCR meter and THz using synchrotron infrared specular reflectance spectroscopy) and supported the experiments by providing the theoretical calculation for HKUST-1. The MHz measurements were carried out using an LCR meter equipped with a parallel-plate capacitor arrangement operating in the frequency range of 4 Hz to 1.5 MHz, and covering the temperature range of 20 to 100 °C. The high-frequency dielectric behaviour over the far-, mid-, and near-IR regions was measured *via* synchrotron infrared specular reflectance spectroscopy covering the range of 1.2 to 150 THz (40-5000 cm^{-1}). The reasoning behind selecting both HKUST-1 (CuBTC) and MIL-100 MOF systems:

- Both the structure of HKUST-1 and MIL-100 (see Figure 2.6) are well known in the field of MOF materials and their properties except dielectric behaviour are well understood.
- Both MOFs are easy to synthesize with green chemistry at room condition, highly scalable, and commercially available.
- They possess a huge pore volume and low electrostatic repulsion between the crystal, making them suitable candidates for interlayer dielectrics.

- Easy structural deformation under high stress allows a transition from crystalline to amorphous structures, making them a promising candidate to study this phase-dependent transition in dielectrics. It will allow us to understand how the dielectric property of the material evolves under the high-stress environment of the interlayers.
- The hydrophilic nature of both MOFs, which can be considered as a drawback for both MOFs can be overcome by activating the deposited interlayer followed by a coating of a super hydrophobic polymer such as acrylic.

These experiments aimed to achieve the following:

- A comparative study was carried out for commercially available Basolite F300 (Fe-BTC; BTC = benzene-1,3,5-tricarboxylate) over in-house synthesized MIL-100 (Fe) to investigate the synthesis-dependent changes in dielectric properties.
- Both HKUST-1 (pore diameter ~ 1.1 and 1.4 nm) and MIL-100 (pore diameter ~ 3 nm) framework systems were employed to understand the role of total pore volume on broadband dielectrics.
- The dielectric measurements were carried out on pelletised polycrystalline pellets (0.5 ton to 10 tons) to understand the impact of stress generated crystalline to the amorphous phase transition of different MOF systems on dielectric constant in the broadband frequency range. The stress-dependent density functional theory (DFT) calculation was also carried out for the

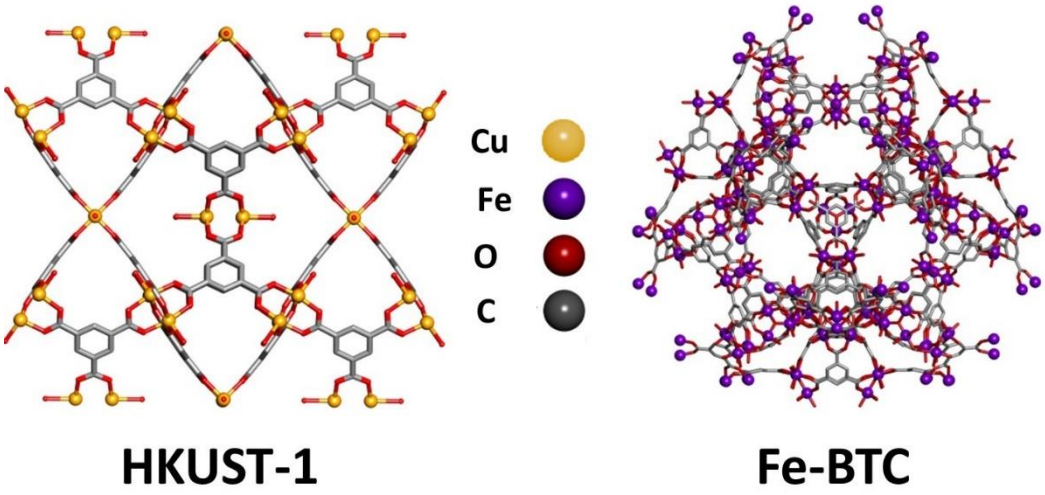

Figure 2.6: Crystal structure of a unit cell of the HKUST-1 and Fe-BTC frameworks.

HKUST-1 to simulate the experiments. The DFT calculations were performed in collaboration with the University of Turin (Italy).

- The temperature-dependent dielectric measurements show the reliability of the frameworks in the operational range of 20-100 °C.

The case studies that are presented in the next sections are the summary of the published work: Paper I and Paper II, respectively, as shown in Part II: Published Papers (at end of the chapter 2).

2.3.1 The HKUST-1 (Cu-BTC) system

The HKUST-1 MOF system was experimentally studied in combination with periodic *ab initio* DFT calculations to provide a complete overview of the contribution of different polarization mechanisms as a function of frequency (See Part II: Paper 1 Table 1). To accomplish this, the dielectric data of pelleted samples (0.5t to 10t) obtained in the radio frequency region (dominated by space charge

polarisation followed by orientational dipole polarization) using the LCR meter equipped with a parallel-plate capacitor arrangement were combined with the infrared region (dominated by ionic and then electronic polarisation) measured *via* synchrotron infrared specular reflectance spectroscopy (as depicted in Figure 2.7). The dielectric spectrum in the radio region was calculated from equations (4) and (6), whereas for the IR region, the dielectric and refractive indices were evaluated by applying the Kramers–Kronig transformation (KKT) on the reflectivity data $R(\omega)$ using the following relations:[30]

$$\text{Frequency dependent reflection, } \phi(\omega_a) = \frac{2\omega_a}{\pi}\int_0^{\infty}\frac{\log\left(\sqrt{R(\omega)}\right)}{\omega^2-\omega_a^2}d\omega \qquad (23)$$

$$n(\omega) = \frac{1-R(\omega)}{1+R(\omega)-2\sqrt{R}\cos(\phi(\omega))} \qquad (24)$$

$$k(\omega) = \frac{-2\sqrt{R}\sin(\phi(\omega))}{1+R(\omega)-2\sqrt{R}\cos(\phi(\omega))} \qquad (25)$$

Where ω_a is the arbitrary frequency, n and k are the real and imaginary parts of the complex refractive index, respectively.

The complex refractive index (n^*) is defined as:

$$n^*(\omega) = n(\omega) + ik(\omega) \qquad (26)$$

$$\varepsilon^*(\omega) = n^*(\omega)^2 \qquad (27)$$

$$\varepsilon'(\omega) = n(\omega)^2 - k(\omega)^2 \qquad (28)$$

$$\varepsilon''(\omega) = 2n(\omega)k(\omega) \qquad (29)$$

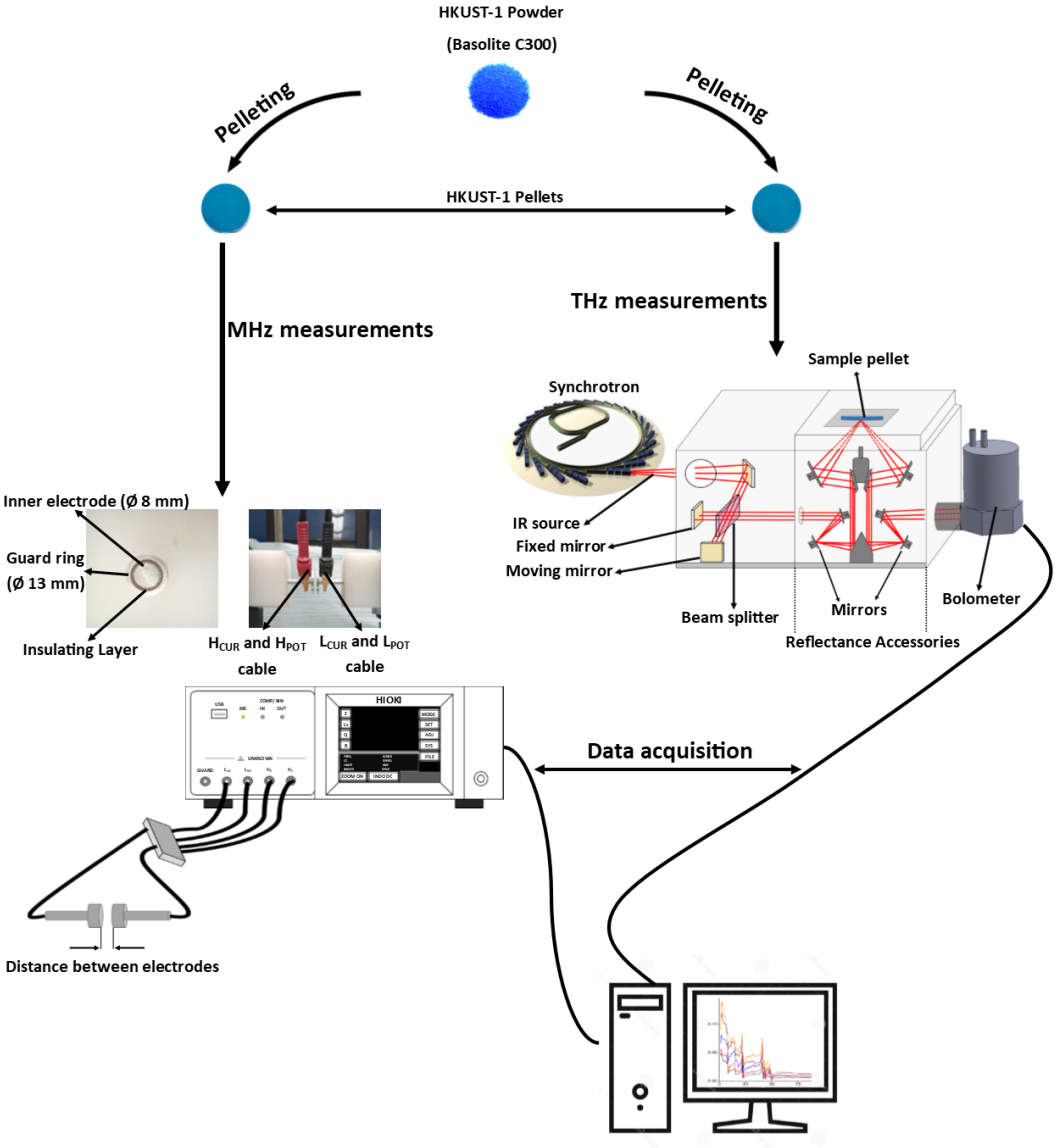

Figure 2.7: Experimental setups used to conduct the broadband dielectric measurements on the HKUST-1 MOF pellets.

A batch of 13-mm diameter pellets was prepared from 0.5, 1, 2, 3, 5, 7 and 10 tons of compressive force to yield a varying degree of structural deformation, amorphisation, and densification to evaluate the impact of free volume and

framework polarisability on dielectric constant. The measurements were carried out under a vacuum to eliminate contribution from the absorbed moisture content. In the radio frequency region, which is mainly dominated by the orientational dipolar polarisation, the dielectric constant of pellets remained thermally stabled between the operating temperature of 20 to 100 °C ($\varepsilon' = 2.42$ to 2.37 for 0.5t pellet at 1 MHz) and scaled in accordance with the pellet density ($\varepsilon' = 2.42$ (0.5t) to 4.88 (10t) at 1 MHz) showing the effect of free volume on permittivity value. As for the optical IR region, unlike the near-IR region, where electronic polarisation plays a dominant role showed a small change in dielectric constant due to its relationship with the framework densification associated with the pore volume, the far-and mid-IR regions are mainly dominated by the ionic polarisation and highly dependent upon the MOF microstructure. The impact of MOFs structural amorphisation resulting from the pelleting pressure on dielectric properties was evaluated by observing the degree of redshift or blueshift in the vibrational modes of copper paddlewheel (metal clusters) and BTC linkers in the far- and mid-IR regions, which resulted from the bond softening and stiffening of the cluster deformation modes, respectively (see Figure 2.8).

The experimental findings were further supported by the pressure-dependent DFT calculations of an ideal HKUST-1 structure at 190 MPa and 360 MPa, which were carried out by a two-step procedure. First, we run a series of constant-volume geometry optimisation in the CRYSTAL-14 code, and then the data were fitted with a Birch-Murnagham (BM) equation of state. Second, the cell

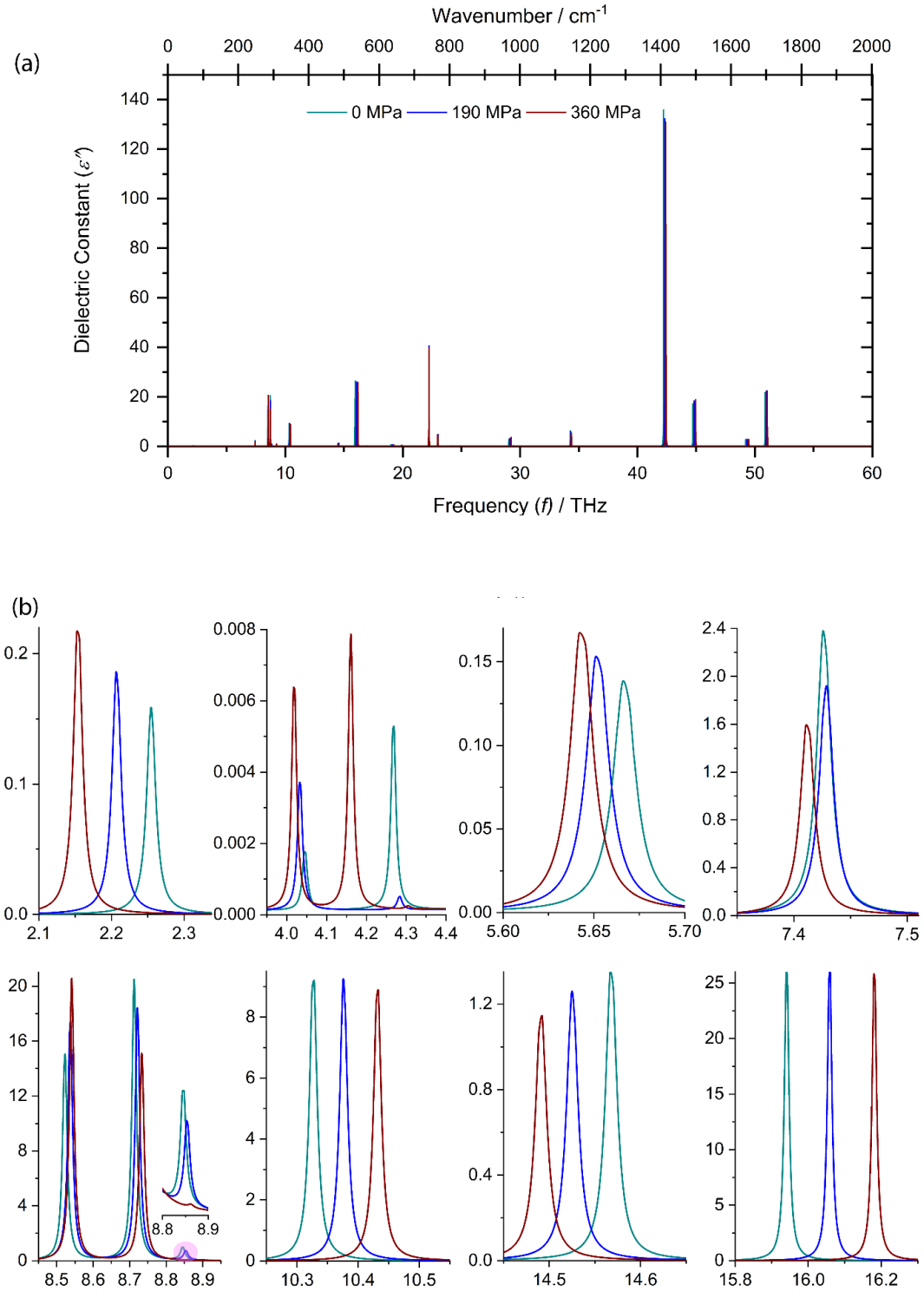
(a)
Wavenumber / cm-1
0 200 400 600 800 1000 1200 1400 1600 1800 2000
0 MPa
190 MPa
360 MPa
Dielectric Constant (ε')
Frequency (f) / THz
(b)

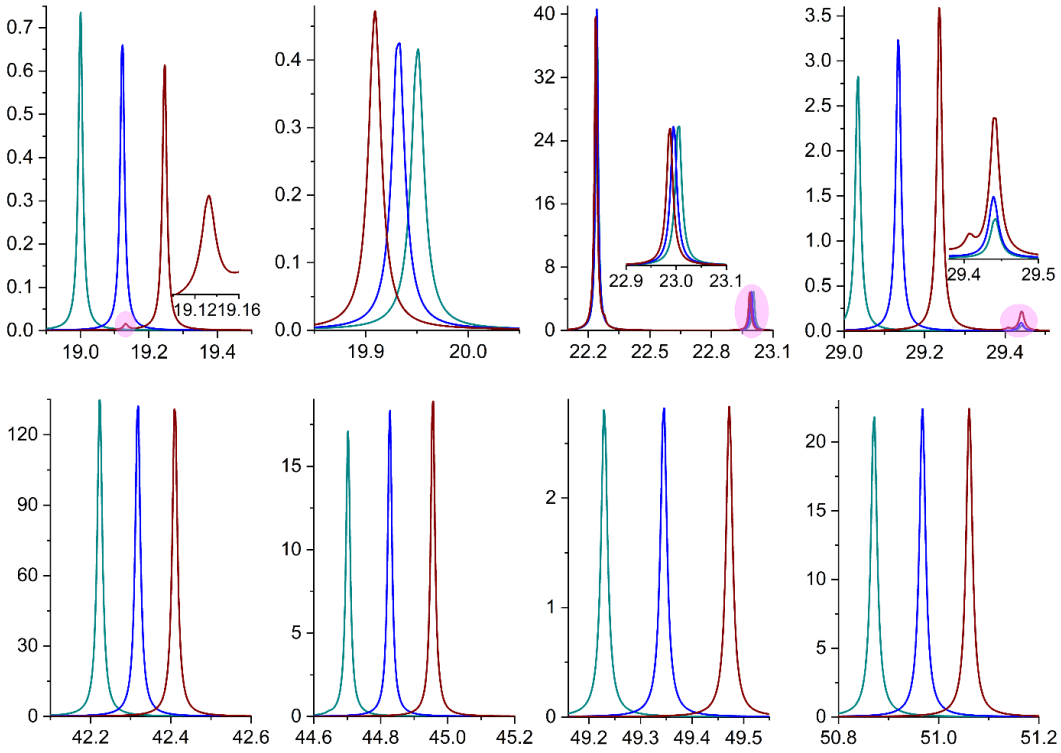

Figure 2.8: Pressure-dependent dielectric constant calculated by DFT. (a) Imaginary part of the dielectric constant (ε''). (b) Zoomed plots of the selected frequencies showing the red/blue shifts.

volume was fixed at the pressure corresponding to 190 MPa and 360 MPa as obtained from the BM fitting. Finally, vibrational frequencies and dielectric response were computed as described above. Note that the present calculations show that at 360 MPa the cubic structure is no longer stable, and a phase transition occurs toward a lower symmetry tetragonal phase. Therefore, the reported results at 360 MPa correspond to the tetragonal unit cell.

The DFT calculations offer insights into the physical mechanisms responsible for dielectric transitions observed in the experiments and enable us to

explain the frequency shifts phenomenon detected under pressure. The phase transition in HKUST-1 can also be associated with the sudden decrease in the rate of a blue shift in vibrational modes of the copper paddlewheel, and a higher decline rate of the red shift in phonon modes of the BTC linkers peak position when the applied stress is greater than 148 MPa (2t pellet) on MOF framework (see Paper I Figure 5 (b)).

This work provided an in-depth insight into the impact of structural deformation, sample amorphisation, framework densification, the operating temperature on the complex dielectric response in the broadband frequency region, which is essential for its practical implementation as an interlayer dielectric and high-frequency THz applications.

2.3.2 The MIL-100 (Fe-BTC) system

The broadband dielectric study of the HKUST-1 system provided a deeper understanding of the MOF's potential, but some challenges were left untouched. To tackle these challenges, two porous iron trimesate frameworks, namely, commercial Basolite F300 (Fe-BTC) with an unknown structure due to its poor crystallinity and in-house synthesized MIL-100(Fe) (using a green mechanochemistry route)[31] of well-defined crystalline structure, have been compared to evaluate the effect of synthesis route on electric and broadband dielectrics properties under similar conditions as the HKUST-1 system, which is described in an earlier section 2.3.1. Interestingly, although the chemical composition of commercial Basolite F300 and

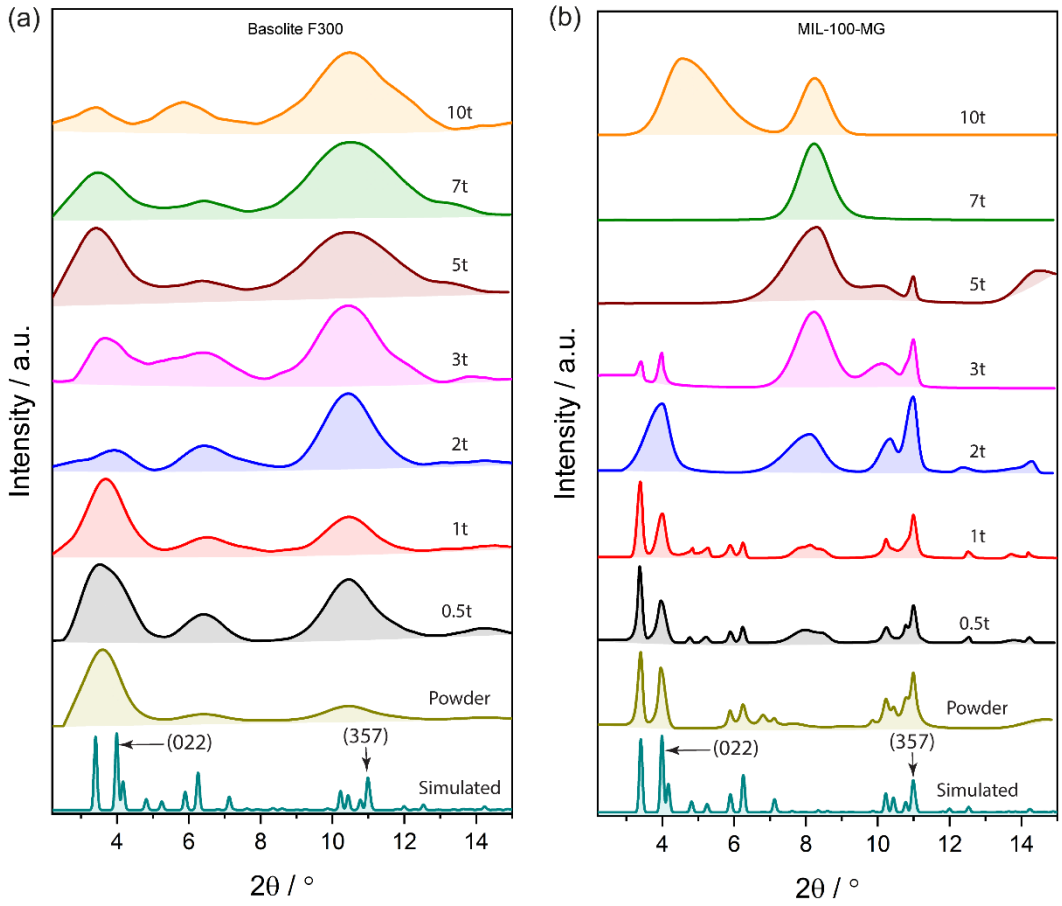

Figure 2.9: The XRD patterns for: (a) BasoliteF300 and (b) MIL-100-MG pellets, both normalized with respect to the highest data point.

MIL-100 (Fe) is similar (both are constituted by Fe(III) and BTC, in fact), the structure, purity, counterion, or remaining solvent differ, whose impact on materials property was evaluated in both the radio and IR frequency range.

For this study, the MOF powders were pressed into 13-mm diameter pellets under a series of compressive forces: 0.5, 1, 2, 3, 5, 7 and 10-ton. For easy understanding, the synthesised MIL-100 was termed as MIL-100-MG, where MG stands for the manual grinding method. Interestingly, the effect of different

synthesis routes can be observed in the dielectric constant values. It was observed that the MIL-100-MG pellets showed higher dielectric value over its counterpart Basolite F300, in addition to the dielectric spread (between 0.5 ton and 10-ton pellets), which was associated with the frameworks pore blockage (resulting from the mechanochemical grinding method even after thorough washing) and a higher degree of amorphisation with pelleting, suggesting that the chosen material synthesis route could significantly impact the resultant dielectric property. At 20 °C, the ε' value shows a sudden surge from 1t pellet to the 2t pellet for Basolite F300 sample (ε' = 2.85 to 3.89, 1 MHz), which can be associated with the loss of long-range periodicity, whereas, in MIL-100-MG pellets, the ε' value at 1 MHz shows a step increase from 1t to 2t (ε' = 3.58 to 4.34), 2t to 3t (4.34 to 5.05), and 3t to 5t (5.05 to 5.78) pellets indicative of an incremental degree of structural amorphisation with increased pelleting pressure. The structural evolution of all the MOF pellets was tracked using the powder XRD (see Figure 2.9). At the highest pelleting pressure, the Basolite F300 material sustains some of its crystallinity whereas the MIL-100-MG was completely amorphised at 7-ton pelleting pressure. The amorphisation effect can also be observed through the dielectric loss (tan δ) and should be kept to a minimum for a promising dielectric candidate. Both MIL-100 and Basolite F300 showed a dielectric loss below 0.07 at 10-ton pressure (see Figure 2.10). Initially, at lower pelleting pressure, MIL-100-MG pellets showed slightly less dielectric loss over Basolite F300 pellets due to their higher crystallinity. However, at higher pelleting pressure, the MIL-100-MG framework completely amorphised hence surpassing the loss of Basolite F300, which still

possess some degree of crystallinity. It was also evident in the MIL-100-MG sample where the framework loses most of its crystallinity causing a sudden surge in tan δ value (see Figure 2.10 (b)). In addition to the radio frequency measurement, the properties in the IR region were also measured to determine the applicability of MOF material for high-speed electronic devices.

In this regard, the MIL-100-MG pellets were later chosen for the broadband dielectric study due to the clear transition of its structure from a crystalline to an amorphous phase as a function of pelleting pressure. It was observed that unlike the softening and stiffening in vibrational modes of HKUST-1 (as shown in section

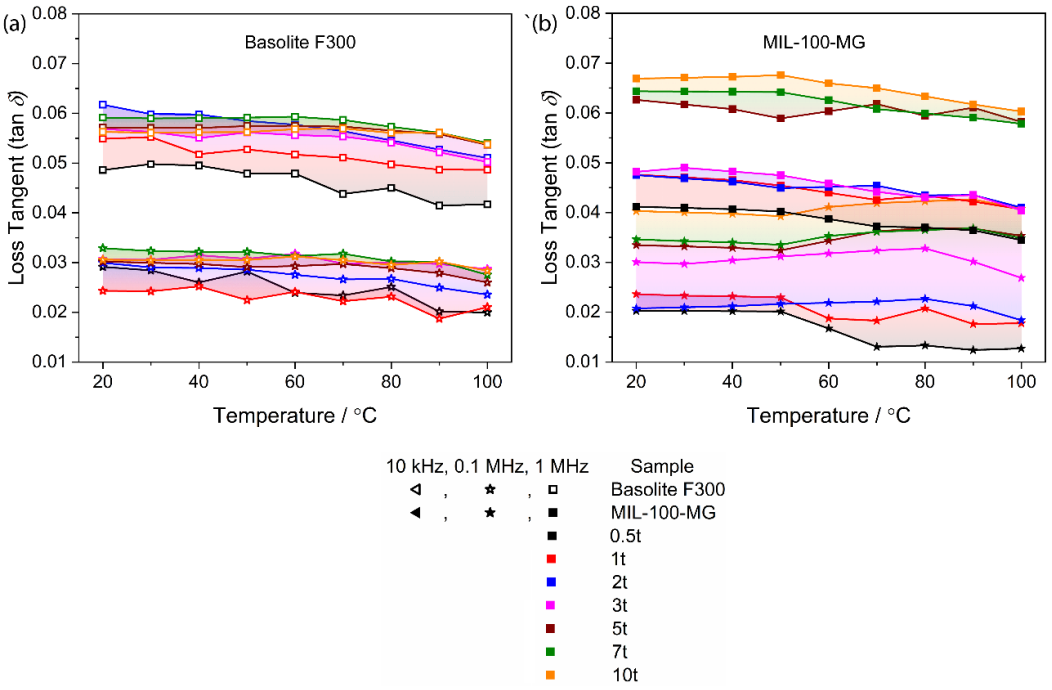

Figure 2.10: Dielectric loss of MOF pellets as a function of pelleting pressure and temperature: (a) Basolite F300 and, (b) MIL-100-MG pellets at specific frequencies of 0.01, 0.1, and 1 MHz.

2.3.1), in MIL-100-MG the mechanical deformation and structural densification of the framework resulted in only the red shift of IR vibrational peaks, which was caused by the softening in the phonon mode (see Figure 2.11). Due to the structural dependency of the ionic polarization, the decline rate of ε' in the far-IR to the mid-IR range is much greater as a function of pelleting pressure when compared to the plateau observed in the near-IR region (mainly associated with the electron density). In the near-IR region, the dielectric constant is mainly dependent upon the framework density and is highly impacted by the pelleting pressure causing an increase in ε' value from 1.29 (0.5 ton) to 2.02 (10 ton) at 150 THz frequency. The contribution of the individual polarisation mechanisms to the overall dielectric constant response is summarised in Table 1 of Paper II.

Finally, we also investigated the impact of amorphisation on the electrical conductivity in alternating current (AC) mode. As expected, the conductivity measurements follow the amorphisation pattern and a surge was observed with higher framework distortion, which facilitated the charge hopping by decreasing the percolation threshold. The MIL100-MG pellets show overall higher conductivity values in addition to a higher temperature-dependent conductivity rate over its Basolite F300 counterpart, which was facilitated by the occupied guest molecules in the framework cavity. The temperature rise eased the electron movement to upper bands and decreased the overall resistance of the insulating behaviour of the MIL-100-MG pellets.

The study of the derivatives of Fe-BTC has allowed us to better understand the impact of amorphisation and the different material processing techniques on

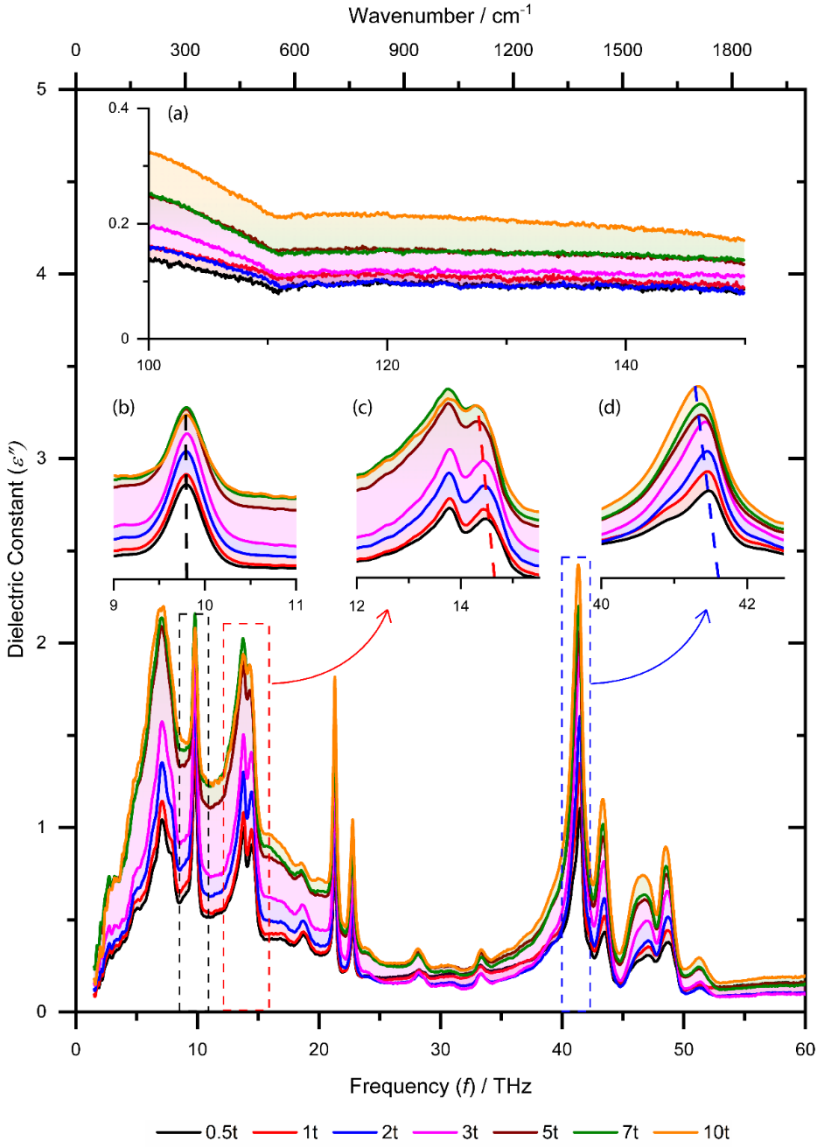

Figure 2.11: The imaginary part of dielectric constant (ε'') in the IR frequency range for MIL-100-MG pellets. Inset (a) shows the ε'' spectrum in the near-IR region. Inset (b) doesn't show any shift in the transition mode, whereas, in insets (c)-(d) the redshift is evident in the transition modes caused by the pelleting force-induced amorphisation.

both the electrical and dielectric properties. Combined with the HKUST-1 case study, these experiments provided in-depth knowledge about the broadband MOF dielectric spectrum by addressing some of the long-standing challenges, which have puzzled the minds of the MOF community and hindered the progress of MOFs to becoming a true interlayer dielectric material that will revolutionise high-speed electronics and communications.

Published Papers

Paper I

Impact of pressure and temperature on the broadband dielectric response of the HKUST-1 metal−organic framework

THE JOURNAL OF PHYSICAL CHEMISTRY C

Article

Cite This: J. Phys. Chem. C 2019, 123, 29427−29435

pubs.acs.org/JPCC

Impact of Pressure and Temperature on the Broadband Dielectric Response of the HKUST-1 Metal−Organic Framework

Arun S. Babal,[†] Lorenzo Donà,[‡] Matthew R. Ryder,[§] Kirill Titov,[†] Abhijeet K. Chaudhari,[†] Zhixin Zeng,[†] Chris S. Kelley,[∥] Mark D. Frogley,[∥] Gianfelice Cinque,[∥] Bartolomeo Civalleri,[‡] and Jin-Chong Tan*[,†]

[†]Multifunctional Materials and Composites (MMC) Laboratory, Department of Engineering Science, University of Oxford, Parks Road, Oxford, OX1 3PJ, U.K.

[‡]Department of Chemistry, NIS and INSTM Reference Centre, University of Turin, via Pietro Giuria 7, 10125 Torino, Italy

[§]Neutron Scattering Division, Oak Ridge National Laboratory, Oak Ridge, Tennessee 37831, United States

[∥]Diamond Light Source, Harwell Campus, Chilton, Oxford, OX11 0DE, U.K.

Supporting Information

ABSTRACT: Research on the broadband dielectric response of metal−organic frameworks (MOFs) is an emergent field that could yield exciting device applications, such as smart optoelectronics, terahertz sensors, high-speed telecommunications, and microelectronics. Hitherto, a detailed understanding of the physical mechanisms controlling the frequency-dependent dielectric and optical behavior of MOFs is lacking because a large number of studies have focused only on static dielectric constants. Herein, we employed high-resolution spectroscopic techniques in combination with periodic *ab initio* density functional theory (DFT) calculations to establish the different polarization processes for a porous copper-based MOF, termed HKUST-1. We used alternating current measurements to determine its dielectric response between 4 Hz and 1.5 MHz where orientational polarization is predominant, while synchrotron infrared (IR) reflectance was used to probe the far-IR, mid-IR, and near-IR dielectric response across the 1.2−150 THz range (*ca.* 40−5000 cm^{-1}) where vibrational and optical polarizations are principal contributors to its dielectric permittivity. We demonstrate the role of pressure on the evolution of broadband dielectric response, where THz vibrations reveal distinct blue and red shifts of phonon modes from structural deformation of the copper paddle-wheel and the organic linker, respectively. We also investigated the effect of temperature on dielectric constants in the MHz region pertinent to microelectronics, to study temperature-dependent dielectric losses via dissipation in an alternating electric field. The DFT calculations offer insights into the physical mechanisms responsible for dielectric transitions observed in the experiments and enable us to explain the frequency shifts phenomenon detected under pressure. Together, the experiments and theory have enabled us to glimpse into the complex dielectric response and mechanisms underpinning a prototypical MOF subject to pressure, temperature, and vast frequencies.

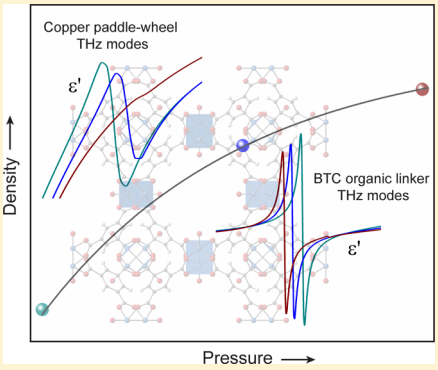

INTRODUCTION

Metal−organic frameworks (MOFs) are renowned for possessing high porosity and ordered structure along with tunable physical and chemical properties. In the past few decades, the main focus of these materials was directed toward applications such as gas storage, drug delivery, and chemical separations.[1−4] The ability to tune the physical behavior of MOFs has opened up new avenues of research and the focus has begun to shift toward device applications, such as microelectronics, optoelectronics, luminescence and sensors.[5−9] For next-generation high-speed devices, an ultra "low-*k*" dielectric material is desirable to reduce the signal delay, power loss and electronic crosstalk with ever-shrinking device dimension and increasing number of active devices packed into an integrated circuit.[10] According to the International Technology Roadmap for Semiconductors (ITRS),[11] the conventional materials such as SiO_2 whose dielectric constant, static ε' value or $k \sim 4$, will be replaced by a highly porous, crystalline or amorphous, chemically, and mechanically stable material in the future.[12] Due to the inherently low dielectric properties of MOFs, they could meet the time scale for the advancement of future low-*k* dielectric materials set by the ITRS.[13]

Hitherto only a handful of experiments have been reported on the dielectric properties of MOF materials. For example, Redel et al.[14] estimated the dielectric constant (k or ε') of HKUST-1 polycrystalline films in the visible wavelength range, assuming $\varepsilon' = n^2$ using the value of refractive index (n)

Received: August 26, 2019
Revised: November 7, 2019
Published: November 11, 2019

DOI: 10.1021/acs.jpcc.9b08125
J. Phys. Chem. C 2019, 123, 29427−29435

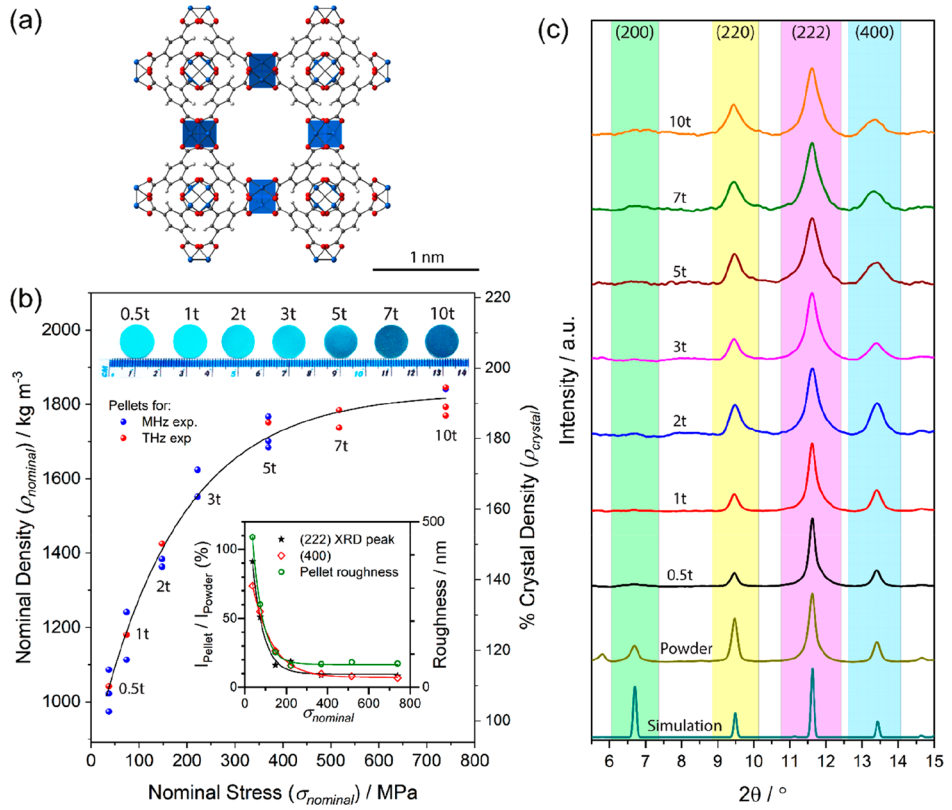

Figure 1. (a) Crystal structure of a unit cell of the HKUST-1 framework, shown here without adsorbed water molecules (color scheme: hydrogen in white, oxygen in red, copper in blue, and carbon in gray). (b) Nominal density of the pellets used for the MHz and THz measurements plotted as a function of the nominal pellet pressure. The pellets were designated in terms of the uniaxially applied force in metric tons, e.g. 0.5t for pellet pressed with a 0.5-ton force onto a 13 mm diameter die; thus, nominal stress = force/nominal area. The crystal density percentage was determined relative to the crystallographic density of HKUST-1. (c) Normalized XRD patterns of the HKUST-1 powder and pellets compressed under different loads. For comparison, the XRD patterns of pellets in absolute intensities are shown in Figure S3.

measured by spectroscopic ellipsometry. Usman et al.[15] synthesized a thermally stable Sr-based MOF under hydrothermal conditions and measured the dielectric response of pelletized samples using impedance spectroscopy; they suggested that the low dielectric behavior is the materials intrinsic property. Zagorodniy et al.[16] theoretically analyzed a series of hypothetical Zn-based MOF structures using the semiempirical Clausius−Mossotti relation and identified a number of promising candidates as ultralow k dielectrics. Such theoretical work was recently extended by Ryder et al.[17] for a large set of carboxylate-based frameworks. Mendiratta et al.[18] used an experimental and theoretical approach to study the dielectric properties of a Zn-based MOF. They calculated the polarizability using the Clausius−Mossotti relation and reported that in guest-free MOF structures the main dielectric contribution is from electronic polarization.

More recently, Scatena et al.[19] have reported the use of experimental and theoretical techniques to study the dielectric properties of the HKUST-1, measured up to a frequency of 1 MHz and when subjected to polar guest molecules (water and methanol). It was reported that the dielectric constant of the guest-free HKUST-1 pellet is $\varepsilon' \sim 1.72$, while the density functional theory (DFT) calculated value is 1.74. Distinct from other studies, some of us have characterized the frequency-dependent dielectric behavior of MIL-53(Al)[20] and a series of zeolitic imidazolate frameworks (ZIFs)[21] in the infrared regime. The broadband experiments were carried out using synchrotron specular reflectance spectroscopy, further corroborated by DFT calculations that accurately predicted the dynamic dielectric functions observed in the experiments. For the static dielectric constant, it has been proposed that MOFs may obey a scaling rule dominated by the framework porosity and density.[17,21] Despite these developments in the field of MOF dielectrics, there is no attempt yet to consider more rigorously the precise dielectric response and polarization mechanisms of MOFs when crossing the static → kHz → MHz → THz frequency range. Moreover, the impact of temperature and pressure on the polarizability of MOF structures is also little understood.

In this work, we have studied the temperature- and pressure-dependent broadband dielectric behavior of an activated HKUST-1 material under vacuum conditions. The MHz measurements were carried out using an LCR meter equipped with a parallel-plate capacitor arrangement operating in the frequency range of 4 Hz to 1.5 MHz, and covering the temperature range of 20 to 100 °C. The high-frequency dielectric behavior over the far-, mid-, and near-IR regions was measured via synchrotron infrared specular reflectance spectroscopy covering the range of 1.2 to 150 THz (40−5000 cm^{-1}). Details of the experimental setups are presented in the Supporting Information; see Figure S1. We performed density functional theory (DFT) calculations using the periodic CRYSTAL17 code[22] to gain additional insights into the effects of frequency and pressure on the broadband dielectric response of an ideal HKUST-1 structure.

DOI: 10.1021/acs.jpcc.9b08125
J. Phys. Chem. C 2019, 123, 29427−29435

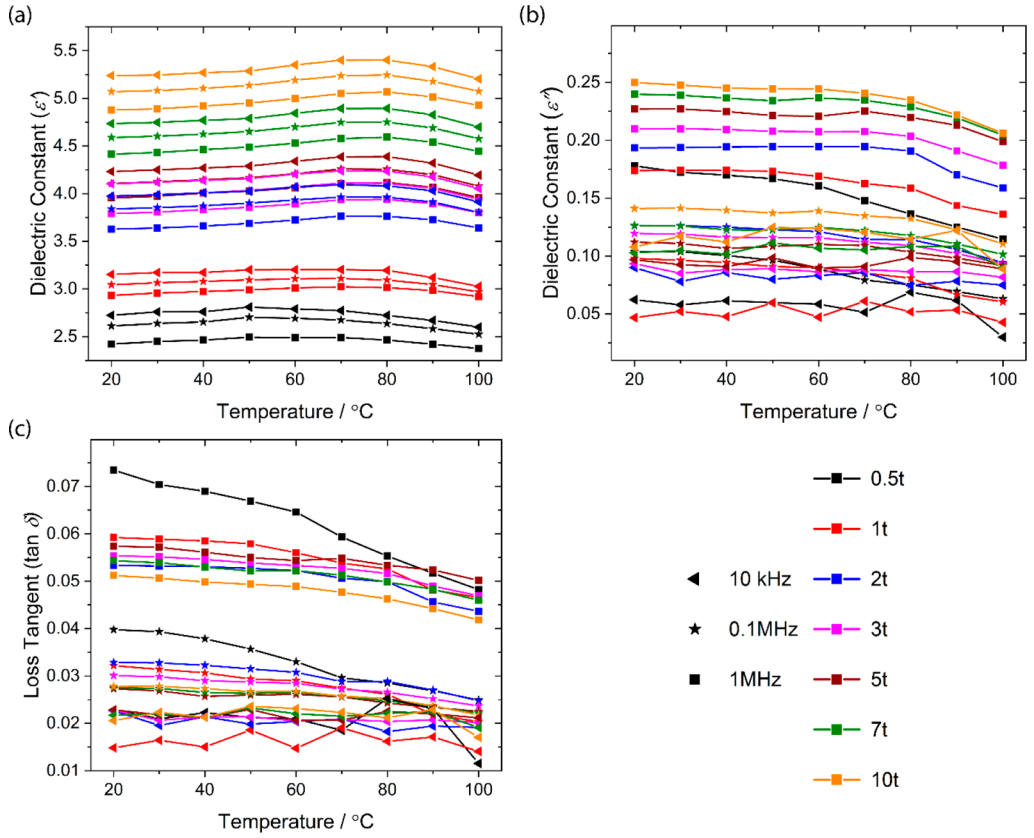

Figure 2. Dielectric properties of HKUST-1 as a function of temperature and pelleting pressure: (a) real part of dielectric constant ε', (b) imaginary part of dielectric constant ε'', and (c) loss tangent, tan $\delta = (\varepsilon''/\varepsilon')$. The marked change in the dielectric constant of the pellets from 1t to 2t can be attributed to pellet densification and framework amorphization, supported by the steep decline in relative XRD intensity and reduction of surface roughness depicted in the inset of Figure 1b.

RESULTS AND DISCUSSION

The as-received Basolite C300 powder (Sigma-Aldrich) also known as HKUST-1 (Figure 1a) or $Cu_3(BTC)_2$ [BTC = benzene-1,3,5-tricarboxylate] was used in this study. Water molecules can readily coordinate to the apical adsorption sites of the copper paddle-wheel,[23] hence affecting the dielectric property of the overall framework due to the strong dipole moment of water ($\varepsilon' \sim 80$ at 20 °C).[24] For this reason, in this study we have performed all dielectric measurements under vacuum conditions to activate the HKUST-1 framework, thereby eliminating the contribution of water molecules toward the total dielectric response.

We have prepared pellets of HKUST-1 with a diameter of 13 mm using a manual hydraulic press, by systematically increasing the applied force from 0.5, 1, 2, 3, 5, and 7 to 10 tons. Figure 1b shows that the prepared pellets and their nominal densities are obeying an exponential relation of the form: $\rho \propto \exp(-\sigma)$, where ρ is the nominal pellet density and σ is the nominal stress. Compared with the theoretical density of a HKUST-1 single crystal (948.9 kg m^{-3}),[23] the 0.5t pellet exhibits a nominal density of ~110% while the 10t pellet attained ~195% of the theoretical density. It can be seen in Figure 1(b) that the color of the pellets is also systematically shifting from turquoise toward dark blue with the rising pressure, indicating the change of its refractive index (*vide infra*).

By increasing the pelleting pressure, one may expect a reduction of free volume between the crystals in the pellet, as evidenced from roughness characterization of the polycrystalline surface, see inset of Figure 1b and Figure S2. Irreversible plastic deformation of the HKUST-1 structure mimicking the trend of the density vs nominal stress curve in Figure 1b is also expected, leading to amorphization[25] of the porous framework. X-ray diffraction (XRD) patterns in Figure 1c and Figure S3 show the evolution of the Bragg peaks with pelleting pressure. The HKUST-1 powder starts to amorphize under stress at 37 MPa (0.5t) as evidenced by the disappearance of the (200) and (111) peaks. The (220), (222) and (400) characteristic peaks also exhibit broadening effect with increased pelleting pressure, indicating pore collapse and framework amorphization (further supported by the full width at half-maximum (fwhm) analysis in Figure S4 and Table S1). The increasing trend in fwhm values is mirroring the change of nominal density of the pellets shown in Figure 1b.

Figure 2 shows the dielectric properties of HKUST-1 with increasing pelleting pressure and temperature at the representative frequencies of 0.01, 0.1, and 1 MHz. For an individual pellet, the real part of the dielectric constant (ε') decreases with increasing frequency at a specific temperature. The MHz data revealed that the dipole moment of the framework cannot keep up with the alternating field switching at higher frequency, therefore resulting in an overall decline in the orientational polarizability of the material. For example, the ε' value of the 0.5t pellet at 20 °C fell from its highest value of 2.72 at 10 kHz to 2.42 at 1 MHz. For the 10t pellet, the value of ε' rose from 4.88 (20 °C) to 5.07 (80 °C) and then slightly declined to yield 4.92 at 100 °C; this effect might be linked to the negative thermal expansion of the HKUST-1 framework.[26]

DOI: 10.1021/acs.jpcc.9b08125
J. Phys. Chem. C 2019, 123, 29427−29435

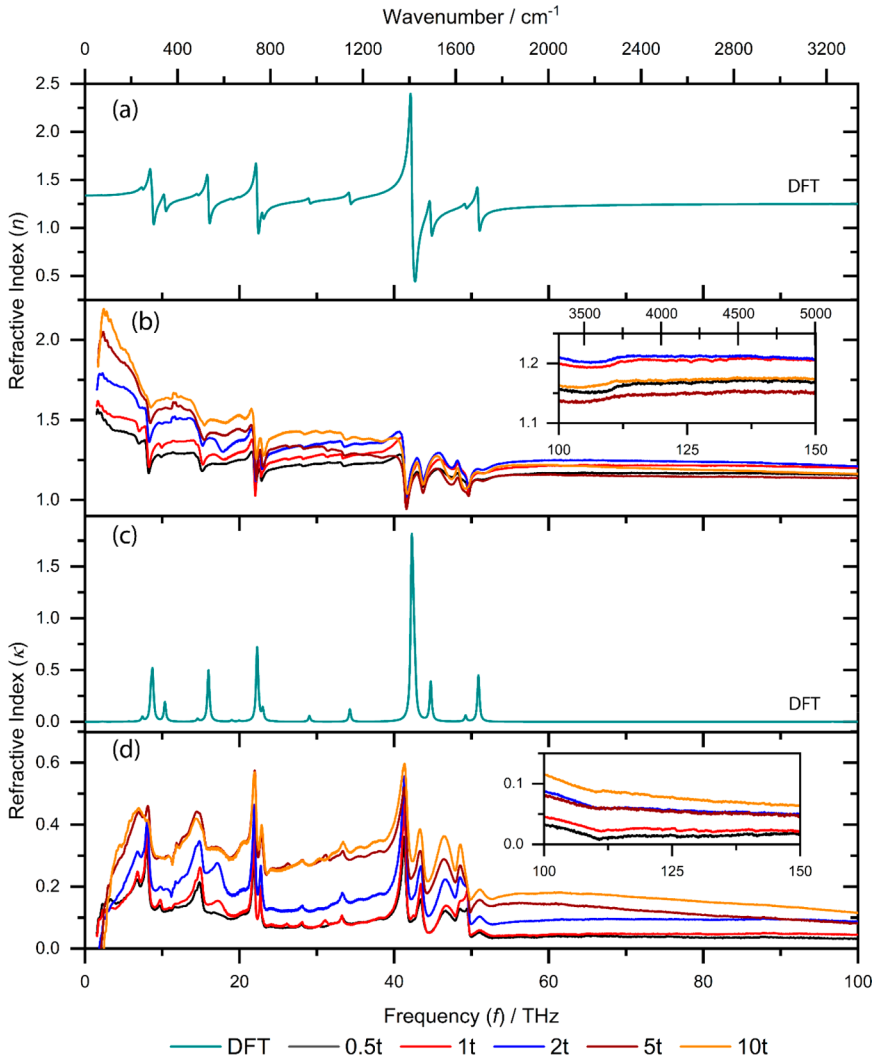

Figure 3. Complex refractive index of HKUST-1, where the real part of the refractive index n and the imaginary part of the refractive index κ are plotted as a function of frequency. Panels a and c are the DFT predictions of an ideal HKUST-1 structure at zero pressure. Panels b and d show the experimental results at 20 °C for the polycrystalline samples of HKUST-1 at different pelleting pressures.

Higher pelleting pressure reduces the free volume between the crystals and increases amorphization of sample, both of which affect the dielectric response. For instance, for 1 MHz frequency at 20 °C, by increasing the pelleting pressure from 0.5t to 10t, it was found that the value of ε' can be doubled from 2.42 to 4.88. It follows that the dielectric behavior of the polycrystalline sample depends upon the pellet density; herein, our data show that it scales nonlinearly with pressure due to plastic deformation (see Figure 1b). This effect, however, is commonly neglected in the literature concerning the dielectric measurements of pelleted powder samples (e.g., refs 18 and 19). Scatena et al.[19] have grown HKUST-1 single crystals (~300 μm) and prepared a pellet by employing a pressure of 200 MPa, but they did not consider the impact of structural amorphization from pelletizing process or attempt to quantify how this structural change might alter its dielectric property.

The imaginary part of the dielectric constant (ε'') is shown in Figure 2b, which represents the energy dissipation of HKUST-1 subject to an alternating electric field. We found that all pellets have a low dielectric loss of tan δ < 0.075 (Figure 2c) between 20 and 100 °C; this value declines with rising temperature, but it increases with rising frequency. For comparison, at 1 MHz, polymers such as PVDF and PMMA exhibit a small tan δ of about 0.12[27] and 0.02,[28] respectively. It has also been reported that at 300 K a Sr-based MOF exhibits a tan δ ~ 0.02 at 0.1 MHz.[15] The complete pressure- and temperature-dependent dielectric data sets of the HKUST-1 pellets are presented in the Supporting Information; see Figures S8–S10.

Now we turn to the optical and dielectric properties of HKUST-1 in the broadband infrared (IR) frequencies, encompassing 40–5000 cm^{-1}. The high-resolution reflectance spectra were measured by employing synchrotron specular reflectance spectroscopy at beamline B22 in the Diamond Light Source (Oxfordshire, U.K.); the collected reflectance spectra of HKUST-1 under different pelleting pressures are presented in Figure S11. Subsequently, the real and imaginary parts of the frequency-dependent refractive indices (Figure 3) and dielectric constants (Figure 4) were determined from the reflectance spectra by implementing the Kramers–Kronig transformation;[20,29] see full descriptions in the Supporting Information, section 2. To gain additional insights into the underpinning physical mechanisms, we have compared our experimental results to periodic *ab initio* DFT calculations

DOI: 10.1021/acs.jpcc.9b08125
J. Phys. Chem. C 2019, 123, 29427–29435

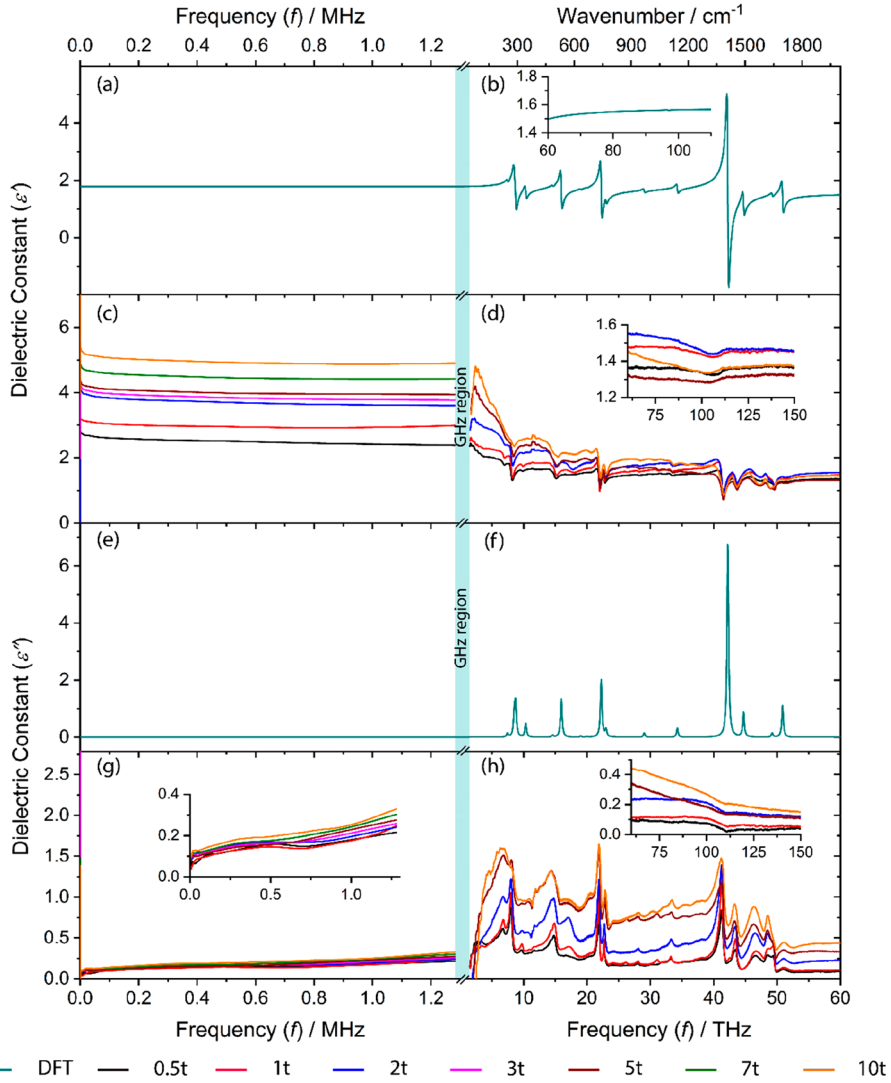

Figure 4. Complex dielectric function of HKUST-1 over the broadband frequency range of 4 Hz to 150 THz. (a, b) Real part of the dielectric constant ε' and (e, f) imaginary part of the dielectric constant ε'', calculated by DFT for an ideal HKUST-1 structure at zero pressure. The IR intensities are mainly related to the transition dipole moment, for instance the most intense IR peak at 1408 cm^{-1} corresponds to the symmetric stretching of the carboxylate group. (c, d) Real part and (g, h) imaginary part of dielectric constants determined from experiments for pelletized HKUST-1 samples prepared under different forces. For the experimental data, the left panels show the Hz-MHz range measured by LCR parallel-plate capacitor technique, while the right panels show the far-IR, mid-IR, and near-IR regions measured by synchrotron specular reflectance spectroscopy. Note that the synchrotron measurements (i) were limited to the 0.5t, 1t, 2t, 5t, and 10t pellets only, and (ii) the drop off in intensity below ~3 THz is an artifact due to frequency cutoff by the far-IR beamsplitter.

carried out with the hybrid B3LYP-D3(ABC) functional incorporating two- and three-body dispersion forces,[30] combined with a triple-zeta quality basis set (see computational methods in the Supporting Information, section 10).

First, we consider the broadband optical properties of HKUST-1 as a function of frequency (ω) and pelleting pressure. Figure 3 shows the real (n) and imaginary (κ) parts of the complex refractive index $\tilde{n}(\omega) = n(\omega) + i\kappa(\omega)$, plotted against the DFT predictions showing the general agreement between experiments and theory across the wide frequency range. The experimental spectra show that the value of n varies from 1.15 to 1.2 for all the pellets in the NIR region (>100 THz), which is reminiscent of the value of $n = 1.34$ calculated by DFT for the ideal HKUST-1 structure. The refractive indices increase as a function of pelleting pressure due to the increment in nominal pellet density (Figure 1b) and mechanically induced amorphization (Figure 1c), which together will result in reduction of free volume ($n \sim 1$) within a polycrystalline sample. For a particular pelleting pressure, we note the following: (a) The refractive index experiences a stepwise decrease with increasing frequency, the mechanisms of which will be addressed in the sections below. (b) At each transition step, there is a discontinuity in the real part of the refractive index n, because of dissipative losses, giving rise to absorption peaks within the imaginary part of the refractive index κ.

Figure 4 presents the combined broadband dielectric spectra (theory vs experiments) starting from 4 Hz up to 150 THz, to enable us to establish a complete understanding of the frequency- and pressure-dependent dielectric response of the HKUST-1 framework. To maintain consistency in the data, the broadband spectra only displays the pellet data collected at 20 °C. The complex dielectric function is $\tilde{\varepsilon}(\omega) = \varepsilon'(\omega) + i\varepsilon''(\omega)$, which comprises the real and imaginary components denoted

DOI: 10.1021/acs.jpcc.9b08125
J. Phys. Chem. C 2019, 123, 29427−29435

Table 1. Contributions of the Main Polarization Mechanisms to the Total Dielectric Response of HKUST-1[a]

	polarization mechanisms				
	$\varepsilon'_{\text{dipole/orientational polarization}}$	$\varepsilon'_{\text{atomic/vibrational polarization}}$		$\varepsilon'_{\text{optical/electronic polarization}}$	$\varepsilon'_{\text{total}}$
pelleting pressure/MPa	MHz (4 Hz to 1.5 MHz)	far-IR (1.5−20 THz)	mid-IR (20−100 THz)	near-IR (100−150 THz)	entire spectrum
0 (DFT)[b]	0	0.12	0.18	1.49	1.79
36.96 (0.5t)	1.32	0.15	0.14	1.36	2.97
73.92 (1t)	1.33	0.2	0.17	1.48	3.18
147.84 (2t)	2.05	0.39	0.26	1.55	4.25
369.60 (5t)	2.03	0.77	0.32	1.30	4.42
739.20 (10t)	3.17	0.71	0.44	1.44	5.76

[a]The contribution of space charge is not considered in this analysis. [b]0 MPa data obtained from DFT calculations of an ideal HKUST-1 structure. We observed that the theoretical value (1.79) is reminiscent of experimental values of the 0.5t and 1t pellets upon removal of their dipolar contributions ($\varepsilon'_{\text{total}} - \varepsilon'_{\text{dipole}}$), resulting in values that lie in the range of 1.65 to 1.85.

by ε' and ε'', respectively. It is evident from the broadband spectral data that the dielectric value decreases with increasing frequency and the static dielectric constant ε' ($\omega = 0$) denotes the maximum value of HKUST-1.

In the near-IR region (100−150 THz), the dielectric spectra of the HKUST-1 pellets show an asymptotic behavior where ε' values were found to be lying in a narrow band of 1.3−1.5 (see inset of Figure 4d). This is in good agreement with the DFT values of ∼1.5 beyond 100 THz. Because the dielectric mechanism in the near-IR region is attributed to femtosecond (10^{-15} s) response of the electron density,[31] the dielectric constants at high frequencies are exclusively optical dielectric responses that are not sensitive to the structural deformation of HKUST-1 or the pelleting pressure used.

Descending the frequency scale, we arrive at the mid-IR (∼10−100 THz) region; here, the dielectric mechanism is controlled by polarization processes ascribed to a subpicosecond response time of 10^{-14}−10^{-13} s, especially atomic oscillations like bending, stretching, and torsional modes of molecular moieties. However, in the far-IR region, <10 THz, the dielectric constants are controlled by the picosecond (10^{-12} s) response of collective atomic vibrations or phonon modes, where the polarizability depends on the polarity of the chemical bonds in the framework and amplitude of the vibrations. From the theoretical DFT spectra of the ideal HKUST-1 structure, it can be seen that the resonance positions of ε' (Figure 4b) and the corresponding absorption peaks of ε'' (Figure 4f) below 50 THz are in good agreement with the experimental spectra; also see the superimposed spectra in Figures S12 and S13. Indeed the distinctive transitions identified in the far-IR region originated from THz lattice dynamics prevalent in the HKUST-1 framework; for exemplar, the copper paddle-wheel vibrational motions and the BTC linker deformations at ∼9 THz and ∼16 THz, respectively.[32] (For description of other THz modes in HKUST-1, the reader should refer to ref 32.) Thus, in the mid- and far-IR regions, the dielectric function is strongly affected by the dynamics of the framework structure and the pellet density, as evidenced from synchrotron data shown in parts d and h of Figure 4, whereby the values of ε' and ε'' systematically increased with pelleting pressure.

In the MHz frequency region, the polarization process is considerably slower with a microsecond (10^{-6} s) response time. The dielectric response in this region could originate from the dipole polarization of the framework surrounding the Cu(II) paddle-wheel sites.[19,33] We reasoned that this process is enhanced by the structural distortion of the framework, resulting in increased of net dipole moments from plastic deformation. This notion is supported by data in parts c and g of Figure 4, showing that the dielectric constant in the MHz range scales with pellet densification; for instance the value of ε' has doubled from ∼ 2.4 to 4.9 (at 1 MHz) when the pelleting pressure was raised from 0.5t to 10t. An additional contribution is from the orientational polarization of dipolar species, such as residual DMF solvents (see Supporting Information, section 5) remained trapped in HKUST-1 after sample evacuation.

Finally, we note that the value of static dielectric constant from DFT calculations for an ideal HKUST-1 structure is 1.79, see Figure 4a, which resembles the previously computed values reported in literature via DFT methods (ε' = 1.6,[17] 1.74)[19] or by using the semiempirical Clausius−Mossotti relation (ε' = 1.7).[16] In contrast, from the experimental data in Figure 4c, we found the dielectric constant value for the 0.5t pellet to be relatively higher at $\varepsilon' \sim 3$ (at 100 Hz). This discrepancy might be attributed to two factors. (i) Framework amorphization and pellet densification will reduce the overall free volume ($\varepsilon' \sim 1$) in sample. (ii) DFT did not account for orientational (dipolar) polarization contribution caused by framework deformation, also the ideal HKUST-1 structure is free from all guest molecules. Note that the Clausius−Mossotti relation neglects both orientational and vibrational polarizations; consequently, the theoretical models underestimate the dielectric permittivity. In addition, thermal effects could also play a role, but in this case, the very small negative thermal expansion[26] of HKUST-1 leads to a tiny contraction of the unit cell when increasing temperature without significant change of the framework. From DFT calculations, it has been estimated that the increment of the dielectric constant is of the order of 10^{-3}.

It follows that the broadband dielectric data gathered experimentally and theoretically have enabled us to further breakdown the individual contributions, into the three main polarization mechanisms. The results for HKUST-1 are summarized in Table 1, where the total dielectric permittivity is taken as $\varepsilon'_{\text{total}} = \varepsilon'_{\text{dipole/orientational}} + \varepsilon'_{\text{atomic/vibrational}} + \varepsilon'_{\text{optical/electronic}}$.

Figure 5a summarizes the changing trend of ε' with frequency, clearly demonstrating that there exists a strong sensitivity toward the mechanically induced structural deformation of HKUST-1 in the frequency region of below 50 THz. We note that the increase of dielectric values when progressing from the mid-IR to the far-IR region is significantly greater than those recorded through the near-IR range. Likewise, in the Hz-MHz range there is a clear dependency on mechanical stress applied during pelleting, as shown in

DOI: 10.1021/acs.jpcc.9b08125
J. Phys. Chem. C 2019, 123, 29427−29435

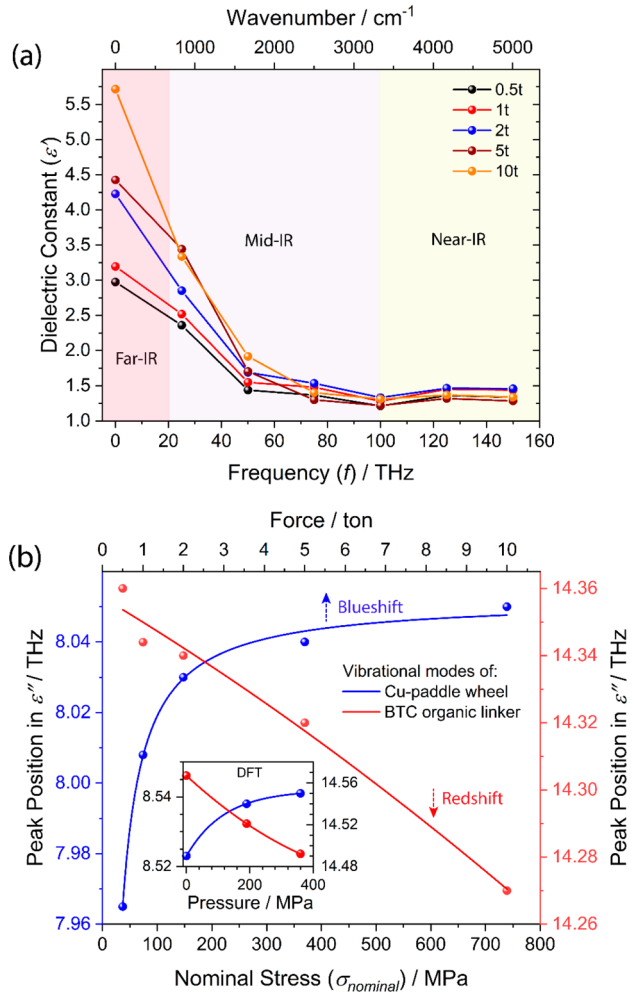

Figure 5. (a) Summary of the dielectric constants of HKUST-1 across the broadband frequencies comprising the far-, mid-, and near-IR regions. (b) Blue and red shifts of the THz peaks linked to the copper paddle-wheel and BTC linker vibrational modes plotted as a function of pelleting pressure; the inset shows the corresponding DFT predictions under hydrostatic pressure.

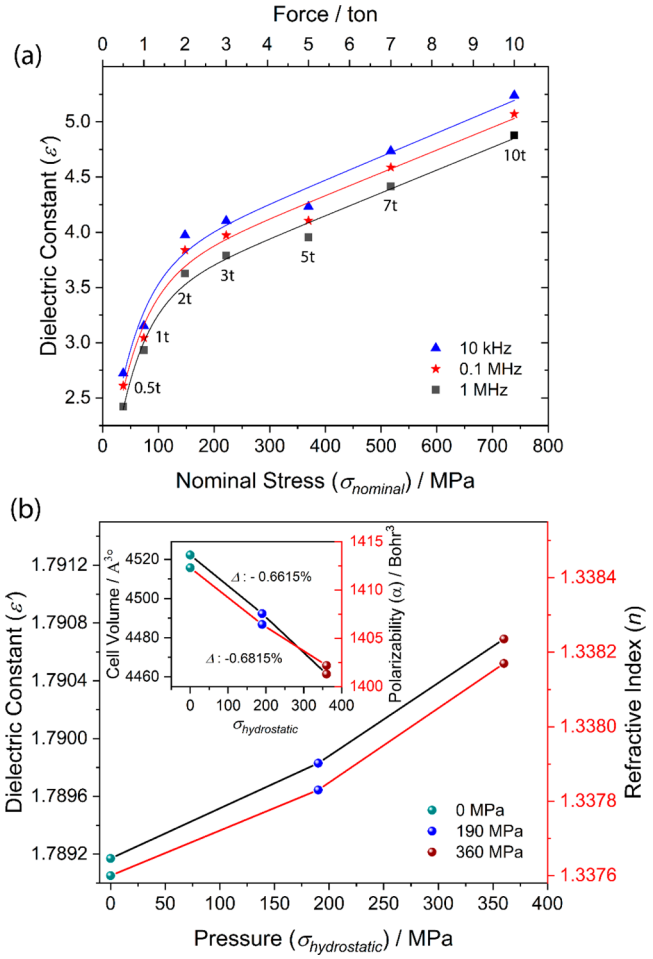

Figure 6. Effects of nominal stress or pressure on the dielectric constants of HKUST-1. (a) Experimental values of ε' obtained from the pelletized sample measured at kHz-MHz frequencies. The curves are guides for the eye. (b) Static dielectric values computed by DFT for ε' and ε'' at 0, 190, and 360 MPa. Inset shows the predicted change of the primitive cell volume with applied pressure, where volumetric strain is defined as $\Delta = \frac{\Delta V}{V_0} \times 100\%$. In turn, polarizability was predicted to decline with pressure, which is not unexpected because polarizability is usually proportional to the unit cell volume.

Figure 6a. To gain further insights, we investigated the effect of mechanical deformation on the dielectric and optical properties of HKUST-1 using DFT calculations, which was achieved by imposing a hydrostatic pressure of 0, 190, and 360 MPa onto a cubic unit cell of HKUST-1; the results are shown in Figure 6b. While the cell volume declines with pressure as expected, we found that from 190 to 360 MPa the unit cell underwent a cubic to tetragonal transformation indicating mechanical instability triggered by a threshold pressure beyond ∼190 MPa. In fact, we recognize that the nature of loading under nominal stress (experienced by pellets) is not identical to the hydrostatic pressure simulated by DFT, but the theoretical results shed light on the scope of employing mechanical deformation for tuning the dielectric response of a porous framework.

As the HKUST-1 framework is mechanically deformed by pellet formation, see Figure 1b (even at the lowest force of 0.5t), we discovered that the applied stress has resulted in THz peak shifts. Two interesting examples are shown in Figure 5b, where the magnitude of peak shifts is plotted as a function of nominal stress. The vibrational modes at ∼8 and ∼14 THz are associated with the collective dynamics of the copper paddle-wheel (metal clusters) and the phonon modes of the BTC linkers, respectively.[32] THz vibrations of the copper paddle-wheel exhibits a blueshift with increasing stress/pressure corresponding to stiffening of the cluster deformation modes also predicted by DFT. Notably, there is a steep rise in the first ∼200 MPa that can be linked to plastic deformation of the framework. On the other hand, phonon modes of the BTC linkers are softening with stress/pressure, because redshifts were detected with an increasing mechanical loading. It is quite fascinating that the simulated and experimental spectra are demonstrating a similar trend (against DFT results in Figure 5 inset), except for the peak broadness of experimental data that can be attributed to polycrystalline nature of the pelletized samples. This peak broadening is more evident in the far-IR region because the pelleting stress will have a higher impact on the collective lattice dynamics of the framework, as compared to the mid-IR region dictated by vibrational modes of the local chemical moieties.[34] In the near-IR region, we note that there is some pressure dependence between *ca.* 55 and 110 THz because of a continuous increase in electronic polarization as a

DOI: 10.1021/acs.jpcc.9b08125
J. Phys. Chem. C 2019, 123, 29427−29435

function of structural deformation generated by the pelleting stress. Complete analysis of the individual peak shifts in the dielectric and refractive index spectra is presented in Figures S15–S18 of the Supporting Information. Finally, the loss tangent spectra of pellets across the broadband frequencies are shown in Figure S14, demonstrating the substantially greater dissipation detected in the THz region (relative to the MHz losses) due to collective lattice dynamics and phonon vibrations of the HKUST-1 framework.

CONCLUSIONS

In conclusion, we reported pressure- and temperature-dependent broadband dielectric response for HKUST-1 covering the vast frequency region of 4 Hz to 150 THz. This study was made possible by employing a combination of experimental and theoretical methods. The main findings are summarized as follows:

- Dielectric constants of HKUST-1 can be modified through the application of pelleting pressure and temperature, indicating its dependency on the structural deformation, sample amorphization, and densification which are associated with the free volume and framework polarizability.
- The dielectric (and optical) response of HKUST-1 in the MHz, far-IR, and mid-IR regions scales very strongly with the sample microstructure, but it is independent of the framework structure within the near-IR region.
- Multiple dielectric mechanisms and polarization processes are present in HKUST-1 that can be triggered using different frequencies, namely the following: (i) Microsecond response in MHz region—dipole polarization of the framework and orientational polarization of guest molecules. (ii) Picosecond response in far-IR—soft modes and THz collective dynamics of flexible framework. (iii) Subpicosecond response in mid-IR—atomic oscillations of molecular moieties of the framework. (iv) Femtosecond response from electronic polarization in near-IR—optical dielectric response, which is also sensitive to the structural densification of the HKUST-1 framework.
- In the far- and mid-IR regions, the degree of redshift or blueshift experienced by the vibrational modes controlling the optical and dielectric response is tunable by mechanical deformation imposed by an externally applied stress/pressure. This result is confirmed by pressure-dependent DFT calculations of an ideal HKUST-1 structure.
- The dielectric values of evacuated MOF materials can be appreciably lower than conventional dielectrics (e.g., SiO_2, $\varepsilon' \sim 4$), they could function as a tunable dielectric for development into high-frequency applications targeting photonic sensors and THz communication devices.
- This study also led us to identifying key challenges that could hinder the use of MOFs for engineering ultra low-k dielectrics: (i) Complete activation of MOFs is not trivial, to eliminate trapped solvents effecting dipole polarizations at low frequencies. (ii) Porous MOF is susceptible to amorphization and structural deformation subject to thermo-mechanical stresses. (iii) MOF powders are difficult to shape for device integration.

ASSOCIATED CONTENT

Supporting Information

The Supporting Information is available free of charge at https://pubs.acs.org/doi/10.1021/acs.jpcc.9b08125.

Materials characterization, TGA and FTIR analyses, pellets surface topography, reflectivity spectra, MHz and THz dielectric data, methods for DFT calculations, and detailed analyses of pressure-dependent DFT data (PDF)

CRYSTAL input files for the ideal HKUST-1 structure for both the high and low symmetry phases (ZIP)

AUTHOR INFORMATION

Corresponding Author

*(J.-C.T.) E-mail: jin-chong.tan@eng.ox.ac.uk.

ORCID

Matthew R. Ryder: 0000-0002-1363-8148

Bartolomeo Civalleri: 0000-0003-3198-3161

Jin-Chong Tan: 0000-0002-5770-408X

Author Contributions

J.-C.T. conceived the project. A.S.B. performed the MHz experiments and analyzed the dielectric data with input from J.-C.T. L.D. and B.C. performed the DFT calculations and theoretical analysis. M.R.R., K.T., A.K.C., and Z.Z. performed the THz synchrotron experiments with guidance from M.D.F. and C.S.K., and under the supervision of G.C.. A.S.B. analyzed the synchrotron data with input from K.T. and J.C.T. A.S.B. and J.-C.T. wrote the manuscript with input from all coauthors.

Notes

The authors declare no competing financial interest.

ACKNOWLEDGMENTS

A.S.B. is grateful to the Engineering Science (EPSRC DTP—Samsung) Studentship that supports this D.Phil. research. J.-C.T. acknowledges the European Union's Horizon 2020 research and innovation programme (ERC Consolidator Grant Agreement No. 771575-PROMOFS), the EPSRC Impact Acceleration Account Award (EP/R511742/1), and the Samsung GRO Award (DFR00230) for supporting this research. M.R.R. acknowledges the U.S. Department of Energy Office of Science (Basic Energy Sciences) for research funding and thanks the Engineering and Physical Sciences Research Council for an EPSRC Doctoral Prize Award (2017–2018). We acknowledge the Diamond Light Source for the provision of beamtime SM14902 at B22 MIRIAM. We thank the Research Complex at Harwell (RCaH) for the provision of TGA and FTIR. We are grateful to Dr. Marek Jura and Dr. Gavin Stenning at R53 Materials Characterisation Laboratory in ISIS RAL for access to the XRD facilities.

REFERENCES

(1) Gao, C. Y.; Tian, H. R.; Ai, J.; Li, L. J.; Dang, S.; Lan, Y. Q.; Sun, Z. M. A microporous Cu-MOF with optimized open metal sites and pore spaces for high gas storage and active chemical fixation of CO_2. *Chem. Commun.* **2016**, *52*, 11147–11150.

(2) Tchalala, M. R.; Bhatt, P. M.; Chappanda, K. N.; Tavares, S. R.; Adil, K.; Belmabkhout, Y.; Shkurenko, A.; Cadiau, A.; Heymans, N.; De Weireld, G.; Maurin, G.; Salama, K. N.; Eddaoudi, M. Fluorinated MOF platform for selective removal and sensing of SO_2 from flue gas and air. *Nat. Commun.* **2019**, *10*, 1328.

(3) McKinlay, A. C.; Allan, P. K.; Renouf, C. L.; Duncan, M. J.; Wheatley, P. S.; Warrender, S. J.; Dawson, D.; Ashbrook, S. E.; Gil, B.;

DOI: 10.1021/acs.jpcc.9b08125
J. Phys. Chem. C 2019, 123, 29427–29435

Marszalek, B.; Düren, T.; Williams, J. J.; Charrier, C.; Mercer, D. K.; Teat, S. J.; Morris, R. E. Multirate delivery of multiple therapeutic agents from metal-organic frameworks. *APL Mater.* **2014**, *2*, 124108.
(4) Belmabkhout, Y.; Zhang, Z. Q.; Adil, K.; Bhatt, P. M.; Cadiau, A.; Solovyeva, V.; Xing, H. B.; Eddaoudi, M. Hydrocarbon recovery using ultra-microporous fluorinated MOF platform with and without uncoordinated metal sites: I- structure properties relationships for C_2H_2/C_2H_4 and CO_2/C_2H_2 separation. *Chem. Eng. J.* **2019**, *359*, 32−36.
(5) Stassen, I.; Burtch, N.; Talin, A.; Falcaro, P.; Allendorf, M.; Ameloot, R. An updated roadmap for the integration of metal-organic frameworks with electronic devices and chemical sensors. *Chem. Soc. Rev.* **2017**, *46*, 3185−3241.
(6) Chaudhari, A. K.; Kim, H. J.; Han, I.; Tan, J. C. Optochemically responsive 2D nanosheets of a 3D metal-organic framework material. *Adv. Mater.* **2017**, *29*, 1701463.
(7) Dolgopolova, E. A.; Shustova, N. B. Metal−organic framework photophysics: Optoelectronic devices, photoswitches, sensors, and photocatalysts. *MRS Bull.* **2016**, *41*, 890−896.
(8) Chaudhari, A. K.; Souza, B. E.; Tan, J.-C. Electrochromic thin films of Zn-based MOF-74 nanocrystals facilely grown on flexible conducting substrates at room temperature. *APL Mater.* **2019**, *7*, No. 081101.
(9) Lustig, W. P.; Mukherjee, S.; Rudd, N. D.; Desai, A. V.; Li, J.; Ghosh, S. K. Metal-organic frameworks: functional luminescent and photonic materials for sensing applications. *Chem. Soc. Rev.* **2017**, *46*, 3242−3285.
(10) Volksen, W.; Miller, R. D.; Dubois, G. Low Dielectric Constant Materials. *Chem. Rev.* **2010**, *110*, 56−110.
(11) Hoefflinger, B. ITRS: The International Technology Roadmap for Semiconductors. *Chips 2020* **2011**, 161−174.
(12) Maex, K.; Baklanov, M. R.; Shamiryan, D.; Iacopi, F.; Brongersma, S. H.; Yanovitskaya, Z. S. Low dielectric constant materials for microelectronics. *J. Appl. Phys.* **2003**, *93*, 8793.
(13) Usman, M.; Lu, K.-L. Metal−organic frameworks: The future of low-κ materials. *NPG Asia Mater.* **2016**, *8*, e333.
(14) Redel, E.; Wang, Z.; Walheim, S.; Liu, J.; Gliemann, H.; Woell, C. On the dielectric and optical properties of surface-anchored metal-organic frameworks: A study on epitaxially grown thin films. *Appl. Phys. Lett.* **2013**, *103*, No. 091903.
(15) Usman, M.; Lee, C.-H.; Hung, D.-S.; Lee, S.-F.; Wang, C.-C.; Luo, T.-T.; Zhao, L.; Wu, M.-K.; Lu, K.-L. Intrinsic low dielectric behaviour of a highly thermally stable Sr-based metal−organic framework for interlayer dielectric materials. *J. Mater. Chem. C* **2014**, *2*, 3762−3768.
(16) Zagorodniy, K.; Seifert, G.; Hermann, H. Metal-organic frameworks as promising candidates for future ultralow-*k* dielectrics. *Appl. Phys. Lett.* **2010**, *97*, 251905.
(17) Ryder, M. R.; Donà, L.; Vitillo, J. G.; Civalleri, B. Understanding and controlling the dielectric response of metal-organic frameworks. *ChemPlusChem* **2018**, *83*, 308−316.
(18) Mendiratta, S.; Usman, M.; Chang, C.-C.; Lee, Y.-C.; Chen, J.-W.; Wu, M.-K.; Lin, Y.-C.; Hsu, C.-P.; Lu, K.-L. Zn(II)-based metal−organic framework: an exceptionally thermally stable, guest-free low dielectric material. *J. Mater. Chem. C* **2017**, *5*, 1508−1513.
(19) Scatena, R.; Guntern, Y. T.; Macchi, P. Electron density and dielectric properties of highly porous MOFs: binding and mobility of guest molecules in $Cu_3(BTC)_2$ and $Zn_3(BTC)_2$. *J. Am. Chem. Soc.* **2019**, *141*, 9382.
(20) Titov, K.; Zeng, Z.; Ryder, M. R.; Chaudhari, A. K.; Civalleri, B.; Kelley, C. S.; Frogley, M. D.; Cinque, G.; Tan, J. C. Probing dielectric properties of metal-organic frameworks: MIL-53(Al) as a model system for theoretical predictions and experimental measurements via synchrotron far- and mid-infrared spectroscopy. *J. Phys. Chem. Lett.* **2017**, *8*, 5035−5040.
(21) Ryder, M. R.; Zeng, Z.; Titov, K.; Sun, Y.; Mahdi, E. M.; Flyagina, I.; Bennett, T. D.; Civalleri, B.; Kelley, C. S.; Frogley, M. D.; Cinque, G.; Tan, J. C. Dielectric properties of zeolitic imidazolate frameworks in the broad-band infrared regime. *J. Phys. Chem. Lett.* **2018**, *9*, 2678−2684.
(22) Dovesi, R.; Erba, A.; Orlando, R.; Zicovich-Wilson, C. M.; Civalleri, B.; Maschio, L.; Rerat, M.; Casassa, S.; Baima, J.; Salustro, S.; Kirtman, B. Quantum-mechanical condensed matter simulations with CRYSTAL. *WIREs Comput. Mol. Sci.* **2018**, *8*, e1360.
(23) Chui, S. S.; Lo, S. M.; Charmant, J. P.; Orpen, A. G.; Williams, I. D. A chemically functionalizable nanoporous material $[Cu_3(TMA)_2(H_2O)_3]_n$. *Science* **1999**, *283*, 1148−50.
(24) Malmberg, C. G.; Maryott, A. A. Dielectric constant of water from 0° to 100 °C. *J. Res. Natl. Bur. Stand.* **1956**, *56*, 1−8.
(25) Bennett, T. D.; Goodwin, A. L.; Dove, M. T.; Keen, D. A.; Tucker, M. G.; Barney, E. R.; Soper, A. K.; Bithell, E. G.; Tan, J. C.; Cheetham, A. K. Structure and properties of an amorphous metal-organic framework. *Phys. Rev. Lett.* **2010**, *104*, 115503.
(26) Wu, Y.; Kobayashi, A.; Halder, G. J.; Peterson, V. K.; Chapman, K. W.; Lock, N.; Southon, P. D.; Kepert, C. J. Negative thermal expansion in the metal-organic framework material Cu_3(1,3,5-benzenetricarboxylate)$_2$. *Angew. Chem., Int. Ed.* **2008**, *47*, 8929−8932.
(27) Song, Y.; Shen, Y.; Hu, P.; Lin, Y.; Li, M.; Nan, C. W. Significant enhancement in energy density of polymer composites induced by dopamine-modified $Ba_{0.6}Sr_{0.4}TiO_3$ nanofibers. *Appl. Phys. Lett.* **2012**, *101*, 152904.
(28) Tamboli, M. S.; Palei, P. K.; Patil, S. S.; Kulkarni, M. V.; Maldar, N. N.; Kale, B. B. Polymethyl methacrylate (PMMA)-bismuth ferrite (BFO) nanocomposite: low loss and high dielectric constant materials with perceptible magnetic properties. *Dalton Trans.* **2014**, *43*, 13232−13241.
(29) Roessler, D. M. Kramers-Kronig analysis of reflection data. *Br. J. Appl. Phys.* **1965**, *16*, 1119−1123.
(30) Grimme, S.; Antony, J.; Ehrlich, S.; Krieg, H. A consistent and accurate ab initio parametrization of density functional dispersion correction (DFT-D) for the 94 elements H-Pu. *J. Chem. Phys.* **2010**, *132*, 154104.
(31) Wilson, J. N.; Frost, J. M.; Wallace, S. K.; Walsh, A. Dielectric and ferroic properties of metal halide perovskites. *APL Mater.* **2019**, *7*, No. 010901.
(32) Ryder, M. R.; Civalleri, B.; Cinque, G.; Tan, J. C. Discovering connections between terahertz vibrations and elasticity underpinning the collective dynamics of the HKUST-1 metal−organic framework. *CrystEngComm* **2016**, *18*, 4303−4312.
(33) Lin, K.-S.; Adhikari, A. K.; Ku, C.-N.; Chiang, C.-L.; Kuo, H. Synthesis and characterization of porous HKUST-1 metal organic frameworks for hydrogen storage. *Int. J. Hydrogen Energy* **2012**, *37*, 13865−13871.
(34) Ryder, M. R.; Civalleri, B.; Bennett, T. D.; Henke, S.; Rudić, S.; Cinque, G.; Fernandez-Alonso, F.; Tan, J. C. Identifying the Role of Terahertz Vibrations in Metal-Organic Frameworks: From Gate-Opening Phenomenon to Shear-Driven Structural Destabilization. *Phys. Rev. Lett.* **2014**, *113*, 215502.

DOI: 10.1021/acs.jpcc.9b08125
J. Phys. Chem. C 2019, 123, 29427−29435

Statement of Authorship for joint/multi-authored papers for PGR thesis
To appear at the end of each thesis chapter submitted as an article/paper
The statement shall describe the candidate's and co-authors' independent research contributions in the thesis publications. For each publication there should exist a complete statement that is to be filled out and signed by the candidate and supervisor **(only required where there isn't already a statement of contribution within the paper itself).**

Title of Paper	Impact of pressure and temperature on the broadband dielectric response of the HKUST-1 metal-organic framework
Publication Status	Published
Publication Details	A. S. Babal; L. Dona; M. R. Ryder; K. Titov; A. K. Chaudhari; Z. Zeng; C. S. Kelley; M. D. Frogley; G. Cinque; B. Civalleri, Impact of pressure and temperature on the broadband dielectric response of the HKUST-1 metal–organic framework. *J. Phys. Chem. C* **2019**, 123, 29427-29435.

Student Confirmation

Student Name:	Arun Singh Babal		
Contribution to the Paper	A. S. Babal performed the MHz experiments, analysed the dielectric data (MHz and THz) and wrote the manuscript. L. Dona and B. Civalleri performed the DFT calculations and theoretical analysis. M. R. Ryder, K.Titov, A.K. Chaudhari, and Z. Zeng performed the THz synchrotron experiments with guidance from M. D. Frogley and C. S. Kelley, and under the supervision of G. Cinque. J. C. Tan supervised the whole project.		
Signature	Arun Singh Babal	Date	15/12/2021

Supervisor Confirmation

By signing the Statement of Authorship, you are certifying that the candidate made a substantial contribution to the publication, and that the description described above is accurate.

Supervisor name and title: Prof. Jin-Chong Tan		
Supervisor comments: The provided description is accurate.		
Signature	Date	15/12/2021

This completed form should be included in the thesis, at the end of the relevant chapter.

Paper II

Broadband dielectric behavior of an MIL-100 metal–organic framework as a function of structural amorphization

ACS APPLIED ELECTRONIC MATERIALS

pubs.acs.org/acsaelm Article

Broadband Dielectric Behavior of an MIL-100 Metal–Organic Framework as a Function of Structural Amorphization

Arun Singh Babal, Barbara E. Souza, Annika F. Möslein, Mario Gutiérrez, Mark D. Frogley, and Jin-Chong Tan*

Cite This: *ACS Appl. Electron. Mater.* 2021, 3, 1191–1198 Read Online

ACCESS | Metrics & More | Article Recommendations | Supporting Information

ABSTRACT: The performance of modern electronics is associated with multi-layered interconnects, encouraging the development of low-*k* dielectrics. Herein, we studied the effects of phase transition from crystalline to amorphous on dielectric, optical, and electrical properties of MIL-100 (Fe) and Basolite F300 metal–organic frameworks obtained using different synthesis techniques in both the radio (4–1.5 MHz) and infrared (IR, 1.2–150 THz) frequency regimes, which are important for the microelectronics, IR optical sensors, and high-frequency telecommunications. The impact of amorphization on the broadband dielectric response was established based on the following: (1) by comparison of the dielectric characteristics of commercially available amorphous Basolite F300 versus mechanochemically synthesized crystalline MIL-100 (Fe) in the MHz region and (2) by tracking the frequency shifts in the vibrational modes of the MIL-100 structure in the far-IR (phonons) and mid-IR regions. We showed that various parameters such as the pelleting pressure, temperature, frequency, density, and degree of amorphization greatly affect the dielectric properties of the framework. We also investigated the influence of temperature (20–100 °C) on the electric and dielectric responses in the MHz region, which are crucial for all electronic devices.

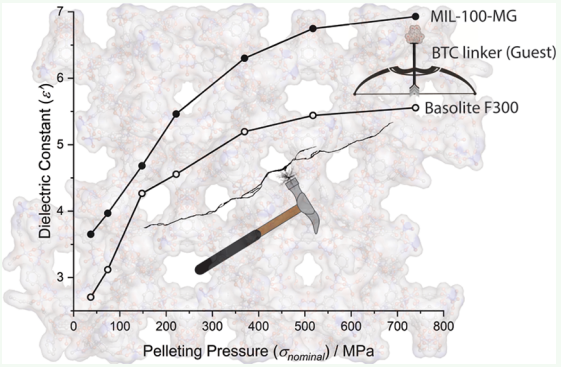

KEYWORDS: *metal–organic framework, amorphization, broadband dielectrics, nano-FTIR, synchrotron infrared specular reflectance spectroscopy, conductivity*

1. INTRODUCTION

For 60 years, the development efforts in microelectronics to integrate new dielectric insulator materials in the interconnects of very large-scale integration along with several billions of components and their interconnects in ever-shrinking chips have paved the way for continuous performance enhancement following Moore's law.[1] The dimension shrinking increases the resistance and capacitance of the back end of line structures, which causes signal delay, power dissipation, and cross-talk between the devices and becomes a bottleneck for the next-generation ultralarge-scale integration devices.[2] Due to low mechanical and chemical stability of both organic and hybrid dielectric materials, there are challenges in incorporating them into integrated circuits (ICs) and recently porous organosilicate glasses ($\varepsilon' \sim 3.0$) are being used as an alternative to the traditional SiO_2 materials ($\varepsilon' \sim 4.0$).[3,4]

Metal–organic frameworks (MOFs) are a subset of nanoporous inorganic–organic materials and display the potential for yielding a good combination of chemical and mechanical stability required for interconnects. MOFs exhibit a low dielectric constant value caused by their low density[5] and uniform pore distribution (<2 nm), which can potentially be used between the intermetal spacing (~10 nm).[6] Due to the frequency dependence of dielectric constant, static (DC) values are considered as a good approximation in modern microprocessors, whose operating limit is of the order of 10^9 Hz (GHz). For developing high-speed communication devices in infrared (IR) and optical regions, understanding of the dielectric constant dependency on the atomic and ionic polarization, which are structural dependent, is essential. The effect of various key parameters such as material density, stress-dependent amorphization, operating temperature, and so forth on new dielectric materials is also necessary for their implementation in the real-world scenario. Only a handful of studies are available on pressure-induced amorphization of MOFs and its relation to their physical properties.[7−9]

MOF materials have started to gain attention from the scientific community as a promising low-*k* dielectric due to their tunable physical and chemical properties.[10,11] A complete

Received: November 28, 2020
Accepted: February 15, 2021
Published: February 24, 2021

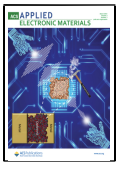

https://dx.doi.org/10.1021/acsaelm.0c01045
ACS Appl. Electron. Mater. 2021, 3, 1191–1198

dielectric spectrum over the frequency is required to exploit its full potential, while only a single type of polarization is studied mainly in the radio frequency region for most of the cases[12,13] and rarely in the higher frequency regions.[14−16] For instance, one study reported the dielectric property of a ZIF-based MOF in the IR region[15] using synchrotron specular reflectance spectroscopy, whereas other studies focused on the dielectric behavior in the kHz to MHz region.[17] Similarly, HKUST-1 films were studied in the optical frequency (visible region) for electronic polarization using the spectroscopic ellipsometry technique.[18] While other studies on HKUST-1 MOF have focused on the radio frequency region.[19] Therefore, a complete dielectric study of the system is a must to grasp the full understanding and to gauge the potential of the material as a dielectric interlayer for next-generation electronics, sensors, and telecommunication devices.

Here, we have studied for the first time the electric and broadband dielectric (Hz to MHz to THz) properties of both MIL-100 (Fe) and Basolite F300 systems at varying temperatures and pelleting pressures. The key feature of this study is to establish the relation between the degree of structural amorphization and how it may affect the electric, dielectric, and optical properties of the MOF. For this purpose, a comparative measurement was carried out on the MOF samples, which were obtained from two different synthetic routes. Furthermore, the MHz and THz dielectric data obtained from the LCR meter (inductance−capacitance−resistance) and synchrotron IR specular reflectance spectroscopy, respectively, were combined to give us a deeper understanding of the dielectric and optical responses of the MIL-100 (Fe) system, surpassing the static dielectric behavior commonly found in the literature.

2. EXPERIMENTAL SECTION

2.1. Materials. Basolite F300, a form of Fe-BTC, along with iron(III) nitrate nonahydrate [$Fe(NO_3)_3{\cdot}9H_2O$], and the linker benzene-1,3,5-tricarboxylic acid (H_3BTC) were purchased from Sigma-Aldrich and used without further purification.

2.2. Mechanochemistry of MIL-100 (Fe). 3 mmol of iron(III) nitrate (1.212 g) and 2 mmol of H_3BTC (0.420 g) were ground in an agate mortar for 10 min. The resulting material was heated in an oven for 4 h at 160 °C to complete the annealing process. The product was then washed by centrifugation (8000 rpm for 10 min) with methanol and deionized water to remove the unreacted molecules. It was first activated in a vacuum oven at 150 °C for 12 h and then immersed in deionized water and kept under stirring for the next 12 days at room temperature to perform the framework reconstruction. The obtained MIL-100 (Fe) powder is termed MIL-100-MG, where MG stands for manual grinding. Finally, the sample was recovered and reactivated. The synthesis method of MIL-100-MG was adapted from ref 20.

2.3. Pellet Preparation. A manual hydraulic press (Specac 15 ton capacity) was used to prepare pellets (150 mg each) from the MIL-100 powder under different mechanical loads (0.5, 1, 2, 3, 5, 7, and 10 ton force) onto a 13-mm diameter die. The pellets obtained from commercially available Basolite F300 powder are designated as Basolite F300-*N*-ton, whereas pellets obtained from the MIL-100 powder using the mechanochemistry technique are called MIL-100-MG-*N*-ton, where *N* is the applied mechanical load during pelleting.

2.4. Fourier-Transform Infrared Spectroscopy. The mid-IR modes of the MOF pellets were characterized at 0.5 cm^{-1} spectral resolution using the Nicolet iS10 FTIR spectrometer equipped with an attenuated total reflection accessory. The nano-Fourier-transform infrared (nano-FTIR) spectra were acquired using a neaSNOM instrument (Neaspec GmbH), where an AFM tip in the tapping mode is illuminated by a broadband mid-IR laser source (Toptica). Recently, the nano-FTIR technique has been successfully employed to characterize the local IR spectra of MOF nanocrystals.[21] To probe the near-field signal without the interference of background contributions, the detector signal is demodulated at higher harmonics of the oscillation frequency of the AFM tip (Ω = 253 kHz). Each spectrum is an average of more than five individual point spectra probed with a spot size of 20 nm. These were acquired by Fourier-transform spectroscopy averaging over 13 individual interferograms with 1024 pixels and an integration time of 11 ms per pixel, normalized by a reference spectrum measured on the silicon substrate.

2.5. Thermogravimetric Analysis. Thermogravimetric analysis (TGA) was carried out to examine the thermal stability of the MIL-100 powder and pellets using the TGA-Q50 (TA Instruments) equipped with an induction heater (1000 °C, max temperature) under an inert atmosphere of N_2. The samples were heated in a platinum sample holder at a rate of 10 °C/min from 40 to 500 °C.

2.6. X-ray Diffraction. The pressure-dependent amorphization effect in both Basolite F300 and the MIL-100 system was studied using X-ray diffraction (XRD) patterns collected using the Rigaku MiniFlex bench-top X-ray diffractometer at a scan rate of 0.2°/min with a step size of 0.05°.

2.7. Using the LCR Meter to Measure the Hz to MHz Range. The dielectric response of pellets in the radio frequency range (4 Hz to 1.5 MHz) was investigated using the IM3536 LCR meter, which is based on the parallel plate capacitor principle. The silver coating was applied on both sides of the pellet to emulate the parallel plate electrodes. The dielectric sample holder was placed in the high vacuum oven (pressure = 10^{-3} Torr) and calibrated for the pellet thickness. Samples were evacuated for 16 h at 20 °C before starting the measurements. The temperature-dependent dielectric response was noted at a step size of 10 °C. The real (ε') and imaginary (ε'') parts of the dielectric constant as a function of frequency (ω) were calculated from the following standard equations

$$\varepsilon'(\omega) = \frac{C(\omega)d}{\varepsilon_0 A} \tag{1}$$

$$\varepsilon''(\omega) = \varepsilon'(\omega)\tan\delta \tag{2}$$

where C is the capacitance, d is the distance between the pair of parallel plate electrodes, A is the area of the electrode, ε_0 is the vacuum permittivity, and tan δ is the loss tangent.

2.8. Using Synchrotron IR Specular Reflectance Spectroscopy to Measure the Far-IR (THz), Mid-IR, and Near-IR Frequencies. The dielectric response of pellets in the IR region (1.2−150 THz) was obtained by transforming the reflectivity spectrum, collected from the Bruker Vertex 80V FTIR interferometer equipped with the Pike Technologies VeeMAX II variable angle specular reflectance accessory at the Beamline B22 MIRIAM in the Diamond Light Source (Harwell, UK).

Two beam splitters were used in the IR region: (i) a 6 μm thick Mylar broadband multi-layer-coated beam splitter for far-IR and (ii) a KBr beam splitter for mid-IR. The background and pellet spectra were collected for both regions at an angle of 30° from the normal axis of the pellet surface at 2 cm^{-1} resolution and 512 scans per spectral scan, which were kept constant for all the pellets for comparison. The dielectric and refractive indices were evaluated by applying the Kramers−Kronig transformation (KKT)[22] on the reflectivity data $R(\omega)$ using the following relations

$$\phi(\omega_a) = \frac{2\omega_a}{\pi}\int_0^\infty \frac{\log(\sqrt{R(\omega)})}{\omega^2 - \omega_a^2}\mathrm{d}\omega \tag{3}$$

$$n(\omega) = \frac{1 - R(\omega)}{1 + R(\omega) - 2\sqrt{R}\cos(\phi(\omega))} \tag{4}$$

$$\kappa(\omega) = \frac{-2\sqrt{R}\sin(\phi(\omega))}{1 + R(\omega) - 2\sqrt{R}\cos(\phi(\omega))} \tag{5}$$

where $\phi(\omega)$ is the phase angle as a function of wavenumber (cm^{-1}), ω_a is the arbitrary wavenumber, n is the real part of refractive index, and κ is the imaginary part of the refractive index.

https://dx.doi.org/10.1021/acsaelm.0c01045
ACS Appl. Electron. Mater. 2021, 3, 1191−1198

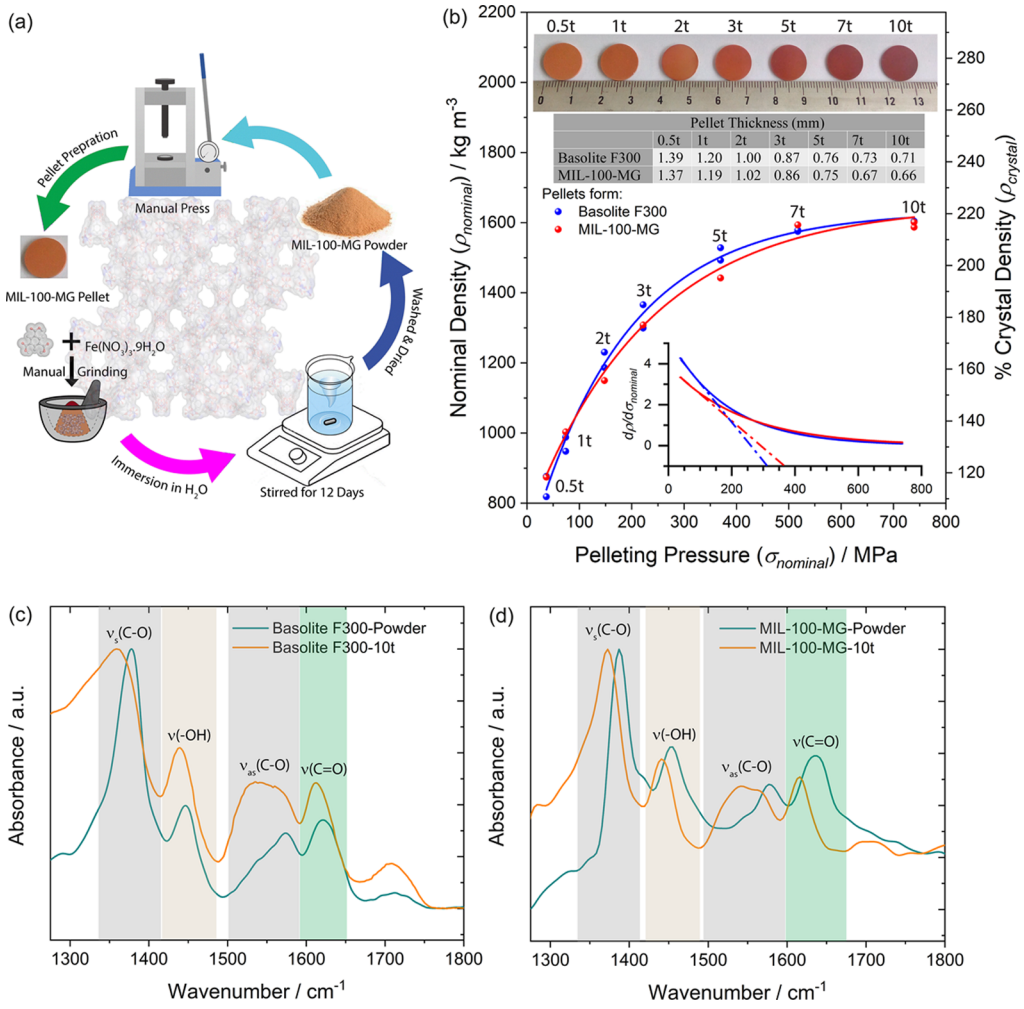

Figure 1. (a) MIL-100-MG powder synthesized by the mechanochemistry route and its subsequent pellet preparation process. (b) Pelleting pressure-dependent nominal density plot for Basolite F300 and MIL-100-MG pellets used in the experiments. The pellets were labeled in terms of the applied uniaxial force, e.g., 0.5 t for pellet pressed at 0.5 ton force. The photograph of pellets used in the experiments is also shown here. The inset shows the plot for the derivative of density over the pelleting pressure and was used to estimate the yield strength of the compressed powder of Basolite F300 and MIL-100-MG as 310 and 366 MPa, respectively. The table inset shows the average pellet thickness determined from three samples. (c,d) Nano-FTIR spectra for Basolite F300 and MIL-100-MG samples (powder and 10 t pellet), respectively.

$$\tilde{\varepsilon}(\omega) = \tilde{n}(\omega)^2 \tag{6}$$

$$\varepsilon'(\omega) = n(\omega)^2 - \kappa(\omega)^2 \tag{7}$$

$$\varepsilon''(\omega) = 2n(\omega)\kappa(\omega) \tag{8}$$

where ε' and ε'' are the real and imaginary parts of the dielectric constant, respectively.

3. RESULTS AND DISCUSSION

In this study, a series of 13 mm diameter disk pellets were prepared using the manual hydraulic press by applying 0.5, 1, 2, 3, 5, 7, and 10 tons of force (see Figure 1a, which summarizes the MIL-100 powder synthesis and the pellet preparation). The nominal density curve was plotted for both types of pellets: commercially available (Basolite F300) and in-house synthesized MIL-100 (mechanochemistry technique, termed MIL-100-MG), which were used in the dielectric experiment, confirm that similar density pellets were used to compare and obtain an understanding of the effect of amorphization on material dielectrics (see Figure 1b). In contrast to the Basolite F300 pellets, the MIL-100-MG pellets are slightly denser due to the presence of residual linker molecules in the framework cavity, which is a common occurrence in MOFs synthesized using the mechanochemistry technique.[20] The estimated yield strengths of the compressed powder Basolite F300 and MIL-100-MG were 310 and 366 MPa, respectively, indicating that the confinement of guests in the framework cavity increases its mechanical stability under compression (see the inset of Figure 1b). A systematic shift in the color of the pellets from light brown to dark brown was also observed, which hints toward the increase in the refractive index with pellet density.

The MIL-100 structure has a large pore (~3 nm mesocage); thus, it is highly susceptible to mechanical pressure-induced amorphization. Herein, we track the structural evolution upon pelleting using powder XRD. The XRD spectra of Basolite F300 powder show significant broadness in its characteristic Bragg peaks, followed by diminishing of the long-range periodicity over increased pelleting pressure (see Figure S1a), whereas MIL-100-MG powder demonstrates high crystallinity, and with increased pelleting pressure, an amorphous hump arises at $2\theta = 8°$ starting from 37 MPa (0.5 t) (see Figure S1b). The XRD spectra of MIL-100-MG pellets prepared at higher pelleting pressures (>221.76 MPa)

https://dx.doi.org/10.1021/acsaelm.0c01045
ACS Appl. Electron. Mater. 2021, 3, 1191−1198

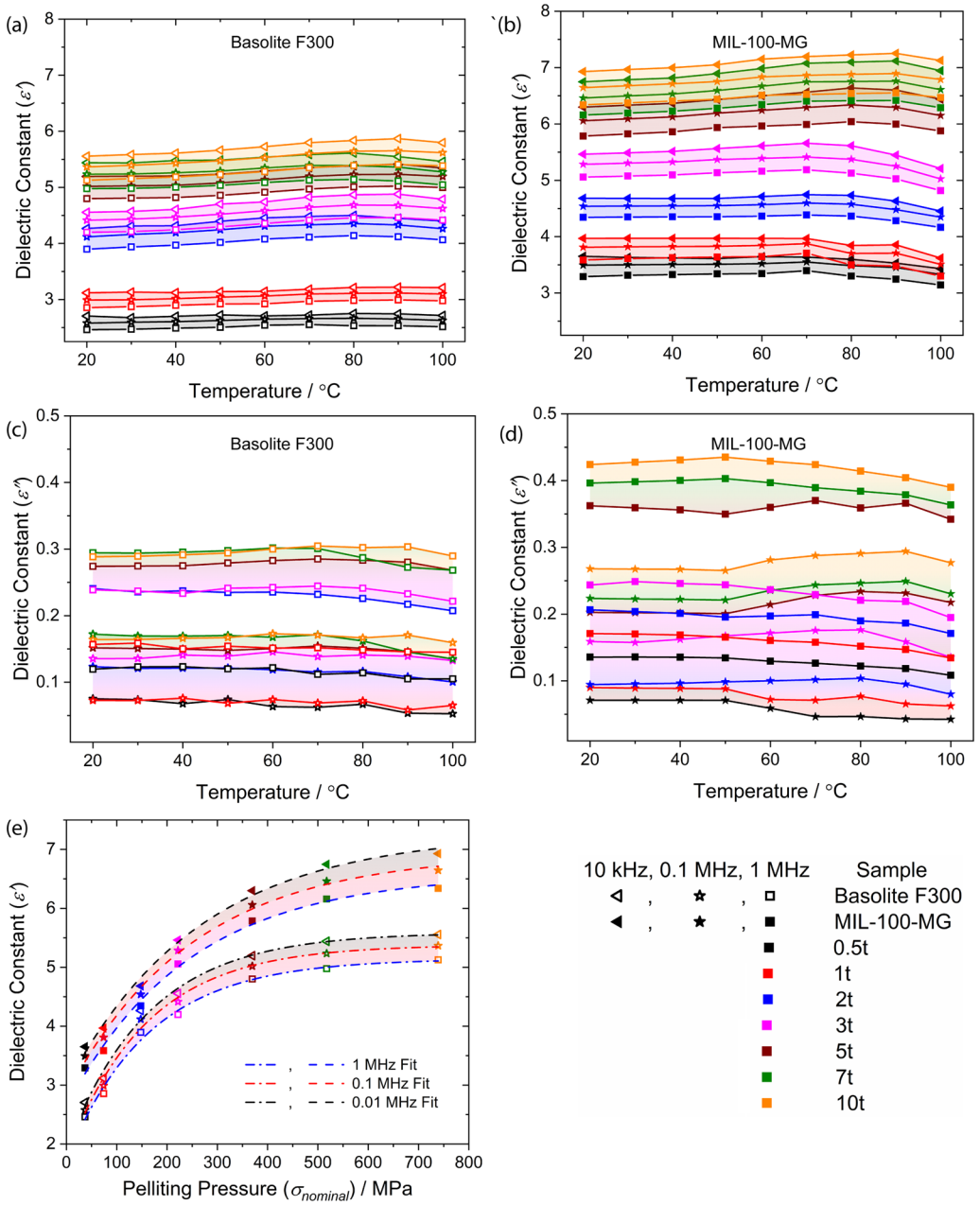

Figure 2. Dielectric properties of MOF pellets as a function of temperature: the real part of dielectric constant ε' for (a) Basolite F300 and (b) MIL-100-MG pellets. The imaginary part of dielectric constant ε'' for (c) Basolite F300 and (d) MIL-100-MG pellets. (e) ε' as a function of pelleting pressure for the three specific frequencies of 0.01, 0.1, and 1 MHz.

are mainly dominated by the amorphous peak, which is obvious from Figure S1c. Both the broadness in characteristic peaks and the appearance of an amorphous hump in the spectra can be attributed to the complete pore collapse and structural amorphization in the MIL-100 framework. The FTIR spectrum of the Basolite F300 system also shows broadness in its characteristic peaks and a frequency-dependent red shift under compression, which follows the density pattern (see Figure S2). As the pelleting pressure was increased to 10 tons, the nano-FTIR spectra in Figure 1c,d revealed that the main IR absorption bands (except the carboxylate stretch) remained unchanged with some broadening, followed by a red shift in the peak positions. In contrast, the carboxylate asymmetric stretch at 1578 cm^{-1} showed significant broadening and the appearance of a shoulder band at ~1535 cm^{-1}, which is the characteristic asymmetric stretch of monodentate coordinated carboxylates indicating the broken bonds of Fe–O_{COO}.[7] The result supports the notion that bond breakage is responsible for the amorphization of MIL-100 subject to mechanical stress. Basolite F300 also shows higher thermal stability of up to 300 °C, which increases slightly with the pelleting pressure, even after amorphization (see Figure S3).

Figure 2 contrasts the amorphization effect on the dielectric properties in both types of MOF pellets as a function of pelleting pressure and temperature at 0.01, 0.1, and 1 MHz frequencies. For both Basolite F300 and MIL-100-MG pellets, the real part of dielectric constant (ε') shows a systematic increase under compression. Interestingly, for individual pressure pellet, the ε' value decreases as a function of frequency, which can be associated with the decline in the

https://dx.doi.org/10.1021/acsaelm.0c01045
ACS Appl. Electron. Mater. 2021, 3, 1191−1198

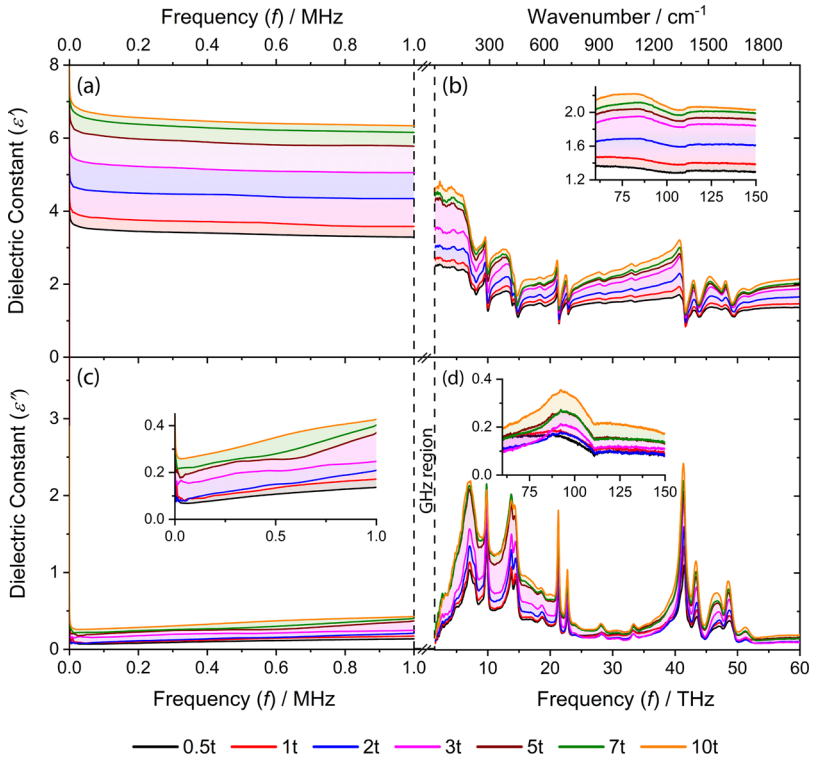

Figure 3. Pressure-dependent broadband dielectric spectrum for MIL-100 MOF in the frequency range of 4 Hz to 150 THz. (a,b) The real part of the dielectric constant ε' and (c,d) imaginary part of the dielectric constant ε''. In the radio frequency (Hz to MHz) range, the dielectric measurements are based on the LCR parallel-plate capacitor technique, whereas synchrotron specular reflectance spectroscopy was used to study the optical properties in the IR region (2−150 THz), which were converted into dielectric parameters. The pellets studied for dielectrics are 0.5, 1, 2, 3, 5, 7, and 10 t pellets.

orientational polarizability (inherent dipole moment inertia cannot keep up with the oscillating field) caused by the higher alternating field.

In Figure 2a, the ε' shows a sudden surge from 1 t pellet to the 2 t pellet of Basolite F300 sample, which can be associated with the loss of long-range periodicity confirmed by XRD. Similarly, in Figure 2b of MIL-100-MG pellets, the ε' value shows a step increase from 1 to 2, 2 to 3, and 3 to 5 t pellets, which follows the XRD trend revealing the amorphization of the open framework. The rising temperature also assists in better alignment of the dipole moment of the amorphized structures, resulting in a higher ε' value in both pellet types. Additionally, the MIL-100-MG pellets show a higher dielectric value over its counterpart Basolite F300 pellets due to pore blockage (resulting from the mechanochemical grinding method).

For all the pellets, the increase in the imaginary part of dielectric constant (ε'') with frequency is associated with the higher energy dissipation resulting from the dipole motion. As evident from Figure 2c,d, MIL-100-MG pellets showed slightly higher energy dissipation over its counterpart Basolite F300 pellets, resulting from the pore blockage and higher degree of amorphization (Figure S1). Figure 2e summarizes the ε' values for both Basolite F300 and MIL-100-MG pellets. The complete datasets of the temperature- and frequency-dependent MHz dielectrics for the individual pellets of Basolite F300 and MIL-100-MG MOFs are presented in the Supporting Information, see Figures S4−S10.

The MIL-100-MG pellets were chosen to study the optical properties, due to their phase transition from the crystalline to amorphous phase under compression, whereas the as-received Basolite F300 already had some amorphous phase associated with it (see Figure S1). The dielectric and refractive properties in the broadband IR frequencies (40−5000 cm^{-1}) were evaluated by implementing KKT[22] on the high-resolution reflectance spectra (Figure S11). The optical properties of the framework in terms of refractive index mainly depend upon its optical density, surroundings, temperature, and the frequency of the incident light. The components of complex refractive index, the real (n) and (κ) imaginary parts associated with the phase velocity and incidental light beam absorption on the framework, respectively, show an increase with pellets' optical density resulting from the pelleting pressure and decrease as a function of higher frequency (see Figure S12).

The calculated dielectric properties of MIL-100-MG pellets in the IR region are presented in conjunction with the Hz to MHz data for a better illustration of the broadband dielectric spectrum (4 Hz to 150 THz frequency range) of the MIL-100 framework (see Figure 3). Their overall dielectric constant can be expressed in terms of different polarization mechanisms, as follows

$$\varepsilon'_{\text{Total}} = \varepsilon'_{\text{Space charge (below 100 Hz)}} + \varepsilon'_{\text{Dipole/Orientational (MHz region)}} + \varepsilon'_{\text{Atomic/Vibrational (THz region)}} + \varepsilon'_{\text{Optical/Electronic (above 100 THz)}} \quad (9)$$

Switching the frequency from MHz to THz causes a step decrease in dielectric values, correlated with the loss of dipole-based polarization. The step increase in the dielectric values of

https://dx.doi.org/10.1021/acsaelm.0c01045
ACS Appl. Electron. Mater. 2021, 3, 1191−1198

Table 1. Contributions of the Main Polarization Mechanisms to the Total Dielectric Response of MIL-100-MG[a]

polarization mechanisms → pelleting pressure (MPa) ↓	$\varepsilon'_{\text{Dipole/Orientational polarization}}$ MHz (4 Hz to 1.5 MHz)	$\varepsilon'_{\text{Atomic/Vibrational polarization}}$ far-IR to mid-IR (1.5−100 THz)	$\varepsilon'_{\text{Optical/Electronic polarization}}$ near-IR (100−150 THz)	$\varepsilon'_{\text{Total (MIL-100-MG)}}$ full-spectrum (100 Hz)	$\varepsilon'_{\text{Total (Basolite F300)}}$ full-spectrum (100 Hz)
36.96	1.83	1.18	1.29	4.30	2.96
73.92	2.06	1.26	1.39	4.71	3.20
147.84	2.37	1.38	1.6	5.35	4.63
221.76	2.53	1.60	1.84	5.97	4.87
369.60	2.97	2.31	1.91	7.19	5.64
517.44	3.45	2.37	2.00	7.82	5.75
739.20	3.36	2.50	2.10	7.96	6.13

[a]The contribution of space charge is not considered in this analysis.

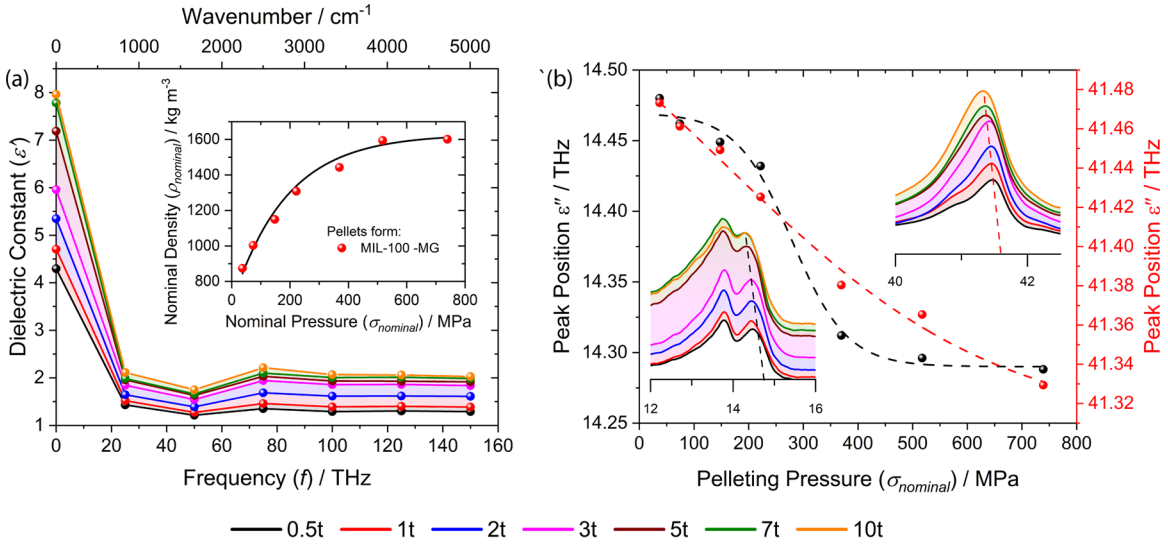

Figure 4. (a) Effect of crystalline to amorphous transition of MIL-100-MG pellets on the real part of dielectric constants at specific broadband frequencies comprising the far-, mid-, and near-IR regions. (b) Pelleting pressure-dependent red shifts in the THz peaks associated with the phonon modes (collective THz vibrations) of molecular moieties.

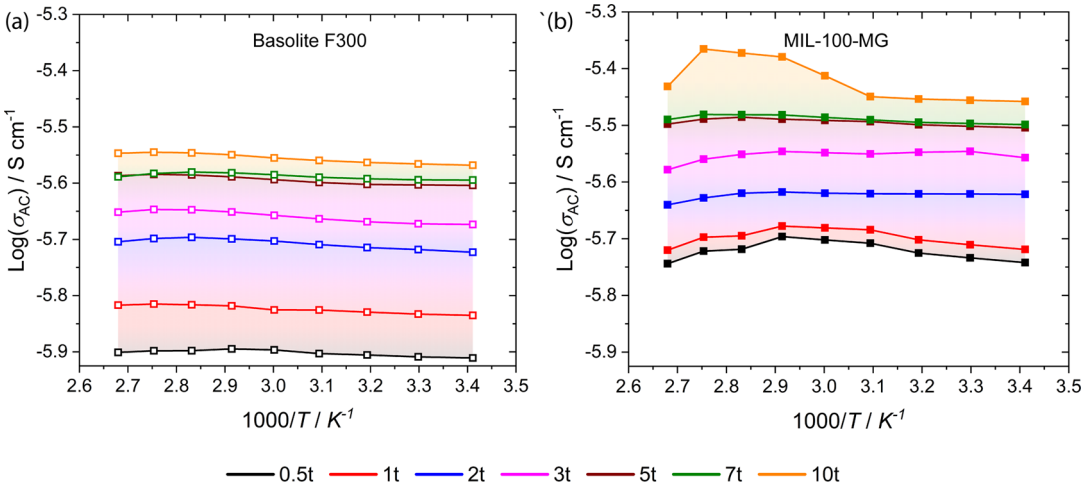

Figure 5. AC conductivity of MIL-100 pellets: (a) Basolite F300 and (b) MIL-100-MG as a function of residual pressure and temperature.

individual pellets in the IR region is proportional to the pressure-induced framework amorphization and pelleting density, which follows the low-frequency (Hz to MHz) trend.

In the far-IR region (<20 THz), the dielectric properties of a material depend upon the bond polarity and the phonons of the structure. The distinctive transitions evidenced in the individual pellet ε' curve (Figure 3b) are associated with the collective vibrational modes, that is, metal-linker and linker deformations of the MIL-100 system, accompanied by an absorption peak (dissipation) in the ε'' plot associated with the loss of energy during these collective vibrations.[23,24] Our data suggest that pelleting pressure-dependent amorphization also

https://dx.doi.org/10.1021/acsaelm.0c01045
ACS Appl. Electron. Mater. 2021, 3, 1191−1198

yields chemical bond polarization in the framework, thereby contributing to a higher ε' value observed under compression. Similarly, the dielectric polarization associated with the vibrational modes of molecular moieties, that is, torsional, bending, and stretching, dominate the mid-IR (~20−100 THz) region.

The absence of transition modes in the near-IR region (100−150 THz) shows the insensitivity of the dielectric response of MIL-100 toward its structural deformation. Due to the dependency of electronic polarization on the atomic volume and its density, the effect of pelleting pressure-dependent amorphization can be evidenced in this region, thus limiting the ε' values lying within the dielectric band to be 1.3−2.1. The individual contribution of all these mechanisms can be further broken down as summarized in Table 1.

A summary of the ε' trend of MIL-100-MG pellets is shown in Figure 4a to reveal the effect of transition from the crystalline to amorphous phase on the broadband dielectric behavior. We found that the mechanical deformation and structural densification of the framework cause phonon mode softening. Due to the structural dependency of the atomic polarization, the decline rate of ε' in the far-IR to mid-IR range is much greater as a function of pelleting pressure when compared to the plateau observed in the near-IR region (mainly associated with the electron density). Interestingly, for both far- and mid-IR regions, a systematic pelleting pressure-dependent red shift was observed for a few of the ε'' absorption peaks of the pellets, from which the amplitude of two majorly shifted peaks is plotted against the nominal pressure, as shown in Figures 4b and S13. These step changes in the red shifts indicate the softening in the phonon modes within THz frequencies, and the results can be explained by the amorphization trend underpinning the pellets.

In addition to the dielectric and optical properties, the pelleting pressure-dependent electrical conductivity measurements were also carried out on both types of pellets in the frequency range of 4 Hz to 1.5 MHz. Figure 5a,b shows the pelleting pressure and temperature-dependent AC conductivity values for Basolite F300 and MIL-100-MG pellets at 1 MHz frequency, respectively. Similar to ε', the increase in conductivity values also follows the amorphization pattern, suggesting that framework distortion may facilitate charge hopping (by decreasing the percolation threshold in the pellets) resulting in a sudden increase in conductivity values from 1 to 2 and 3 to 5 t pellets for Basolite F300 pellets and 1−2, 2−3, and 3−5 t for MIL-100-MG pellets at 20 °C. The MIL-100-MG pellets show overall higher conductivity values in addition to a higher temperature-dependent conductivity rate over its Basolite F300 counterpart, which was facilitated by the occupied guest molecules in the framework cavity. The temperature rise will ease the electron movement to upper bands and decrease the resistance of the insulating MIL-100 pellet. The temperature- and frequency-dependent conductivity plots for the individual Basolite F300 and MIL-100-MG pellets are shown in Figures S14 and S15, respectively.

4. CONCLUSIONS

In addition to the surrounding temperature and operating frequency, both the pelleting pressure-dependent amorphization and the pore occupancy greatly affect the dielectric, optical, and electrical properties of the MOF framework. Herein, we contrasted the properties of both Basolite F300 and MIL-100 (Fe) frameworks obtained via different processing techniques and studied their framework properties at different instances during their transition from the crystalline to amorphous phase. The MIL-100 pellets obtained using mechanochemistry was chosen to further explore the dependence of dielectric constant on the dipole orientation, phonon, and electronic polarization due to their clear phase transition from crystalline to amorphous as a function of pelleting pressure. To this end, we studied their effect on dielectric properties in different frequency regimes: (i) radio frequency region (4−1.5 MHz) for dipole polarization in the framework, (ii) IR region (1.2−150 THz)—framework collective modes in the far-IR (<20 THz), atomic vibrations in the mid-IR (20−100 THz), and electronic response in the near-IR (>100 THz). Interestingly, only red shifts were observed for the few transition modes in optical and dielectric spectra due to bond softening. A greater understanding of broadband dielectrics under the influence of structural amorphization provides a cornerstone to new technologies bridging the domains of microelectronics and high-frequency telecommunications.

■ ASSOCIATED CONTENT

Supporting Information

The Supporting Information is available free of charge at https://pubs.acs.org/doi/10.1021/acsaelm.0c01045.

Material characterization (XRD, FTIR, and TGA) and the effect of pelleting pressure and temperature on the properties of dielectric (real, imaginary, and loss), optical (reflectivity, real and imaginary parts of refractive index), and electrical conductivity for Basolite F300 and MIL-100-MG pellets (PDF)

■ AUTHOR INFORMATION

Corresponding Author

Jin-Chong Tan − *Multifunctional Materials and Composites (MMC) Laboratory, Department of Engineering Science, University of Oxford, Oxford OX1 3PJ, U.K.*; orcid.org/0000-0002-5770-408X; Email: jin-chong.tan@eng.ox.ac.uk

Authors

Arun Singh Babal − *Multifunctional Materials and Composites (MMC) Laboratory, Department of Engineering Science, University of Oxford, Oxford OX1 3PJ, U.K.*

Barbara E. Souza − *Multifunctional Materials and Composites (MMC) Laboratory, Department of Engineering Science, University of Oxford, Oxford OX1 3PJ, U.K.*; orcid.org/0000-0001-6315-2149

Annika F. Möslein − *Multifunctional Materials and Composites (MMC) Laboratory, Department of Engineering Science, University of Oxford, Oxford OX1 3PJ, U.K.*; orcid.org/0000-0002-2056-6437

Mario Gutiérrez − *Multifunctional Materials and Composites (MMC) Laboratory, Department of Engineering Science, University of Oxford, Oxford OX1 3PJ, U.K.*; orcid.org/0000-0001-9222-3647

Mark D. Frogley − *Diamond Light Source, Oxford OX11 0DE, U.K.*

Complete contact information is available at: https://pubs.acs.org/10.1021/acsaelm.0c01045

https://dx.doi.org/10.1021/acsaelm.0c01045
ACS Appl. Electron. Mater. 2021, 3, 1191−1198

Notes

The authors declare no competing financial interest.

■ ACKNOWLEDGMENTS

A.S.B. is grateful to the Engineering Science (EPSRC DTP—Samsung) Studentship that supports this DPhil research. J.-C.T., A.F.M., and M.G acknowledge the European Union's Horizon 2020 Research and Innovation Programme (ERC Consolidator Grant agreement no. 771575-PROMOFS) for supporting this research. J.-C.T. thanks the Samsung GRO Award (DFR00230) for funding this research. We acknowledge the Diamond Light Source for the provision of beamtime SM21472 at B22 MIRIAM. We thank the Research Complex at Harwell (RCaH) for the provision of TGA and FTIR instrumentation.

■ REFERENCES

(1) Moore, G. E. *Solid-State Circuits Society Newsletter*; IEEE, 2006; Vol. *20*, pp 33−35.
(2) Bohr, M. T. In Interconnect scaling-the real limiter to high performance ULSI. *Proceedings of International Electron Devices Meeting*; IEEE, 1995; pp 241−244.
(3) Grill, A.; Perraud, L.; Patel, V.; Jahnes, C.; Cohen, S. Low dielectric constant SiCOH films as potential candidates for interconnect dielectrics. *MRS Online Proc. Libr.* **1999**, *565*, 107−116.
(4) Thompson, S.; Anand, N.; Armstrong, M.; Auth, C.; Arcot, B.; Alavi, M.; Bai, P.; Bielefeld, J.; Bigwood, R.; Brandenburg, J. In A 90 nm logic technology featuring 50 nm strained silicon channel transistors, 7 layers of Cu interconnects, low-k ILD, and 1 μm SRAM cell, Digest. *International Electron Devices Meeting*; IEEE, 2002; pp 61−64.
(5) Zagorodniy, K.; Seifert, G.; Hermann, H. Metal-organic frameworks as promising candidates for future ultralow-κ dielectrics. *Appl. Phys. Lett.* **2010**, *97*, 251905.
(6) Farrell, R.; Goshal, T.; Cvelbar, U.; Petkov, N.; Morris, M. A. Advances in ultra low dielectric constant ordered porous materials. *Electrochem. Soc. Interface* **2011**, *20*, 39.
(7) Su, Z.; Miao, Y.-R.; Zhang, G.; Miller, J. T.; Suslick, K. S. Bond breakage under pressure in a metal-organic framework. *Chem. Sci.* **2017**, *8*, 8004−8011.
(8) Bennett, T. D.; Saines, P. J.; Keen, D. A.; Tan, J.-C.; Cheetham, A. K. Ball-Milling-Induced Amorphization of Zeolitic Imidazolate Frameworks (ZIFs) for the Irreversible Trapping of Iodine. *Chem.—Eur. J.* **2013**, *19*, 7049−7055.
(9) Cao, S.; Bennett, T. D.; Keen, D. A.; Goodwin, A. L.; Cheetham, A. K. Amorphization of the prototypical zeolitic imidazolate framework ZIF-8 by ball-milling. *Chem. Commun.* **2012**, *48*, 7805−7807.
(10) Stassen, I.; Burtch, N.; Talin, A.; Falcaro, P.; Allendorf, M.; Ameloot, R. An updated roadmap for the integration of metal−organic frameworks with electronic devices and chemical sensors. *Chem. Soc. Rev.* **2017**, *46*, 3185−3241.
(11) Mendiratta, S.; Usman, M.; Lu, K.-L. Expanding the dimensions of metal-organic framework research towards dielectrics. *Coord. Chem. Rev.* **2018**, *360*, 77−91.
(12) Li, W. J.; Liu, J.; Sun, Z. H.; Liu, T. F.; Lu, J.; Gao, S. Y.; He, C.; Cao, R.; Luo, J. H. Integration of metal-organic frameworks into an electrochemical dielectric thin film for electronic applications. *Nat. Commun.* **2016**, *7*, 11830.
(13) Krishtab, M.; Stassen, I.; Stassin, T.; Cruz, A. J.; Okudur, O. O.; Armini, S.; Wilson, C.; De Gendt, S.; Ameloot, R. Vapor-deposited zeolitic imidazolate frameworks as gap-filling ultra-low-κ dielectrics. *Nat. Commun.* **2019**, *10*, 3729.
(14) Titov, K.; Zeng, Z.; Ryder, M. R.; Chaudhari, A. K.; Civalleri, B.; Kelley, C. S.; Frogley, M. D.; Cinque, G.; Tan, J.-C. Probing dielectric properties of metal-organic frameworks: MIL-53(Al) as a model system for theoretical predictions and experimental measurements via synchrotron far- and mid-infrared spectroscopy. *J. Phys. Chem. Lett.* **2017**, *8*, 5035−5040.
(15) Ryder, M. R.; Zeng, Z.; Titov, K.; Sun, Y.; Mahdi, E. M.; Flyagina, I.; Bennett, T. D.; Civalleri, B.; Kelley, C. S.; Frogley, M. D.; Cinque, G.; Tan, J.-C. Dielectric properties of zeolitic imidazolate frameworks in the broad-band infrared regime. *J. Phys. Chem. Lett.* **2018**, *9*, 2678−2684.
(16) Babal, A. S.; Donà, L.; Ryder, M. R.; Titov, K.; Chaudhari, A. K.; Zeng, Z.; Kelley, C. S.; Frogley, M. D.; Cinque, G.; Civalleri, B.; Tan, J.-C. Impact of pressure and temperature on the broadband dielectric response of the HKUST-1 metal−organic framework. *J. Phys. Chem. C* **2019**, *123*, 29427−29435.
(17) Eslava, S.; Zhang, L.; Esconjauregui, S.; Yang, J.; Vanstreels, K.; Baklanov, M. R.; Saiz, E. Metal-organic framework ZIF-8 films as low-κ dielectrics in microelectronics. *Chem. Mater.* **2012**, *25*, 27−33.
(18) Redel, E.; Wang, Z.; Walheim, S.; Liu, J.; Gliemann, H.; Wöll, C. On the dielectric and optical properties of surface-anchored metal-organic frameworks: A study on epitaxially grown thin films. *Appl. Phys. Lett.* **2013**, *103*, 091903.
(19) Scatena, R.; Guntern, Y. T.; Macchi, P. Electron density and dielectric properties of highly porous MOFs: binding and mobility of guest molecules in $Cu_3(BTC)_2$ and $Zn_3(BTC)_2$. *J. Am. Chem. Soc.* **2019**, *141*, 9382−9390.
(20) Souza, B. E.; Möslein, A. F.; Titov, K.; Taylor, J. D.; Rudić, S.; Tan, J.-C. Green reconstruction of MIL-100 (Fe) in water for high crystallinity and enhanced guest encapsulation. *ACS Sustainable Chem. Eng.* **2020**, *8*, 8247−8255.
(21) Möslein, A. F.; Gutiérrez, M.; Cohen, B.; Tan, J.-C. Near-field infrared nanospectroscopy reveals guest confinement in metal−organic framework single crystals. *Nano Lett.* **2020**, *20*, 7446−7454.
(22) Roessler, D. M. Kramers-Kronig analysis of reflection data. *Br. J. Appl. Phys.* **1965**, *16*, 1119.
(23) Ryder, M. R.; Civalleri, B.; Bennett, T. D.; Henke, S.; Rudic, S.; Cinque, G.; Fernandez-Alonso, F.; Tan, J. C. Identifying the role of terahertz vibrations in metal-organic frameworks: from gate-opening phenomenon to shear-driven structural destabilization. *Phys. Rev. Lett.* **2014**, *113*, 215502.
(24) Ryder, M. R.; Civalleri, B.; Cinque, G.; Tan, J.-C. Discovering connections between terahertz vibrations and elasticity underpinning the collective dynamics of the HKUST-1 metal−organic framework. *CrystEngComm* **2016**, *18*, 4303−4312.

https://dx.doi.org/10.1021/acsaelm.0c01045
ACS Appl. Electron. Mater. 2021, 3, 1191−1198

Statement of Authorship for joint/multi-authored papers for PGR thesis
To appear at the end of each thesis chapter submitted as an article/paper
The statement shall describe the candidate's and co-authors' independent research contributions in the thesis publications. For each publication there should exist a complete statement that is to be filled out and signed by the candidate and supervisor **(only required where there isn't already a statement of contribution within the paper itself).**

Title of Paper	Broadband dielectric behavior of an MIL-100 metal-organic framework as a function of structural amorphization
Publication Status	Published
Publication Details	A. S. Babal; B. E. Souza; A. F. Möslein; M. Gutiérrez; M. D. Frogley; J. C. Tan, Broadband dielectric behavior of an MIL-100 metal–organic framework as a function of structural amorphization. *ACS Appl. Electron. Mater.* **2021**, 3, 1191-1198.

Student Confirmation

Student Name:	Arun Singh Babal		
Contribution to the Paper	A. S. Babal performed the MHz and THz experiments, analysed the data and wrote the manuscript. B. E. Souza provided the mechanically grinded MIL-100 MOF powder for the experiments and helped in the THz reflectivity data collection along with A. F. Möslein and M. Gutiérrez. M. D. Frogley oversaw the THz data collection and Prof. J. C. Tan supervised the whole project.		
Signature	Arun Singh Babal	Date	15/12/2021

Published Papers

Supervisor Confirmation

By signing the Statement of Authorship, you are certifying that the candidate made a substantial contribution to the publication, and that the description described above is accurate.

Supervisor name and title: Prof. Jin-Chong Tan		
Supervisor comments: The provided description is accurate.		
Signature	Date	15/12/2021

This completed form should be included in the thesis, at the end of the relevant chapter.

"Every brilliant experiment, like every great work of art,
starts with an act of imagination."

– Jonah Lehrer

3

Guest-Tunable Dielectric Response of the Metal–Organic Frameworks

The high porosity and tailorability of the metal-organic framework (MOF) materials make them an ideal candidate for user-specific applications. The high porosity of the MOF structure allows them to selectively capture the targeted guest species and investigate the host-guest interaction. The chapter is divided into two sections. In the first section 3.1, we will discuss the tuneability in the dielectric properties of MOF resulting from the encapsulation of guest species in the framework pores and channels. The second section 3.2 comprises a summary of the two case studies: polycrystalline and single crystal of HKUST-1, which are also explained in detail in Part II of the thesis in Paper III and Paper IV, respectively.

3.1 A brief literature review on guest-dependent MOF dielectrics

The dielectric measurement of a polycrystalline powder material included the contribution from the electrostatic field of its surrounding medium. One of the most common techniques, pellet dielectrics, was introduced to exclude the impact of the surrounding medium and for a reliable measurement. It was mainly based on

the parallel-plate capacitance method, in which the material capacitance was measured by applying the electric field across two parallelly oriented electrodes where the sample is located between the gaps. The dielectric property of a MOF material can also be influenced by several other factors including the nature of the reactants used in synthesis, framework density, and the level of crystallinity. To achieve a targeted low-κ dielectric material, in addition to the post-synthetic guest removal, both polar and functional groups such as hydroxyl or carbonyl groups were also usually avoided in the structure because they tend to attract water molecules from the moisture *via* hydrogen bonding. The pellet dielectrics were studied for both guest-free and guest-encapsulated MOFs for a better understanding of the effects of pore occupancy.

3.1.1 Inherent guest-free MOF dielectrics

MOFs with their high porosity and structural tailorability make them attractive for a varied range of applications. For interlayer dielectrics, the guest free MOF structures were particularly desired due to their higher porosity and lack of polarizability resulting from the absence of the occluded guest molecules. In this regard, Lu and co-workers synthesised a robust and low-dielectric 3D MOF $[Mg(phen)(bdc)]_n$ (phen = 1,10-phenanthroline, bdc^{2-}=1,4-benzene dicarboxylate).[32] The framework was solvent-free and had a rare cds-type topology with a non-interpenetrated structure. They utilised fine grinding, high pressure and guest-free analysis to minimise the interference of interparticle voids on the measurements. The low dielectric constant of the MOF framework in a wide

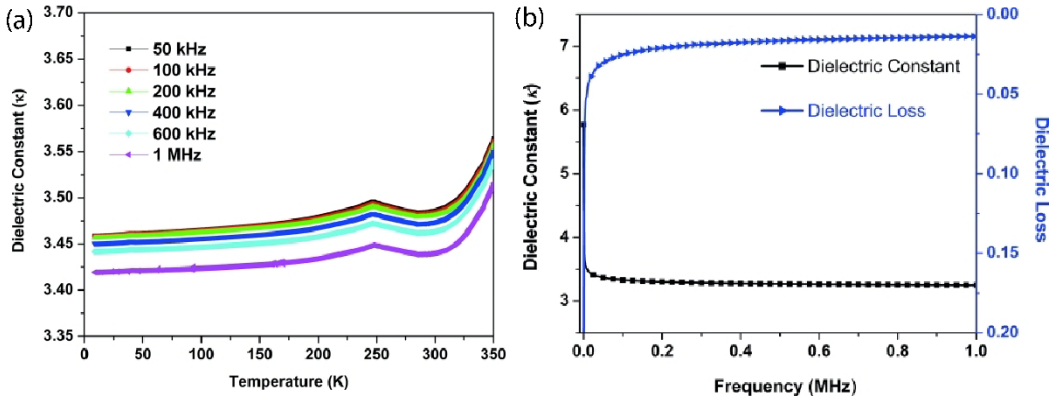

Figure 3.1: A plot of (a) temperature-dependent dielectric constants from 8 to 350 K and (b) variation in dielectric constant and dielectric loss in compound at different frequencies.[32] Reprinted (adapted) with permission from Low dielectric behaviour of a robust, guest-free magnesium(II)–organic framework: A potential application of an alkaline-earth metal Compound. European Journal of Inorganic Chemistry 2015, 2015 (10), 1669-1674. Copyright 2015 WILEY-VCH Verlag GmbH & Co. KGaA, Weinheim.

temperature range was attributed to the alkaline-earth metal (Mg), presence of rigid ligands and a lack of guest molecules in the framework. The dielectric constant (ε') value gradually decreases from 5.7 at 40 Hz to 3.33 at 100 kHz and then becomes constant in the high-frequency region (see Figure 3.1 (b)), indicative of the presence of space charge, dipolar, ionic and electronic polarizations in the lower frequency region. They also synthesised and investigated for the first time the low-κ dielectric property of the Zn-based MOF having a guest-free structure, along with its higher chemical and thermal stability.[33] They reported a decrease in the dielectric constant (ε') value from 3.15 at 1 kHz to 3.05 at 1 MHz due to the gradual loss of each type of polarisation mechanism caused by the lag in dipole moment with the increasing

frequency. The temperature-dependent low-κ property of the compound was mainly associated with the absence of guest molecules, which eliminated the possibilities of hydrogen bonding or ionic interactions in the framework. The low dielectric constant of the framework was also supported by the Clausius–Mossotti relation indicating that the dielectric properties were mainly attributed to electronic polarization.

3.1.2 Guest-dependent dielectrics

The orientation and ionic polarisation are highly dependent upon the presence of polar species, causing a significant increase in the material's overall polarisation. The solvent used during the MOF synthesis can also impact the framework morphologies and its crystal structure, affecting the dielectric behaviour. Only a handful of studies have been carried out to investigate the relationship between the crystal structure and the effect of solvents employed in synthesis. To understand the role of guests on dielectric anomalies and relaxation of MOF structure, Ren and co-workers studied a bimetallic MOF with a pillar-layered structure.[34] The MOF compound contained DMF solvent and water molecules in its cages and channels. The dielectric behaviour was investigated in the temperature range of 173–363 K and frequency range of 1–10^7 Hz for three successive thermal cycles. For the first thermal cycle, a dielectric anomaly peak was observed at lower frequencies of 1 kHz ($\varepsilon' \approx 150$ at 318 K), which vanished for later cycles due to the escape of guest molecules at a higher temperature. The dielectric anomaly was associated with the stacked structure transformation of the

disordered DMF and water molecules at the critical temperature in framework cages or channels. At higher frequencies (~MHz), the ε' remained unchanged with a value of 5.5 (10^6 Hz) for all the thermal cycles. It demonstrated that at lower frequencies the polar solvent molecules reorient themselves faster in comparison to the non-polar molecules causing a significant shift in the dielectric constant value of the MOF system. On the other hand, at higher frequencies (~MHz), the dipole moment cannot keep up with the alternating field resulting in a negligible change in the value of the dielectric constant. It was further supported by the study carried out by Lu and coworkers on two nickel(II)-based low dielectric supramolecular compounds containing different types of polar guest molecules.[35] Both frameworks had a similar backbone but the dielectric measurements showed an elevated value for the framework containing higher polar molecules (Cl^- and H_2O). The extensive hydrogen bonding between the chloride, linker and water molecules enhanced the overall polarization and formed an electric order, suggesting that the solvent molecules and counterions played a crucial role in regulating the value of the dielectric constant. Ling and co-workers took it further by synthesizing the hydrophobic ZIF-8 MOF in methanol (ZIF-8-M), ammonium hydroxide (ZIF-8-A) and water (ZIF-8-W) to study the solvent effect on the dielectric behaviour of the ZIF-8 host.[21] They reported that ZIF-8 synthesised in water and ammonium hydroxide solvent showed a phase coexistence between cubic and monoclinic as well as phase transformation from a crystal symmetry of *I*-43*m* to *Cm*, increasing in pore diameter from 3.4 Å to 3.6 Å. The ZIF-8-A and ZIF-8-W showed higher ε' values of 2.98 and 2.81, respectively, as compared to the $\varepsilon' = 2.25$ of ZIF-8-M at

high frequencies due to the presence of higher water content in its pores. Additionally, the higher dielectric constants of ZIF-8-A and ZIF-8-W can be attributed to their low-symmetry structure, which includes higher lattice polarization (dipoles) associated with the changes of bond angles and preferred orientation.

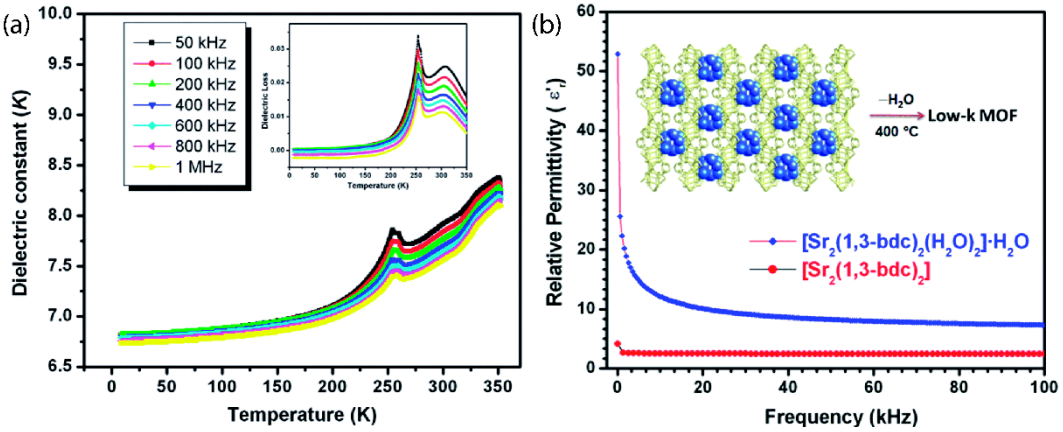

Figure 3.2: (a) Temperature-dependent dielectric constants from 0 to 350 K at different frequencies for the hydrated MOF compound with dielectric loss in the inset. (b) Relative permittivity vs. frequency for hydrated and dehydrated sample at room temperature.[36] Republished with permission of Royal Society of Chemistry, from Intrinsic low dielectric behaviour of a highly thermally stable Sr-based metal-organic framework for interlayer dielectric materials. M. Usman; C. H. Lee; D. S. Hung; S. F. Lee; C. C. Wang; T. T. Luo; L. Zhao; M. K. Wueg; K. L. Lu, 2 (19), 2015; permission conveyed through Copyright Clearance Center, Inc.

The guest species form weak interaction such as hydrogen bonding with the framework pores and can be eliminated by material post-processing to realise a low-κ material, however, this sometimes results in the loss of crystallinity due to the framework collapse upon solvent extraction. Lu and coworkers synthesised a 2D layered Sr-based MOF, which contained water in its structure.[36] In the temperature-dependent study, the sample was heated from 0 to 350 K causing a rise in the dielectric constant value, which was due to the mobility of the water molecules under an applied electric field during defreezing (see Figure 3.2). The sample was dehydrated to achieve a low dielectric constant for the framework. The dehydrated sample with its retained crystallinity showed high thermal stability up to 420 °C and a low dielectric constant of 2.4 at room temperature (see Figure 3.2 (b)), originating from its intrinsic properties. These few studies showed the impact of guest molecules on the dielectric properties of MOFs and the ways they can be manipulated to tune the dielectric response.

3.1.3 Structural based MOF dielectrics

The internal structure of material also plays a vital role in determining the properties of the material. Lu and co-workers presented a unique case showing the importance of the structure in determining the material properties, where the removal of polar guest molecules from the framework pore caused a significant increase in the dielectric constant.[37] The framework was synthesised by reacting the copper ions with 4,4′-(hexafluoroisopropylidene) diphthalic anhydride (HFDPA). The hydrophobic nature of the framework protected it from reabsorbing the water

molecules. In its fully hydrated state, the interactions that affected the dielectric constant of the structure were guest water–guest water, guest water–oxide chains, coordinated water–oxide chains. With stepwise heating, first, the guest water molecules and then the coordinated water molecules were removed from the structures causing the ε' to increase from 67.44 to 91.29 and then ultimately reached an ε' value of 98.99 at 1 kHz (see Figure 3.3). The increase in dielectric constant was associated with the loss of the internal hydrogen bonding and the shrinkage in the (020)[38] planes, causing a reduction in the total void volume. They demonstrated a structural-property relationship, where framework alteration causes a change in dielectric constant and hydrophobicity. In another study, Zheng and co-workers investigated the role of the organic linker in the gate-opening or breathing behaviour using the dielectric constant of metal-oxide@MOFs (ZnO@ZIF-7 and ZnO@ZIF-71), where ZnO nanorods were used as a sacrificial template for MOF growth.[39] The dielectric anomalies obtained in the temperature-dependent dielectric spectra resulted from the dipolar relaxation of the rotational polar groups of the molecule. The observed dielectric constant for the ZIF-7 system varied between 3.3-4.1 in a frequency range of $10^{2.5}$–$10^{5.5}$ Hz. In the ZnO@ZIF-7 system, the dielectric anomaly at lower temperature region (50-200 K) was associated with the free rotation of the bIm linker (bIm = benzimidazole), whereas at higher temperature (200-400 K) it was coupled with the cooperative interaction between the bIm linker and solvent, which was eliminated for the pre-processed pellet. The

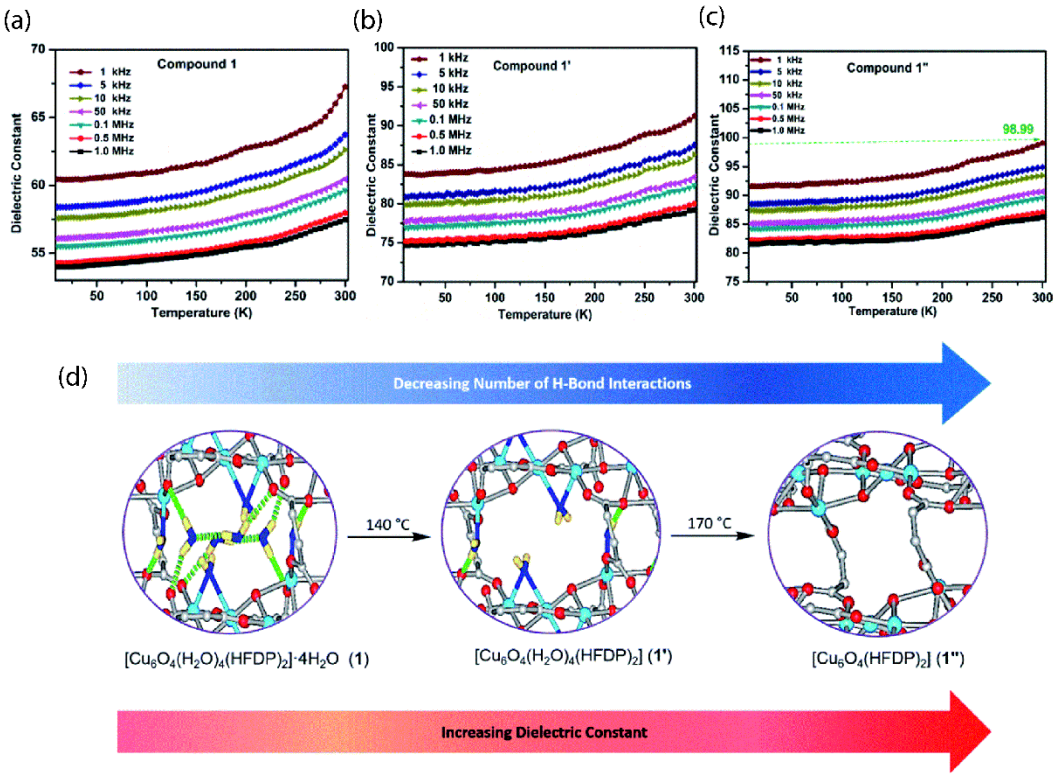

Figure 3.3: Temperature-dependent dielectric constant of (a) fully hydrated (1), (b) intermediate hydrated (1′), and (c) dehydrated (1′′) frameworks at various frequencies. (d) Influence of hydrogen-bonding interactions on dielectric behaviour of a 3D hydrophobic MOF, showing hydrogen bonding interactions of guest and coordinated water molecule and oxide chains after stepwise heating.[37] Republished with permission of Royal Society of Chemistry, from Highly hydrophobic metal–organic framework for self-protecting gate dielectrics. A. I. Inamdar; A. Pathak; M. Usman; K. R. Chiou; P. H. Tsai; S. Mendiratta; S. Kamal; Y. H. Liu; J. W. Chen; M. H. Chiang, 8 (24), 2020; permission conveyed through Copyright Clearance Center, Inc.

MOFs dielectric properties also depend upon their degree of framework interpenetration. Interpenetrated structures have a higher density, which is not desirable for the low-κ dielectrics. Luo and coworkers carried out both

experimental and theoretical studies on interpenetrated (MOF-246) and non-interpenetrated (MOF-123) MOF structures and provided useful insight in this area.[22] They reported that MOF thin films ($\varepsilon' = 19.5$ at 1 MHz) showed a relatively higher dielectric constant than its bulkier counterpart ($\varepsilon' = 5.9$ at 1 MHz), which was associated with the packing of the microcrystal, the polarization of the encapsulated solvent molecules and the interpenetrated framework on the conductive supports. The structure of both the MOFs is shown in Figure 3.4 (a) and (b). It was observed that the interpenetration of MOF-246 causes a rise in the framework density, which in turn increases the ε' value from 6.3 (MOF-123) to 14.7 (MOF-246) (see Figure 3.4 (d)). The experimental observations were also

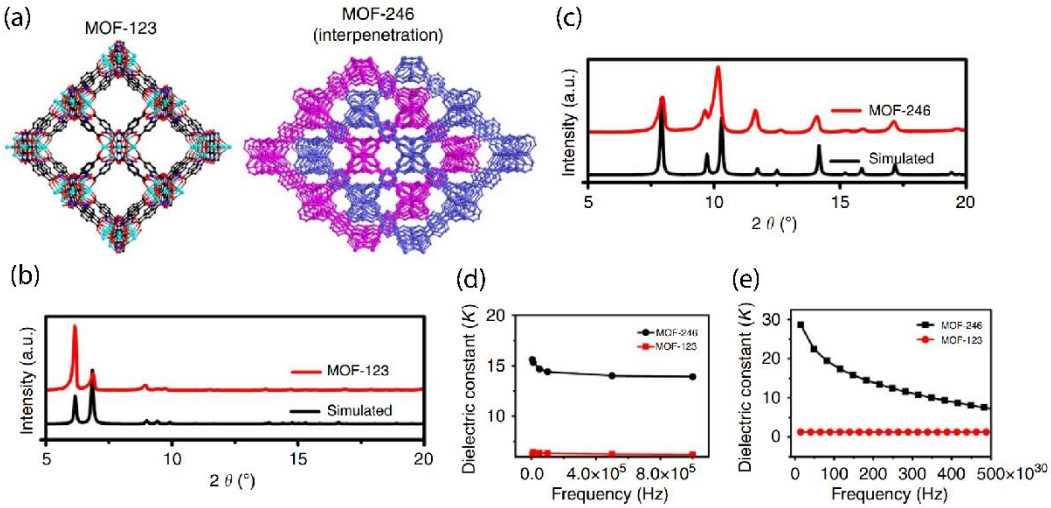

Figure 3.4: (a) 3D view of the non-interpenetrated structure of MOF-123 and the interpenetrated structure of MOF-246. (b) PXRD of MOF-123. (c) PXRD pattern of MOF-246. (d) Experimental study of the dielectric properties of MOF-123 and MOF-246 at 323.15 K. (e) Theoretical studies of the dielectric properties of MOF-123 and MOF-246 at 0 K.[22]

supported by the theoretical calculation, which also showed a rise in the dielectric constant due to framework interpenetration (see Figure 3.4 (e)). These studies showed that it is important to establish the structure-property relation so that materials can be tailored according to industrial demands.

These studies showed that the dielectric values determined from polycrystalline thin films or compressed pellets are sensitive to grain boundary defects, structural collapse or framework amorphization, and can comprise these induced polarisation effects in the overall material dielectrics. In contrast, single-crystal dielectric measurements are an effective way to study the intrinsic dielectric properties. While there is a previous report on the dielectric measurement of a single crystal of perovskite MOF, this was performed using a dense MOF structure with no accessible porosity.[40] Yet, the dielectric property of a single-crystal of porous MOF with reversible guest uptake has not been measured directly, to yield an intrinsic value independent of pelleting pressure and free from the grain boundary influence.

3.2 Case studies

In this section, we extensively studied the impact of different guests on MOF properties i.e., dielectric and electric response in the frequency range of 4 Hz – 8 MHz, intending to discover a suitable industrially viable MOF candidate. To perform a comprehensive study and understanding of dielectric sensing in MOF structure, we performed experiments on a single-crystal. It is well known that growing large single crystals with a large pore size and surface area is a challenging

task because the larger crystals tend to be more defective. The HKUST-1 [$Cu_3(BTC)_2$, BTC = benzene-1,3,5-tricarboxylate] MOF was chosen because it provides several advantages over other MOFs as described in Chapter 2 section 2.3, and to overcome single-crystal related challenges. First, the guest-dependent dielectric and electric response of the polycrystalline HKUST-1 was evaluated and then these insights were further employed to perform the tuneable dielectric sensing using the HKUST-1 single-crystal. These experiments aimed to achieve the following:

- To deepen the scientific understanding about guest-dependent changes in electric and dielectric properties of a porous MOF structure.
- It was also aimed to investigate the tuneability in MOF properties based on the different external stimuli i.e., pelleting pressure, temperature and humidity conditions for its practical viability.
- To investigate the different guest-dependent variations in the dielectric response of a single-crystal to demonstrate the potential for leveraging MOF dielectrics as a sensing mechanism.

The case studies that are presented in the next sections are the summary of the published work: Paper III and Paper IV, respectively, as shown in Part II: Published Papers (at the end of the chapter 3).

3.2.1 The polycrystalline HKUST-1 system

The HKUST-1 MOF system was synthesised using two different solvothermal routes to yield a porous and guest-encapsulated HKUST-1. The entrapped guest molecule was triethylamine (NEt_3), which was used to deprotonate the linker molecule. In its trapped state, the triethylamine cation had a lower dipole moment as compared to its noncationic form, making it suitable for identifying the role of guest in tuneable dielectric response of MOFs. To study the influence of mechanical and thermal stimuli on MOF properties, a series of powder pellets (0.5, 1, 3, 5 and 7-ton) were prepared for both porous and guest-loaded MOFs, which were termed as HKUST-1-S and HKUST-1-T, respectively. For these compressed

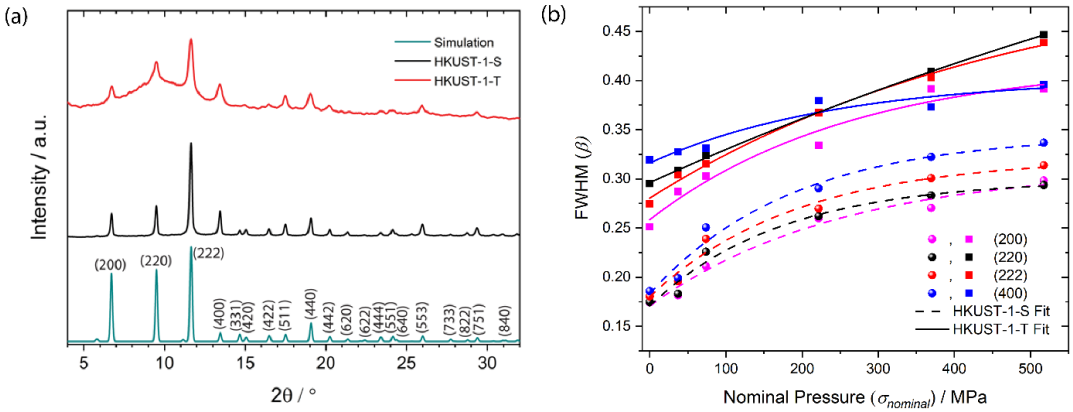

Figure 3.5: (a) Comparison of the simulated XRD pattern of HKUST-1 with the as-synthesised powders of HKUST-1-S and HKUST-1-T. (b) FWHM vs pelleting pressure plot for HKUST-1-S and HKUST-1-T samples.

pellets, the structural amorphization of the framework was studied using powder XRD. The XRD patterns are shown in Figure 3.5 (a), without background subtraction and normalised to the (222) peak, which has the highest intensity.

HKUST-1-T exhibited a broad peak from ~6° to 14° that superimposed the sharp Bragg peaks in the same region, thereby suggesting the presence of some semicrystalline or amorphous products. The full width at half maximum (FWHM) analysis of pellet XRD patterns followed the same trend of the pellet density, pointing to the pressure-induced amorphization of the framework (see Figure 3.5 (b)). A series of Brunauer-Emmett-Teller (BET) and Thermogravimetric analysis (TGA) experiments were also carried out to confirm the encapsulation of NEt_3 guest molecules in HKUST-1-T pores. The BET surface area analysis is the multi-point measurement of materials specific surface area (m^2/g) through gas adsorption

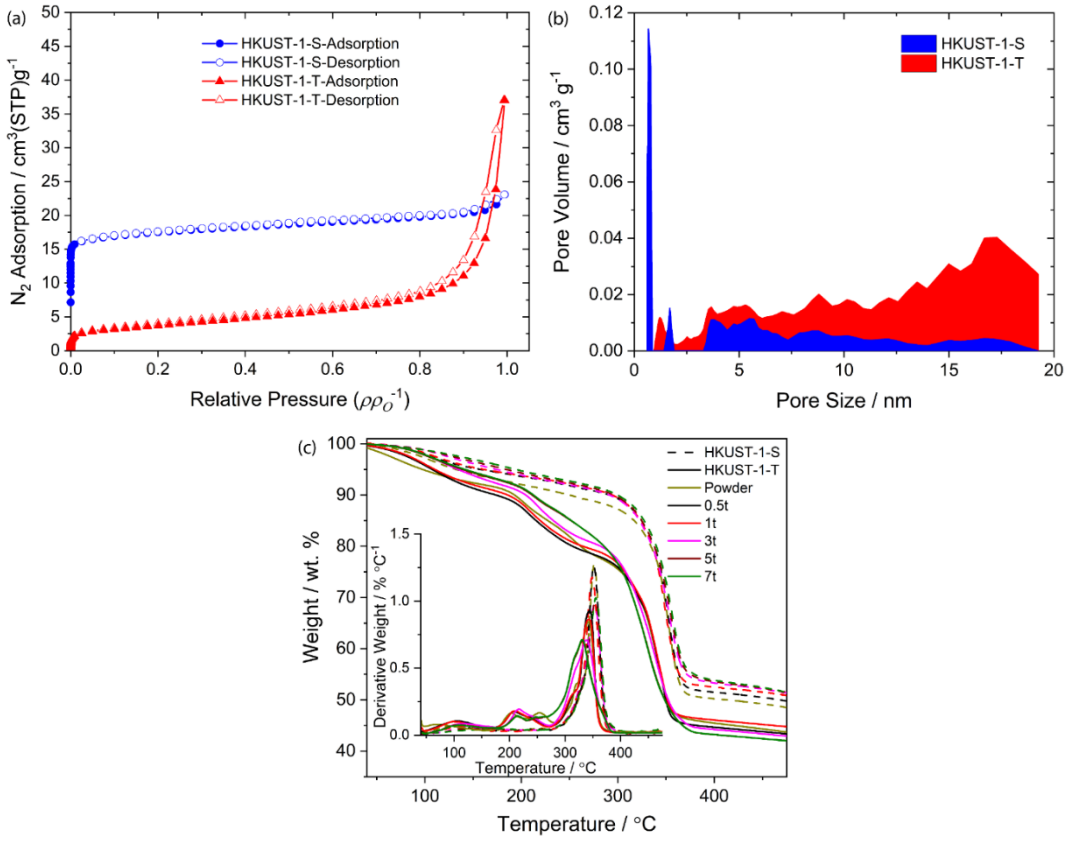

Figure 3.6: (a) Nitrogen adsorption-desorption isotherms of HKUST-1 powder samples and (b) its pore distribution. (c) A plot of TGA for different pellet samples.

analysis, where an inert gas such as nitrogen is continuously flowed over sample, or the sample is suspended in a defined gaseous volume. In TGA, thermal stability of the material was measured by obtaining the weight change in sample with respect to the increasing temperature. The nitrogen adsorption-desorption isotherms of powder samples were carried out at 77 K and shown in Figure 3.6 (a). The BET surface areas of the HKUST-1-S and HKUST-1-T samples were found to be 1007 m^2/g and 165 m^2/g, respectively. Additionally, we also determined the pore size distributions from the non-linear DFT model, assuming a combination of slit-shaped and cylindrical-shaped pores typically applied in MOF analysis. It was established that HKUST-1-S has predominantly micropores of < 2 nm, whereas HKUST-1-T is comprised of mesopores from *ca*. 2-20 nm. TGA plot of HKUST-1 samples showed the thermal stability of the frameworks (see Figure 3.6 (c)). It was deduced from the sample weight loss that both the presence of guests inside the pore and pressure-induced amorphization resulted in lower thermal stability of the framework. The hump in the obtained derivative plot suggests the presence of NEt_3 molecules, further analysis of the encapsulated guest content resulted in $[Cu_3(BTC)_2].1.5N(CH_2CH_3)_3$.

The electrical and dielectric measurements for these pellet samples were carried out in both vacuum and 44% RH (relative humidity) conditions. From HKUST-1-S pellet measurements in a vacuum, it was established that the materials dielectric constant (ε') is highly dependent upon the framework density. The MOF framework showed a sudden rise in ε' value with the increased pelleting pressure

resulting from the pressure-induced densification of the porous framework and structural amorphization. The HKUST-1-S pellets also showed a lack of temperature-dependent dipole moment resulting in a stable value of ε' both at lower frequencies and at a higher temperature. On the other hand, the guest encapsulation greatly influenced the HKUST-1-T properties. At lower pelleting pressure, the HKUST-1-T pellets behaved similar to their counterpart but at higher pelleting pressure the NEt_3 guest molecule formed weak interaction with the oxygen at the Cu-paddle wheel, causing a surge in the ε' value. The densification associated contribution in ε' value was also observed in the HKUST-1-T pellets but at slightly higher pelleting pressure, suggesting an increase in mechanical resilience due to guest confinement within the MOF pores. Moreover, the temperature arguments the dipole moment of the guest molecules causing a rise in the overall ε' value of the framework. The presence of guests also enhances the electrical conductivity of the framework. It was deduced that the weak interaction of NEt_3 with the framework caused by the pelleting pressure increased the charge hopping probability and decreased the percolation threshold causing a sudden increase in conductivity beyond the pelleting pressure of 1 ton, which was not observed in the HKUST-1-S pellets.

When tested in humid conditions, the framework behaviour changed drastically (see Figure 3.7). The HKUST-1-T pellets showed a relatively lower ε' value over HKUST-1-S pellets due to the presence of NEt_3 molecule in the pore, causing lesser moisture adsorption. In the case of HKUST-1-T samples, the ε' value

increased with pelleting pressure up to a certain extent due to the increase in the structural density and interaction between the water and guest molecule, whereas the decrease in the ε' value of HKUST-1-S samples was mainly contributed by the water expulsion causing the reduction in the overall dipole moment.

It was concluded from this case study that the mechanical property of the open framework can be tailored by means of guest encapsulation, where we show that the yield strength and structural stability of the compressed pellets can be improved by guest confinement (see details in Paper III). The dielectric and electric response of the framework is highly dependent upon the polarizability of the encapsulated guest molecule and can vary significantly based on the pelleting pressure and temperature used.

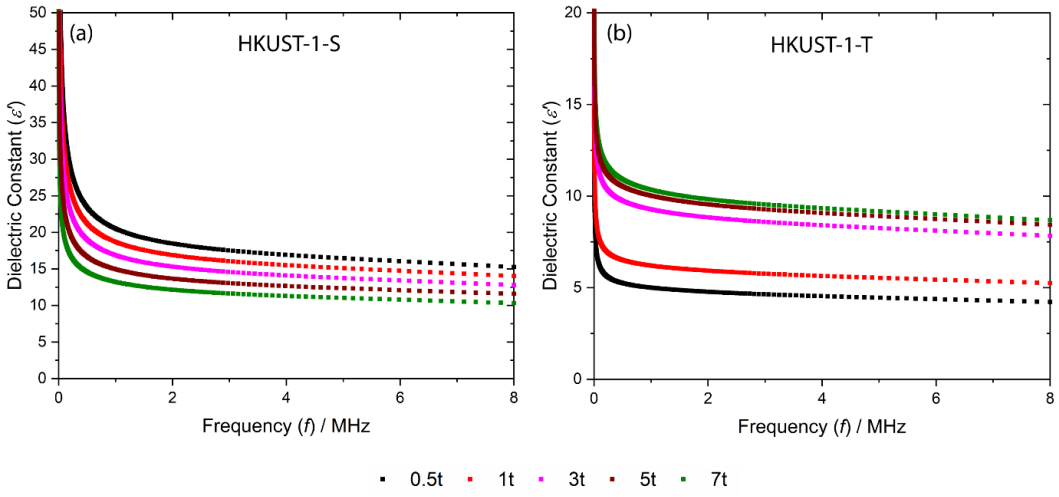

Figure 3.7: Real part of dielectric constant of (a) HKUST-1-S and (b) HKUST-1-T pellets at ambient condition (44% RH).

3.2.2 The HKUST-1 single-crystal system

This study was aimed at studying the tunable intrinsic dielectric behaviour of the porous MOF, which is independent of the pelleting pressure and free of grain boundary influence. The porous MOF, such as HKUST-1, readily accommodates guest molecules that will alter their dielectric properties through host-guest interactions. These physicochemical alterations are molecule specific, and thus can

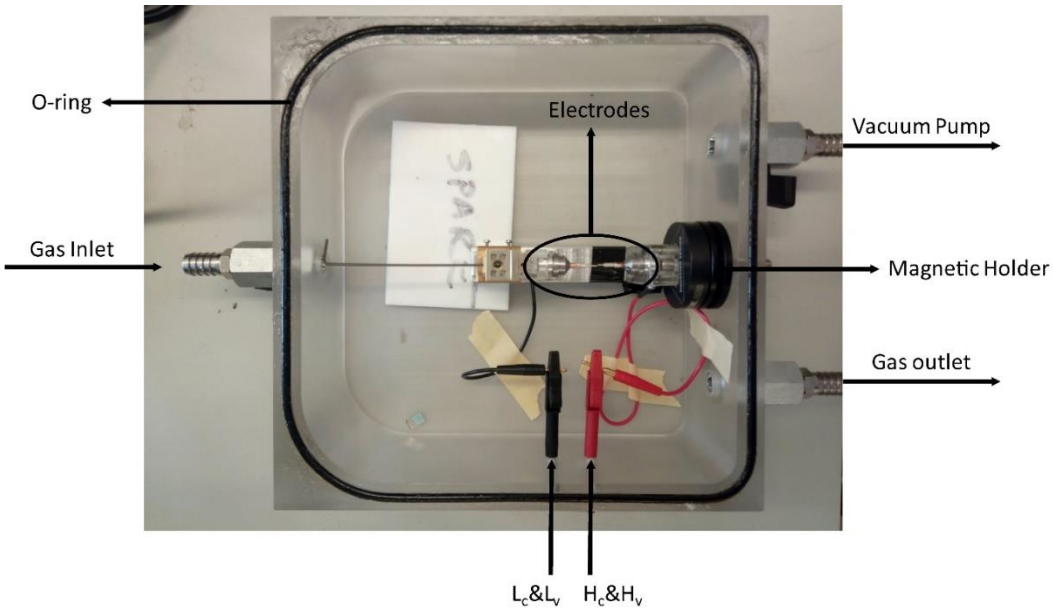

Figure 3.8: Experimental setup designed to conduct the single-crystal dielectric measurements on HKUST-1 MOF. The top lid is not shown for clarify. The connections to the electrodes are: L = low, H = high, C = current, V = voltage.

be exploited to achieve highly selective sensors. In this regard, we envisage that encapsulated polar molecules (as the "guest") will add an extra dipole to the MOF

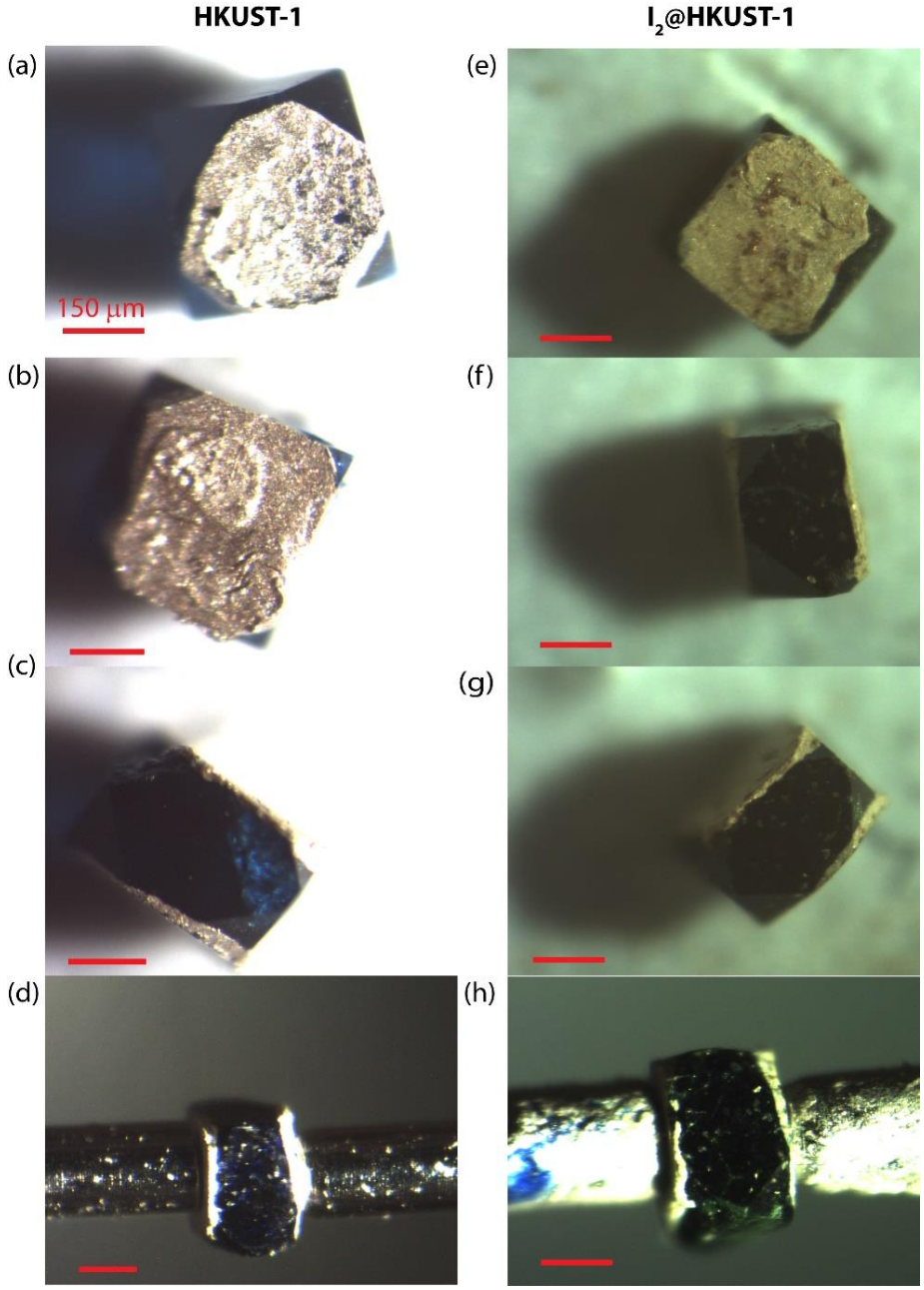

Figure 3.9: Silver-coated single crystals viewed from top and sides (a)-(c) HKUST-1 crystal and (e)-(g) I_2@HKUST-1 crystal. (d) and (h) show the mounting of the crystal between the spring-loaded electrodes. Scale bar is 150 µm.

framework (as the "host"), thereby enabling highly responsive detection of analytes when sensing subtle changes by leveraging transient dielectric response of a single-crystal. These changes in electrical properties (dielectric and AC conductivity) of the HKUST-1 crystal on the lattice direction was measured using the Hioki-IM3536 LCR meter in the frequency range of 4 Hz to 2 MHz at room temperature. To do this, an enclosed chamber made from polycarbonate was designed to expose one single-crystal to a specific guest environment (Figure 3.8). The crystals were silver-coated on the opposite (100)-oriented planes because measurements were based on a parallel-plate capacitor principle (see Figure 3.9). Two spring-loaded electrodes (Ø 210 µm) were aligned using a multi-axis stage. Before guest exposure, the setup was calibrated (open and short LCR compensation), the crystal was evacuated with inert gas nitrogen (N_2) and its structure and vibrational bands were determined.

The powder XRD of the HKUST-1 single-crystal was carried out to confirm the presence of the (200)- and (400)-oriented planes (see Figure 3.10 (a)). Analysis of the XRD peak profiles revealed an increase in FWHM of the iodine-encapsulated crystal (see Figure 3.10 (b)), indicative of strain developed in the framework from adsorbed iodine. Raman spectroscopy was performed to validate the encapsulation of molecular iodine in HKUST-1 (see Figure 3.10 (c)). The distinct Raman band at ≈ 210 cm^{-1} can be assigned to the I_2 molecules, while the peak at ≈ 420 cm^{-1} is the first overtone of I_2.[41] These results confirmed that the I_2@HKUST-1 crystals were successfully obtained.

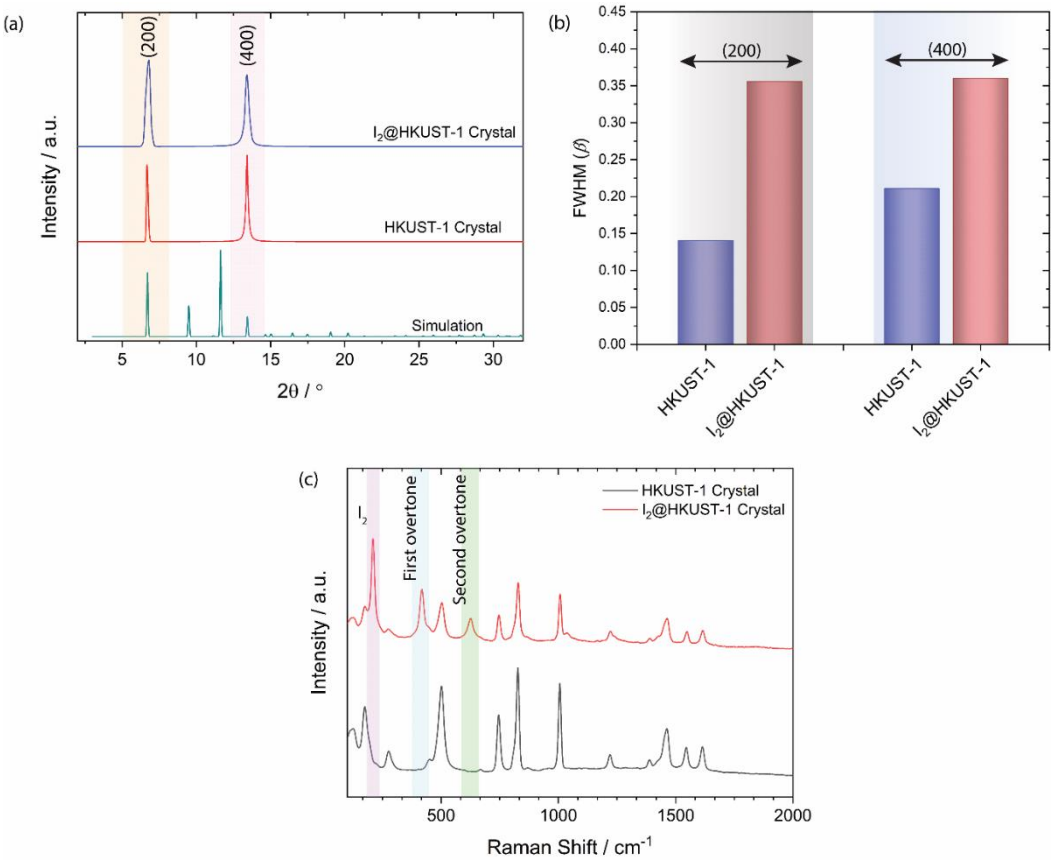

Figure 3.10: (a) X-ray diffraction patterns of pristine and I_2 encapsulated HKUST-1 single crystals, showing broadening of the (100)-oriented Bragg peaks upon I_2 sorption. The simulated XRD pattern is for a powder sample hence all peaks are visible. (b) Comparative FWHM plot of the (200) and (400) planes of the HKUST-1 single-crystal with and without the encapsulated I_2 molecules. (c) Raman spectra of the pristine and I_2 encapsulated HKUST-1 single crystals.

After confirming the crystal characteristics, the crystal was placed between a pair of spring-loaded electrodes (Figure 3.9 (d, h)). The polar guest solvents were poured into the bubbler and carried to the crystal by the nitrogen flow (12 L/h) through the gas inlet shown in Figure 3.8. A constant gas influx was maintained

throughout the experiment. Each inclusion and expulsion cycle of guests was carried out after ensuring the stability in the LCR output data under a constant nitrogen flow (12 L/h). The relative concentration of guests in the chamber was maintained by controlling the overall inert gas pressure. The humidity was measured using a thermo-hygrometer with a sensitivity range of 2%-98% RH.

A cyclic sorption-desorption experiment was carried out for different guest molecules to study the influence on the dielectric response of a single-crystal of HKUST-1. It was observed that the presence of hydrophobic I_2 acts as a

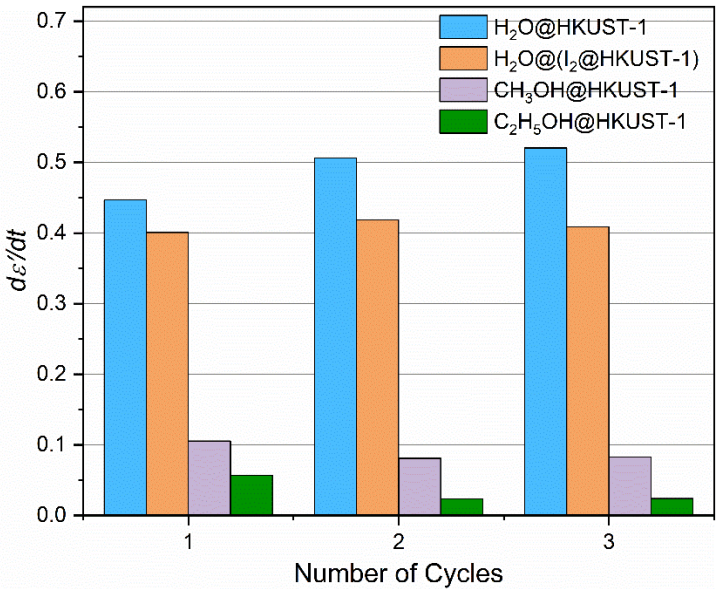

Figure 3.11: Comparative inclusion rates of the different guest molecules for the first three cycles. The vertical axis represents the rate of change of dielectric constant with time.

hydrophobic barrier for the water molecules and the size of the guest molecule greatly impacts their mobility to and from the framework pore, as shown in Figure

3.11. The relative concentration of the guest also had an impact on the magnitude of the properties. Figure 3.12 shows the cyclic electrical and dielectric response of the HKUST-1 crystal at different relative humidity conditions (30-70% RH). The dielectric constant of the HKUST-1 crystal increased with H_2O sorption, up to the value of $\varepsilon' = 57$ for 30% RH and $\varepsilon' = 64$ for 70% RH at 1 MHz). The increase in ε' was associated with the inherent dipole of the guest water molecule. The modest rise of ε' and electrical conductivity at 70% RH, indicating there is a good water occupancy even at 30% RH. We also reported that the overall framework polarisation depends upon the size of the guest molecule, its adsorption concentration and the dipole moment, reflected by the magnitude of $d\varepsilon'/dt$ as $C_2H_5OH < CH_3OH < I_2@H_2O < H_2O$. The dielectric response of MOF crystals can considerably be altered by host-guest interactions (at open metal sites or ligands) *via* hydrophobic–hydrophilic interactions, and by harnessing guest molecular size effect and guests clustering attributed to the nanoconfinement effect.

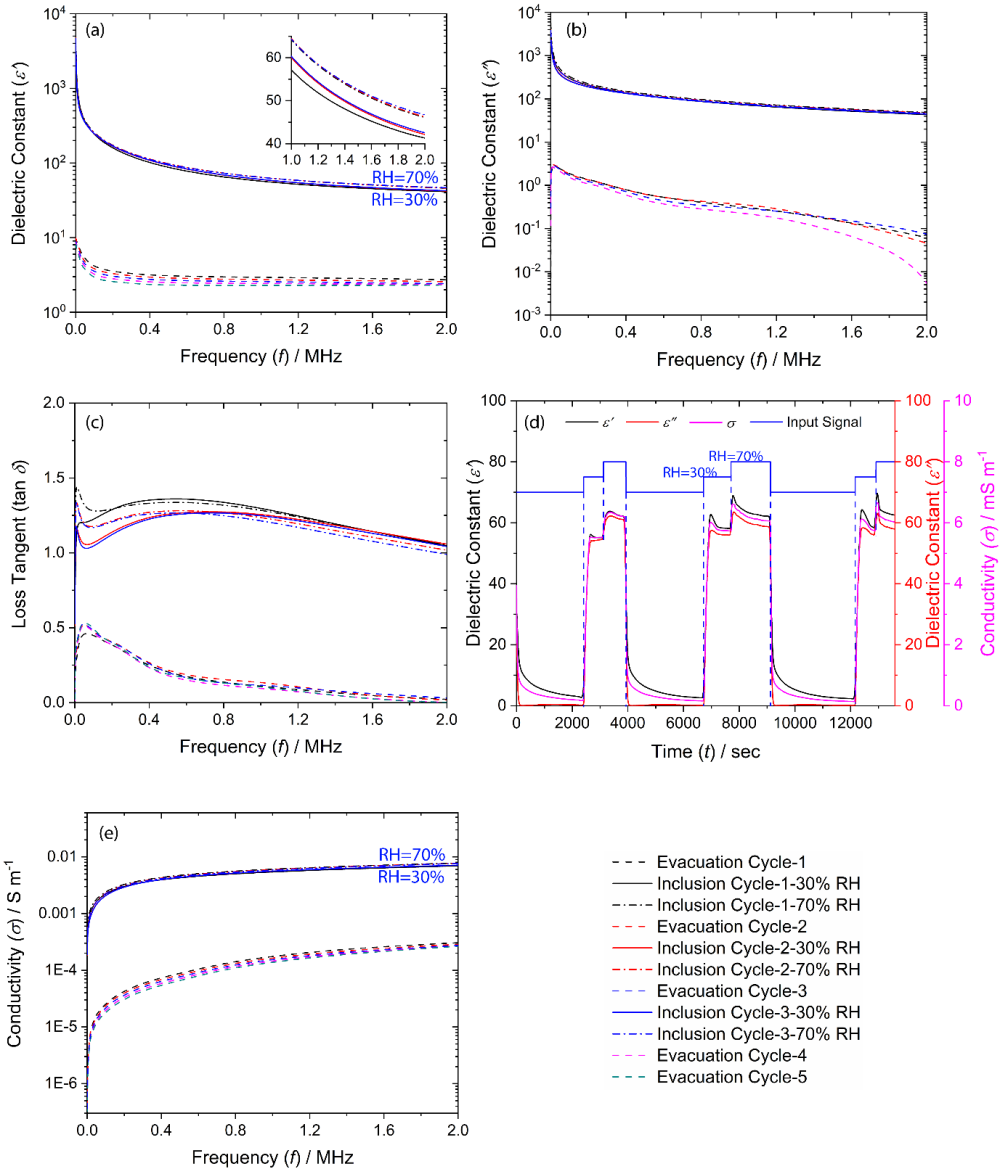

Figure 3.12: Electrical properties of HKUST-1 crystal at 30% and 70% RH conditions. (a)-(b) Real and imaginary parts of the dielectric constant, (c) loss tangent, (d) cyclic measurements during guest inclusion and expulsion, and (e) frequency-dependent AC conductivity.

Published Papers

Paper III

Influence of mechanical, thermal, and electrical perturbations on the dielectric behaviour of guest-encapsulated HKUST-1 crystals

Journal of Materials Chemistry C

ROYAL SOCIETY OF CHEMISTRY

PAPER

View Article Online
View Journal | View Issue

Cite this: J. Mater. Chem. C, 2020, 8, 12886

Influence of mechanical, thermal, and electrical perturbations on the dielectric behaviour of guest-encapsulated HKUST-1 crystals†

Arun Singh Babal and Jin-Chong Tan *

Received 2nd June 2020,
Accepted 12th August 2020

DOI: 10.1039/d0tc02637a

rsc.li/materials-c

Metal–organic frameworks (MOFs) are emerging low-k dielectric materials for application in next-generation microelectronics and telecommunication devices. MOF dielectrics can function as smart sensors with high sensitivity and chemical selectivity, by leveraging the ubiquitous dielectric response of MOFs and overcoming the limitations of DC conductivity and fluorescence approaches. Herein we study the effects of material synthesis, applied mechanical stress (37–520 MPa), varying temperature (20–100 °C), and guest encapsulation on the frequency-dependent dielectric response (4 Hz to 1 MHz) and AC conductivity of the HKUST-1 MOF. Particularly, we show that the confinement of the triethylamine (NEt_3) guest molecules in HKUST-1 (host) yields a NEt_3@HKUST-1 system that is tuneable *via* mechanical, thermal and electrical perturbations. Within the frequency range of 10 kHz to 1 MHz, at 20 °C, we show that the dielectric constant (ε') of the guest-encapsulated system could be tuned to attain a value in the range of 2.8 to 7.2; at 100 °C, an even greater value of ε' in the range of 3.1 to 9.5 could be achieved. Conversely, we found that the dielectric tuneability of the porous (guest-free) HKUST-1 is relatively more limited (ε' = 2.8 to 4.9) whilst employing the same operational parameters. Furthermore, the confinement of guest molecules in HKUST-1 enhances the mechanical resilience and yield strength of the powders subject to a compressive pelleting stress. Together, the results elucidate the new potential for exploiting host–guest interactions in MOFs, coupled with electrical, thermal, and mechanical stimuli to regulate the precise dielectric response of a designer low-k material.

1. Introduction

In recent years, the research on low-k dielectric materials has gained attention due to their potential for enhancing the performance of next-generation electronic devices and telecommunications. Metal–organic frameworks (MOFs) are highly porous hybrid materials consisting of organic linkers connected to inorganic metal sites to yield tuneable crystalline materials.[1–3] Their unique properties such as ordered framework structures having long-range porosity, low density and high thermal/chemical stability make them a potential candidate for the interlayer dielectric applications. Electronic device miniaturisation has introduced new challenges such as higher RC time delay, crosstalks between the circuits, and power consumption penalty.[4,5] The aforementioned challenges can be addressed by implementing new ultralow-k dielectric materials. Theoretical calculations of MOF-based dielectrics have predicted hypothetical static dielectric constant values of less than 2.0,[6,7] which are well below the conventionally used SiO_2 whose static dielectric constant is $k \sim 4$.

While the studies concerning the dielectric properties of MOFs are quite limited compared to their research pertaining to adsorption/desorption and separations, the nascent field of MOF dielectrics is steadily growing. For example, we have studied the dielectric properties of a commercial grade of HKUST-1 powder [Cu_3BTC_2; BTC = benzene-1,3,5-tricarboxylate] in the broadband frequency region (Hz and THz). The work has revealed all the dielectric transitions as a function of pelleting pressure, and elucidated a number of polarisation mechanisms in HKUST-1.[8] More recently, we characterised the transient dielectric response of a single crystal of HKUST-1 by subjecting it to different guest environments.[9] Other earlier exemplars include Lu *et al.* who synthesized two different Ni-based supramolecular compounds that possess different types of polar guest molecules.[10] They reported that the solvent molecule and counterions play an important role in regulating the dielectric property of the resulting material. Usman *et al.* reported the temperature-dependent dielectric behaviour of a

Multifunctional Materials and Composites (MMC) Laboratory, Department of Engineering Science, University of Oxford, Parks Road, Oxford, OX1 3PJ, UK. E-mail: jin-chong.tan@eng.ox.ac.uk

† Electronic supplementary information (ESI) available. See DOI: 10.1039/d0tc02637a

strontium-based MOF $([Sr_2(1,3\text{-bdc})_2(H_2O)_2]\cdot H_2O)_n$ (1,3-bdc = 1,3-bis(4,5-dihydro-2-oxazolyl)benzene).[11] They reported an increase in dielectric constant with temperature because of the freezing and defreezing of water molecules. The dehydrated sample showed a low dielectric constant value of 2.4 at 1 MHz frequency and thermally stable up to 420 °C. Lu *et al.* also reported a guest-free and solvent resistant Zn-based MOF $[Zn_2(Hbbim)_2(bbim)]_n$ (H_2bbim = bisbenzimidazole).[12] They showed a low dielectric constant of 3.05 at 1 MHz, which was found to be stable in the temperature range tested (3.5–350 K).

MOF materials can be tuned by different synthesis methods,[13] controlled reaction parameters[14] and modulators.[15] Using a modulator is an effective way of controlling the size and morphology of MOF crystals. Xin *et al.* studied the effects of modulators (sodium acetate and triethylamine (NEt_3)) and the type of copper source on the structure and morphology of the resulting HKUST-1.[16] They showed that the effect of the modulator varies according to the copper system and it depends on the nucleation rate.

In this work, we have employed two synthesis routes to yield a porous and guest-encapsulated HKUST-1 MOF crystal exhibiting different morphologies. The dielectric response of the guest-encapsulated material is contrasted against that of the porous guest-free framework by imposing a range of stimuli, such as the alternating electric field, temperature variation, and mechanical stress. To the best of our knowledge, this study represents the first example of its kind where the tuneable dielectric response of a MOF material has been systematically probed subject to different physical and chemical stimuli. The results reveal the scope to engineer bespoke MOF dielectrics targeting technological applications ranging from low-*k* to high-*k* integrated electronics, sensors, and telecommunication devices.

2. Experimental section

2.1 Materials

Copper nitrate trihydrate ($Cu(NO_3)_2\cdot 3H_2O$, 99%), 1,3,5-benzenetricarboxylic acid (H_3BTC, 98%), methanol (CH_3OH, 99.5%) and triethylamine (NEt_3, 99%) were purchased from Sigma Aldrich. All the chemicals were used without further purification.

2.2 Synthesis of HKUST-1 (without using NEt_3)

The solvothermal synthesis of HKUST-1 was carried out under ambient conditions. Both $Cu(NO_3)_2\cdot 3H_2O$ (6 g) and H_3BTC (2.52 g) were dissolved separately in 150 mL of CH_3OH and later on, an additional 100 mL of CH_3OH was added into the mixture and stirred for 30 min. The synthesized product was washed several times using methanol to remove excess linkers and then dried overnight in the oven at 80 °C. The yield of the final product was about 10% with respect to the metal content. The obtained powder sample was denoted as HKUST-1-S.

2.3 Synthesis of HKUST-1 using NEt_3

The lack of precipitation in the standard HKUST-1 synthesis described above was obvious. To improve the product yield, an excess of NEt_3 (6.06 mL) was added to the solution to expedite the deprotonation of the H_3BTC linkers. A blue precipitate comprising nanocrystals of HKUST-1 was formed instantly when the metal and organic linker solutions were combined.[17] After the reaction (same steps as a standard reaction), the mother liquor was colourless indicating the depletion of copper ions after HKUST-1 synthesis. The yield of the final product was about 90% with respect to the metal content. The powder sample obtained using this method was designated as HKUST-1-T. This method leads to the encapsulation of NEt_3 guest molecules in the HKUST-1 pores.

2.4 HKUST-1 pellet preparation and density measurements

The pellets of 13 mm diameter were prepared under different compressive loads (uniaxial force = 0.5, 1, 3, 5 to 7 tons) using a hydraulic press (Specac 15 tons). The mass of each pellet was kept constant at 150 mg. These pellets were designated as HKUST-1-S-*N* or HKUST-1-T-*N*, where *N* is the pelleting load in tons. Subsequently, the nominal density of the pellets was determined from mass/volume.

2.5 Morphology studies

The HKUST-1 crystals were characterised using a scanning electron microscope (SEM, Carl Zeiss EVO LS15). The HKUST-1 crystals mounted on the carbon tape were gold sputter coated for 60 s, prior to SEM imaging at 30 keV under high vacuum.

AFM imaging was carried out using the Veeco Dimension 3100 instrument operating under tapping mode, equipped with a Tap300-G probe with a resonant frequency of 300 kHz and a force constant of 40 N m^{-1}.

2.6 Infrared spectroscopy

FTIR spectra of the powders and pellets were recorded in the mid-IR region (400–4000 cm^{-1}) using the Nicolet-iS10 FTIR spectrometer equipped with an ATR sample accessory. The spectral resolution of the instrument was 0.5 cm^{-1}.

2.7 Thermogravimetric analyses

Thermogravimetric analysis (TGA) was used to investigate the thermal stability of the HKUST-1 samples. The measurements were performed using the TGA-Q50 machine (TA Instruments) under an inert atmosphere of nitrogen. For this study, the samples were heated from 40 °C to 500 °C at 10 °C min^{-1} in a platinum sample holder.

2.8 X-Ray diffraction

X-ray diffraction (XRD) of the pellets was carried out in a transmission mode using the Xenocs NanoInXider machine (using the Cu $K_{\alpha 1}$ source operating at 30 W, λ = 0.154 nm). The XRD spectrum of each pellet was recorded at 2θ = 4–60° under a very high-resolution (VHR) beam setting for 2000 s (scan rate = 0.00357° s^{-1}, step size = 0.01°). The spot size and the flux of the beam were 400 μm and 15 Mph s^{-1}, respectively. Before the XRD characterization, pellets were pre-evacuated for 16 h to mimic the conditions of the samples in dielectric measurements.

2.9 Dielectric properties studies

The electrical properties of HKUST-1 in the frequency range of 4 Hz to 1 MHz were investigated using the Hioki-IM3536 LCR meter. These measurements were performed in the temperature range of 20–100 °C with a step size of 10 °C under a vacuum of 1×10^{-3} bar. A thin layer of silver conducting paint (RS) was applied on the opposing sides of the pellets to yield a parallel-plate capacitor configuration. The silver-coated pellets were mounted between two flat and circular aluminium electrodes (13 mm diameter). The setup was calibrated in the vacuum oven to eliminate any parasitic impedance and admittance. All pellets were evacuated in a vacuum (10^{-3} bar) for 16 h beforehand to activate the HKUST-1 framework by removing any moisture content. The real part of dielectric constant (ε') and the imaginary part of the dielectric constant (ε'') were determined using the following equations:

$$\varepsilon' = \frac{Cd}{\varepsilon_0 A} \quad (1)$$

$$\varepsilon'' = \varepsilon' \tan\delta \quad (2)$$

where C is the capacitance, d is the distance between the pair of parallel plate electrodes, A is the area of the electrode, ε_0 is vacuum permittivity and $\tan\delta$ is the loss tangent.

3. Results and discussion

3.1 Effects of NEt_3 on the size, morphology, and porosity of HKUST-1 crystals

The SEM micrograph shown in Fig. 1(a) shows the HKUST-1-S sample comprising crystals with an average size of 1.5 ± 0.7 μm. However, the morphology of the HKUST-1-T sample is completely different, suggesting the formation of larger aggregates as can be seen in Fig. 1(b). However, using AFM imaging we established that these aggregates are in fact made from nanosized crystals, whose size is *ca.* 48 ± 17 nm, as shown in Fig. 1(c and d). Additional SEM and AFM images of the HKUST-1 crystals are given in the ESI† (Fig. S1 and S2). The significant difference in terms of their crystal morphology can be explained by the use of NEt_3 in the synthesis of HKUST-1-T, where the rapid deprotonation of H_3BTC by NEt_3 (as a base) has resulted in a high nucleation rate but this suppressed subsequent crystal growth. Upon drying the small nanocrystals will fuse together to yield agglomerates like those found in Fig. 1(b and c).

Fig. 2(a) shows the variation of nominal density as a function of pelleting pressure for the two series of samples prepared from the HKUST-1-S and HKUST-1-T crystals. The density curves for the pellets obey an exponential function of the form $\rho \propto -\exp(-\sigma)$, where ρ and σ are the nominal pellet density and nominal stress, respectively. At the highest 7 ton load, the nominal densities of the resulting pellets have risen to ~185% (HKUST-1-S) and ~200% (HKUST-1-T) compared with the theoretical density of an ideal HKUST-1 crystal (948.9 kg m^{-3}). The curve of HKUST-1-S approaches a plateau beyond the application of about 3 ton load, but this effect is delayed in the case of the HKUST-1-T pellets. The densification data suggest that the occluded guest molecules within HKUST-1-T (Fig. 2(b)) could increase the mechanical stiffness of the porous framework,[18,19] thus improving its resilience against mechanical deformation and collapse. The guest encapsulation and pelleting pressure-dependent systematic colour shift, from turquoise to dark blue (Fig. 2(a) inset), can be explained by the change in the refractive index ($n^2 = k$) which is also evident in the pressed powder pellets.

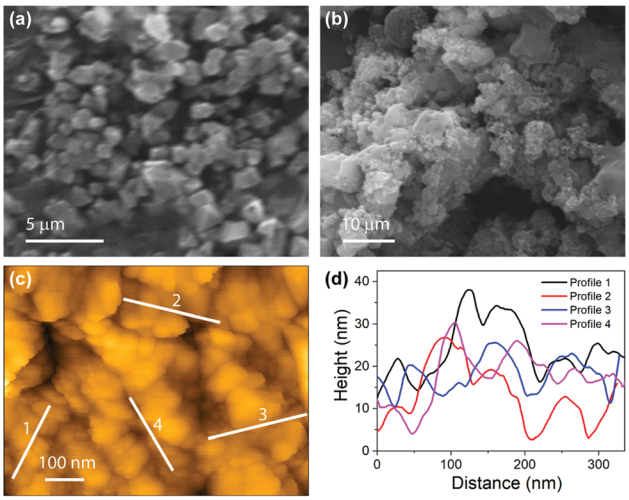

Fig. 1 Morphological study of the HKUST-1 MOF materials. SEM images of (a) HKUST-1-S crystals and (b) HKUST-1-T aggregates. (c) AFM topography image of the HKUST-1-T sample. (d) Height profiles of nanocrystals of HKUST-1-T extracted from the AFM topography (c).

In order to confirm the presence of NEt_3 guest molecules encapsulated in HKUST-1-T (Fig. 2(b)), we have employed a range of complementary techniques. Fig. 2(c) shows the distinctively different FTIR spectra of the two samples, wherein in addition to the common characteristic peaks of HKUST-1, a new vibrational band was detected at 1224 cm^{-1} assigned to the C–N stretching mode of NEt_3 (guest) found in HKUST-1-T. Additionally, the pressure-induced amorphization of the pellets was also evident from the systematic peak broadening of the characteristic vibrational modes in FTIR spectra as a function of pelleting pressure (Fig. S3, ESI†). The amorphization of the HKUST-1 framework was corroborated by X-ray diffraction (Fig. S4 and S5, ESI†), where the outcome of the FWHM analysis (Fig. S5, ESI†) points to the pressure-induced amorphization of the framework.[20,21] We note that the comparatively higher FWHM values of the compressed pellets of HKUST-1-T over HKUST-1-S can be ascribed to the prevalence of nanocrystals found in the former sample (Fig. 1(c)).

The encapsulation of NEt_3 in the HKUST-1 framework was also investigated by N_2 adsorption at 77 K. The HKUST-1-T powder sample showed a BET surface area of 165 $m^2\ g^{-1}$, which is appreciably lower than 1007 $m^2\ g^{-1}$ determined for the HKUST-1-S powder. The adsorption data support the notion that the pores of HKUST-1-T are not fully accessible due to guest occlusion. From the nitrogen sorption isotherms in Fig. S6(a) (ESI†), it can be surmised that HKUST-1-S and HKUST-1-T have

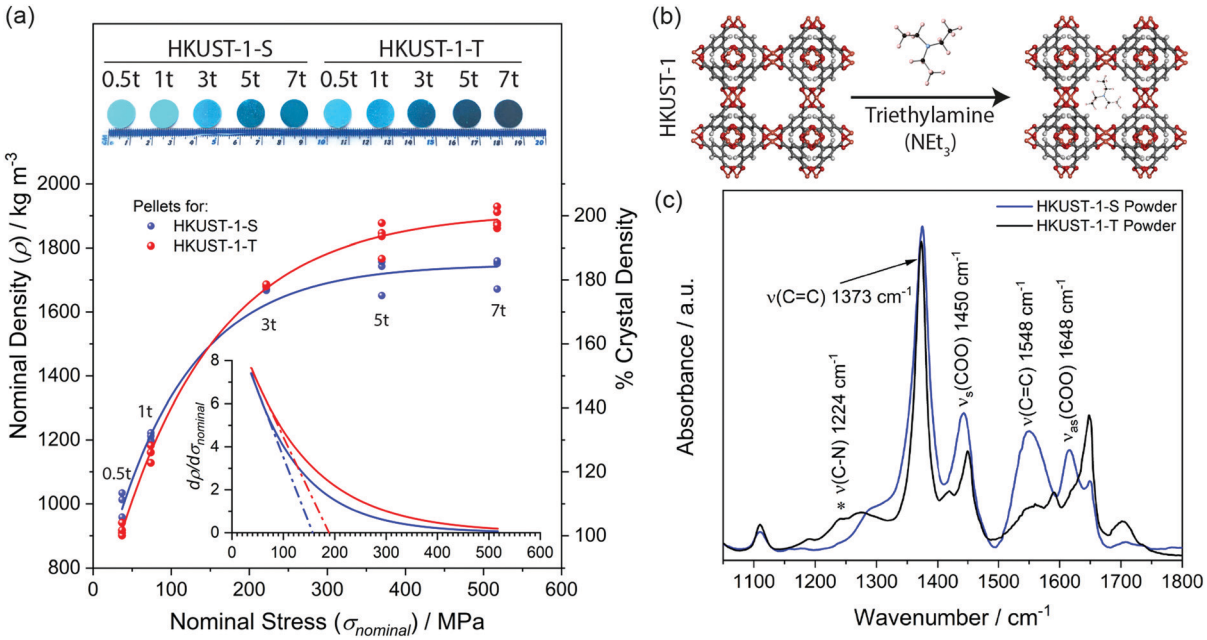

Fig. 2 (a) Density of HKUST-1 pellets as a function of the applied nominal pressure. A crystal density of 100% corresponds to the theoretical density of 948.9 kg m^{-3} calculated for a unit cell of an ideal HKUST-1 crystal. The top inset shows photographs of the pellets used in this study. The bottom inset shows the change in density with respect to the applied pelleting stress, where intercepts on the abscissa were used to estimate the yield strength of the compressed powder of HKUST-1-S and -T as 160 MPa and 190 MPa, respectively. (b) Illustration of the encapsulation of triethylamine in the porous framework of HKUST-1. (c) FTIR spectra of HKUST-1-S and HKUST-1-T powders. The symmetric and asymmetric stretching modes are denoted as ν_s and ν_{as}, respectively.

more pronounced microporosity and mesoporosity, respectively. Subsequently, we have confirmed this *via* pore size distribution analysis shown in Fig. S6(b) (ESI†), where HKUST-1-S has predominantly micropores of <2 nm, whereas HKUST-1-T is composed of mesopores ranging from *ca.* 2–20 nm. The mesoporosity of HKUST-1-T can again be attributed to the nanosized crystal aggregates shown in Fig. 1(b and c). Finally, TGA data in Fig. S6(c) (ESI†) show that in contrast to HKUST-1-S, HKUST-1-T shows an additional weight loss from 170 °C to 280 °C, which can be associated with the expulsion of NEt_3. Subsequently we estimated an average of 1.5 NEt_3 guest molecule per unit cell of HKUST-1-T.

3.2 Dielectric behaviour

The activated HKUST-1 pellets were used to investigate the effects of pelleting pressure and guest encapsulation on the dielectric properties, as a function of temperature from 20 °C to 100 °C. All dielectric measurements were performed under vacuum and over the frequency range of 4 Hz to 1 MHz. The dielectric constant of a porous framework material, such as MOFs, depends on its effective density[22,23] and its polarizability.[7] In the proceeding section, it has been established that the pellet nominal density rises exponentially as $-\exp(-\sigma)$, with pelleting stress σ. Fig. 3(a) shows the real part of the dielectric constant (ε') of HKUST-1-S pellets at 20 °C, which increases from 2.79 (0.5*t*) to 4.46 (7*t*) at 1 MHz frequency, *i.e.* ε' has risen by a factor of $\sim$1.6. Clearly, this is caused by the pressure-induced densification of the porous framework and structural amorphization elucidated in Section 3.1. Notably, there is a marked jump of $\Delta\varepsilon > 0.57$ between the 0.5*t* and 1*t* pellets followed by $\Delta\varepsilon > 0.43$ between the 1*t* and 3*t* pellets, which could be linked to framework collapse when the applied stress approaches $\sim$160 MPa. Raising the temperature of the 0.5*t* pellet from 20 °C to 100 °C has caused only a small increase of ε' from 2.79 to 2.86, this finding suggests the absence of temperature-dependent dipole moments.[24] Overall, we did not see a strong influence of temperature on the ε' and ε'' values of HKUST-1-S, although the densest 7*t* pellet appears to be more sensitive to temperature change compared to the lower density pellets.

Turning to the guest-encapsulated samples, Fig. 3(b) shows that the dielectric response of HKUST-1-T is significantly different from that of HKUST-1-S, both in terms of the magnitude of ε' and its response to heating. Initially at 20 °C, we determined that ε' of HKUST-1-T at 1 MHz has increased from 2.81 (0.5*t*) to 6.48 (7*t*), *i.e.* a factor of 2.3 times higher due to the pelleting pressure. Upon compression, the NEt_3 molecules (guest) may form weak interaction with the oxygen found at the Cu-paddle wheel of HKUST-1 (host) and contribute to the overall dielectric property in addition to the effect arising from framework densification, thus resulting in an increased of ε' value. A jump of $\Delta\varepsilon > 1.34$ occurring between the 1*t* and 3*t* pellets of HKUST-1-T could be attributed to framework collapse, but this is detected at a stress of $\sim$190 MPa which is relatively higher than HKUST-1-S ($\sim$160 MPa, see Fig. 2(a) inset). This finding supports the hypothesis that the encapsulation of NEt_3 guest molecules in HKUST-1-T improves its mechanical resilience. For the 0.5*t* pellet, ε' at 1 MHz increases from 2.81 (20 °C) to 3.16 (100 °C). The rate of increase in the temperature-dependent ε' value is notably

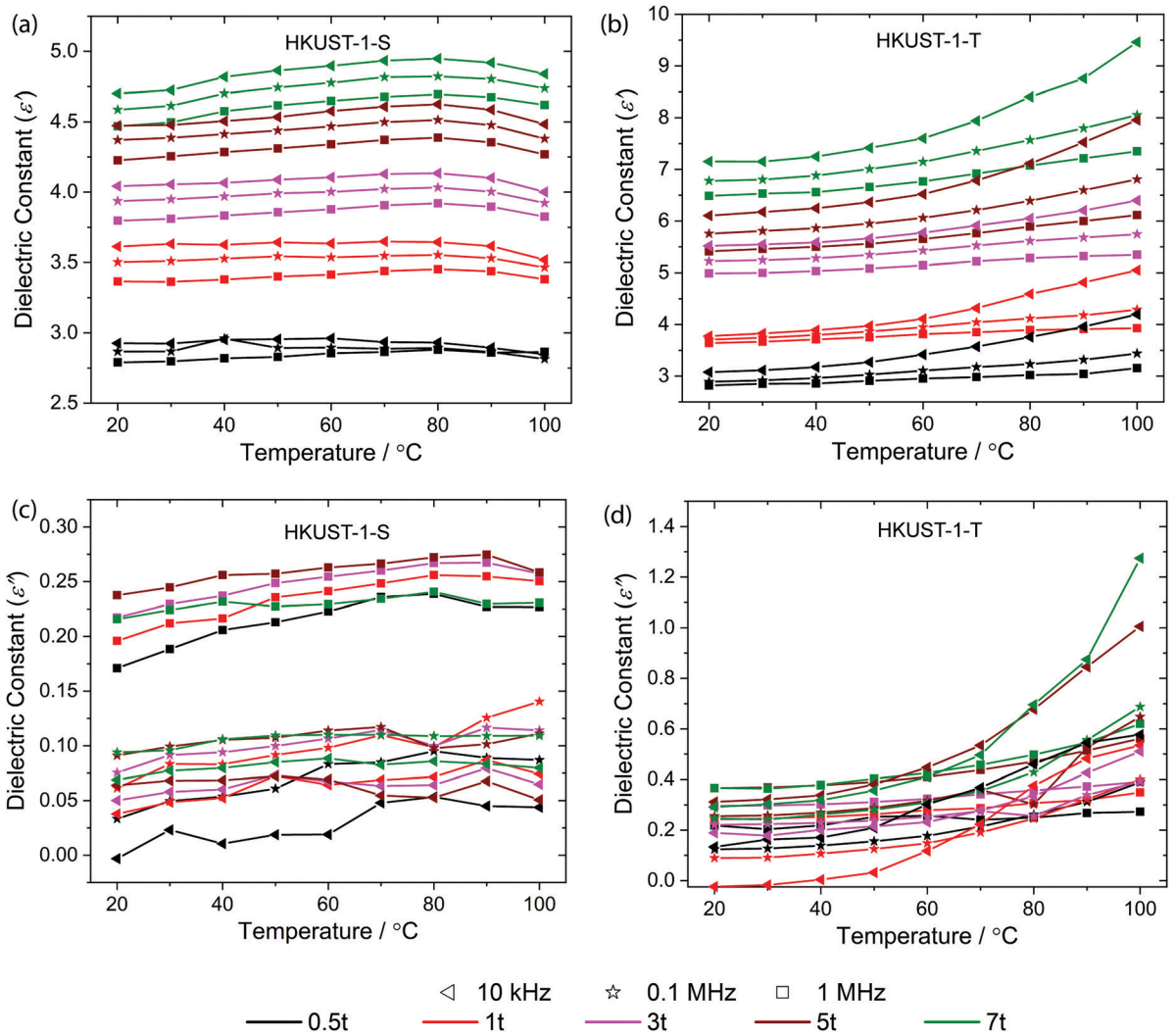

Fig. 3 Dielectric response as a function of temperature for the 0.5*t*, 1*t*, 3*t*, 5*t*, and 7*t* pelleted samples of HKUST-1-S (left panels) and HKUST-1-T (right panels), all of which measured under vacuum conditions. (a and b) Real part of the dielectric constant ε'. (c and d) Imaginary part of the dielectric constant ε''.

greater for samples obtained by higher pelleting pressure. For example, in the 7*t* pellet, the value of ε' at the lower frequency of 10 kHz went up drastically from 7.15 to 9.46 when the 20 °C sample was heated to 100 °C. Our results suggest that the higher temperature will augment the dipole motion of the encapsulated NEt_3 guests under an alternating electric field (10 kHz > 0.1 MHz > 1 MHz), thereby giving a marked rise in the ε' and ε'' values with pelleting stress. The guest-encapsulated HKUST-1 thus exhibits a considerably stronger temperature-induced dipole moment, which is different from that of the porous (guest-free) HKUST-1-S sample described above.

At higher frequency and temperature, the dipole moment cannot be kept up with the higher alternating field, resulting in energy loss and its contribution to polarization drops. This can be explained using the imaginary part of the dielectric constant (ε''), which represents the dissipative losses. For the HKUST-1-S pellets, the dissipation of the porous framework was found to be notably greater at 1 MHz frequency, and the loss gently increases with heating due to thermal perturbations. For the HKUST-1-T pellets, the steep increase in ε'' at the lower frequency of 10 kHz in response to heating is associated with the loss induced by the encapsulated NEt_3 molecules. This effect can be suppressed by elevating the frequency. The detailed frequency-dependent dielectric plots of both samples are presented in the ESI† (Fig. S9–S14).

We further investigated the dielectric properties of HKUST-1 under ambient conditions of 44% RH (relative humidity), in the frequency range of 4 Hz to 8 MHz. The results are presented in Fig. S15–S17 of the ESI.† Interestingly, as shown in Fig. S15 (ESI†), the pellets of HKUST-1-T show a relatively lower ε' value than HKUST-1-S, because the presence of NEt_3 molecules occupying the pores of the former has lessened moisture uptake. The framework density and interaction between water and the NEt_3 guest molecule play a major role in the HKUST-1-T pellets, both factors become more prevalent for higher pressure pellets resulting in the overall rise of the ε' values. In contrast, the dielectric response of the HKUST-1-S pellets is dominated by the adsorbed water molecules (because $\varepsilon' \sim 80$ at 20 °C for water), whose occupancy will decline with higher pelleting pressure (giving reduced porosity), resulting

in an overall reduction of dipole moments and thereby the lowering of the ε' values.

3.3 Alternating current (AC) conductivity behaviour

The frequency-dependent electrical properties of different HKUST-1 pellets were studied at increasing temperatures. Fig. 4(a) and (b) show the temperature-dependent conductivity of the HKUST-1 pellets. The slight increase in the conductivity of the HKUST-1-T pellets can be attributed to the NEt_3 guest molecules present in the pores of the host framework. From the results it was deduced that the weak interaction of NEt_3 with the framework caused by the pelleting pressure will increase the charge hopping probability and also decrease the percolation threshold causing a sudden increase in conductivity beyond the pelleting pressure of 1 ton, which was not observed in the HKUST-1-S pellets. Both the frequency and temperature affect the conductivity of HKUST-1 pellets, which can be observed for the individual pellet in the ESI† (Fig. S18 and S19).

Fig. 4(c and d) shows the real *vs.* imaginary part of the impedance of 0.5 and 7 ton pellets for a better understanding of the effect of pelleting pressure. The impedance data were fitted into a large arc using the resistance and two equivalent circuits connected in series (implemented in ZView software). The instrumental noise caused by the connections during measurement was represented by resistance R_1 in the circuit. In the second circuit, the constant phase element (CPE_1) and resistance (R_2) are related to the bulk property of HKUST-1, whereas the constant phase element (CPE_2) and resistance (R_3) of the third circuit are related to the interface between the electrode and the HKUST-1 pellets. The estimated capacitance value from the impedance curve was found to lie in the range of pF cm^{-1}, which can be attributed to the intrinsic property of the bulk material. The conductivity of pellets can be calculated using the equation $\sigma_c = d/(R \times A)$, where σ_c is the conductivity, d is the distance between electrodes, A is the cross-section area and R is the curve-fitted resistance. The calculated conductivity values of all the pellets are shown in Table S1 (ESI†).

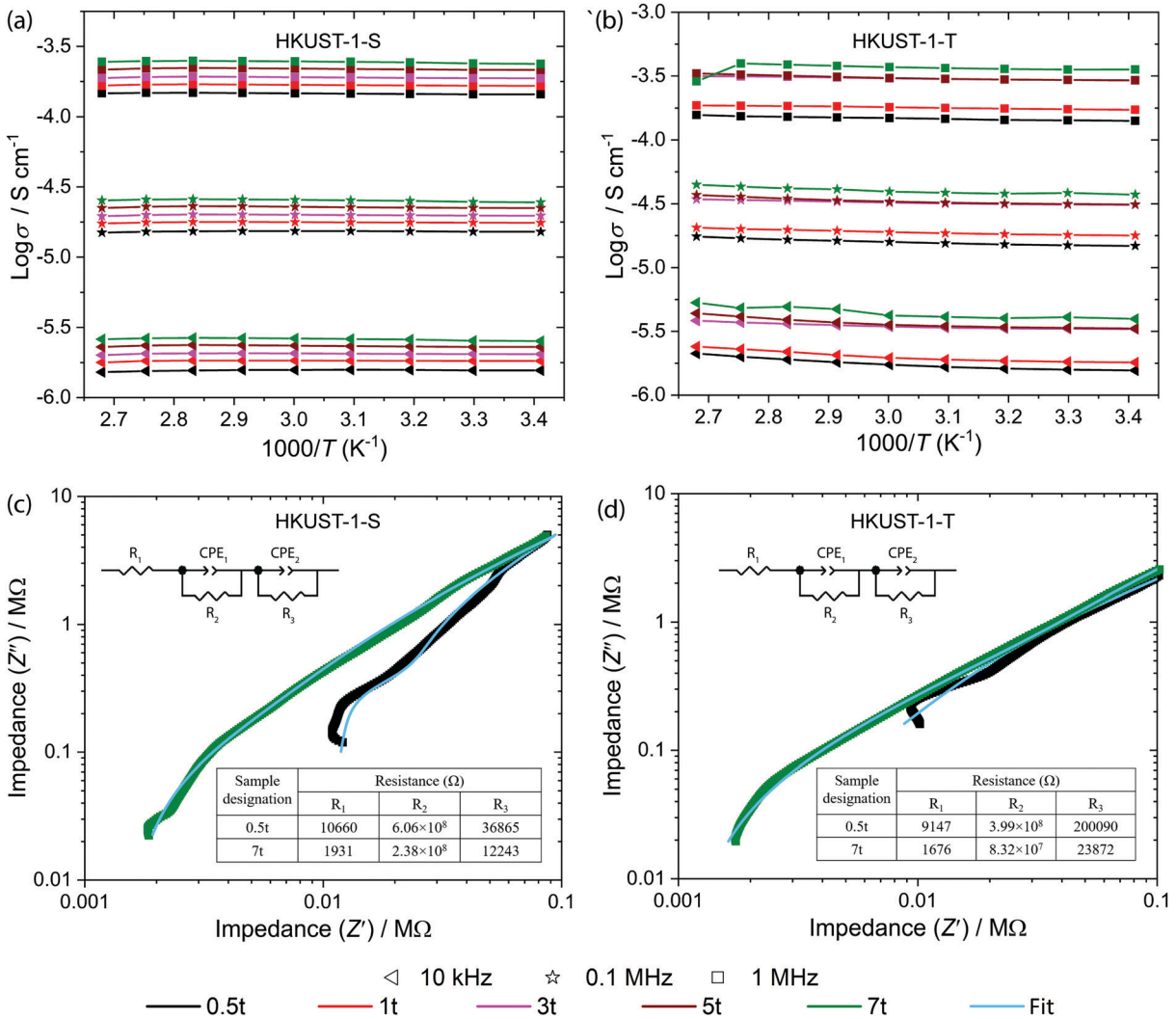

Fig. 4 AC conductivity as a function of temperature for (a) HKUST-1-S and (b) HKUST-1-T pellets prepared by different compression forces. Measurements were performed in a vacuum at three different frequencies of 10 kHz, 0.1 MHz and 1 MHz. Impedance plots of imaginary *vs.* real parts with the equivalent circuit for the 0.5 ton pellet at 20 °C and 100 °C for (c) HKUST-1-S and (d) HKUST-1-T. Note: CPE = constant phase element.

The pattern of increase in the conductivity values of the HKUST-1-T pellets is consistent with the experimentally obtained dielectric and conductivity values. These conductivity results confirm the highly insulating nature of HKUST-1, which is central to the function of low-*k* materials. All the fitted parameters of the real and imaginary parts of the impedance data are given in the ESI† (Fig. S24 and S25).

4. Conclusions

In summary, we presented a high-yield HKUST-1 MOF synthesis technique for low-*k* and tuneable dielectric applications, where trimethylamine (NEt_3) guest molecules are confined in the porous host framework to yield a NEt_3@HKUST-1 system (herein termed as HKUST-1-T). From thermogravimetric analysis, NEt_3 was determined to be 1.5 molecules per formula unit of the host framework, thus resulting in a chemical formula of HKUST-1-T as $[Cu_3(BTC)_2]\cdot 1.5[N(CH_2CH_3)_3]$. At 1 MHz frequency, the 0.5*t* pellet of the guest-encapsulated material has a dielectric constant value of $\varepsilon' = 2.81$ at 20 °C and 3.14 at 100 °C, which is an exceptional example of guest@MOF dielectrics at elevating temperatures, in contrast to the guest-free HKUST-1-S that exhibits a relatively smaller difference of $\varepsilon' = 2.79$ (20 °C) and 2.87 (100 °C). Electrical impedance measurements and analysis revealed that the low-dielectric constant values are an intrinsic property of the host framework that can be modified by mechanical stress. Uniquely, we show that the guest-encapsulated material exhibits a broadly tuneable dielectric response through precise adjustments to parameters such as the frequency, temperature, and pelleting pressure. Moreover, the mechanical property of the open framework can be enhanced by guest encapsulation, where we show that the yield strength and structural stability of the compressed pellets can be improved by guest confinement. Collectively, the results demonstrate an innovative pathway for tailoring the physical behaviour of MOFs for dielectrics and other multifunctional devices.

Conflicts of interest

There are no conflicts to declare.

Acknowledgements

This research was funded by the EPSRC DTP-Samsung studentship award to A. S. B. J. C. T. thanks the European Research Council (ERC) Consolidator Grant through the grant agreement 771575 (PROMOFS) for funding the Guest@MOF research in the group. We are grateful to Dr Gavin Stenning and Mr Daniel Nye for providing access to the XRD facilities at the R53 Material Characterization Lab in ISIS Rutherford Appleton Laboratory, and to Dr James Taylor for performing the nitrogen adsorption measurements. We thank the Research Complex at Harwell (RCaH) for access to FTIR-ATR and TGA instruments. We are grateful to Carlos Cuadrado and Prof. Joaquin Silvestre who performed the NLDFT pore size distribution analysis.

References

1 O. Shekhah, J. Liu, R. A. Fischer and A. Woll, *Chem. Soc. Rev.*, 2011, **40**, 1081–1106.
2 G. Ferey, *Chem. Soc. Rev.*, 2008, **37**, 191–214.
3 M. R. Ryder and J. C. Tan, *Mater. Sci. Technol.*, 2014, **30**, 1598–1612.
4 Semiconductor Industry Association, 2013, (SEMATECH, Albany, NY, USA, 2013).
5 W. Volksen, R. D. Miller and G. Dubois, *Chem. Rev.*, 2009, **110**, 56–110.
6 K. Zagorodniy, G. Seifert and H. Hermann, *Appl. Phys. Lett.*, 2010, **97**, 251905.
7 M. R. Ryder, L. Dona, J. G. Vitillo and B. Civalleri, *ChemPlusChem*, 2018, **83**, 308–316.
8 A. S. Babal, L. Dona, M. R. Ryder, K. Titov, A. K. Chaudhari, Z. Zeng, C. S. Kelley, M. D. Frogley, G. Cinque and B. Civalleri, *J. Phys. Chem. C*, 2019, **123**, 29427–29435.
9 A. S. Babal, A. K. Chaudhari, H. H.-M. Yeung and J. C. Tan, *Adv. Mater. Interfaces*, 2020, **7**, 2000408.
10 S. Mendiratta, M. Usman, T. T. Luo, S. F. Lee, Y. C. Lin and K. L. Lu, *CrystEngComm*, 2014, **16**, 6309–6315.
11 M. Usman, C. H. Lee, D. S. Hung, S. F. Lee, C. C. Wang, T. T. Luo, L. Zhao, M. K. Wueg and K. L. Lu, *J. Mater. Chem. C*, 2014, **2**, 3762–3768.
12 S. Mendiratta, M. Usman, C. C. Chang, Y. C. Lee, J. W. Chen, M. K. Wu, Y. C. Lin, C. P. Hsu and K. L. Lu, *J. Mater. Chem. C*, 2017, **5**, 1508–1513.
13 E. Biemmi, S. Christian, N. Stock and T. Bein, *Microporous Mesoporous Mater.*, 2009, **117**, 111–117.
14 D. Zacher, J. Liu, K. Huber and R. A. Fischer, *Chem. Commun.*, 2009, 1031–1033.
15 X. Mu, Y. Chen, E. Lester and T. Wu, *Microporous Mesoporous Mater.*, 2018, **270**, 249–257.
16 C. Xin, H. Zhan, X. Huang, H. Li, N. Zhao, F. Xiao, W. Wei and Y. Sun, *RSC Adv.*, 2015, **5**, 27901–27911.
17 A. K. Chaudhari, I. Han and J. C. Tan, *Adv. Mater.*, 2015, **27**, 4438–4446.
18 J. C. Tan, T. D. Bennett and A. K. Cheetham, *Proc. Natl. Acad. Sci. U. S. A.*, 2010, **107**, 9938–9943.
19 T. D. Bennett, J. Sotelo, J. C. Tan and S. A. Moggach, *CrystEngComm*, 2015, **17**, 286–289.
20 T. Ungar, *Scr. Mater.*, 2004, **51**, 777–781.
21 T. D. Bennett and A. K. Cheetham, *Acc. Chem. Res.*, 2014, **47**, 1555–1562.
22 M. R. Ryder, Z. Zeng, K. Titov, Y. Sun, E. Mahdi, I. Flyagina, T. D. Bennett, B. Civalleri, C. S. Kelley and M. D. Frogley, *J. Phys. Chem. Lett.*, 2018, **9**, 2678–2684.
23 K. Titov, Z. X. Zeng, M. R. Ryder, A. K. Chaudhari, B. Civalleri, C. S. Kelley, M. D. Frogley, G. Cinque and J. C. Tan, *J. Phys. Chem. Lett.*, 2017, **8**, 5035–5040.
24 S. Eslava, L. Zhang, S. Esconjauregui, J. Yang, K. Vanstreels, M. R. Baklanov and E. Saiz, *Chem. Mater.*, 2012, **25**, 27–33.

Published Papers

Statement of Authorship for joint/multi-authored papers for PGR thesis
To appear at the end of each thesis chapter submitted as an article/paper
The statement shall describe the candidate's and co-authors' independent research contributions in the thesis publications. For each publication there should exist a complete statement that is to be filled out and signed by the candidate and supervisor **(only required where there isn't already a statement of contribution within the paper itself).**

Title of Paper	Influence of mechanical, thermal, and electrical perturbations on the dielectric behaviour of guest-encapsulated HKUST-1 crystals
Publication Status	Published
Publication Details	A. S. Babal; J. C. Tan, Influence of mechanical, thermal, and electrical perturbations on the dielectric behaviour of guest-encapsulated HKUST-1 crystals. *J. Mater. Chem. C* **2020**, 8, 12886-12892.

Student Confirmation

Student Name:	Arun Singh Babal		
Contribution to the Paper	A. S. Babal carried out the experiments, analysed the data and wrote the published manuscript under the supervision of Prof. Jin-Chong Tan.		
Signature	Arun Singh Babal	Date	15/12/2021

Published Papers

Supervisor Confirmation

By signing the Statement of Authorship, you are certifying that the candidate made a substantial contribution to the publication, and that the description described above is accurate.

Supervisor name and title: Prof. Jin-Chong Tan		
Supervisor comments: The provided description is accurate.		
Signature	Date	15/12/2021

This completed form should be included in the thesis, at the end of the relevant chapter.

Paper IV

Guest-tunable dielectric sensing using a single-crystal of HKUST-1

ADVANCED MATERIALS INTERFACES
www.advmatinterfaces.de

Guest-Tunable Dielectric Sensing Using a Single Crystal of HKUST-1

*Arun S. Babal, Abhijeet K. Chaudhari, Hamish H.-M. Yeung, and Jin-Chong Tan**

There is rising interest on low-*k* dielectric materials based on porous metal–organic frameworks (MOFs) for improved electrical insulation in microelectronics. Herein, the concept of MOF dielectric sensor built from a single crystal of HKUST-1 is demonstrated. Guest encapsulation effects of polar and non-polar molecules are studied, by monitoring the transient dielectric response and AC conductivity of the crystal exposed to different vapors (water, iodine, methanol, and ethanol). The dielectric properties are measured along the <100> crystal direction in the frequency range of 100 Hz to 2 MHz. The dielectric data show the efficacy of MOF dielectric sensor for discriminating the guest analytes. The time-dependent transient response reveals dynamics of the molecular inclusion and exclusion processes in the nanoscale pores. Since dielectric response is ubiquitous to all MOF materials (unlike DC conductivity and fluorescence), the results demonstrate the potential of dielectric MOF sensors compared to resistive sensors and luminescence-based approaches.

Metal–organic frameworks (MOFs) are open-framework compounds that feature interconnected functionally active pores with vast chemical and physical tunability. Because of their chemical structure and highly porous architecture, indeed the majority of MOFs are excellent electrical insulators. Therefore, there is a growing interest to study the "low-*k*" dielectric properties of MOFs,[1,2] as a next-generation dielectric for replacing conventional silicon dioxide (whose real part of dielectric constant, $\varepsilon' = 3.9–4.3$), or silicon nitride ($\varepsilon' = 6.0–7.0$) prevalent in microelectronics today.[3] Low-*k* dielectrics are important for boosting the performance of miniaturized integrated circuits (IC), reducing losses due to power dissipation, electronic crosstalk, and resistive-capacitive delays of ICs. Low-*k* materials can be designed by introducing air pockets into solids, because air (or vacuum) has the lowest attainable $\varepsilon' \approx 1$.[4] Of course, this feature is easily fulfilled by MOF-type materials given their high porosity and low framework density.[5,6] However, outstanding challenges encompass interface adhesion, mechanical, chemical, and thermal stability to afford practical applications.[7]

Nearly all the MOF dielectric experiments reported, however, were determined from powder samples (in pressed pellet form) that may suffer from structural collapse and/or framework amorphization from pressure.[8,9] Several studies have employed polycrystalline thin-film samples,[10–12] where grain boundaries defects may be prevalent. While there is previous report on the dielectric measurement of a single crystal of perovskite MOF, this was performed using a dense MOF structure with no accessible porosity.[13] Yet, the dielectric property of a single crystal of porous MOF with reversible guest uptake has not been measured directly, to yield an intrinsic value independent of pelleting pressure and free of grain boundary influence. Importantly, porous MOFs can readily accommodate guest molecules that will alter their dielectric properties by means of host–guest interactions. These physicochemical alterations are molecule specific, and thus can be exploited to achieve highly selective sensors. One way to detect host–guest interactions is by monitoring the transient response of the electrical signals through capacitive impedance or alternating current (AC) conductivity measurements.[14] We envisage that encapsulated polar molecules (as the "guest") will add an extra dipole to the MOF framework (as the "host"), thereby enabling highly responsive detection of analytes when sensing subtle changes by leveraging transient dielectric response of a single crystal. Importantly, because all MOFs exhibit a dielectric response, this proposed sensing approach will have major advantages over competitive techniques in the field, including resistive sensing[15,16] or fluorescent sensing [17,18] that require an electrically conductive framework (uncommon for MOFs)[19,20] or luminescence (not true for all MOFs, unlike the dielectric response).

A. S. Babal, Dr. A. K. Chaudhari, Prof. J.-C. Tan
Multifunctional Materials & Composites (MMC) Laboratory
Department of Engineering Science
University of Oxford
Parks Road, Oxford OX1 3PJ, UK
E-mail: jin-chong.tan@eng.ox.ac.uk
Dr. H. H.-M. Yeung
Inorganic Chemistry Laboratory
University of Oxford
South Parks Road, Oxford OX1 3QR, UK
Dr. H. H.-M. Yeung
School of Chemistry
University of Birmingham
Haworth Building, Edgbaston, Birmingham B15 2TT, UK
The ORCID identification number(s) for the author(s) of this article can be found under https://doi.org/10.1002/admi.202000408.

DOI: 10.1002/admi.202000408

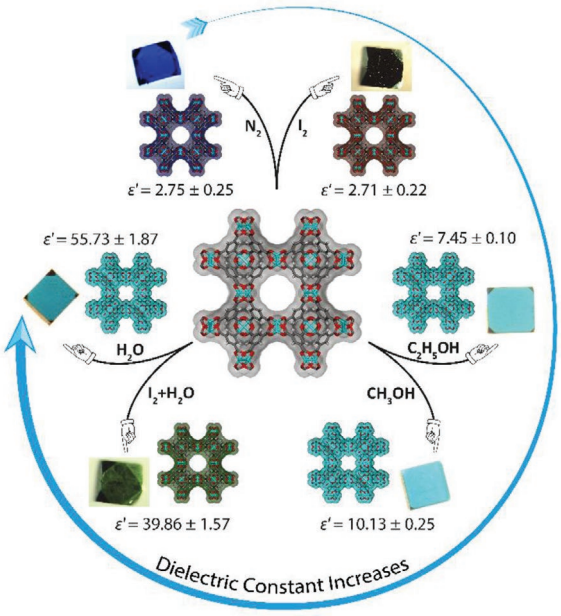

Figure 1. Single-crystal dielectric properties of HKUST-1 at 1 MHz, demonstrating its dielectric (ε') tunability through the encapsulation of specific guest molecules. The highest dielectric value was detected for H_2O@HKUST-1, while other guest-loaded crystals exhibited a rising trend of ε' as indicated by the arrow. Photographs show the actual HKUST-1 single crystals tested, whose sizes were ≈250–300 µm.

To probe the effects of guest inclusion on the dielectric properties of a MOF crystal, we have chosen the copper-based MOF, termed HKUST-1 [$Cu_3(BTC)_2$, BTC = benzene-1,3,5-tricarboxylic acid], to serve as a porous "host" framework because of its ability to form relatively large (≈250–300 µm) and mechanically stable single crystals needed for this study (**Figures 1** and **2**). Notably, the coordinatively unsaturated metal sites (CUS) in HKUST-1 are ideal adsorption sites for binding various guest molecules.[21,22] We study the effects of both polar (water, methanol, and ethanol) and non-polar molecules (iodine, I_2) on the dielectric properties of the HKUST-1 crystal, in the frequency range of 100 Hz to 2 MHz at room temperature. We characterized the dielectric properties of individual HKUST-1 crystals along the <100> direction employing the principle of a parallel-plate capacitor, probing its dielectric response in the activated versus guest-encapsulated states. The primary results are summarized in Figure 1, showing the transformation of crystal color and dependency of the crystal dielectric response upon the uptake of different guest molecules (vide infra). Subsequently, single-crystal cyclic sensing tests were performed at 1 MHz to probe the transient dielectric response and host–guest dynamics during the sorption/desorption cycles of guest molecules.

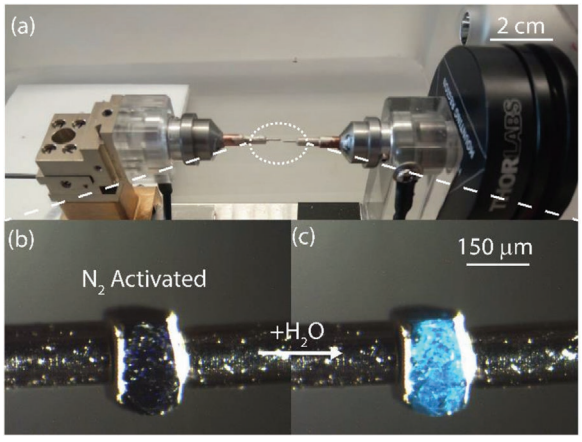

Figure 2. a) A custom-built single-crystal dielectric probe setup comprising a pair of spring-loaded electrodes mounted on a 3D translational stage. The entire setup is positioned in an enclosed chamber to permit the controlled flow of different guest species (see Figure S1, Supporting Information). b,c) Color change of an activated HKUST-1 single crystal when it was subjected to moisture in air.

Synthesis of the HKUST-1 single crystals was carried out using the solvothermal method described in Section 1.1, Supporting Information. The cuboidal crystals obtained were characterized under the stereo optical microscope, and found to have a lateral dimension of ≈250–300 µm and a thickness of ≈150 µm. A thin layer of silver coating was applied onto the opposite surfaces of the (100)-oriented facets (Figure S2, Supporting Information), to achieve a parallel-plate configuration for dielectric measurements (Figure S3, Supporting Information). Figure 2 shows the electrode arrangement of the single-crystal dielectric setup. The deep blue color of the pristine crystal (after N_2 activation) transforms into light blue on exposure to water vapor, causing a change in its refractive index.

Figure 1 presents a summary of the results showing the variation of the guest-dependent optical and dielectric properties of the HKUST-1 crystal, with its dielectric constant tunable between ε' = 2.8–55.6. The activated crystal switches from deep blue to light blue upon moisture adsorption, accompanied by a ≈20-fold rise in its dielectric constant. Non-polar iodine molecules (I_2) were encapsulated into the framework by vapor diffusion of sublimated iodine, resulting in color alteration of the HKUST-1 crystal, from deep blue to brown in dehydrated state, and to light green in hydrated state. When exposed to methanol (CH_3OH) and ethanol (C_2H_5OH) vapors, the crystal switches to a transparent light blue.

Figure S4, Supporting Information, shows the X-ray diffraction (XRD) pattern of the HKUST-1 single crystal, where the (200)- and (400)-oriented planes were confirmed. Analysis of the XRD peak profiles (Figure S5, Supporting Information) revealed an increase in FWHM of the iodine-encapsulated crystal, indicative of strain developed in framework from adsorbed iodine. Raman spectroscopy was performed to validate the encapsulation of molecular iodine in HKUST-1 (Figure S6, Supporting Information). The distinct Raman band at ≈210 cm^{-1} can be assigned to the I_2 molecules, while the peak at ≈420 cm^{-1} is the first overtone of I_2.[23] These results confirmed that I_2@HKUST-1 crystals were successfully obtained.

Figure 3 shows the influence of different guest molecules on the dielectric properties of HKUST-1 under cyclic sorption and desorption conditions, measured as a function of frequency up to 2 MHz. The pristine crystals were activated in N_2 (Figure 2b) before commencing the guest influx experiments. Guest inclusion into the porous framework was carried out by flowing N_2 through a bubbler containing the guest species (as liquid)

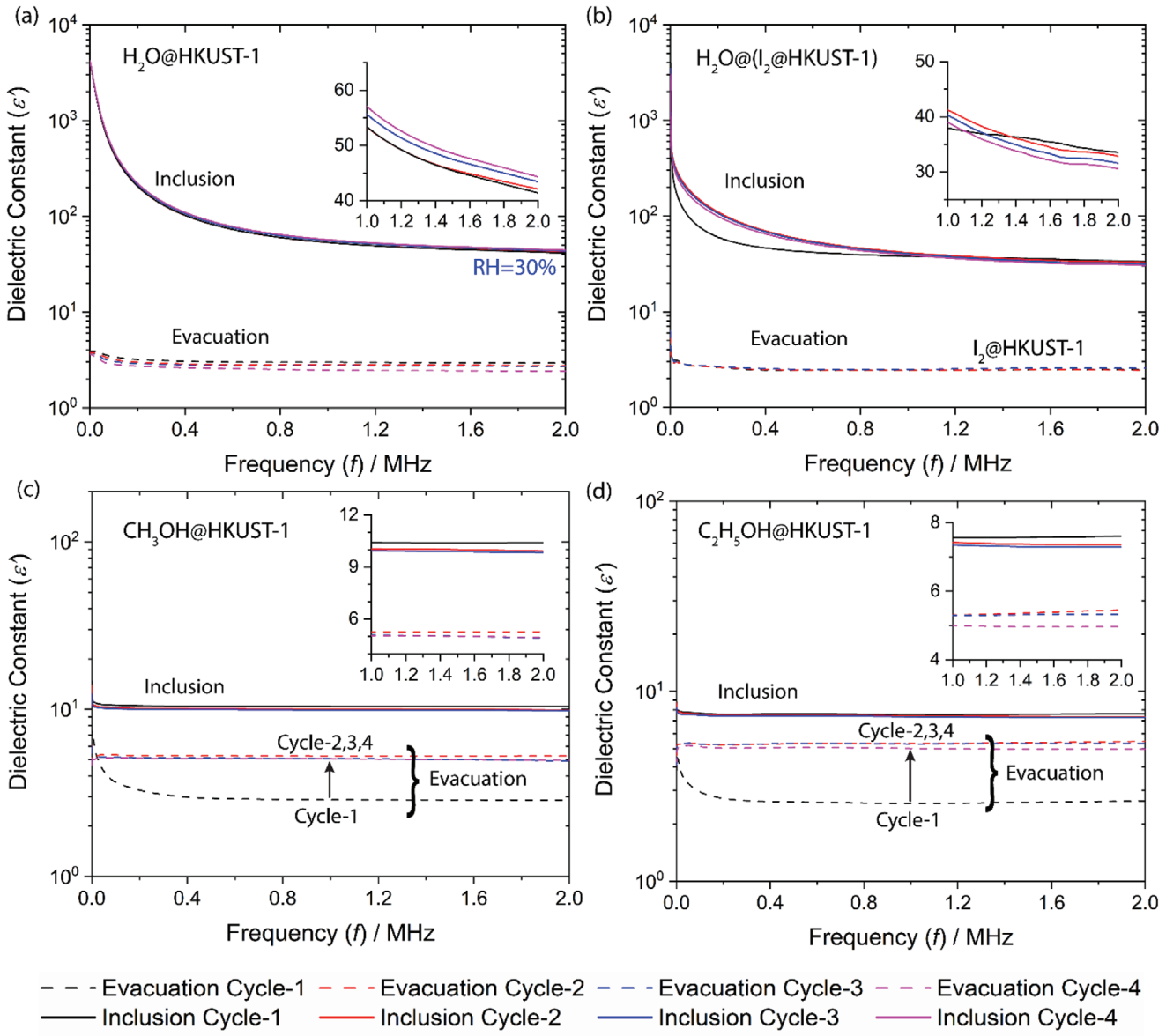

Figure 3. Effect of the encapsulation of different guest molecules into the HKUST-1 single crystal under a constant flow rate of 12 L h^{-1}: a) H_2O, b) H_2O and I_2, c) methanol (CH_3OH), and d) ethanol (C_2H_5OH), respectively, on the dielectric constant from 100 Hz to 2 MHz measured along the <100> lattice direction. The insets show the magnified views of the dielectric response in the range of 1–2 MHz.

to create a vapor phase at 30% and 70% relative humidity (RH). The dielectric constant of the HKUST-1 crystal in its activated state was found to be $\varepsilon' = 2.95$ at 1 MHz frequency (Figure 3a) determined in the <100> lattice direction. However, we observed a minor decline in ε' with further evacuation and guest inclusion cycles likely due to strain-induced cracking in the crystal interior; inclusion of microscopic air gaps may decrease ε' (Figure S3, Supporting Information). The dielectric constant of the HKUST-1 crystal increases dramatically with H_2O sorption, up to the value of $\varepsilon' = 57$ for 30% RH and $\varepsilon' = 64$ for 70% RH at 1 MHz (see Figure 3a and Figure S10, Supporting Information). The increase in ε' is associated with the inherent dipole of the guest water molecule. Water molecules coordinate to CUS of the copper-paddlewheel in HKUST-1 framework, whereas uncoordinated molecules in the pore will form clusters via hydrogen bonding (maximum of 186 molecules per unit cell).[24] We found only a modest rise of ε' at 70% RH (Figure S10, Supporting Information), indicating there is good water occupancy even at 30% RH. This finding is also consistent with the adsorption isotherm of water vapor reported by Alvarez et al.[22], showing a weight change of only ≈20% for HKUST-1 when the relative humidity was more than doubled from 30% to 70% RH.

The non-polar molecular iodine (I_2) was sublimated into gaseous form and then encapsulated into HKUST-1 to yield the I_2@HKUST-1 crystal. At this stage, although HKUST-1 framework has a higher propensity to adsorb I_2 over water, the presence of coordinated water on CUS will impede the direct

interaction between I_2 and the copper centers. Additional preferential interaction sites for molecular iodine are carbonyl oxygen atoms in the copper paddlewheel (3.23–3.30 Å) and the BTC linker (3.47–4.31 Å).[25] Figure 3b shows that in the first water inclusion cycle of I_2@HKUST-1, the value of ε' increased from 2.55 to 37.94 at 30% RH. The maximum value recorded is thus well below the value of $\varepsilon' = 57$ achieved by iodine-free HKUST-1 at 30% RH (Figure 3a). This result reveals that due to the preferential adsorption sites of molecular I_2 near the copper paddlewheel and the BTC linker, it could form a hydrophobic barrier that hinders water uptake (inside the otherwise hydrophilic pores). Due to this hydrophobic barrier, the activation time of the I_2@HKUST-1 crystal increases over other guests (under N_2 flow). The data clearly show that the presence of I_2 does not affect ε' due to non-polar nature of molecular iodine.

Further to water molecules, we carried out measurements on other polar guest molecules, namely methanol and ethanol. We note that activated HKUST-1 crystals from all the measurements gave an averaged $\varepsilon' = 2.75 \pm 0.25$. Figure 3c,d shows that for the first guest inclusion cycle, the ε' for methanol and ethanol increased to 10.40 and 7.51, respectively. The second inclusion cycle resulted in a minor decline of their ε' values to 9.92 and 7.35, respectively. Upon evacuation, however, their ε' values only partially reverted to ≈5.26 (cycle 1) and declined to 4.95 (cycle 2), instead of reverting to the initial value of ≈2.75. This phenomenon can be explained by trapping of guest molecules in the pores of HKUST-1. Confined solvent molecules tend to form a weak hydrogen bonding with the framework[22] and with the adjacent molecules, therefore become harder to evacuate without heating. Because methanol molecules are more polar than ethanol,[26] the presence of high polar species as a guest in HKUST-1 pores will result in higher ε', which we established in a systematic way at 1 MHz as: H_2O@HKUST-1 ($\varepsilon' \approx 60$) > methanol@HKUST-1 (≈10) > ethanol@HKUST-1 (≈7.5).

Figure 4 shows the transient response of the dielectric and conductivity behavior of HKUST-1 crystal during guest inclusion–expulsion study at 1 MHz. The cyclic ε' values in the encapsulated and activated states exceptionally match the ε' values determined from the frequency sweep measurements of Figure 3. It can be seen that the cyclic data show good repeatability, when the induced cracks have stabilized after the second cycle (Figure S3, Supporting Information). We found that encapsulation of non-polar I_2 affects the AC conductivity at 1 MHz, which increased from 0.16 mS m^{-1} for activated HKUST-1 to 0.29 mS m^{-1} for I_2@HKUST-1, and the latter increased to 7.9 mS m^{-1} at 30% RH. Uptake of water molecules thus enhances AC conductivity of the H_2O@(I_2@HKUST-1) crystal. HKUST-1 with methanol is relatively more conducting than ethanol; thus, we determined 0.50 and 0.42 mS m^{-1}, respectively (Figures S9 and S10, Supporting Information).

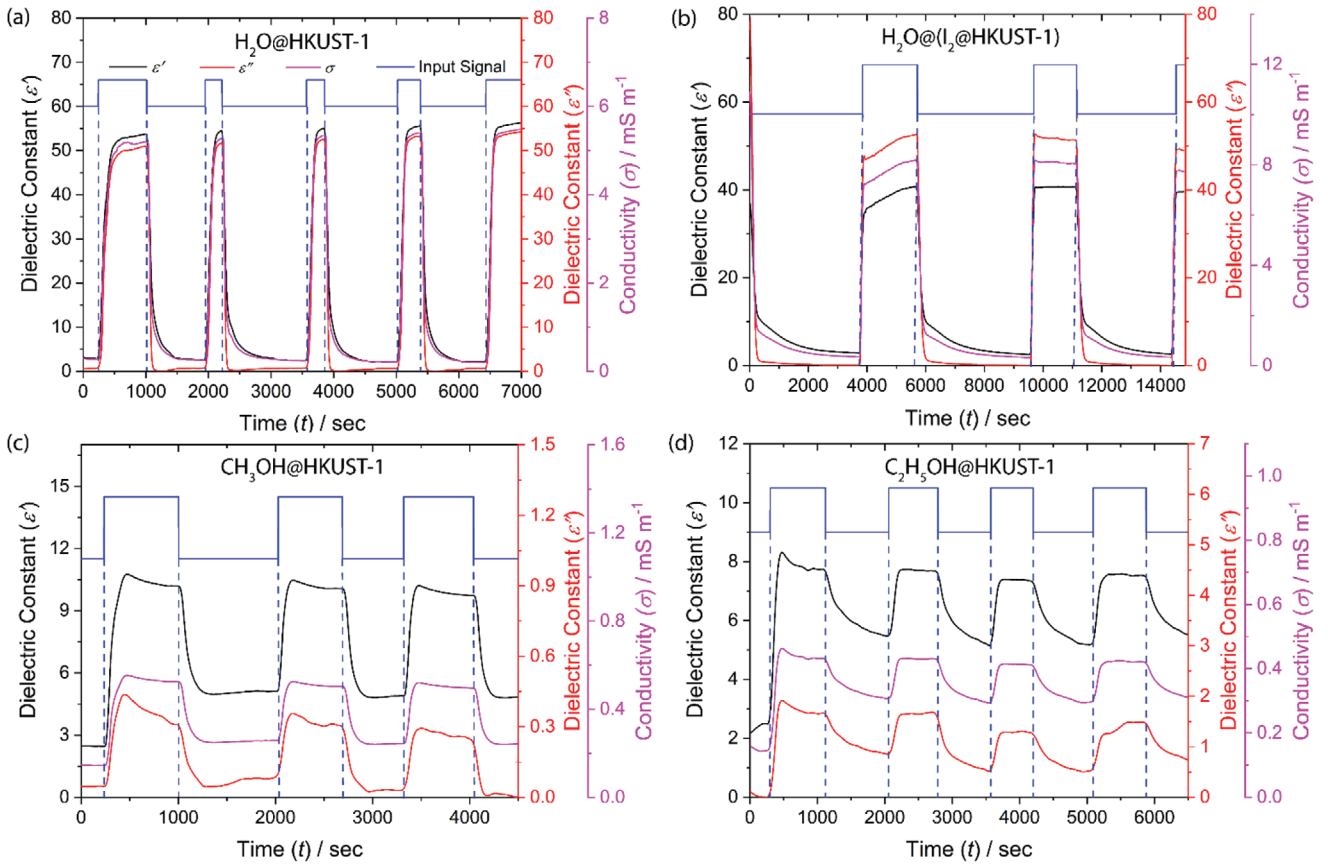

Figure 4. Cyclic dielectric (real and imaginary part) and conductivity measurements of HKUST-1 when being subjected to the following guest species: a) H_2O, b) H_2O and I_2, c) methanol (CH_3OH), and d) ethanol (C_2H_5OH). All measurements were performed at 1 MHz.

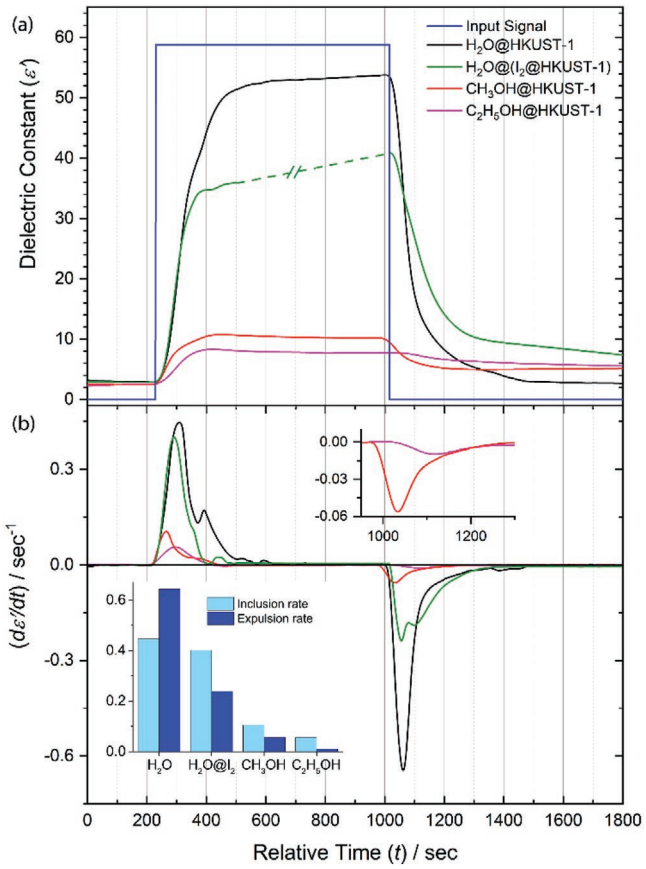

Figure 5. Comparison of time-dependent response for the inclusion and expulsion of different guest species in HKUST-1 single crystal. a) First cycle of dielectric response under guest environment. b) First-order derivative of the real part of dielectric constant with respect to time. The inset shows the inclusion and expulsion rates of different guest species. The I_2@HKUST-1 data were truncated on the time axis for better comparison with other guests.

Figure 5 is a representative plot of ε' and its first-order derivative with time ($d\varepsilon'/dt$) for the first cycle, allowing a comparative study of rate-dependent response subject to different guests. The rise (t_r) and fall (t_f) times are summarized in **Table 1**. Unlike the inclusion rate, the expulsion rate of water from the crystal is significantly higher compared to the I_2-encapsulated framework. Similarly, the rise and fall times for the I_2-encapsulated framework is higher than the I_2-free crystal (Table 1); the data suggest that the hydrophobic barrier provided by molecular I_2 hinders the mobility of water molecules to and from the uncoordinated copper sites on the paddlewheel. The size of the guest molecule could also influence the inclusion–expulsion time and rate. Given the relatively larger size of ethanol, its mobility will be lower compared to other guest molecules considered, as reflected by magnitudes of $d\varepsilon'/dt$, ranked as: $C_2H_5OH < CH_3OH < I_2@H_2O < H_2O$ (Figure 5b inset). Figure S12, Supporting Information, shows the increase in RH from 30% to 70% causes a sharp increase in the rise and fall time values in transient inclusion–expulsion cycles of H_2O guest. This increase suggests a good occupancy of H_2O molecules at 30% RH that acts as a barrier for inbound H_2O molecules resulting in a higher rise time. The effect of additional guest molecules in the host was also observed in the dielectric measurements (see inset of Figure S10a, Supporting Information), where the rise in ε' is very small from 30 →70% RH ($\Delta\varepsilon' \approx 4$ at 1 MHz) compared with 0 →30% RH ($\Delta\varepsilon' \approx 60$ at 1 MHz).

Table 1. Rise time and fall time for the inclusion and expulsion of guest molecules from a single crystal of HKUST-1.

Guest@HKUST-1	Rise time, t_r [s]	Fall time, t_f [s][a)]
H_2O	158.3	172.4
*H_2O	≈160 (0→30% RH); 77.2 (30→70% RH)	395 (70% → 0% RH)
$H_2O@I_2$	419.2	941.1
CH_3OH	104.5	144.7
C_2H_5OH	72.8	1088.6

[a)]Defined as the time required for the signal to rise from its low value (10% of the step height) to high value (90% of the step height), and vice versa. All values correspond to 0 ⇄ 30% RH apart from those indicated by an asterisk (*).

We reasoned that the larger guest molecules will fill the pores faster hence giving a lower rise time, while the clustering of spatially confined guests will impede their expulsion thus causing a higher fall time. Additionally, it is anticipated that weak chemical interaction between the guest species and the host framework will play a role in confinement of guest molecules (either strongly or weakly), which will determine the kinetics of cluster making–breaking process. This kinetics control the fall time of guest species being expelled from the pores. For instance, ethanol molecules can make a stronger hydrophobic interaction with the BTC linker, while interaction with methanol will be weaker comparatively. However, water will form strong bonding interaction with copper sites, and due to absence of any hydrophobic groups, the interaction of water with the BTC linker will be relatively weaker compared with ethanol and methanol. On this basis, we could explain why the ethanol-encapsulated HKUST-1 exhibits a shorter rise time followed by a longer fall time over methanol (Table 1). Interestingly, our transient data also reveal that residual clusters of methanol and ethanol trapped in the pores (after the first inclusion cycle) will result in a lower inclusion rate in the subsequent cycles, see Figure S13c,d, Supporting Information.

In conclusion, we show that frequency-dependent dielectric measurement of a MOF single crystal is no longer insurmountable. Because of its high sensitivity for discriminating different molecular guests, this single-crystal dielectric approach will enable accurate characterization of transient phenomena. The ability to measure the dielectric response of an individual crystal yields intrinsic properties, which cannot be obtained by existing techniques relying on larger samples in the form of a compacted powder pellet or a polycrystalline sample. This is an important achievement because, to date, the dielectric characterization of pellets are affected by problems linked to unwanted framework deformation and/or phase amorphization from pelleting pressure. More generally, our results revealed that the dielectric response of MOF crystals can considerably be altered by host–guest interactions (at open metal sites or ligands) via hydrophobic–hydrophilic interactions, and by harnessing guest molecular size effect and guests clustering attributed to

nano-confinement. Finally, the ubiquitous dielectric properties and AC conductivity of MOFs bode well for future application, as a Guest@MOF sensor featuring vast tunability and chemical selectivity, setting it ahead of the other competing resistive and fluorescent sensors in the field.

Supporting Information

Supporting Information is available from the Wiley Online Library or from the author.

Acknowledgements

A.S.B. is grateful to the Engineering Science (EPSRC DTP—Samsung) Studentship that supports this D.Phil. research. J.-C.T. and A.K.C. acknowledge the European Union's Horizon 2020 research and innovation programme (ERC Consolidator Grant agreement No. 771575—PROMOFS), the EPSRC Impact Acceleration Account Award (EP/R511742/1), and the Samsung GRO Award (DFR00230) for supporting this research. H.H.-M.Y. acknowledges the Glasstone Bequest for a Samuel and Violette Glasstone Fellowship. The authors acknowledge the mechanical workshop at Physical and Theoretical Chemistry laboratory, University of Oxford, for assistance in constructing the single-crystal cell. The authors thank Dr. Mark Frogley and Dr. Gianfelice Cinque at Diamond Light Source for the provision of Raman spectroscopy.

Conflict of interest

The authors declare no conflict of interest.

Keywords

conductivity, dielectrics, host–guest interaction, metal–organic frameworks, single crystal

Received: March 5, 2020
Revised: April 25, 2020
Published online: May 27, 2020

[1] M. Usman, K. L. Lu, *NPG Asia Mater.* **2016**, *8*, 333.
[2] I. Stassen, N. Burtch, A. Talin, P. Falcaro, M. Allendorf, R. Ameloot, *Chem. Soc. Rev.* **2017**, *46*, 3185.
[3] W. Volksen, R. D. Miller, G. Dubois, *Chem. Rev.* **2009**, *110*, 56.
[4] Semiconductor Industry Association, *The International Technology Roadmap for Semiconductors (ITRS) Annual Report*, 2013 Edition, SEMATECH, Albany, NY, USA **2013**.
[5] M. R. Ryder, Z. Zeng, K. Titov, Y. Sun, E. Mahdi, I. Flyagina, T. D. Bennett, B. Civalleri, C. S. Kelley, M. D. Frogley, *J. Phys. Chem. Lett.* **2018**, *9*, 2678.
[6] K. Zagorodniy, G. Seifert, H. Hermann, *Appl. Phys. Lett.* **2010**, *97*, 251905.
[7] K. Titov, Z. X. Zeng, M. R. Ryder, A. K. Chaudhari, B. Civalleri, C. S. Kelley, M. D. Frogley, G. Cinque, J. C. Tan, *J. Phys. Chem. Lett.* **2017**, *8*, 5035.
[8] A. S. Babal, L. Dona, M. R. Ryder, K. Titov, A. K. Chaudhari, Z. Zeng, C. S. Kelley, M. D. Frogley, G. Cinque, B. Civalleri, *J. Phys. Chem. C* **2019**, *123*, 29427.
[9] R. Scatena, Y. T. Guntern, P. Macchi, *J. Am. Chem. Soc.* **2019**, *141*, 9382.
[10] E. Redel, Z. Wang, S. Walheim, J. Liu, H. Gliemann, C. Woll, *Appl. Phys. Lett.* **2013**, *103*, 091903.
[11] S. Eslava, L. Zhang, S. Esconjauregui, J. Yang, K. Vanstreels, M. R. Baklanov, E. Saiz, *Chem. Mater.* **2012**, *25*, 27.
[12] M. Krishtab, I. Stassen, T. Stassin, A. J. Cruz, O. O. Okudur, S. Armini, C. Wilson, D. De Gendt, R. Ameloot, *Nat. Commun.* **2019**, *10*, 1.
[13] Y. Tian, A. Stroppa, Y. Chai, L. Yan, S. Wang, P. Barone, S. Picozzi, Y. Sun, *Sci. Rep.* **2014**, *4*, 6062.
[14] L. J. Small, T. M. Nenoff, *ACS Appl. Mater. Interfaces* **2017**, *9*, 44649.
[15] M. G. Campbell, S. F. Liu, T. M. Swager, M. Dinca, *J. Am. Chem. Soc.* **2015**, *137*, 13780.
[16] W. T. Koo, J. S. Jang, I. D. Kim, *Chem* **2019**, *5*, 1938.
[17] A. K. Chaudhari, H. J. Kim, I. Han, J. C. Tan, *Adv. Mater.* **2017**, *29*, 1701463.
[18] Z. Hu, B. J. Deibert, J. Li, *Chem. Soc. Rev.* **2014**, *43*, 5815.
[19] L. Sun, M. G. Campbell, M. Dinca, *Angew. Chem.* **2016**, *55*, 3566.
[20] C. H. Hendon, D. Tiana, A. Walsh, *Phys. Chem. Chem. Phys.* **2012**, *14*, 13120.
[21] B. E. Souza, L. Dona, K. Titov, P. Bruzzese, Z. Zeng, Y. Zhang, A. S. Babal, A. F. Moslein, M. D. Frogley, M. Wolna, *ACS Appl. Mater. Interfaces* **2020**, *12*, 5147.
[22] J. R. Alvarez, E. S. Gonzalez, E. Perez, E. S. Revueltas, A. Martinez, A. T. Cruz, A. I. Jacome, E. G. Zamora, Eduardo, I. A. Ibarra, *Dalton T* **2017**, *46*, 9192.
[23] R. J. Sension, H. L. Strauss, *J. Chem. Phys.* **1988**, *88*, 2289.
[24] A. J. Graham, J. C. Tan, D. R. Allan, S. A. Moggach, *Chem. Commun.* **2012**, *48*, 1535.
[25] D. F. Sava, K. W. Chapman, M. A. Rodriguez, J. A. Greathouse, P. S. Crozier, H. Zhao, P. J. Chupas, T. M. Nenoff, *Chem. Mater.* **2013**, *25*, 2591.
[26] A. Dukhin, S. Parlia, *J. Electrochem. Soc.* **2015**, *162*, H256.

Statement of Authorship for joint/multi-authored papers for PGR thesis
To appear at the end of each thesis chapter submitted as an article/paper
The statement shall describe the candidate's and co-authors' independent research contributions in the thesis publications. For each publication there should exist a complete statement that is to be filled out and signed by the candidate and supervisor **(only required where there isn't already a statement of contribution within the paper itself).**

Title of Paper	Guest-tunable dielectric sensing using a single crystal of HKUST-1
Publication Status	Published
Publication Details	A. S. Babal; A. K. Chaudhari; H. M. Yeung; J. C. Tan, Guest-tunable dielectric sensing using a single crystal of HKUST-1. *Adv. Mater. Interfaces* **2020**, 7, 2000408.

Student Confirmation

Student Name:	Arun Singh Babal		
Contribution to the Paper	A. S. Babal performed the experiments and analysied the data and wrote the manuscript. A. K. Chaudhari provided scientific insights into the project. H. M. Yeung provided the single crystal mounting base for the experiment. The whole single crystal project was carried out under the guidance of Prof. Jin-Chong Tan.		
Signature		Date	15/12/2021

Published Papers

Supervisor Confirmation

By signing the Statement of Authorship, you are certifying that the candidate made a substantial contribution to the publication, and that the description described above is accurate.

Supervisor name and title: Prof. Jin-Chong Tan		
Supervisor comments: The provided description is accurate.		
Signature	Date	15/12/2021

This completed form should be included in the thesis, at the end of the relevant chapter.

"All intelligent thoughts have already been thought;

what is necessary is only to try to think them again."

– Johann Wolfgang von

4

Metal–Organic Framework Electrical Sensor

As discussed in Chapters 2 and 3, the host-guest interaction and external stimuli play a vital role in determining the MOF properties. In this chapter, we utilized our experience in electrical and dielectric properties of MOF to carry out the experiments in a way so that it can lead to a viable practical application such as a prototype gas-phase electrical sensor. We rationally designed a MOF that exhibits an outstanding performance with an almost billion-fold enhancement in the electrical response (impedance) due to its optimized hydrophobicity, which allows the easy migration of iodine molecules through the channels and the presence of suitable interaction sites, temporarily anchoring the target molecule for ultra-trace sensing. In a wider perspective, we propose a general strategy for electrically responsive sensing materials with hybrid functionalities in addition to the next-generation iodine sensor for hazard detection. In section 4.1, we will briefly discuss the past accomplishments and shortcomings in the electrical MOF sensor field

followed by different MOF synthesis techniques, their sensor preparation and operating procedures. After explaining the characterization techniques used in this study, we will describe our accomplishments and detailed findings in section §4.6.

4.1 Background and motivation

Nuclear is the backbone of greenhouse gas-free energy providing up to 10% of the global energy demand.[42] To meet the ever-increasing energy demand of society, it is considered as the most promising alternative source over fossil fuels due to its high energy density, low operational cost, and greenhouse gas-free energy, which leads to a low carbon footprint.[43, 44] Despite these several advantages, in developed countries, the age of nuclear energy starts to fade away due to the concerns associated with the emission of radioactive gases during nuclear accidents and fuel reprocessing that has severe long-term impacts on both environment and human health.[45] Mostly the radionuclides are emitted in the form of gases and can enter our food chain through the contaminated air depositing these radioactive molecules on agricultural soil and drinking water supply. One of the major gases of concern is iodine, with its isotopes including ^{131}I (half-life: 8 days) and ^{129}I (half-life: 1.7 million years), which adversely impact human metabolism and are a major cause of thyroid cancer.[46-49] The conventional iodine sensors have some shortcomings that must be tackled, i.e. low sensitivity, poor selectivity, short-term reusability, and sensing at higher temperatures.[4, 50-52] To address these long-standing challenges, an effective technology needs to be developed to selectively detect the ultra-trace level of radionuclides in case of nuclear breach or

fuel preprocessing to maintain a hazard-free working environment in the nuclear industry and to ensure safety in the widest context.

MOFs are ideal candidates for sensing studies and started gaining the attention of the scientific community due to their high surface area, tunable pore size, design versatility, which can be tailor-made to incorporate the interaction sites to selectively accommodate the target gas molecules along with its structural, thermal, and chemical robustness.[53-56] Currently, optical techniques are widely studied in the field of gas-phase sensing in MOFs, but for industrial applications, a direct electric response far outweighs it due to the real-time, highly compact setup with low-cost manufacturing, high readability, and better assimilation with modern electronics.[5-7, 57] However, electrical sensing of non-polar gases such as I_2 remains an immense challenge due to the shortfall of effective materials to afford practical designs. In this regard, a material with a judicious combination of optimal hydrophobicity and interaction sites could be an ideal candidate in ultra-trace (ppb level) I_2 detection from the gas phase but yet to be achieved.

In this chapter, a series of prototype sensors were prepared by the drop-casting method, in-situ growing of single crystals and inkjet printing of MOFs, on interdigitated electrodes (IDEs) for the aim of fabricating a highly selective and ultra-trace (ppb level) gas-phase iodine sensor. A ppb level of high sensitivity was realized in MOF through a rational combination of optimal hydrophobicity and suitable interaction sites (see Figure 4.1). In the presence of iodine, a very fast reversible million-fold enhancement in alternate current (AC) signals and a

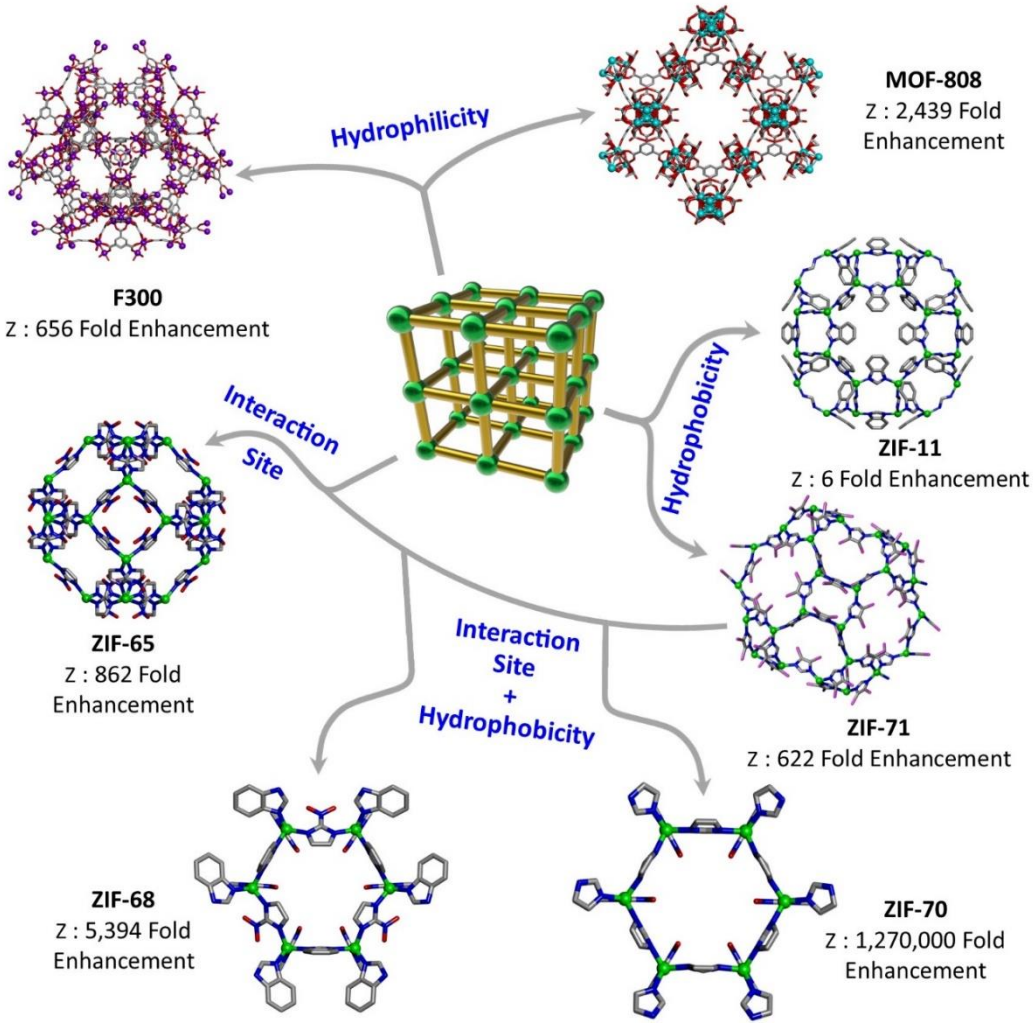

Figure 4.1: Summary of optimal chemical and physical properties to yield highly selective and sensitive MOF for gas phase iodine sensing. The *Z* number denotes the enhancement in electrical response achieved by each MOF structure relative to the "empty" IDE on substrate, i.e., MOF-free IDE as a control.

remarkable billion-fold enhancement in direct current (DC) was achieved for the electrical response of the prototype sensor due to its high adsorption capacity. Here, the optimal hydrophobicity allows adsorption of the non-polar iodine gas molecules and suitable interaction sites selectively trap them to the host framework, enhancing

the overall ppb-level sensitivity. Furthermore, the gas phase ultra-high selectivity of MOF material was tested by collecting the cyclic electrical response in different VOCs and water-saturated environments, in addition to the optimal thickness of MOF layers on the prototype sensor to standardise the whole process for potential industrial application. Finally, a room temperature electrical response was also measured to simulate the real-time application.

4.2 Synthetic procedures

4.2.1 Materials

F300 was purchased from Sigma Aldrich. ZIF-11, ZIF-65, ZIF-68, ZIF-70, ZIF-11, MOF-808 were synthesized by following the previously reported literature method with slight modifications.[58-62] All the reagents and solvents were commercially available and used as received, sourced from Fisher Scientific, Alfa Aesar, Fluorochem depending on their availability.

4.2.2 MOF synthesis

ZIF-11: 2 mmol of benzimidazole was dissolved in 10 mL of ethanol and 8.5 mL of toluene, followed by the addition of ammonia hydroxide (2 mmol NH_3) under stirring at room temperature. After that, 1 mmol of zinc acetate dehydrate was added and stirred for the next 3 h at room temperature. The product of ZIF-11 was collected by centrifugation and washed with 50 mL of ethanol and dried at room temperature in the open air overnight.

ZIF-65: 0.5 mmol zinc acetate was soluble in 5 mL of DMF and rapidly mixed into 1 mmol of 2-nitroimidazole in 5 mL methanol under vigorous stirring. After 24 h of stirring at room temperature, the sample was centrifuged at 10,000 rpm to collect the product. The product was further washed three times with a copious amount of DMF and methanol to remove the excess reactants and dried at 90 °C for overnight.

ZIF-68: 0.5 mmol of 2-nitroimidazole, 0.16 mmol of benzimidazole and 0.5 mmol of $Zn(NO_3)_2 \cdot 6H_2O$ were separately mixed in the 2 mL of DMF solutions. After that, three different solutions were mixed and heated in a capped vial at 130 °C for 96 h and left at 12 h for cooling. The mother liquor was decanted, and the products were washed with excess DMF for four times.

ZIF-70: 0.36 mmol of 2-nitroimidazole, 0.36 mmol of imidazole and 0.36 mmol of $Zn(NO_3)_2 \cdot 6H_2O$ were mixed separately in the 2 mL of DMF solutions. After that, three different solutions are mixed and heated in a capped vial at 130 °C for 96 h and left at 12 h for cooling. The mother liquor was decanted, and the products were washed with excess DMF for four times.

ZIF-71: 2 mmol zinc acetate was dissolved in 50 mL of methanol and rapidly mixed into a 50 mL methanol solution of 8 mmol of 4,5 dichloroimidazole, under stirring conditions. The mixed solution transformed clean to turbid after a few seconds. After 24 hours of stirring at room temperature, the sample was centrifuged at 10,000 rpm to collect the product. The product was further washed three times with a copious amount of methanol to remove the excess reactants.

MOF-808: Trimesic acid (210 mg, 1 mmol) and zirconyl chloride octahydrate (970 mg, 3 mmol) were dissolved in DMF/formic acid (30 mL/30 mL) and placed in a large screw-capped glass jar, which was heated to 130 °C for two days. A white precipitate of MOF-808 was collected by filtration and washed four times with 400 mL of fresh DMF. The DMF-washed compound was then immersed in 100 mL of acetone for four days, and during this time the acetone was replaced two times per day to facilitate the solvent exchange process. The acetone-exchanged sample was then evacuated at room temperature for 24 h and at 150 °C for 24 h to yield an activated sample.

4.3 Prototype sensor preparation

The thin-film gold interdigitated electrodes (IDEs) on a glass substrate were used as a sensing platform on which MOF material was deposited. These prefabricated IDEs were purchased from Micrux (ED-IDE3-Au) containing 184 pairs of gold microelectrode with a width and a gap size of 5 μm, respectively. Before sample deposition, the IDE electrodes were rinsed with isopropanol (HPLC grade, Sigma-Aldrich, ≥ 99.9%) and then later dried under the nitrogen gas. The impedance value of empty IDEs was measured beforehand to perform a qualitative comparison between the sensitivity of different MOF samples. To prepare the prototype sensor three different techniques were used, which are described in sections below.

4.3.1 Drop-casting method

As described in section 4.2.2, the MOF materials were synthesized and left in the solvent suspension to avoid aggregation. In this method, the MOF suspension was carefully pipetted out and drop cast on the active area of the IDE in such a way that after drying on average ~ 1 mg of material was deposited for each of the MOF samples. Afterwards, the IDE was first dried under room conditions and then exposed to nitrogen gas. The amount of the deposited MOF was estimated using a high precision balance (0.01 mg). In the case of ZIF-70 MOF, for drop-casting and inkjet printing, the synthesized crystals were first broken down into fine particles using an ultrasonic probe sonicator and then deposited on the IDE electrode.

4.3.2 Single-crystal

To prepare a single-crystal prototype sensor, the cleaned IDE is placed inside the reaction vial of ZIF-70 MOF. The MOF synthesis reaction parameters were kept the same as described in section 4.2.2. After the completion of the reaction, the IDE electrode was gently washed in the methanol solvent to avoid any stress-related cracking and then dried at room temperature. The IDE electrode was weighed before and after the crystal growth step to keep track of the amount of deposited ZIF-70, which was later used to quantify the adsorbed iodine amount.

4.3.3 Inkjet printing

The MOF ink, without any additives, were printed using a commercially available printing system (Jetlab-II, MicroFab Technologies Inc.) which can

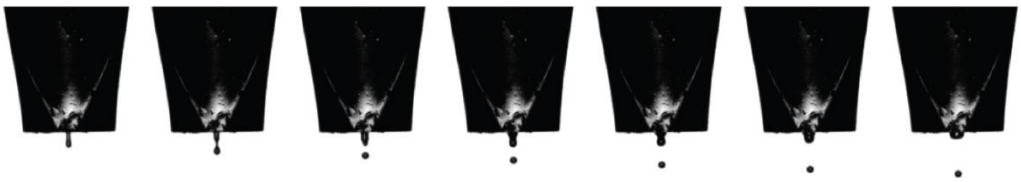

Figure 4.2: High-speed photography images of the printing process of an exemplar ZIF-70 MOF solution. The size of the nozzle orifice is 80 μm. The time interval between two adjacent frames is about 48 µs.

deposit droplets within ± 5 µm accuracy. To print MOF droplets without any satellite droplet an 80 µm nozzle diameter dispenser was employed. The dispenser was plugged with a pneumatic pressure control system to control the back pressure to reduce the solvent evaporation phenomenon at the tip of the nozzle (the fast evaporation at the tip could lead to nozzle blockage). Figure 4.2 shows the dynamic shadowgraph images of the smooth MOF droplet formation process. The in-flight diameter of the falling droplet is approximately 50 µm. The IDE patterned substrate (interdigitated electrodes) was placed onto the bed of the printer. During printing, the substrate and printhead were maintained at room temperature of 21 ºC. A rectangular array of droplets, according to the area of the IDE electrodes, were printed at a droplet spacing of 20 µm. Iodine sensing MOF based devices with a range of film thicknesses were produced by changing the print pass of the printhead.

4.4 Iodine exposure on MOF sensor

For iodine experiments, the MOF deposited IDE electrode and an excess of 50 mg of dry iodine was placed inside a 500 mL glass bottle. The sealed glass bottle was then placed inside an oven at 70 °C for 30 mins and later cooled down to room temperature. The iodine adsorption causes a visible change in MOF colour (see Figure 4.3). For each MOF, three IDEs were prepared to ensure the repeatability of data. MOF sample with the highest iodine sensitivity was chosen to further carry out cyclic adsorption and desorption measurement for 3 cycles to

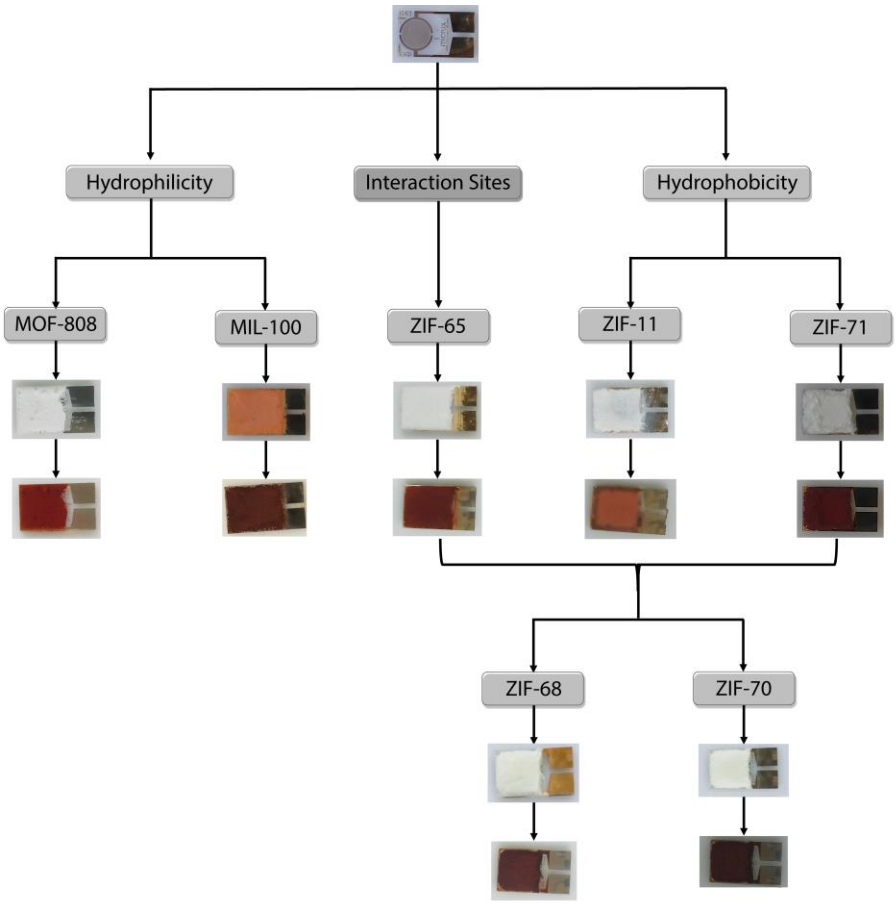

Figure 4.3: Photographs of prototype MOF@IDEs, before and after iodine.

confirm its reversibility. To do so, the sample was heated at 70 °C overnight. Furthermore, we also simulated a real-time situation by continuously measuring the electrical response of the sensor during an iodine exposure test.

4.5 Material characterisation

4.5.1 X-ray diffraction (XRD)

The powder X-ray diffraction (PXRD) pattern for the different MOF samples was determined using the Rigaku MiniFlex benchtop X-ray diffractometer with a Cu Kα source (1.541 Å) at a scan rate of 0.2°/min and a step size of 0.05°. Diffraction data of MOF samples were collected from 2° to 40° and then normalised to the most intense peak for phase identification. Before the data collection, the MOF samples were pre-evacuated in a vacuum oven at 100 °C overnight to remove any residual solvents trapped in the MOF pores.

4.5.2 Fourier-transform infrared (FTIR) spectroscopy

The FTIR spectra for the MOF samples were recorded using the Nicolet-iS10 FTIR spectrometer equipped with an ATR sample accessory in the mid-IR region (650–4000 cm^{-1}) at a spectral resolution of 0.5 cm^{-1} after collecting the background spectrum using the identical parameters. The impact of iodine adsorption and desorption on infrared vibrational modes of MOF at room temperature as well as with time-dependent heating was studied by ATR-FTIR.

4.5.3 Raman spectroscopy

The Raman spectra were collected using the Bruker MultiRAM Raman spectrometer with sample compartment D418, equipped with an Nd-YAG-Laser (1064 nm) and an LN-Ge diode as the detector. The laser power used for sample excitation was 50 mW, and 64 scans were accumulated at a resolution of 1 cm^{-1}. Raman spectroscopy was used as the main technique to detect the presence of non-polar iodine species in the MOF framework and its interaction with the pore structure by determining the shift in the vibrational modes.

4.5.4 Thermogravimetric analyses (TGA)

The thermal stability of the empty and guest loaded ZIF-71 MOF was measured using the TGA-Q50 (TA Instruments) equipped with an induction heater (max temperature 1000 °C) and platinum sample holder (maximum volume 50 µL) under an N_2 inert atmosphere. Approximately 5 mg of sample was placed in the pan and then heated from 30 to 800 °C at a rate of 10 °C/min under a dry nitrogen flow of 40 $mL.min^{-1}$. TGA was used as one of the techniques to reveal the presence of different loading of guest species in the framework pore by calculating its weight derived from the provided temperature-dependent weight loss.

4.5.5 UV–Vis spectrophotometer

The adsorption spectra for ZIF-70 MOF were obtained using the 2600 UV−Vis spectrophotometer (Shimadzu) in the wavelength range of 200-1400 nm, equipped with an integrating sphere. The diffused reflectance spectra for both

iodine adsorbed and desorbed ZIF-70 MOF was measured and converted using the Kubelka−Munk (KM) transformation to estimate the optical band gaps. The iodine-dependent change in bandgap explained the sharp decline in the impedance value of the framework.

4.5.6 Optical microscopy and surface profilometry

Alicona profilometer was used to measure the surface texture such as the thickness of the deposited MOF layer. The surface topography was characterised by the infinite focus microscopy technique (Alicona Infinite Focus 3D profilometer) using the 5× optics on the profilometer.

4.5.7 Prototype sensor response

The electrical response from the IDE sensor was recorded at room temperature at 35% RH using the HIOKI IM3536 LCR meter in the frequency range of 4 Hz to 8 MHz at 1 V. To measure the sensitivity of the sample IDE at a point of time, the impedance, capacitance, and phase angle parameters were obtained in parallel as a function of frequency. For in-situ experiments, a 467.6 ppb and 8.35, 16.7, 25.05, 33.40 ppm level I_2 environment was maintained by placing meshed iodine inside a custom-built closed chamber alongside the sample IDE to simulate the real-time application. Subsequently, the impedance measurements were continuously collected at 10 Hz (1 V) as well as over the frequency range of 4 Hz to 8 MHz.

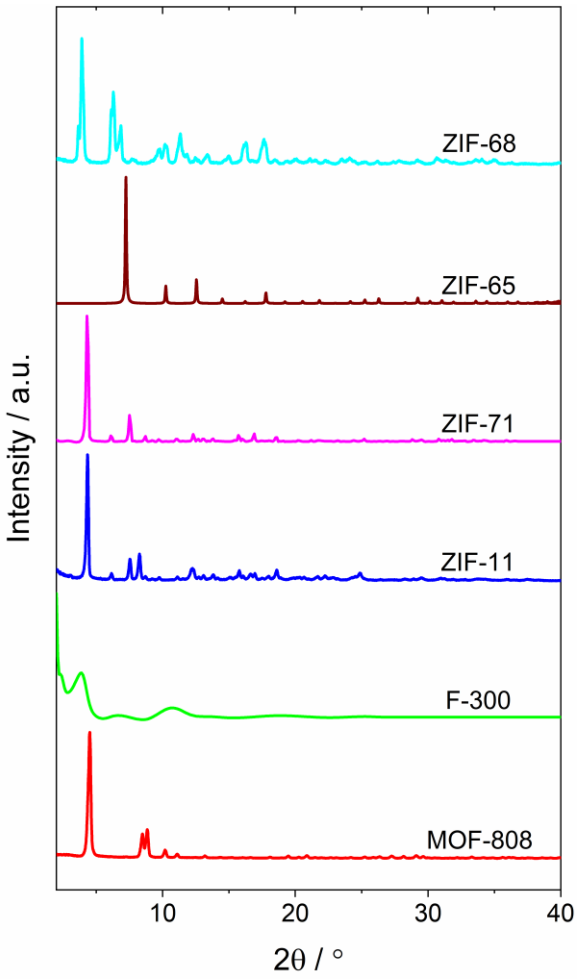

Figure 4.4: Normalised PXRD patterns of activated MOF powder samples.

4.6 Results and discussion

4.6.1 Drop-casted MOF prototype sensor

The prototype sensor consists of interdigitated comb-like electrode (IDE) structures on a glass substrate coated with an insulating polymeric film. For the qualitative comparison between the sensors, the electrical response (impedance, capacitance, and phase angle) from the empty IDE was measured in addition to their

response toward the iodine gas, which remained unchanged. Later, thin films of different MOFs were prepared on the sensors *via* various methods i.e., drop-casting, in-situ single-crystal growth and inkjet printing (controlled layered deposition) and then dried in the presence of inert N_2 gas (as described in section 4.3). PXRD was carried out for all the MOFs to confirm their crystalline structure before collecting the electrical response from the prototype sensors (see Figure 4.4). The variance in the electrical response of empty and MOF deposited sensors was non-existent, which indicates the insulating nature of MOFs. The effect of hydrophilicity, hydrophobicity, and interaction sites of candidate MOF materials on high selectivity and ultra-trace sensitivity toward the specific gas was monitored to study

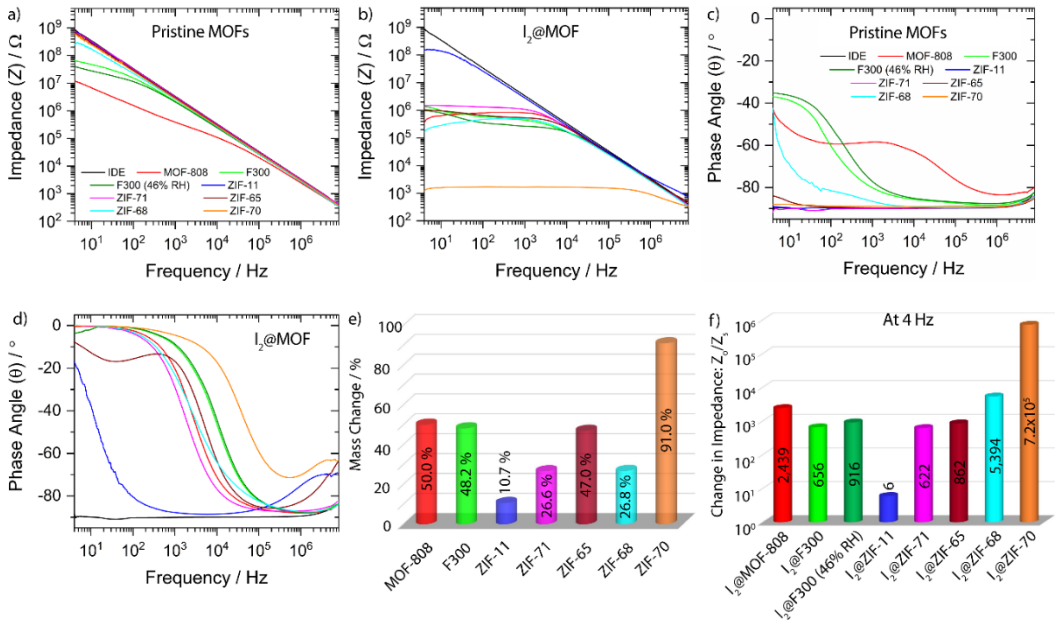

Figure 4.5: Electrical response from the MOF@sensor prototypes at room temperature: before and after iodine adsorption: (a), (b) Impedance and (c), (d) phase angle, respectively. (e) Percentage change in sample mass and, (f) the change in impedance ratio of various MOF structures, after the iodine adsorption.

their impact and later those individual properties are combined to establish the final optimized material.

The different prototype MOFs: MOF-808 and F300 for hydrophilicity, ZIF-11 and ZIF-71 for hydrophobicity, ZIF-65 for its functional nitro-group and ZIF-68 and ZIF-70 for their interaction site and optimal hydrophobicity were selected as a sensing material for gas-phase I_2 sensing (see Figure 4.5 (a)-(d)). Unlike the other MOFs, which showed a lack of H_2O induced contribution in the

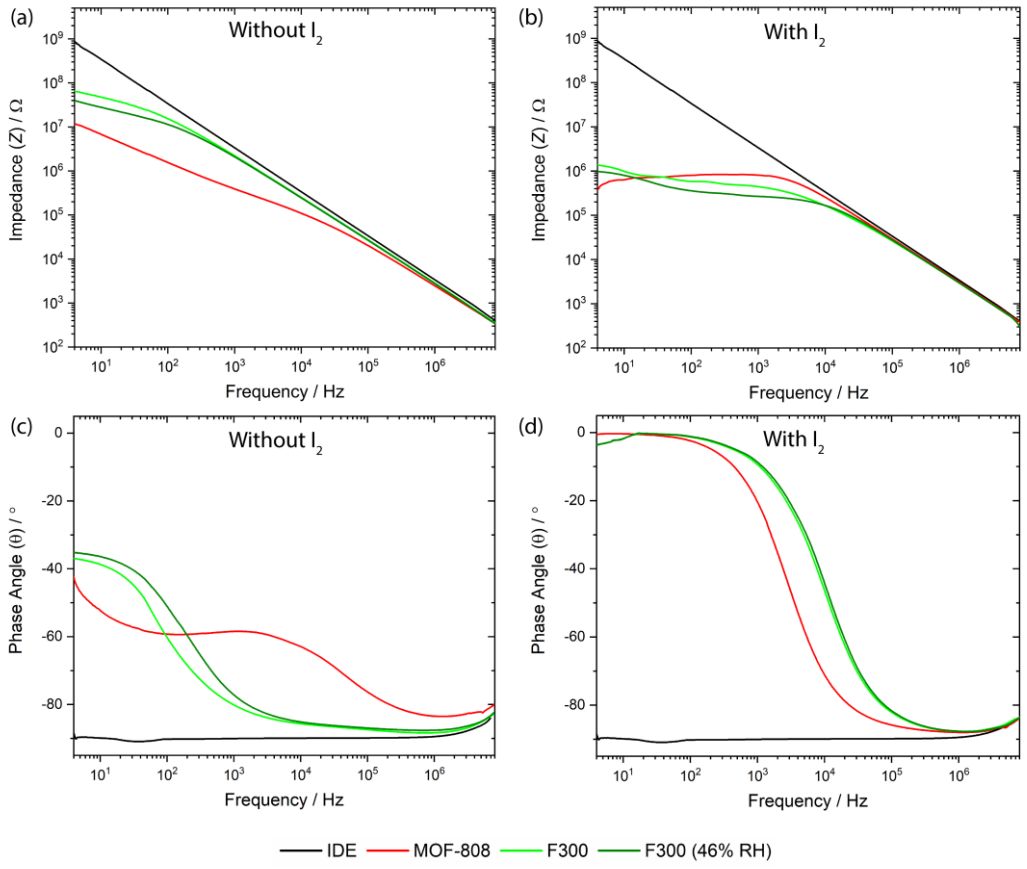

Figure 4.6: Effect of hydrophilicity on sensor impedance and phase angle: (a), (c) before and (b), (d) after iodine adsorption, respectively.

sensor response, the hydrophilic MOFs: MOF-808 and F300 showed a significant shift in electrical response at room conditions in contrast to the empty sensor, suggesting that the high conductivity and polarizability of the H_2O molecules absorbed on the hydrophilic sites of the porous framework greatly influence the sensor response. To evaluate the impact of moisture on sensor response, F300@IDE was tested at 2 different RH conditions (35 and 46% RH), validating that higher electrical response is associated with the increasing humidity (see Figure 4.6). In the presence of iodine gas, the overall sensitivity of hydrophilic prototype MOFs: MOF-808 (mass change of ~ 50 %) and F300 (mass change of ~ 48 %) is a combination of both H_2O and I_2 molecules (present in the MOF pores), decreasing the impedance response further by 656 and 2,439 folds, respectively (see Figure 4.5 (f)) and showed a noticeable transition in the phase angle (θ) from -42° (MOF-808) and -37° (F300) to almost 0° at lower frequencies, indicating a transition in electrical behaviour from capacitive to resistive type (see Figure 4.5 (d)). The slightly higher sensitivity of F300 MOF over MOF-808 can be associated with its higher iodine adsorption capacity (see Figure 4.5 (e)). The presence of H_2O molecules in the hydrophilic pore negatively affects the inbound target molecules (shrinks the adsorption capacity of the framework) and decreases the overall sensitivity as well as reusability of the sensor devices, rendering them ineffective for the real-time gas phase sensing except for the application as a humidity sensor. In consideration of these factors and to eliminate the impact of moisture on sensor sensitivity, we selected ZIF-11 and ZIF-71 as a prototype hydrophobic MOF for I_2 sensing, which showed no alterations in the

electrical response under ambient conditions. Despite the advantages of not being affected by moisture, the hydrophobicity causes a decrease in iodine adsorption, which in turn leads to an unwanted lower electrical response of the sensor. Unlike the extreme hydrophobicity of the ZIF-11, which bring about a decline in the iodine adsorption (mass change of ~ 11%) and causes an exceedingly low enhancement in the impedance ratio of only 6-fold, the ZIF-71 framework has comparatively higher iodine adsorption capacity (mass change of ~ 27%), enhancing its electrical response to 622-fold, which is comparable with the hydrophilic MOF sensors (see Figure 4.5 (e) and (f)).

In addition to the characterization of MOF candidates hydrophilicity and hydrophobicity, the interaction sites can also play a key role in the selective capturing of the targeted molecules. In this regard, ZIF-65 was chosen to evaluate the impact of interaction sites on iodine adsorption and its electrical sensing response because it has a nitro-group as part of its linker molecule.

The ZIF-65@IDE is unaffected by the presence of moisture, and it adsorbs a significant amount of iodine molecule yielding a mass change of 47% when exposed to the iodine gas (see Figure 4.5 (e)). The electron-deficient nitro-group acts as anchor points for the inbound iodine molecules and partially polarizes them. An increase in the polarization causes a huge rise in the capacitance value (1876% enhancement) as seen in Figures 4.7, which is comparable to the hydrophilic MOFs, where water is highly polarizable. For ZIF-65 MOF, the phase angle showed a slight deviation in the pattern compared to the other tested MOFs by not showing a

complete transition from almost -90° to 0°, when exposed to the iodine gas (Figure 4.5 (d)). The effect was assumed to have resulted from the interaction of iodine molecules with the framework, producing a marked 862-fold enhancement in the ratio of impedance values at 4 Hz, which is higher than the hydrophobic MOFs ZIF-71 as well as F300 hydrophilic MOF values (see Figure 4.5 (f)). The data obtained from the hydrophilic, hydrophobic and interaction site-based MOFs collectively indicate that to achieve an ultra-high sensitivity I_2 sensor, the individual properties of MOFs are insignificant. An interaction site-based MOF with optimal hydrophobicity, which is a combination of extreme hydrophobicity and hydrophilicity could be a way forward to harness the MOF potential in the field of electrical sensing for iodine gas.

For this purpose, two different prototypes of MOFs: ZIF-68 and ZIF-70 were chosen, comprising the same interaction site (nitro-group from 2-nitroimidazole) and different hydrophobicity based on the secondary linker molecule. The hydrophobicity of MOFs was adjusted by varying the secondary linker molecule from imidazole (Im) to benzimidazole (bIm) for ZIF-70 and ZIF-68, respectively. The presence of an additional benzene ring makes the ZIF-68 framework more hydrophobic compared with the ZIF-70 structure and can provide further validation to the optimal hydrophobicity requirement theory for the ultra-high electrical gas sensing of non-polar gases. The hydrophobic linker molecule provides protection from the highly polar water molecules by impeding their negative impact on sensor performance, and the electron-deficient nitro-group acts as a temporary anchor point for the inbound iodine molecules and partially

polarize them causing an overall shift in the structure properties, which generates a very high electrical response from the prototype sensors. The iodine adsorption capacity of ZIF-68 MOF (mass change ~ 27%) was lower as compared to the ZIF-70 MOF (mass change ~ 91%), which was a direct result of its higher hydrophobic nature (see Figure 4.5 (e)). Although in the presence of iodine gas, the increase in impedance ratio of 5,394-fold for ZIF-68 is impressive and indicative of the formation of a percolation network at a smaller amount of iodine, albeit this is nowhere near the astonishing increase of 0.73-million-fold in impedance ratio at 4 Hz for ZIF-70, which is an exemplar of an optimal combination of hydrophobicity and interaction site (see Figure 4.5 (f)). We propose that the adsorbed iodine provides new and faster charge transfer pathways in the framework causing a decrease in the material impedance. It is well established that at higher iodine concentration, after adsorption in framework pores they form interconnected networks of polyiodides, which decreases the material resistance by providing the charge transfer pathways.[63, 64] Similarly, for the other measurement for ZIF-70 MOF, such as phase angle the transition from -90° to 0° was stable up to < 10^3 Hz, showing its potential as a frequency-dependent sensing material for iodine gas. From all the different experiments, it was established that the ZIF-70 MOF, which contains both interaction site and optimal hydrophobicity is the unrivalled candidate, and it should be studied in depth to further optimize the different sample preparation parameters and operational conditions that can impact its gas phase iodine sensing.

To confirm whether the location of iodine is inside or outside the framework pore, we have conducted a controlled experiment, where the guest is encapsulated

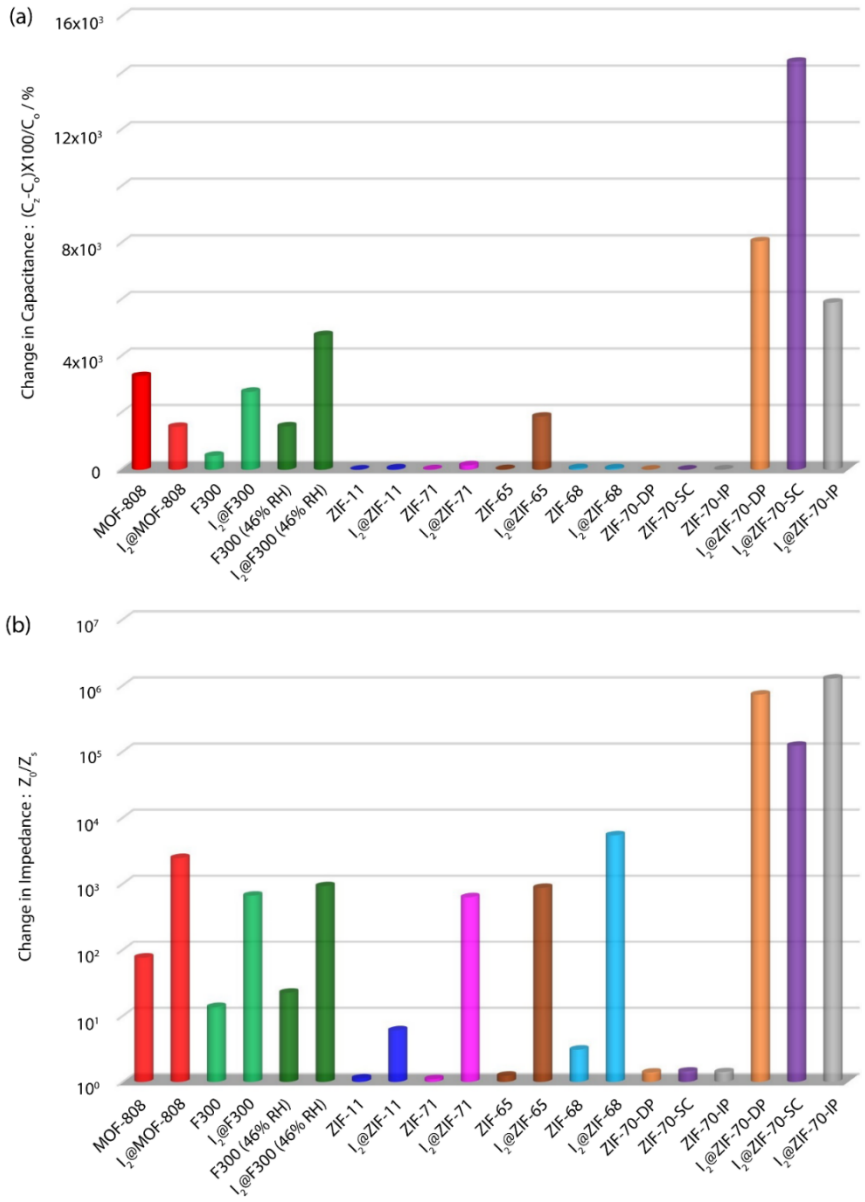

Figure 4.7: Comparative plot of the change in MOF@sensor output parameters determined at 4 Hz: (a) Percentage change in capacitance, and (b) ratio of sample impedance relative to an empty IDE. Note: DP = drop casting, SC = single crystal, IP = inkjet printing.

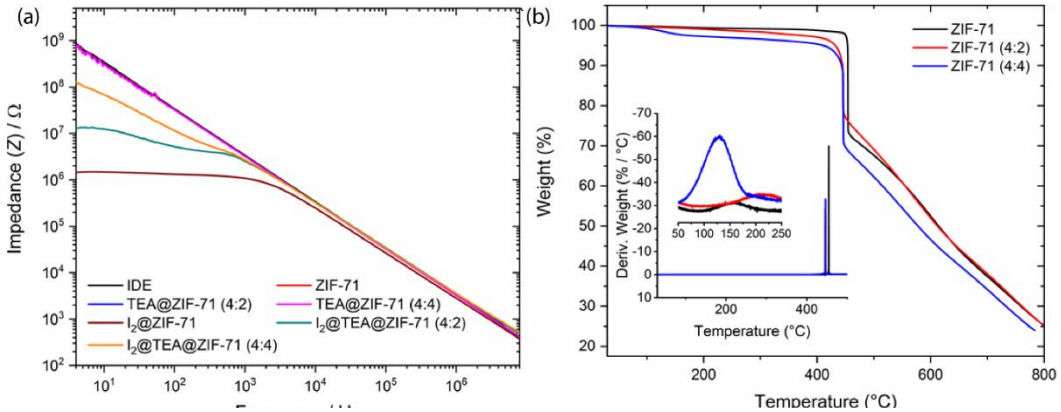

Figure 4.8: (a) Impedance as a function of frequency, showing the effect of different amount of guest encapsulation in ZIF-71 framework on iodine sensing. (b) TGA analysis to reveal the presence of triethylamine (TEA) guests in framework pores.

inside the MOF pore. In this context, the ZIF-71 MOF was chosen due to the ease of encapsulation of the triethylamine (TEA) guest molecule in the pore. From Figure 4.8, it is evident that the impedance value of ZIF-71 is much lower compared to the guest-encapsulated framework and it keeps decreasing with increased guest concentration, suggesting that the iodine inside the pore plays a major role in decreasing the impedance value. So, it can be stated that the electrical response obtained for the ZIF-70 MOF is contributed by iodine present both on the surface and inside the pores.

In a way forward, to reveal the true performance of ZIF-70 MOF, we simulated a real-time sensing environment by exposing the prototype sensor to the iodine gas at room temperature and continue collecting the sensors transient electrical response: impedance and phase angle at 10 Hz frequency as shown in the scheme of Figure 4.9 (a). The electrical response of empty IDE sensor (no MOF

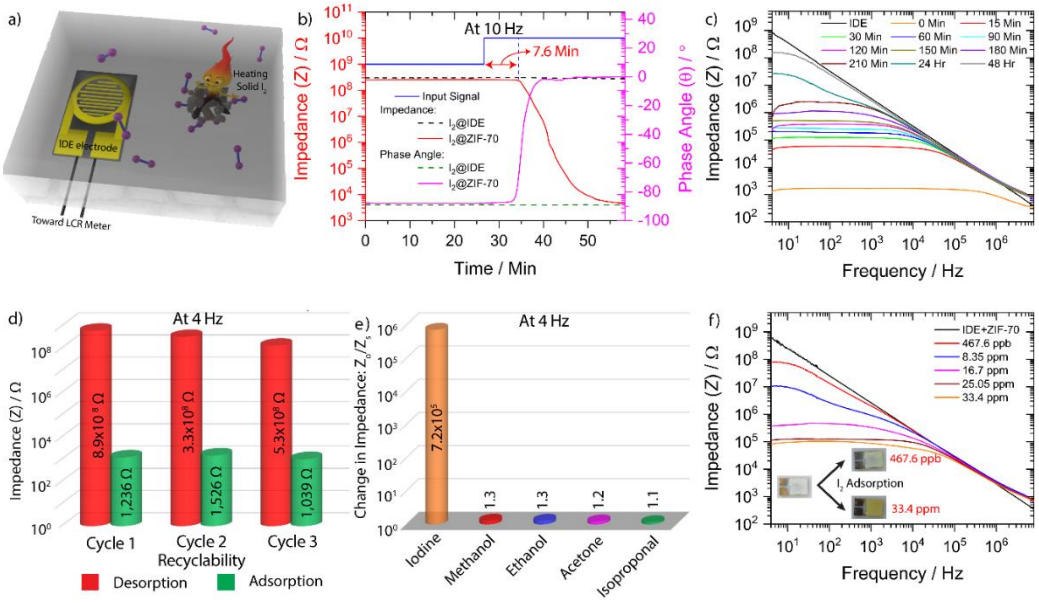

Figure 4.9: Drop-casting of ZIF-70 on IDE electrode for iodine gas sensing: (a) A scheme of real time iodine sensing setup. (b) Continuous impedance and phase angle measurements as a function of time, during iodine exposure, and (c) the effect of time-dependent iodine desorption on impedance value of ZIF-70@sensor. (d) Recyclability study of prototype sensor over several adsorption-desorption cycles. (e) The change in impedance ratio of various MOF structures after iodine adsorption. (f) The impedance sensitivity of ZIF-70 prototype sensor at different ppm levels.

coating) was also recorded for comparison, which remained unaffected by the presence of iodine gas. After iodine exposure, it takes 7.6 min to register an electrical response from the prototype sensor, which can be observed in Figure 4.9 (b). In addition to the iodine adsorption, a time-dependent iodine desorption response from ZIF-70@IDE was also measured at room temperature. It is evident from Figure 4.9 (c) that the adsorbed iodine starts to desorb from the framework structure as soon as it is removed from the iodine-rich surrounding. For

the initial first few hours the desorption rate is much higher, which decreases as a function of time. After 48 h, most of the iodine had desorbed causing a significant decrease in the impedance value, which is closer to the impedance value of iodine-free MOFs, suggesting a disruption in the percolation pathway. To further validate the sensor reversibility, the impedance measurement was carried out for ZIF-70 at 4 Hz for several iodine adsorptions (at 70 °C for 30 min) - desorption (at 70 °C for overnight) cycles, which remained quite stable and shows a highly reversible electrical response (see Figure 4.9 (d)). It further strengthens the practicability of using the ZIF-70 as a sensing material. Another important factor that can severely impact the sensor performance is its selectivity toward the targeted

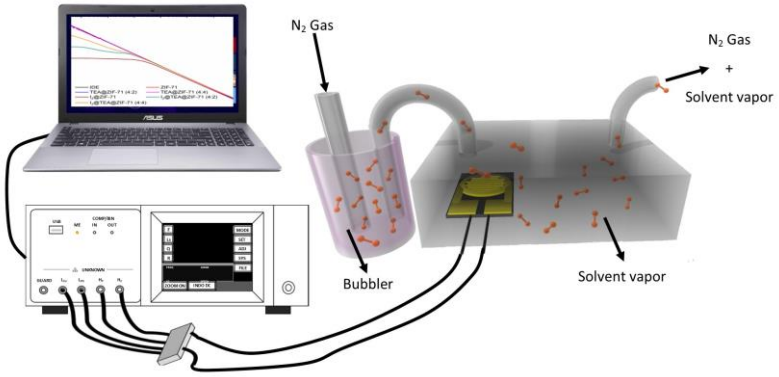

Figure 4.10: A test setup for dosing various saturated vapours onto the ZIF 70@IDE sensor.

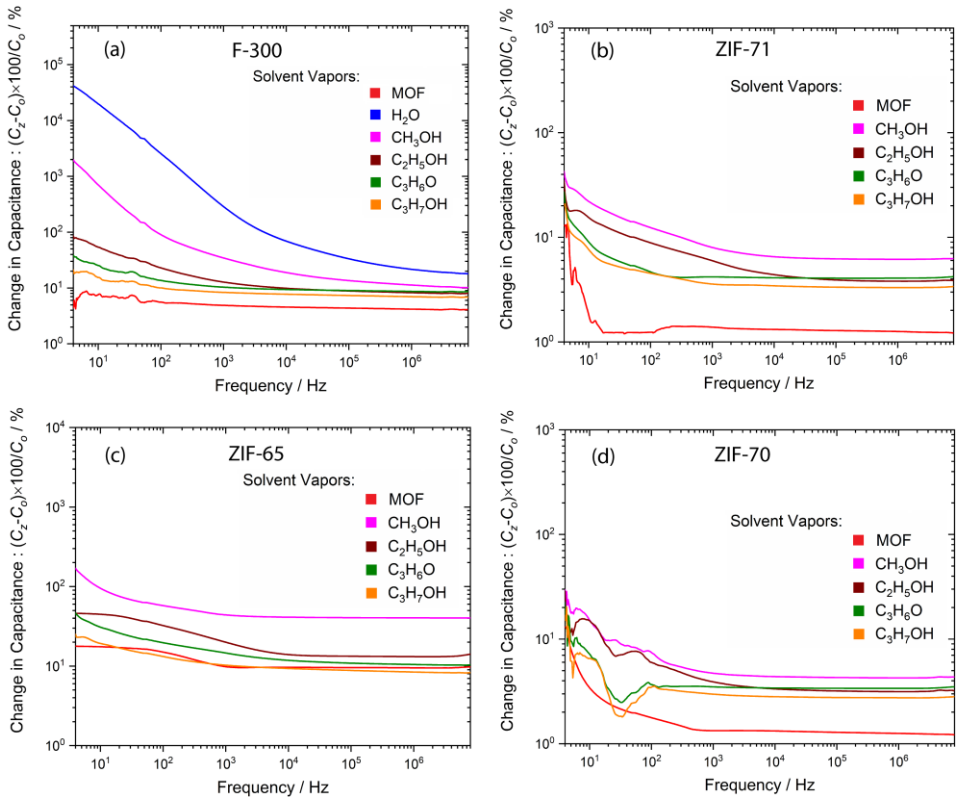

Figure 4.11: Solvent vapor dependent change in capacitance response for different MOF prototype sensors: (a) F300, (b) ZIF-71, (c) ZIF-65 and ZIF-70 MOFs.

molecule. For this purpose, we investigated hydrophilic MOF F300, hydrophobic MOF ZIF-71, ZIF-65 MOF with interaction site and ZIF-70 with optimal hydrophobic-interaction site, to determine their solvent dependent sensitivity for practical use. As shown in Figure 4.10, an enclosed chamber was specifically designed to carry out the vapor saturation study. The prototype sensors were first flushed with nitrogen gas to get rid of any moisture content and subsequently the nitrogen was flowed through the solvent-containing bubbler to form a saturated environment to carry out the electrical measurements. It was clear from Figures 4.11 and 4.12 that except for ZIF-70 (see Figure 4.9 (e)), all other MOFs

show an enhanced capacitance and impedance at lower frequencies in the presence of common solvent vapors, which will limit the iodine gas sensing under real-world applications. Furthermore, the sensitivity of a sensor is also a key criterion to evaluate its performance, which is dependent upon the adsorbent gas concentration. In this regard, we performed impedance measurements on ZIF-70 MOF at different iodine concentrations to validate its potential for sensing the ultra-trace amount of I_2 in the gas phase, evidenced in Figure 4.9 (f). It was observed that even at ppb

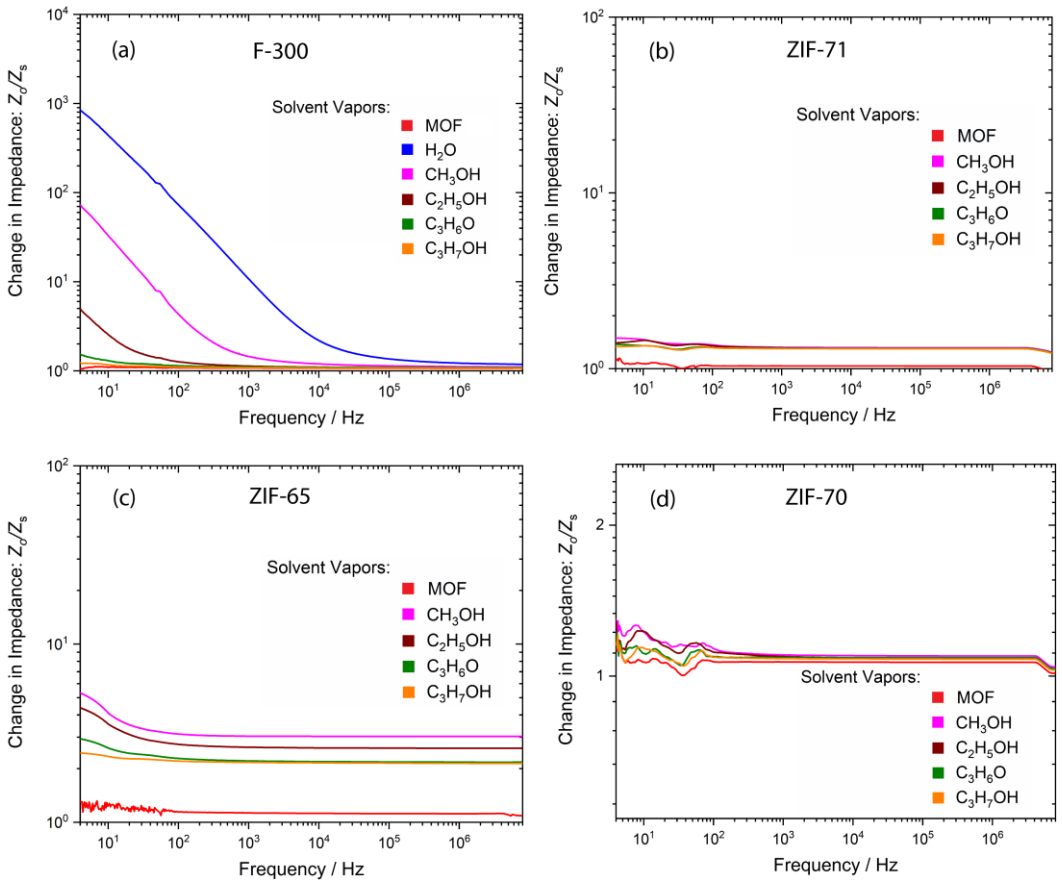

Figure 4.12: Solvent vapor dependent change in impedance response for different MOF prototype sensors: (a) F300, (b) ZIF-71, (c) ZIF-65 and ZIF-70 MOFs.

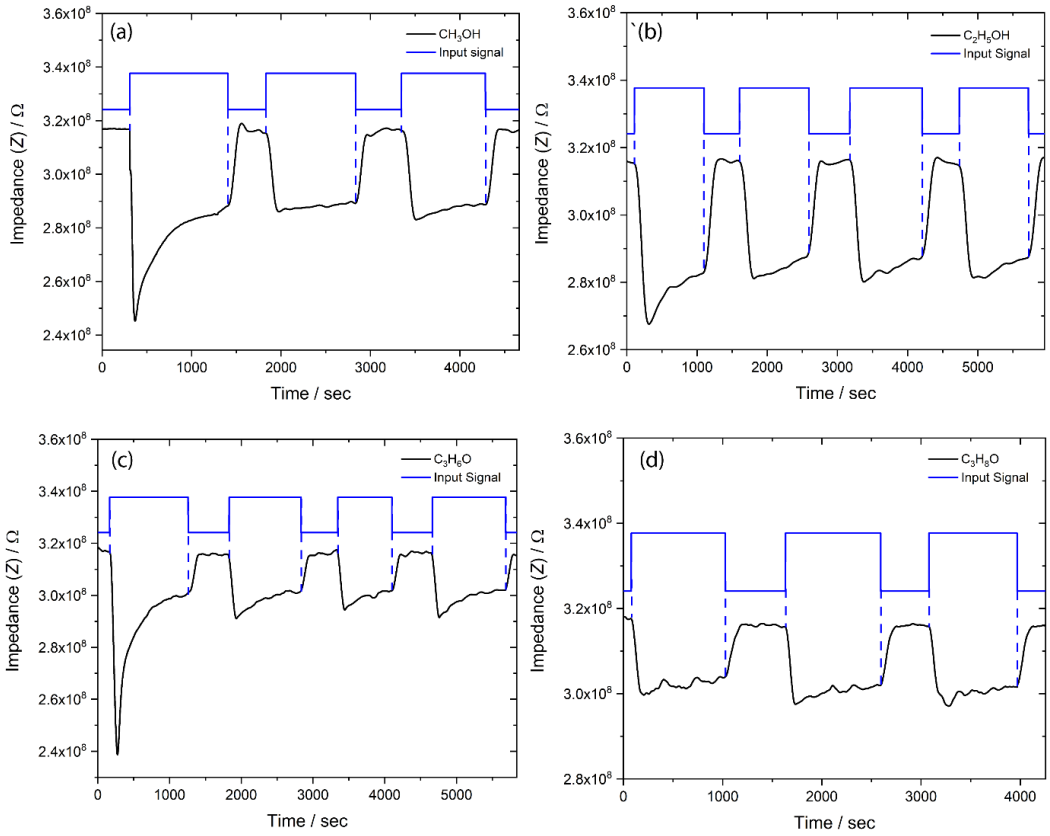

Figure 4.13: Solvent adsorption-desorption dependent cyclic impedance response for ZIF-70 MOF at 10 Hz, when exposed to (a) methanol, (b) ethanol, (c) acetone and (d) isopropanol.

level the material shows a clear transition from white to yellow color and the impedance change in ZIF-70 MOF is still significantly higher, which confirms its capability to accomplish ppb-level sensing of iodine gas and further strengthens the case for deploying ZIF-70 as an ideal iodine gas sensing material, possessing both ultra-high sensitivity and excellent selectivity. Additionally, an adsorption desorption cyclic study of solvent vapor was carried out on

ZIF 70@IDE at 10 Hz frequency to confirm the repeatability of the electrical response (see Figure 4.13).

4.6.2 Single-crystal MOF prototype sensor

For a comprehensive understanding of I_2 gas phase sensing in the ZIF-70 framework structure, we carried out the single-crystal sensing experiments by growing large single crystals of ZIF-70 (> 200 μm) on the surface of IDE sensor chip, as shown in Figure 4.14 (b). Interestingly, as compared to the drop-casted sensors, the electrical response of the prototype single-crystal (SC) sensor is lower due to the crystal thickness, which delayed the electrical response by extending the I_2 adsorption time. It was further validated by measuring the time-dependent electrical response of the crystals in the presence of gas-phase I_2, which showed a time lag in registering the response of about 13.5 min, compared to the 7 min observed for the drop-casted sensor (see Figure 4.14 (c)). The single crystal showed a negligible electrical response in-room condition, which can be attributed to the residual solvents in the pore. In the presence of iodine vapor, the single-crystal showed a remarkable increase of 0.12-million-fold in impedance ratio at 4 Hz. It was also observed that the I_2 desorption rate in the crystal is much higher than the drop-casted sensors and can be associated with the stress-induced cracks on the crystal surface. It was further supported by the reversibility experiment, in which several adsorption-desorption cycles were carried out and it showed a systemic decline in the impedance of the I_2 adsorbed sensor, suggesting a crack generated enhancement in iodine adsorption. To the best of our knowledge, we demonstrated

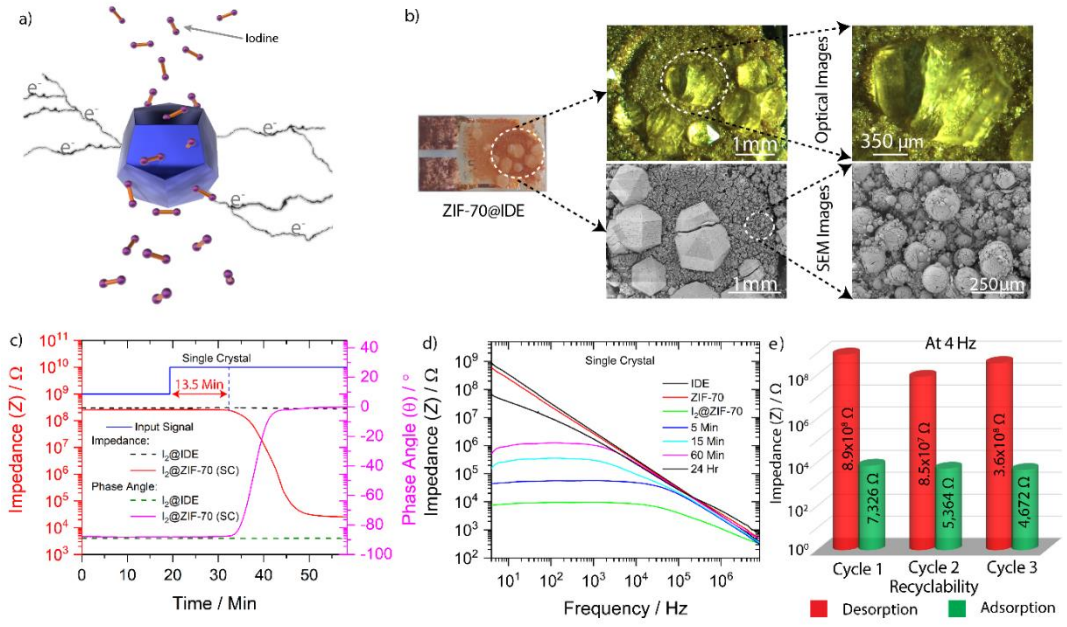

Figure 4.14: Single-crystal (SC) based iodine gas sensing of ZIF-70(SC)@IDE: (a) A scheme of increase in electron conduction in single-crystal resulted from the iodine adsorption. (b) Optical and SEM images of ZIF-70 crystals grown on IDE electrode at different magnifications. (c) A real time measurement of impedance and phase angle at 10 Hz frequency for ZIF-70 crystals, exposed to iodine gas. (d) A time-dependent desorption study of ZIF-70 crystals. (e) A cyclic adsorption and desorption data to demonstrate sensor reusability.

for the first time the gas phase sensing using MOF single crystals integrated on an IDE platform with unprecedented sensitivity.

4.6.3 Inkjet-printed MOF prototype sensor

Inkjet printing offers several benefits over the commonly used printing techniques, which include superior print resolution, higher control of drop volume, ability to deposit material in multiple layers, scalable, maskless, and additive in nature. To carry the study forward and mimic the real-time application, we standardized the thickness of the deposited MOF thin film by using the inkjet printing (IP) method. In this regard, 3 different prototype sensors were prepared by varying the number of deposited layers (1, 3 and 5 layers) of ZIF-70. As can be seen from Figures 4.15 and 4.16 (b) that unlike the 1-layer of ZIF-70, the sample with 3 layers has completely and uniformly covered the IDE sensor surface with minimum film thickness (~ 8 μm). In the presence of the I_2 gas, the electrical response from the 1-layer-ZIF-70@IDE is insignificant, whereas 3-layer ZIF-70@IDE showed a record-breaking enhancement of 1.27 million due to its full

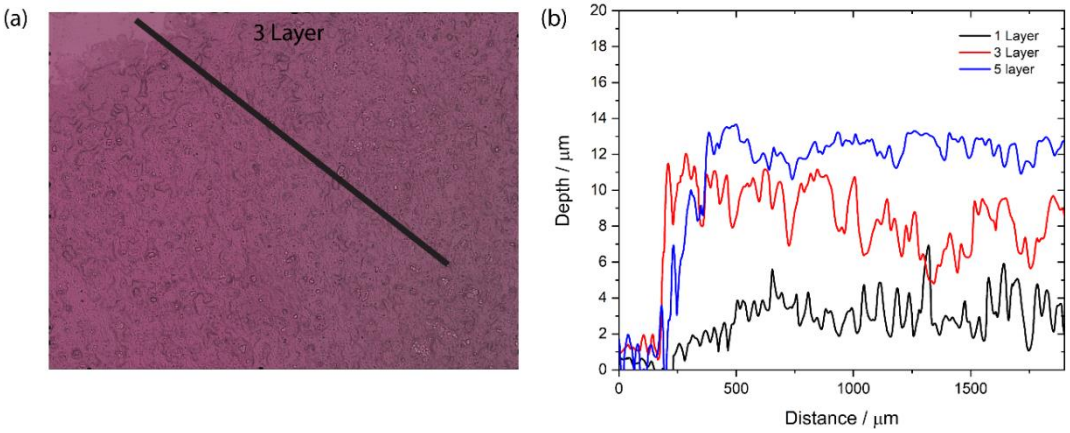

Figure 4.15: (a) 3D profilometry image of inkjet-printed ZIF-70 comprising 3- layers. (b) Height topography of inkjet-printed ZIF-70 with respect to the distance associated with the black line drawn in the relevant optical images, for samples of 1, 3, 5 layers.

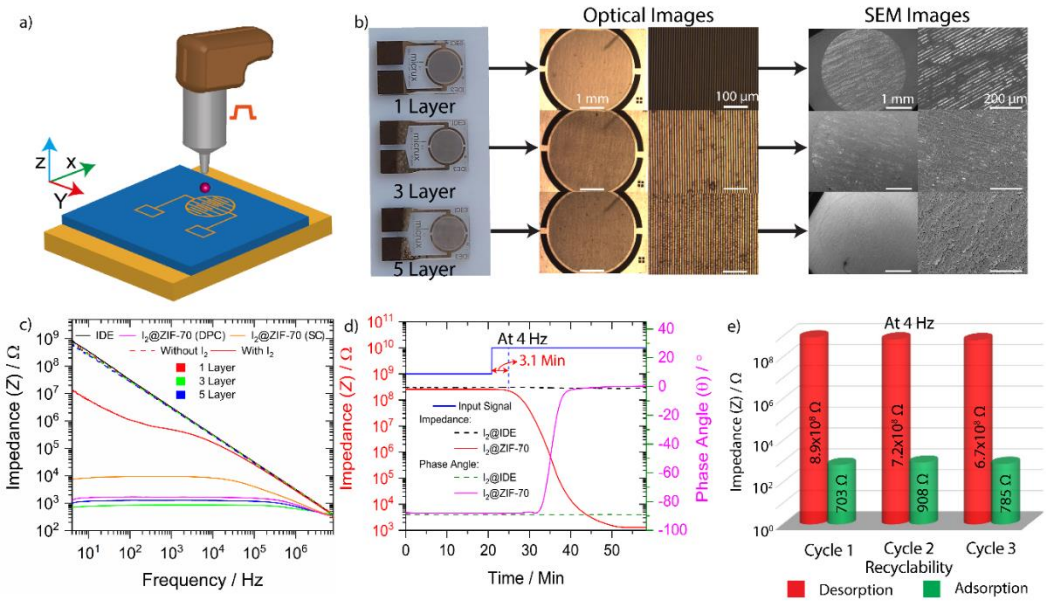

Figure 4.16: Inkjet printing (IP) of ZIF-70 on IDE electrode for iodine gas sensing: (a) An illustration of the inkjet printing technique. (b) Optical and SEM images of inkjet printed prototype IDE sensors. (c) Frequency-dependent change in impedance values for inkjet printed sensors, before and after iodine adsorption, where DPC stands for drop-casted technique and SC for single-crystal method. For 3-layer-ZIF-70@sensor: (d) A real-time transient measurement of impedance and phase angle at 10 Hz frequency, and (e) a cyclic adsorption and desorption data for testing sensor reusability at 4 Hz in AC.

coverage of IDE and minimum film thickness, which allowed the I_2 to adsorb more rapidly and efficiently. It was further supported by two experimental observations: (i) The impedance values of 5-layer ZIF-70@IDE showed a decline, which can be associated with the increased film thickness as compared to the 3-layer ZIF-70@IDE causing an increase in the adsorption time (see Figure 4.16 (c)). (ii) A time-dependent electrical response measurements of 3-layer ZIF-70@IDE,

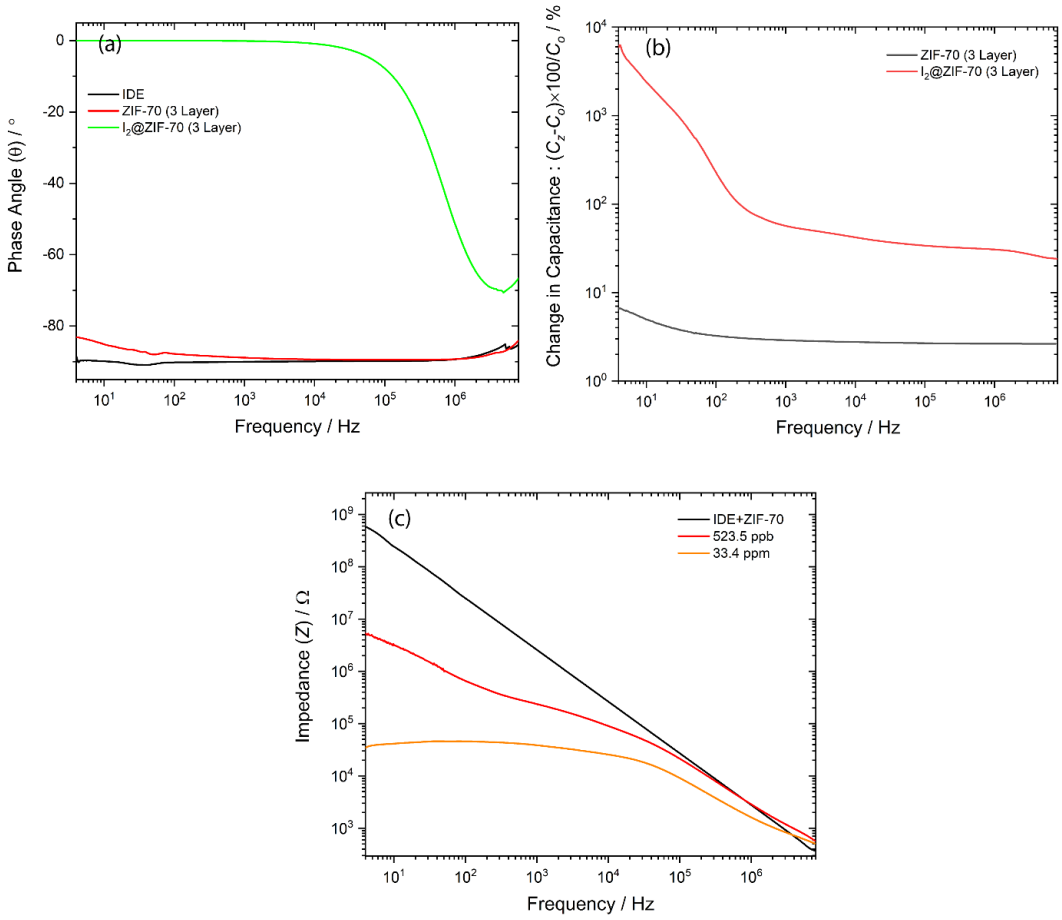

Figure 4.17: (a) Phase angle and (b) change in capacitance of 3-layer ZIF-70@MOF, before and after the iodine exposure. (c) The impedance sensitivity of 3-layer ZIF-70@MOF prototype sensor performance at ppm and ppb levels.

which showed a detection time of 3.1 min revealing its rapid and efficient I_2 adsorption (see Figure 4.16 (d)). The 3-layer ZIF-70@IDE was also examined for its reversibility by carrying out adsorption-desorption cycles showing the astonishingly stable electric response of the inkjet-printed films (see Figure 4.16 (e)). The ppb-level sensitivity of the 3-layer ZIF-70@IDE for detection of iodine gas is shown in Figure 4.17. Furthermore, the MOF film showed

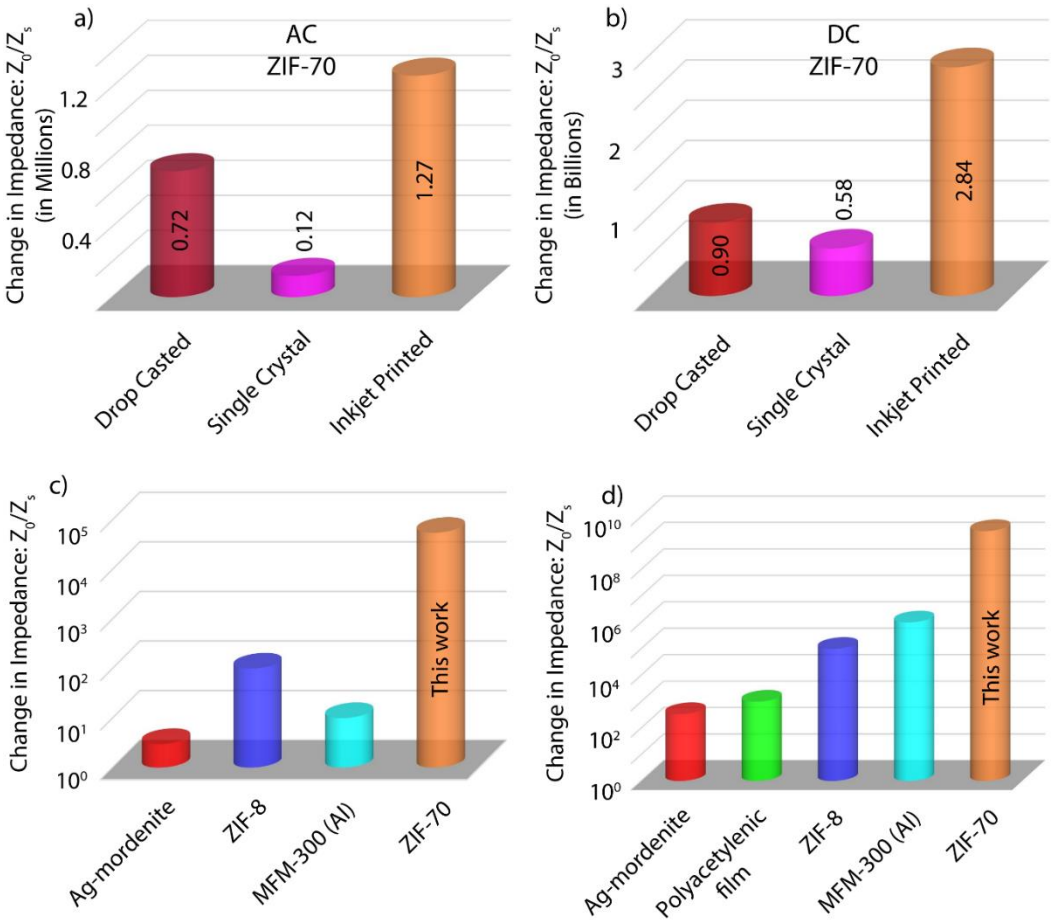

Figure 4.18: A comparative bar plot for the impedance dependent sensitivity response of drop-casted, single-crystal and inkjet-printed sensors in (a) 4 Hz alternate field (AC) and (b) direct current (DC). A comparison of sensor sensitivity between this work and the previously reported IDE-based iodine sensors performance in (c) AC at 50 Hz to emulate the Great Britain's grid frequency and (d) DC.

an astonishingly high 2.84-billionfold enhancement in the electrical response in direct current (DC), which is exceedingly higher than the drop-casted and single-crystal MOF@IDE responses (see Figure 4.18 (b)). To the best of our knowledge, this value is the highest reported enhancement in the iodine sensitivity

for both the DC and AC frequencies (see Figure 4.18 (c) and (d)), signifying a new record for the field of I_2 adsorbent sensors.[65-68]

The post-I_2 capture phase was analysed by PXRD, FTIR, Raman spectroscopy and solid-state UV-Vis (Figure 4.19 and 4.20). The structural integrity remained intact after several sensing experiments confirmed by the unaltered PXRD patterns for both powder and ZIF-70 single crystal, matching the simulated XRD pattern (see Figure 4.19 (a) and (b)). In the presence of iodine, a shift in characteristic vibrational bands of ZIF-70 MOF was also observed in the FTIR spectra (see Figures 4.19 (c) and 4.20), indicating its ultra-high sensitivity towards the detection of iodine molecules. Unlike the blue shift in IR mode at 1174 cm^{-1} (see Figure 4.20 (h)), most of the characteristic peaks show a red shift in peak positions along with peak broadening and a noticeable increase in the intensity of some vibrational bands, which are inline with literature reports. [69] The FTIR spectra were also measured for a time- and temperature-dependent iodine desorbed ZIF-70 MOF to show the reversibility of the peak shift. It suggests that the iodine confined in the framework is interacting with its surroundings and forming a percolation network, causing a decrease in the overall impedance. The Raman spectra were also recorded to confirm the existence of the iodine species. Two distinct vibrations were observed for the iodine adsorbed ZIF-70 MOF, which are not present in its pristine state (see Figure 4.19 (d)). The Raman peak at 112 cm^{-1} was associated with the existence of the polyiodide, whereas another peak at 166 cm^{-1} was ascribed to the weakly coordinated iodine.[70, 71] The underlying higher area of 166 cm^{-1} peaks over

its counterpart suggests that iodine is present in the solid form rather than the ionized form. For bandgap calculation, the absorbance spectra for ZIF-70 MOF were obtained from the UV-Vis spectrophotometry and were transformed to optical band gaps employing the Kubelka–Munk (KM) method. The presence of iodine in the pore channels causes a significant reduction in the framework bandgap from 2.78 eV (pristine ZIF-70) to 1.35 eV (I_2@ZIF-70), which can be seen in the inset of Figure 4.19 (e), further substantiating the observed decrease of impedance in the prototype MOF@IDEs described above.

In this chapter, for a highly selective and ultra-trace sensitive electrical sensing of iodine gas, we provided a mechanism to identify the properties in a material with suitable functionalities to meet this task. The performance of the MOF@IDE here challenges the existing iodine sensing technologies by demonstrating a highly selective and even ultra-trace ppb-level sensing with outstanding precision, both at lower and higher frequencies (<60 Hz), making it suitable for easy integration to the AC electronics at 50 Hz frequency. This breakthrough was achieved by optimizing the level of hydrophilicity-hydrophobicity in the material in addition to leveraging the suitable interaction sites. The mechanism is that the optimized hydrophilicity-hydrophobicity level will facilitate an uninterrupted migration of the inbound target gas species through the pore channels, and the suitable interaction sites will act as a temporary anchor point

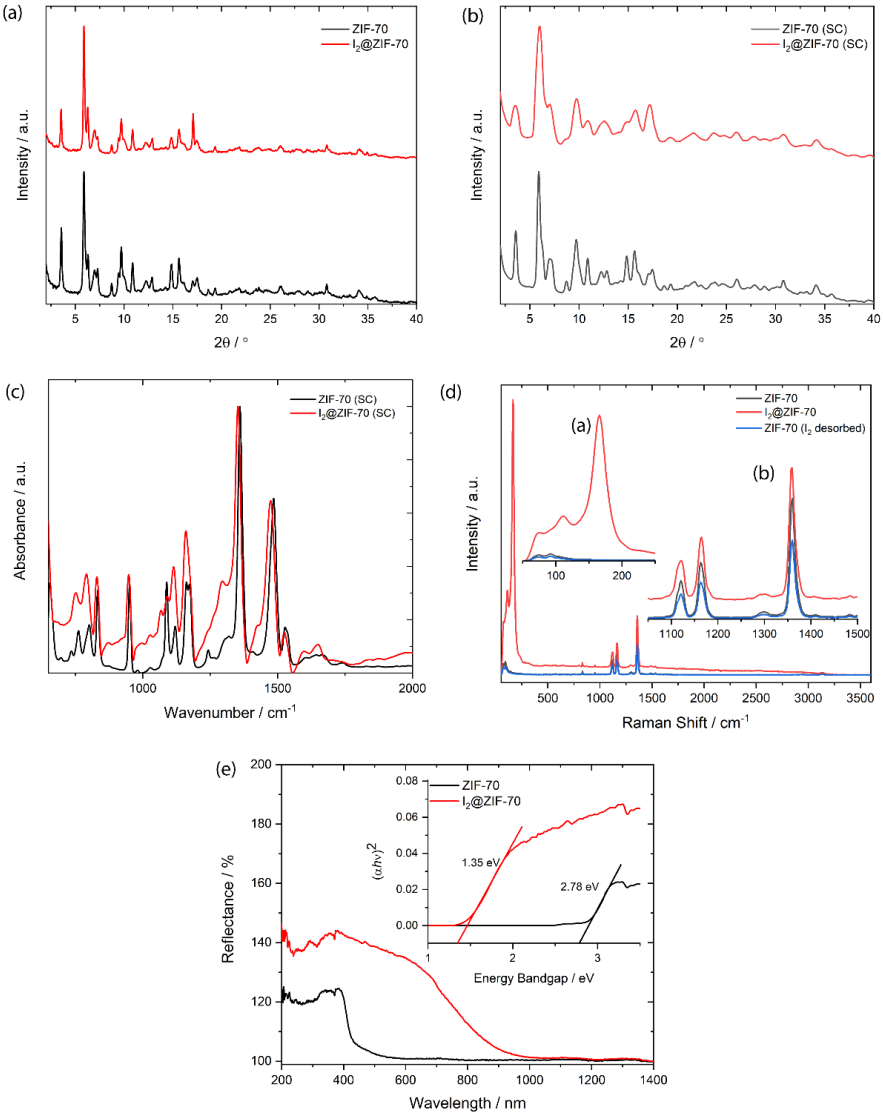

Figure 4.19: Material characterisation of ZIF-70 MOF, before and after iodine exposure: XRD patterns of (a) powder and (b) single crystal of ZIF-70. (c) FTIR spectrum of ZIF-70 single crystal, and (d) Raman spectra of ZIF-70 powders. (e) UV adsorption spectrum of ZIF 70 powders with an inset of bandgaps estimated from KM method.

to hold the gas molecules in place for the time being. In the wider perspective, our work opens the door for the next-generation electrical gas sensors focusing on optimal hydrophobicity and interaction sites. The deployment of such sensing

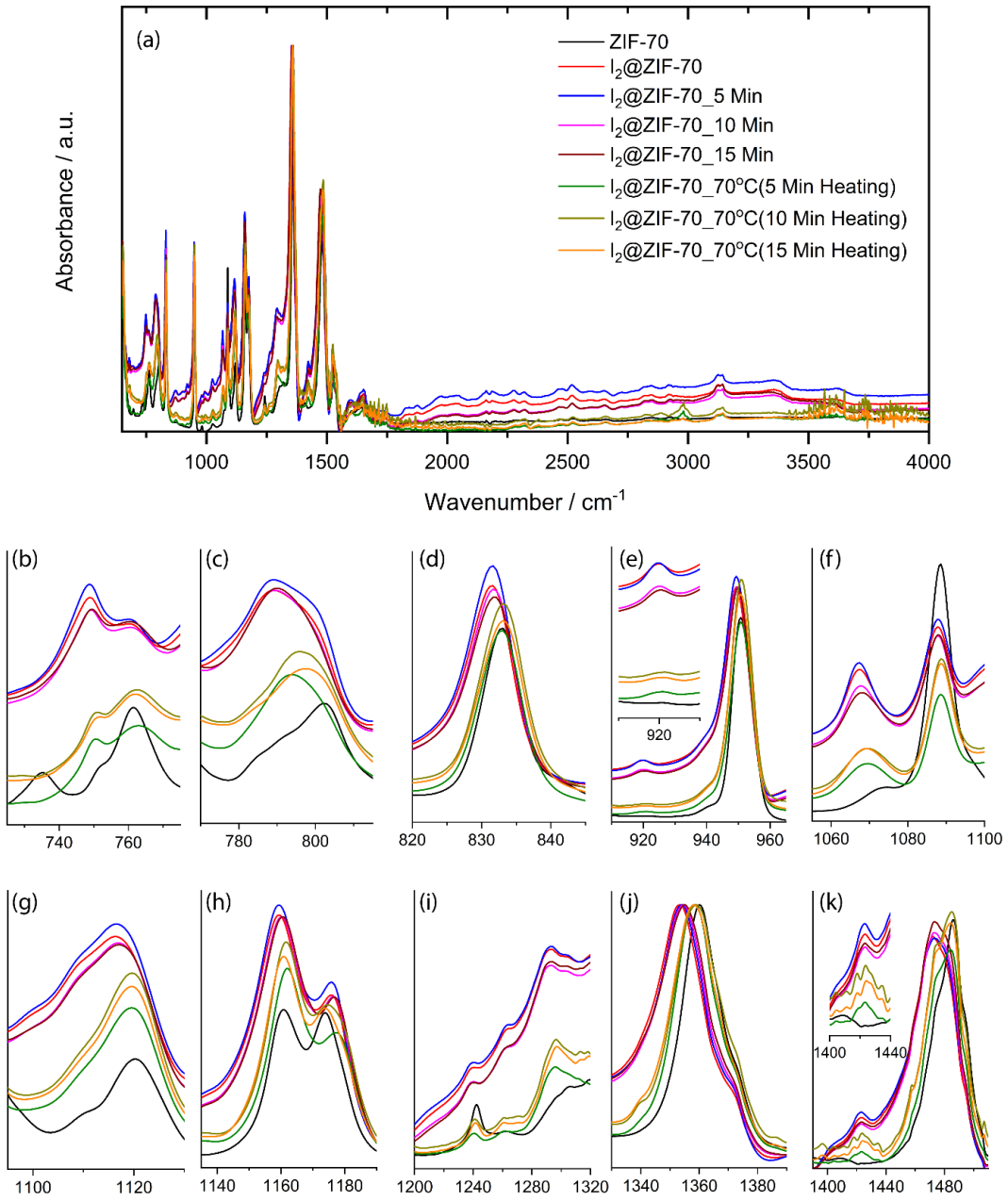

Figure 4.20: Time- and temperature-dependent iodine adsorption and desorption analysis for ZIF-70 MOF using ATR-FTIR spectroscopy.

technology could prevent accidents by selectively determining the ultra-trace amount of harmful substances in the environment, thereby robustly and reversibly meeting the ever-increasing demand in the field of the advanced sensor. We show

the fabrication of MOF films using the inkjet printing approach helps to tailor and significantly boost the IDE sensor performance.

"You cannot teach a man anything; you can only help
him discover it in himself."

– Galileo

5

Conclusions and Future Outlooks

The thesis is focused on the interlayer dielectrics (ILD) and novel sensing applications by harnessing both the electrical and dielectric properties of MOF materials. The physical and chemical insights gained from the results presented in Part 1 of the thesis can be extended to develop a varied range of MOF based devices and potentially for future engineering of applications as per industrial requirements.

- Understanding the impact of external stimuli, such as applied mechanical stress and operating temperature on MOF properties in broadband frequency range provides a safeguard against unforeseen circumstances, which will ensure the reliable performance of the functional devices.
- The in-depth studies of host-guest interactions in polycrystalline and single-crystal systems enable the general understanding of the intrinsic properties of MOF structures.

- The high porosity and tailorability of the MOF structures make them an ideal candidate for capturing the targeted gas species selectively, which can be exploited to yield inexpensive and easy-to-use electrical sensors for gas-phase detection.

This chapter provides an intertwining conclusion made throughout this thesis. The main purpose is to overview the findings and novelty of the research and present prospective areas in which the work could be advanced in the future. Chapter 2 has identified the existing challenges and gaps in the knowledge of the scientific community to fully realize the potential of MOFs as an interlayer dielectric, in which the case studies encompass the well-known HKUST-1 and MIL-100 frameworks. The studies were focused on several operating parameters that can impact the low-dielectric performance of the frameworks in a vast broadband frequency range (Hz to THz). It was shown that the dielectric properties of MOFs can be tailored according to the application requirements, by varying stress levels, operating temperature, and host-guest interaction. The results elucidate the significant effect of framework amorphization, structural deformation and densification, which are closely associated with the overall free volume and framework polarizability. In addition to the HKUST-1, the effect of amorphization on dielectric response was further contrasted using the Basolite F300 and MIL-100 (Fe) frameworks obtained *via* different processing techniques and studied at different states from crystalline to amorphous phase. Multiple dielectric mechanisms and polarization processes that are present in the MOF structure can

be triggered using different frequencies. The individual contribution from these different polarisation mechanisms (dipole orientation, phonon (THz modes), and electronic polarization) was quantified and reported, which can be seen in detail in Papers I and II. Interestingly, it was observed that, unlike the near-IR region, the dielectric response of the framework correlates well with the MOF microstructure, suggesting its dependency on the underlying framework structure. These experimental findings were further supported by the pressure-dependent DFT calculations of an ideal HKUST-1 structure, revealing the structure-property relationships. It was also confirmed that the guest molecules play an adverse role in the dielectric response at lower frequencies, and they should be eliminated by appropriate material activation techniques (without inducing framework collapse) to realize its full potential as an interlayer dielectric.

Chapter 3 explores the tuneability of the polycrystalline and single-crystal HKUST-1 MOF properties, focusing on the impact of host-guest interactions. The result laid out in this chapter evidenced that the MOFs' electrical and dielectric properties can be tailored and used to detect the targeted guest species. The polycrystalline HKUST-1 was synthesised using two different routes to yield a porous and a guest-encapsulated framework material. It was determined from the measurements and analysis that the low-dielectric constant values of the framework are its intrinsic properties and, can be modified through precise adjustments in the frequency, operating temperature, and applied stress. It was revealed that guest encapsulation enhances the mechanical properties by increasing the yield strength and structural stability of the framework against (irreversible) plastic deformation.

These are important findings that pave the way for molecular-level vapour phase detection using the HKUST-1 MOF acting as a single-crystal sensor. It offered the potential of measuring the transient dielectric response in the presence of different guest molecules and reveal that the dielectric response of MOF crystals can considerably be altered by host-guest interactions (at open metal sites or ligands) *via* hydrophobic-hydrophilic interactions, and by harnessing guest molecular size effect and guests clustering attributed to nanoscale confinement in the pores.

Finally, Chapter 4 presented a comprehensive study on MOF based gas-phase sensors by utilising the knowledge gained from studies summarised above. For a highly selective and ultra-trace sensitive electrical sensing of iodine gas, we provided a mechanism to identify the properties in a material with suitable functionalities for this demanding task. The performance of the MOF@IDE sensor here challenges the existing iodine sensing technologies by demonstrating a highly selective and even ultra-trace ppb-level sensing with outstanding precision, both at lower and higher frequencies (DC-AC, 0-50 Hz), making it suitable for easy integration to the AC electronics operating at 50 Hz frequency. This breakthrough was achieved by optimising the level of hydrophilicity-hydrophobicity in the MOF material in addition to leveraging the suitable interaction sites. The mechanism is that the optimised hydrophilicity-hydrophobicity level will facilitate an uninterrupted migration of the inbound target I_2 gas species through the pore channels, and the suitable interaction sites will act as a temporary anchor point to hold the gas molecules in place for reversible sensing to occur. In the wider

perspective, our work opens the door for the next-generation electrical gas sensors with the focus on optimal hydrophobicity and interaction sites for use in hazard protection and environmental sustainability. It was demonstrated that the inkjet printing of MOF films holds promise for fabricating revolutionary sensors with a record-breaking performance.

The extent of topics explored in this thesis notably, the fundamental understanding of the factors contributing to the electric and dielectric properties, the possibility of tuning these factors for both polycrystalline and single-crystal MOFs, utilizing the high adsorption capacity of MOFs for electrical sensing purposes, and a mechanism to identify the functionalities in the material for a specific practical assignment. Therefore, this thesis shows the potential of the MOF materials by contributing to the future development of MOF based interlayer dielectrics, which is central to the miniaturisation of the next-generation devices and provided a real-world application in form of a highly compacted gas-phase iodine sensor. The MOF has been extensively studied in the last decade, however, the expertise in utilising their electrical and dielectric properties for various real-time applications remain scarce. To effectively utilise the results presented in the thesis, a future investigation on hydrophobic MOFs and their processing on a range of technical substrates is required for both interlayer dielectric and sensor applications. The methods and techniques used to study the MOFs in this thesis can be further explored for other polycrystalline and single crystal MOF systems to gain an in-depth understanding of external stimuli dependent alterations to electrical and

dielectric properties at the broadband frequency range, employing multimodal characterisation techniques. For an industrial application, the material properties must not alter over time with relative humidity, temperature (up to 425 °C) and are compatible with existing chip processing workflow. These are grand challenges yet to be overcome by the family of MOF materials to date. The formation of defect-free MOF thin films and their compatibility with the substrate is a key component in MOF processing, which can be achieved through precise control over the microstructure, coating techniques, film-substrate interface interaction etc. The compatibility between the MOF and substrate can be enhanced by chemical modification but it can lead to framework degradation or guest encapsulation in the pores and channels. Porosity plays a key role in decreasing the materials dielectric constant and an in-depth analysis on individual contribution of inter and intraparticle porosity in MOFs has not been done yet. To this end, more in-depth studies are needed in this area. As these challenges are addressed in follow-on studies, the new findings will enrich understanding of the scientific community and will open new avenues in MOF research i.e., low-loss dielectric resonators for THz wireless communication and tuneable dielectrics for microelectronics.

References

1. M. Xie; M. Li; Q. Sun; W. Fan; S. Xia; W. Fu, Research progress on porous low dielectric constant materials. *Mater. Sci. Semicond. Process.* **2021**, 106320.

2. B. D. Hatton; K. Landskron; W. J. Hunks; M. R. Bennett; D. Shukaris; D. D. Perovic; G. A. Ozin, Materials chemistry for low-k materials. *Mater. Today* **2006,** *9* (3), 22-31.

3. D. Shamiryan; T. Abell; F. Iacopi; K. Maex, Low-k dielectric materials. *Mater. Today* **2004,** *7* (1), 34-39.

4. L. E. Kreno; K. Leong; O. K. Farha; M. Allendorf; R. P. Van Duyne; J. T. Hupp, Metal-organic framework materials as chemical sensors. *Chem. Rev.* **2012,** *112* (2), 1105-1125.

5. J. Rocha; L. D. Carlos; F. A. A. Paz; D. Ananias, Luminescent multifunctional lanthanides-based metal–organic frameworks. *Chem. Soc. Rev.* **2011,** *40* (2), 926-940.

6. J. F. Olorunyomi; S. T. Geh; R. A. Caruso; C. M. Doherty, Metal–organic frameworks for chemical sensing devices. *Mater. Horiz.* **2021,** *8* (9), 2387-2419.

7. L. T. Zhang; Y. Zhou; S. T. Han, The role of metal-organic frameworks in electronic sensors. *Angew. Chem.* **2021,** *60* (28), 15192–15212.

8. S. Kawata; S. Kitagawa; H. Kumagai; C. Kudo; H. Kamesaki; T. Ishiyama; R. Suzuki; M. Kondo; M. Katada, Rational design of a novel intercalation system. Layer-gap control of crystalline coordination polymers,{[Cu

$(CA)(H_2O)_m](G)\}_n$ (m=2, G=2, 5-dimethylpyrazine and phenazine; m=1, G=1, 2, 3, 4, 6, 7, 8, 9-octahydrophenazine). *Inorg. Chem.* **1996,** *35* (15), 4449-4461.

9. A. C. Fischer-Cripps, The 2nd Edition Materials Physics Companion. 2015.

10. V. F. Lvovich, Impedance spectroscopy: Applications to electrochemical and dielectric phenomena. John Wiley & Sons: 2012.

11. R. Freund; S. Canossa; S. M. Cohen; W. Yan; H. Deng; V. Guillerm; M. Eddaoudi; D. G. Madden; D. F. Jimenez; H. Lyu; L. K. Macreadie; Z. Ji; Y. Zhang; B. Wang; F. Haase; C. Wöll; O. Zaremba; J. Andreo; S. Wuttke; C. S. Diercks, 25 Years of reticular chemistry. *Angew. Chem. Int. Ed.* **2021,** *60* (45), 23946-23974.

12. K. Zagorodniy, K.; g. Seifert, G.; H. Hermann, H. J. A. P. L., Metal-organic frameworks as promising candidates for future ultralow-k dielectrics. *Appl. Phys. Lett.* **2010,** *97* (25), 251905.

13. L. M. Yang; P. Vajeeston; P. Ravindran; H. Fjellvag; M. Tilset, Theoretical investigations on the chemical bonding, electronic structure, and optical properties of the metal−organic framework MOF-5. *Inorg. Chem.* **2010,** *49* (22), 10283-10290.

14. L. M. Yang; P. Ravindran; M. Tilset, Solid-state structure and calculated electronic structure, formation energy, chemical bonding, and optical properties of ZN_4O $(FMA)_3$ and its heavier congener Cd_4O $(FMA)_3$. *Inorg. Chem.* **2013,** *52* (8), 4217-4228.

15. C. H. Hendon; A. Walsh; M. Dincă, Frontier orbital engineering of metal–organic frameworks with extended inorganic connectivity: Porous alkaline-earth oxides. *Inorg. Chem.* **2016,** *55* (15), 7265-7269.

16. B. Ni; X. Cai; J. Lin; Y. Li; S. Huang; Z. Li; Y. Zhang, Tailoring the linear and second-order nonlinear optical responses of the titanium-MIL-125 metal–organic framework through ligand functionalization: a first principles study. *J. Phys. Chem. C* **2018,** *123* (1), 653-664.

17. B. Ni; W. Sun; J. Kang; Y. Zhang, Understanding the linear and second-order nonlinear optical properties of UiO-66-derived metal–organic frameworks: A comprehensive DFT study. *J. Phys. Chem. C* **2020,** *124* (21), 11595-11608.

18. S. Mendiratta; M. Usman; C. C. Chang; Y. C. Lee; J. W. Chen; M. K. Wu; Y. C. Lin; C. P. Hsu; K. L. Lu, Zn (ii)-based metal–organic framework: an exceptionally thermally stable, guest-free low dielectric material. *J. Mater. Chem. C* **2017,** *5* (6), 1508-1513.

19. J. Gascon; M. D. Hernández-Alonso; A. R. Almeida; G. P. van Klink; F. Kapteijn; Mul, G., Isoreticular MOFs as efficient photocatalysts with tunable band gap: An operando FTIR study of the photoinduced oxidation of propylene. *Chemsuschem* **2008,** *1* (12), 981-983.

20. M. R. Ryder; L. Donà; J. G. Vitillo; B. Civalleri, Understanding and controlling the dielectric response of metal–organic frameworks. *Chempluschem* **2018,** *83* (4), 308-316.

21. L. Cheng; P. Yan; X. Yang; H. Zou; H. Yang; H. Liang, Microstructure controlling and dielectric relaxation dynamic of ZIF-8 synthesized in different solvents. *Mater. Chem. Phys.* **2020,** *247*, 122869.

22. W. J. Li; J. Liu; Z. H. Sun; T. F. Liu; J. Lu; S. Y. Gao; C. He; R. Cao; J. H. Luo, Integration of metal-organic frameworks into an electrochemical dielectric thin film for electronic applications. *Nat. Commun.* **2016,** *7*, 11830.

23. S. Eslava; J. Urrutia; A. N. Busawon; M. R. Baklanov; F. Iacopi; S. Aldea; K. Maex; J. A. Martens; C. E. Kirschhock, Zeolite-inspired low-k dielectrics overcoming limitations of zeolite films. *J. Am. Chem. Soc.* **2008,** *130* (51), 17528-17536.

24. S. Eslava; L. Zhang; S. Esconjauregui; J. Yang; K. Vanstreels; M. R. Baklanov; E. Saiz, Metal-organic framework ZIF-8 films as low-κ dielectrics in microelectronics. *Chem. Mater.* **2013,** *25* (1), 27-33.

25. M. Krishtab; I. Stassen; T. Stassin; A. J. Cruz, A.; O. O. Okudur; S. Armini; C. Wilson; S. De Gendt; R. Ameloot, Vapor-deposited zeolitic imidazolate frameworks as gap-filling ultra-low-κ dielectrics. *Nat. Commun.* **2019,** *10* (1), 1-9.

26. K. Titov; Z. Zeng; M. R. Ryder; A. K. Chaudhari; B. Civalleri; C. S. Kelley; M. D. Frogley; G. Cinque; J. C. Tan, Probing dielectric properties of metal–organic frameworks: MIL-53 (Al) as a model system for theoretical predictions and experimental measurements via synchrotron far-and mid-infrared spectroscopy. *J. Phys. Chem. Lett.* **2017,** *8* (20), 5035-5040.

27. M. R. Ryder; Z. Zeng; K. Titov; Y. Sun; E. Mahdi; I. Flyagina, I.; T. D. Bennett; B. Civalleri; C. S. Kelley; M. D. Frogley, Dielectric properties of zeolitic imidazolate frameworks in the broad-band infrared regime. *J. Phys. Chem. Lett.* **2018,** *9* (10), 2678-2684.

28. D. Edelstein; J. Heidenreich; R. Goldblatt; W. Cote; C. Uzoh; N. Lustig; P. Roper; T. McDevitt; W. Motsiff; A. Simon, Full copper wiring in a sub-0.25/spl mu/m CMOS ULSI technology, International Electron Devices Meeting. IEDM Technical Digest, IEEE: 1997; pp 773-776.

29. The international technology roadmap for semiconductor 2.0. https://www.semiconductors.org/wp-content/uploads/2018/06/6_2015-ITRS-2.0_Interconnect.pdf.

30. P. R. Griffiths; J. M. Chalmers, *Handbook of vibrational spectroscopy*. Wiley Online Library: 2002.

31. B. E. Souza; A. F. Möslein; K. Titov; J. D. Taylor; S. Rudic; J. C. Tan, Green reconstruction of MIL-100 (Fe) in water for high crystallinity and enhanced guest encapsulation. *ACS Sustain. Chem. Eng.* **2020,** *8* (22), 8247-8255.

32. S. Mendiratta; M. Usman; T. W. Tseng; T. T. Luo; S. F. Lee; L. Zhao; M. K. Wu; M. M. Lee; S. S. Sun; Y. C. Lin, Low dielectric behavior of a robust, guest-free magnesium(II)–organic framework: A potential application of an alkaline-earth metal Compound. *Eur. J. Inorg. Chem.* **2015,** *2015* (10), 1669-1674.

33. S. Mendiratta; M. Usman; C. C. Chang; Y. C. Lee; J. W. Chen; M. K. Wu; Y. C. Lin; C. P. Hsu; K. L. Lu, Zn(ii)-based metal–organic framework: An

exceptionally thermally stable, guest-free low dielectric material. *J. Mater. Chem. C* **2017,** *5* (6), 1508-1513.

34. C. Xue; Z. Y. Yao; S. X. Liu; H. B. Luo; Y. Zou; L. Li; X. M. Ren, Dielectric anomaly and relaxation natures in a Zn-Cr pillar-layered metal-organic framework with cages and channels. *J. Solid State Chem.* **2017,** *250*, 107-113.

35. S. Mendiratta; M. Usman; T. T. Luo; S. F. Lee; Y. C. Lin; K. L. Lu, Guest dependent dielectric properties of nickel(II)-based supramolecular networks. *CrystEngComm* **2014,** *16* (28), 6309-6315.

36. M. Usman; C. H. Lee; D. S. Hung; S. F. Lee; C. C. Wang; T. T. Luo; L. Zhao; M. K. Wueg; K. L. Lu, Intrinsic low dielectric behaviour of a highly thermally stable Sr-based metal-organic framework for interlayer dielectric materials. *J. Mater. Chem. C* **2014,** *2* (19), 3762-3768.

37. A. I. Inamdar; A. Pathak; M. Usman; K. R. Chiou; P. H. Tsai; S. Mendiratta; S. Kamal; Y. H. Liu; J. W. Chen; M. H. Chiang, Highly hydrophobic metal–organic framework for self-protecting gate dielectrics. *J. Mater. Chem. A* **2020,** *8* (24), 11958-11965.

38. S. Eslava; M. R. Baklanov; A. V. Neimark; F. Iacopi; C. E. Kirschhock; K. Maex; J. A. Martens, Evidence of large voids in pure-silica-zeolite low-*k* dielectrics synthesized by spin-on of nanoparticle suspensions. *Adv. Mater.* **2008,** *20* (16), 3110-3116.

39. W. Zhan; Y. He; J. Guo; L. Chen; X. Kong; H. Zhao; Q. Kuang; Z. Xie; L. Zheng, Probing the structural flexibility of MOFs by constructing metal oxide@

MOF-based heterostructures for size-selective photoelectrochemical response. *Nanoscale* **2016,** *8* (27), 13181-13185.

40. Y. Tian; A. Stroppa; Y. Chai; L. Yan; S. Wang; P. Barone; S. Picozzi; Y. Sun, Cross coupling between electric and magnetic orders in a multiferroic metal-organic framework. *Sci. Rep.* **2014,** *4*, 6062.

41. R. J. Sension; H. L. Strauss, Comparison of experiment and theory for the resonance Raman spectrum of I_2 in solution. IV. Band shapes and hot bands. *J. Chem. Phys.* **1988,** *88* (4), 2289-2295.

42. World Energy Needs and Nuclear Power. https://www.world-nuclear.org/information-library/current-and-future-generation/world-energy-needs-and-nuclear-power.aspx.

43. G. Cicia; L. Cembalo; T. Del Giudice; A. Palladino, Fossil energy versus nuclear, wind, solar and agricultural biomass: Insights from an Italian national survey. *Energy Policy* **2012,** *42*, 59-66.

44. P. A. Kharecha; J. E. Hansen, Prevented mortality and greenhouse gas emissions from historical and projected nuclear power. *J. Environ. Sci. Technol.* **2013,** *47* (9), 4889-4895.

45. Y. H. Abdelmoaty; T. D. Tessema; F. A. Choudhury; O. M. El-Kadri; H. M. El-Kaderi; interfaces, Nitrogen-rich porous polymers for carbon dioxide and iodine sequestration for environmental remediation. *ACS Appl. Mater. Interfaces* **2018,** *10* (18), 16049-16058.

46. A. R. Brosi; T. W. DeWitt; H. Zeldes, Decay of 8-day iodine 131 to a metastable state of xenon 131. *Phys. Rev.* **1949,** *75* (10), 1615.

47. R. Edwards, Iodine-129: Its occurrenice in nature and its utility as a tracer. *J. Sci.* **1962,** *137* (3533), 851-853.

48. J. Robbins, J.; A. B. Schneider, A. B., Thyroid cancer following exposure to radioactive iodine. *Rev. Endocr. Metab. Disord.* **2000,** *1* (3), 197-203.

49. J. E. Ten Hoeve; M. Z. Jacobson, Worldwide health effects of the Fukushima Daiichi nuclear accident. *Energy Environ. Sci.* **2012,** *5* (9), 8743-8757.

50. W. P. Lustig; S. Mukherjee; N. D. Rudd; A. V. Desai; J. Li; S. K. Ghosh, Metal-organic frameworks: Functional luminescent and photonic materials for sensing applications. *Chem. Soc. Rev.* **2017,** *46* (11), 3242-3285.

51. L. Huang; Z. Wang; X. Zhu; L. Chi, Electrical gas sensors based on structured organic ultra-thin films and nanocrystals on solid state substrates. *Nanoscale Horiz* **2016,** *1* (5), 383-393.

52. H. Yuan; J. Tao; N. Li; A. Karmakar; C. Tang; H. Cai; S. J. Pennycook; N. Singh; D. Zhao, On-chip tailorability of capacitive gas sensors integrated with metal-organic framework films. *Angew. Chem.* **2019,** *131* (40), 14227-14232.

53. H. Deng; S. Grunder; K. E. Cordova; C. Valente; H. Furukawa; M. Hmadeh; F. Gándara; A. C. Whalley; Z. Liu; S. Asahina, Large-pore apertures in a series of metal-organic frameworks. *J. Sci.* **2012,** *336* (6084), 1018-1023.

54. H. Furukawa; K. E. Cordova; M. O. Keeffe; O. M. Yagi, The chemistry and applications of metal-organic frameworks. *Sci.* **2013,** *341* (6149), 1230444.

55. O. K. Farha; A. O. Yazaydın; I. Eryazici; C. D. Malliakas; B. G. Hauser; M. G. Kanatzidis; S. T. Nguyen; R. Q. Snurr; J. T. Hupp, De novo synthesis of a

metal–organic framework material featuring ultrahigh surface area and gas storage capacities. *Nat. Chem.* **2010,** *2* (11), 944-948.

56. Z. Wang; S. M. Cohen, Postsynthetic modification of metal–organic frameworks. *Chem. Soc. Rev.* **2009,** *38* (5), 1315-1329.

57. L. E. Kreno; K. Leong; O. K. Farha; M. Allendorf; R. P. Van Duyne; J. T. Hupp, Metal–organic framework materials as chemical sensors. *Chem. Rev.* **2012,** *112* (2), 1105-1125.

58. M. He; J. Yao; Q. Liu; Z. Zhong; H. Wang, Toluene-assisted synthesis of RHO-type zeolitic imidazolate frameworks: Synthesis and formation mechanism of ZIF-11 and ZIF-12. *Dalton Trans.* **2013,** *42* (47), 16608-16613.

59. R. Banerjee; A. Phan; B. Wang; C. Knobler; H. Furukawa; M. O. Keeffe; O. M. Yaghi, High-throughput synthesis of zeolitic imidazolate frameworks and application to CO2 capture. *Sci.* **2008,** *319* (5865), 939-943.

60. R. Banerjee; H. Furukawa; D. Britt; C. Knobler; M. O. Keeffe; O. M. Yaghi, Control of pore size and functionality in isoreticular zeolitic imidazolate frameworks and their carbon dioxide selective capture properties. *J. Am. Chem. Soc.* **2009,** *131* (11), 3875-3877.

61. Y. Zhang; M. Gutiérrez; A. K. Chaudhari; J. C. Tan, Dye-encapsulated zeolitic imidazolate framework (ZIF-71) for fluorochromic sensing of pressure, temperature, and volatile solvents. *ACS Appl. Mater. Interfaces* **2020,** *12* (33), 37477-37488.

62. E. Aunan; C. W. Affolter; U. Olsbye; K. P. Lillerud, Modulation of the thermochemical stability and adsorptive properties of MOF-808 by the selection of non-structural ligands. *Chem. Mater.* **2021,** *33* (4), 1471-1476.

63. Y. Q. Hu; M. Q. Li; Y. Wang; T. Zhang; P. Q. Liao; Z. Zheng; X. M. Chen; Y. Z. Zheng, Direct Observation of Confined $I^{-}\cdots I_2\cdots I^{-}$ Interactions in a Metal-Organic Framework: Iodine Capture and Sensing. *Chem. Eur. J.* **2017,** *23* (35), 8409-8413.

64. T. Hasell; M. Schmidtmann; A. Cooper, Molecular doping of porous organic cages. *J. Am. Chem. Soc.* **2011,** *133* (38), 14920-14923.

65. F. Dultsev, F., Polymeric films based on long-chain acetylenes as sensors for iodine vapour. *Sens. Actuators B Chem.* **2008,** *129* (1), 171-175.

66. L. J. Small; T. M. Nenoff, Direct electrical detection of iodine gas by a novel metal-organic framework based sensor. *ACS Appl. Mater. Interfaces* **2017,** *9* (51), 44649-44655.

67. L. J. Small; R. C. Hill; J. L. Krumhansl; M. E. Schindelholz; Z. Chen; K. W. Chapman; X. Zhang; S. Yang; M. Schröder; T. M. Nenoff, Reversible MOF-Based Sensors for the Electrical Detection of Iodine Gas. *ACS Appl. Mater. Interfaces* **2019,** *11* (31), 27982-27988.

68. L. J. Small; J. L. Krumhansl; D. X. Rademacher; T. M. Nenoff, Iodine detection in Ag-mordenite based sensors: Charge conduction pathway determinations. *Micropor. Mesopor. Mat.* **2019,** *280*, 82-87.

69. P. Chen; X. He; M. Pang; X. Dong; S. Zhao; W. Zhang, Iodine capture using Zr-based metal–organic frameworks (Zr-MOFs): Adsorption performance and mechanism. *ACS Appl. Mater. Interfaces* **2020,** *12* (18), 20429-20439.

70. P. H. Svensson; L. Kloo, Synthesis, structure, and bonding in polyiodide and metal iodide− iodine systems. *Chem. Rev.* **2003,** *103* (5), 1649-1684.

71. A. Sen; S. Sharma; S. Dutta; M. M. Shirolkar; G. K. Dam; S. Let; S. K. Ghosh, Functionalized ionic porous organic polymers exhibiting high iodine uptake from both the vapor and aqueous medium. *ACS Appl. Mater. Interfaces* **2021,** *13* (29), 34188-34196.